Improved design of nonlinear energy sink : application to passive vibration control

Zhenhang Wu

Université Fédérale
Toulouse Midi-Pyrénées

THÈSE

En vue de l'obtention du

DOCTORAT DE L'UNIVERSITÉ DE TOULOUSE

Délivré par:
Institut National des Sciences Appliquées de Toulouse (INSA Toulouse)

Présentée et soutenue par :
Zhenhang WU

le Mardi 31 mai 2022

Titre :
Conception avancée d'un absorbeur non linéaire de type NES : application au control passif des vibrations

---

École doctorale et discipline ou spécialité :
ED MEGEP : Génie mécanique, mécanique des matériaux

Unité de recherche :
Institut Clément Ader, CNRS UMR 5312

Directeur/trice(s) de Thèse :

Manuel PAREDES	Professeur, INSA de Toulouse	Directeur
Sébastien SEGUY	MCF HDR, INSA de Toulouse	Co-Directeur

Jury :

Olivier THOMAS	Professeur, Arts et Métiers Lille	Rapporteur
Emeline SADOULET-REBOUL	MCF HDR, Université de Franche Comté Besançon	Rapporteur
Pierre Alain YVARS	Professeur, SUPMECA Paris	Président

Acknowledgment

When I finished my doctoral defence, my heart was full of mixed feelings. All the happy, beautiful, painful, anxious, vivid and enthusiastic memories of my PhD period crowded into my mind. I would like to thank my supervisors and friends for their guidance and companionship and for keeping my most precious time in this land.

I would like to express my extreme gratitude to my two supervisors, Prof. Manuel PAREDES and Dr Sébastien SEGUY, who gave me enough freedom and encouragement to explore this issue. Their deep insight and brilliant guidance helped me save a lot of time, both in terms of experiment and implementation of concepts. I am fortunate to be their student and hope that my work is worthy of their expectations and trust in choosing me as a PhD candidate.

I would like to thank the defence committee members: Prof. Olivier THOMAS, Dr Emeline SADOULET-REBOUL, and Prof. Pierre Alain YVARS. Thank you for the time and effort that is devoted to my PhD thesis. Their rigorous requirements were also a significant part of my PhD thesis. It made me understand that as a researcher, readability and rigour are the things we should always pay attention to.

Thanks to Dr Donghai QIU, Dr Tao Li, and Dr Etienne GOURC for their previous research base. I am grateful for their research foundation, which helped me to enter the research field faster and deeper, and I am standing on their shoulders to do my work. I would also like to thank Jean-Benoit ALIBERT engineer, for helping me to implement and set up my series of experiments and for giving me technical support.

I would also like to thank my homeland and CSC for providing me with financial support and the laboratory ICA where I worked. I would also like to thank researcher Zongfeng LI and associate professor Feng ZHANG for their help and trust in my initial application to CSC. And some of my colleagues and friends: Dingdong, Guillermo, Varun, Taiwei, Zongwei, Tohmy, Georges, Gang, Lei, Hao, Huikangyue... those who accompanied me through happy and unforgettable times and helped me in difficult times. I would also like to express my special thanks to Dr Chao REN, as our similar experiences have enabled us to communicate and understand each other more.

I would like to thank my parents, Ms Jianying HE and Mr Cangsong WU, for raising me. During the days when we were unable to reunite, they were the ones who gave me the courage to let me pursue my dream without any fear by providing me with financial and spiritual support. And they are the greatest motivation for my relentless struggle.

Contents

List of Figures

General Introduction

As structures become more sophisticated, large-scale, and the application scenarios more diverse nowadays, the understanding of vibration phenomena has gradually advanced. Much effort has been devoted in the past decades to develop structural control methods to avoid undesired vibrations, satisfy the requirements for structure safety and human health. Compared with active and semi-active control methods, passive control is widely applied in conventional structure designs without external power supplies, sophisticated algorithms, sensors and real-time data-based processors. The Tuned Mass Damper (TMD), as a part of the passive control method, can engage in relatively large motions by resonating nearby nature frequency of the Linear Oscillator (LO). The attached mass has been built relatively large, introducing other resonance peaks in the vicinity of the natural frequency of the LO to realize ideal vibration mitigation. Moreover, the effectiveness of TMD drops dramatically when the external excitation frequency shifts away from its natural frequency.

A nonlinear absorber termed a Nonlinear Energy Sink (NES) offers an alternative strategy to overcome the limitation of TMD. The NES uses a nonlinear component to substitute the linear stiffness of the attached system in the TMD. According to the characteristic of nonlinearity, the NES can be categorized as cubic NES, bistable NES, vibro-impact NES, rotary NES, track NES, etc. Nonlinearity implies adaptive properties. So the NES performs a broader absorbing frequency than TMD, and it shows strong robustness facing the degradation of systems parameters. The NES can dissipate the energy of LO with high efficiency through damping. This one-way, irreversible energy transfer mechanism is called the Targeted Energy Transfer (TET), where the LO and NES oscillate in the same frequency, 1:1 resonance. TET has another form of manifestation when the LO withstands a modest harmonic excitation: Strongly Modulated Response (SMR). However, this high-efficiency energy dissipation activation requires an excitation threshold, above which the SMR can be triggered. And it has been observed that the negative stiffness helps the bistable NES performs SMR in a lower energy level. A relative small attached mass is also another advantage for NES. The nonlinearity is a key component in the NES system. The experimental device consists of two nonlinear springs: the conical spring or variable pitch springs and two linear springs to realize a cubic nonlinearity. A tunable cubic and bistable nonlinearity can be constructed by choosing a proper pre-compression length of linear springs.

Based on the above discussion, the following essential questions are required to be interpreted:

- How to identify the optimal state for both cubic NES and bistable NES? Which parameters determine the ceiling of the maximal absorbing efficiency? Whether the pre-compression length can be adjusted to optimize the device for different excitations?

- Since the bistable NES introduce an inevitable chaotic motion, is there a way to quantitatively predict its emergence? What is the relationship between SMR's triggering mechanism and bistable's topological structure, and whether it can bring new alternative ideas for optimization?
- A phase trajectory can describe energy pumping motion along with the Slow Invariant Manifold (SIM) structure. However, there are few descriptions of energy pumping on the time scale in the current study. How to estimate the motion duration in which the energy pumping motion occurs, under transient excitation and under harmonic excitation?
- When the NES is applied, other constraints, such as displacement constraints, bring in other nonlinear factors, collisions. How does this affect the response of the system? Are the conventional analytical methods of cubic NES and vibro-impact NES still describing the two nonlinear coupling cases?

The manuscript consists of the following five chapters to answer the above questions. The first chapter gives a general introduction to the nonlinear absorber. The wide application of control methods is presented first. The fundamental concepts, numerical and analytical tools, are introduced to understand the targeted energy transfer mechanism further. Then the different configurations of the nonlinear absorber and experimental construction are compared. The optimal criteria for NES are finally presented.

The second chapter starts with analytical modeling and the analysis of the response regimes. Then, the optimal states are identified both in the cubic and bistable NES through alternating response regimes under various energy levels. And the parameters, which determine the maximal absorbing efficiency, are given. Finally, a tunable nonlinearity device proves the possibility of transferring the cubic NES into a bistable NES and absorbing energy at maximal efficiency for the different excitation amplitudes.

In the third chapter, the relationship between the response regimes of bistable NES and SIM structure is focused on. Firstly, the extra singularity lines and unstable regions help interpret SMR and chaos trigger mechanism in bistable NES case, with the help of an adapted complexification method and a simplified chaos trigger model. Secondly, the categorization of NES and the response evolution at different energies according to the value of negative stiffness are shown. Finally, the various negative stiffness of bistable NES cases are tested from the view of experiments and applications.

The fourth chapter develops an estimation of energy pumping time. Firstly, a complex integration is transferred into an equivalent point corresponding to a descent process of phase trajectory along with SIM structure during the energy pumping. Secondly, the robustness of estimation is examined under the various distribution of parameters. This technology is also extended into harmonic case with adaption of particular integration. Finally, the experimental results also verify the effectiveness of estimation method.

In the fifth chapter, the cubic NES with the collision is considered. Firstly, a dynamic model of Vibro-Impact Cubic (VIC) NES is constructed. The conventional analytical tool of vibro-impact NES and cubic NES proves their availability in this new issue. Secondly, the length of clearance mainly determines the behaviors of VIC NES. According to the location of the extra fold line in the SIM structure, three kinds of VIC NES with different lengths of the cavity are studied combined with response regimes. Then, an experiment confirms the effect of collision, which is also revealed by numerical simulation.

Finally, some remarkable conclusions are drawn. The perspectives of future studies are presented based on current work.

CHAPTER 1

Literature Review

Abstract

The first chapter offers a basic comprehension of the general background, necessary concepts and research method for Nonlinear Energy Sink (NES). The current vibration control methods are classified. According to the source of nonlinearity, the applications of the nonlinear absorbers have been discussed. The core mechanism of NES: Targeted Energy Transfer (TET), is analyzed by the analytical tools and numerical methods. The various experimental configurations are presented to realize the efficient vibration mitigation.

Contents

1.1 Vibration control methods

Analysis of vibration is an inevitable issue in the engineering field. The generation of vibrations can be diverse in terms of unbalanced rotating machines, sliding component, fluid-solid interaction, earthquakes, and even the activity of biological organisms. Some kind of vibration phenomena can be used to optimize production efficiency.

In the production process, vibration is used for the transport of raw materials, screening, crushing. In geological exploration and oil extraction, vibration-generated stress waves for detection and exploration can improve crude oil production [Sun *et al.*, 2020]. In terms of sustainable energy, the energy generated by the waves can be used to generate clean energy. In another aspect, unwanted vibrations also result in component fatigue, system failure under alternating stresses. The vibration of the cutting head in the machine degrades the surface accuracy of the component. The ground resonance produces serious damage to the structure of the helicopter. The productivity of the wind turbine system will be affected and thus reduces the efficiency due to vibration [Rahman *et al.*, 2015]. More generally, earthquakes cause a huge threat to the building construction and people's lives.

So it should be emphasized that the effective attenuation of undesirable vibration is conducive to enhancing machine performance, prolonging the device's service life and promoting the safety and comfort of structure. The current trend to classify the vibration control is identified as passive control, semi-active control and active control, according to whether the system parameters are adjustable and whether external energy is introduced. The detailed schematic of three types of control methods is presented in Fig. 1.1.

1.1.1 Passive control

A conventional linear absorber device, which possesses the fixed linear stiffness k_2, linear damping c_2 and attached mass m_2, is named Tuned Mass Damper (TMD). Frahm firstly proposed this idea of additional free-to-vibrate mass, which is attached to the Linear Oscillator (LO) [Frahm, 1911]. The TMD can achieve a resonant out-of-motion by tuning the mechanical device that connects the attached mass m_2 to the LO m_1. This resonant phenomenon can suppress the oscillation of m_1 efficiently under the harmonic excitation f_e.

The introduction of an attached mass can cause the mitigation of the resonance peak and create two resonance peaks in the vicinity of natural frequency ω_0 under harmonic excitation. The frequency-response curve of different damping conditions passes through the two specific fixed points A and B in Fig. 1.2a. A low TMD damping will lead to significant amplitude reduction in its natural frequency. But it also causes the huge resonance peaks on two sides of ω_0. The frequencies of two fixed points (ω_A and ω_B) can be calculated through the quadratic equation of the system without consideration of damping force. If the system can be tuned to satisfy the condition $(1+\epsilon)\cdot(\omega_A^2+\omega_B^2) = 2\omega_0^2$, ($\epsilon$ means the mass ratio of attached mass and primary mass, m_2/m_1), an optimal criterion that the same dynamic amplification in points A and B can be constructed as Fig. 1.2b shows. And the two resonance peaks possess the same minimal amplitude. This optimization technique of TMD is demonstrated [Krenk, 2005 ; Nishihara et Asami, 2002]. Other optimizations of TMD are addressed under stochastic excitation or seismic excitation to minimize the mean-square response of main sturcture [Marian et Giaralis, 2014 ; Hoang

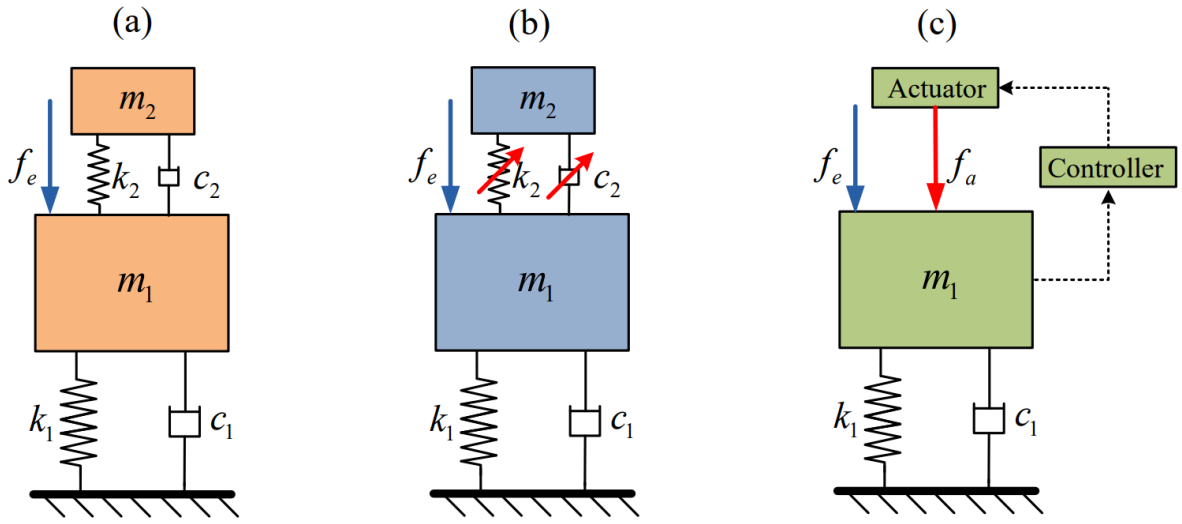

Figure 1.1: Classification of vibration control method (a) passive control (b) semi-active control (c) active control. f_e is external excitation,f_a is actuator force [Qiu, 2018]

et al., 2008 ; Parulekar et Reddy, 2009 ; Bakre et Jangid, 2007]. This kind of control method has been widely used in the area of civil engineering [Xiang et Nishitani, 2014 ; Shi *et al.*, 2018], mechanical equipment [Cho *et al.*, 2020 ; Lian *et al.*, 2018], manufacturing process [Yang *et al.*, 2015] owing to its economical cost and convenient maintenance.

1.1.2 Semi-active control

In the TMD case, if the external force shifts its frequency or the frequency of excitation is not stationary, such as seismic excitation, the suppression effect will decline dramatically. In another aspect, the internal properties of structure may alter with time. A live load distribution leads to the decrease in the vibration absorption effect. The semi-active control provides an alternative way to maintain optimal dynamic performance by adjusting the stiffness and/or damping properties in real-time like Fig. 1.1b.

Compared to the previous method, semi-active can better adapt to a wider range of operating conditions and structures. It was proposed in early 1970 to achieve a similar effect as a fully active control [Karnopp *et al.*, 1974]. Recently, it exists two main methods to regulate the damping force (1) electrorheological (ER) and (2) magnetorheological (MR), which are considered as smart fluid materials [Yao *et al.*, 2002 ; Cai *et al.*, 2007]. The fine particles are mixed into low viscosity liquid. These particles form a chain-like configuration and solidify the suspension liquid when the external magnetic field or current strength reaches a threshold. After solidification in the liquid state, ER has a yield stress of 10 kPa, and MR has a yield stress of 100 kPa. When the electric or magnetic field disappears, the ER, MR will turn back into a liquid state. The time required for transformation is in the millisecond level and requires only watt-level energy control.

A plane rhombus configuration with pivot joints at the vertices was proposed to realize the controllable stiffness [Nagarajaiah et Sonmez, 2007]. It consists of four spring elements, which is controllable by adjusting the aspect ratio of the rhombus configuration through the linear electromechanical actuator. Other kind of resettable variable stiffness devices are also studied [Schleiter et Altay, 2022 ; Lin *et al.*, 2015 ; Liu *et al.*, 2008]

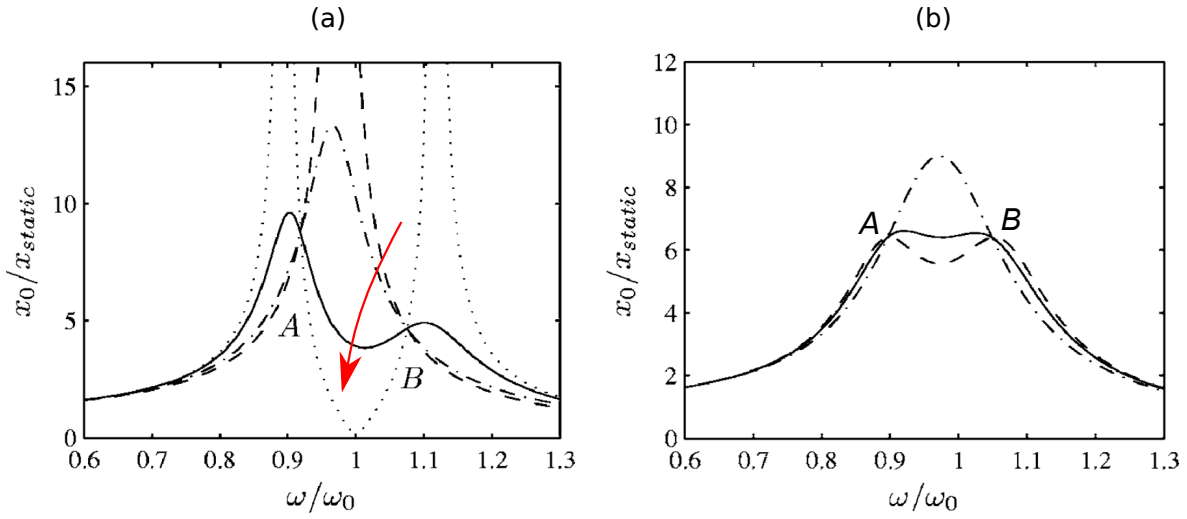

Figure 1.2: (a) Frequency response of amplitude ratio under various TMD damping conditions. The red arrow indicates the designs with lower TMD damping values (b) optimization design of TMD (solid line), classic design (dashed line), larger damping design (chain line) [Krenk, 2005]

The semi-active control method ensures the reliability of absorbing efficiency with low requirement of power and modest cost in seismic protection of structure [Symans et Constantinou, 1999 ; Bitaraf *et al.*, 2010], in aeronautics domain [Hui *et al.*, 2008] and vehicle suspension system [Yao *et al.*, 2002].

1.1.3 Active control

Another strategy to compensate the natural force and minimize the vibration is to apply the required external force f_a in Fig. 1.1c, which is also named as adaptive/active control. A sensor, a real-time feedback controller and an actuator are necessary to realize the active control [Fuller *et al.*, 1996 ; Preumont et Seto, 2008 ; Soong et Costantinou, 2014].

An appropriate active control strategy is crucial to obtain the optimal active control force. Several categories of this control strategy are widely applied i.e the classical linear optimal control [Aldemir *et al.*, 2001], fuzzy control [Nomura *et al.*, 2007], H_2 and H_∞ control [Wang, 2011]. As for the active actuators, they can be hydraulic, pneumatic and other styles. However, involving extra mechanical energy could increase the hardware costs and reduce the reliability of the absorber. Those facts restrict its practical application.

1.2 Nonlinear absorber

The conventional linear vibration absorber possesses lower efficiency under the detuning effect of TMD and nonstationary excitations. A mistuning effect leads to a poor damping performance or even worse response. Although the selection of other semi-active or active control methods can overcome those impacts, it may introduce other problems: increasing cost, introducing external energy, increasing complexity and reducing reliability. However, if the nonlinearity is applied in the implemented passive control system, it will be effective

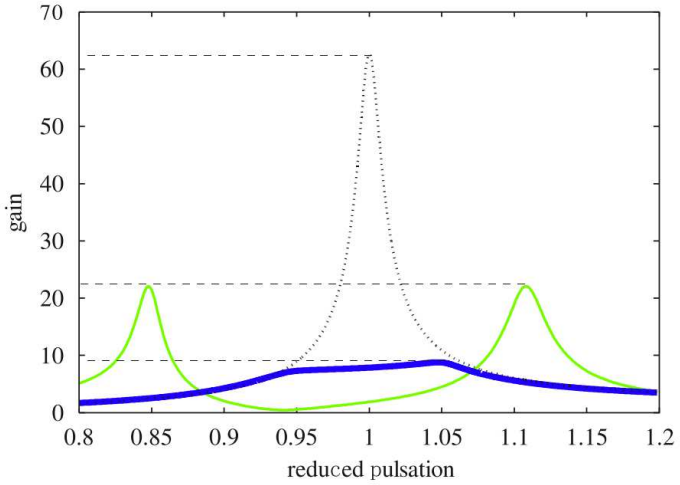

Figure 1.3: Comparison of absorption capacity on frequency band between TMD and NES [Gourdon *et al.*, 2007]. The blue line is the response of the NES. The green line is the response of the TMD. Dotted line is the response of LO without absorber.

for broad frequency bandwidth. At the same time, it maintains the advantage of passive control: relatively low cost, a simple concept and high reliability.

In the past two decades, the Nonlinear Energy Sink (NES), which substitutes linear stiffness with nonlinear component, gained a lot of attentions [Vakakis, 2001]. If the nonlinearity is applied in the TMD, it possesses a non-constant natural frequency. It interprets the NES can effectively dissipate the vibration energy of the LO over a wider frequency band range by damping as illustrated in Fig. 1.3. Compared to the linear absorber, the resonance peak has also been wiped. Non-constant spring rate indicates that it is insensitive to stiffness degradation, so NES has strong robustness facing against changes in the underlying structure [Wang *et al.*, 2015 ; Tripathi *et al.*, 2017]. The mass ratio of TMD is about 10%. Meanwhile, the mass ratio of NES can be 1% while maintaining good performance of absorbing [Gourc *et al.*, 2015a].

Another significant point of distinction is that the high efficient absorbing for NES only can be triggered when the vibration amplitude exceeds a critical threshold. When external excitation exceeds this threshold, the NES will produce irreversible energy transfer from the LO into NES and dissipate energy by damping [Starosvetsky et Gendelman, 2008 ; Gourc *et al.*, 2012]. This mechanism is called Targeted Energy Transfer (TET), which is explained in the following section.

A potential **definition** of NES can be given: *The NES is an absorber that consists of a nonlinear component and an attached mass to achieve the vibration mitigation.* The NES can connect the primary system through the following two methods as Fig. 1.4 shows. In the first configuration, the attached mass is connected to the primary system through a weakly coupling stiffness. On the other side, the attached mass is grounded by the cubic nonlinearity. In the second configuration, NES is linked to the primary system by the cubic nonlinearity directly [Lee *et al.*, 2005a]. In this thesis, the primary system is always referred to as the Linear Oscillator (LO).

The grounded configuration of NES is widely studied [Jiang *et al.*, 2003 ; Malatkar et Nayfeh, 2007 ; Musienko *et al.*, 2006]. The grounded structures can make some

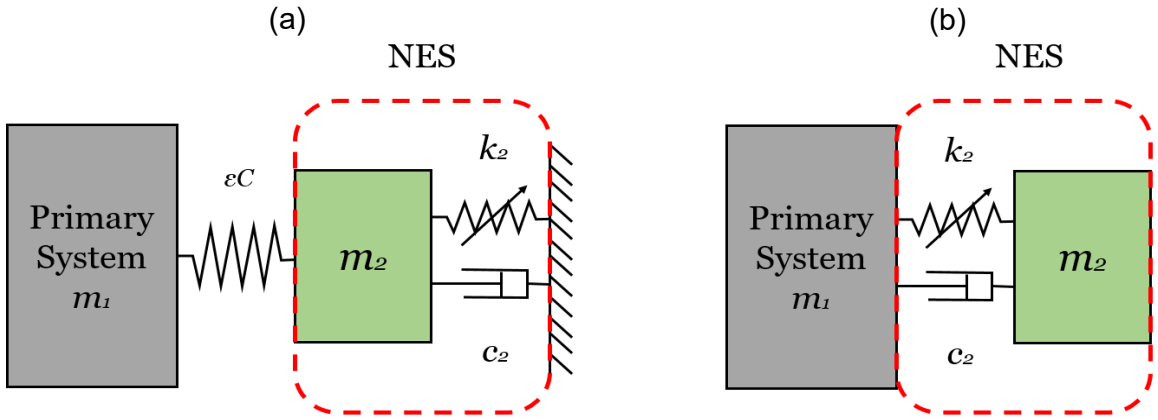

Figure 1.4: Two different installation configurations of NES (a) grounded (b) ungrounded. The NES systems are marked by the dashed red boxes.

convenience in engineering, especially for rotor systems [Yao *et al.*, 2019]. However, the requirement of fixed ground is hard to achieve in some other conditions. The two configurations are compared by Gendelman [Gendelman et Lamarque, 2005]. The second configuration shows a more efficiency in vibration mitigation with a lower mass ratio. So in our thesis, the second configuration is addressed.

1.2.1 Different types of NES

To construct the NES, knowledge about the sources of nonlinearity is necessary. It can originate from geometric nonlinearity, vibro-impact, dry friction or properties of the material.

- Geometric nonlinearity

  The linear stiffness of the spring means that the restoring force is proportional to the displacement. Nonlinearity means that this condition is not satisfied. The relationship between force and displacement may be cubic or piecewise. Fig. 1.5a shows the nonlinear force-displacement relationship comes from the trigonometric arrangement of two linear springs. The force-displacement relationship is a curve instead of a straight line (linear).

- Vibro-impact

  The velocity of two solids will change suddenly in a very short time when contact occurs. This change is accompanied by a variation in velocity magnitude and direction as Fig. 1.5b. The analytical description of the vibro-impact dynamics is studied and shows the possible application in oscillators with inelastic impact [Pilipchuk, 2015].

- Dry friction

  Considering the friction of the system also introduces nonlinearity. Even the simplest dry friction can cause discontinuities. This discontinuity of the frictional force can be described by Coulomb's law as Fig. 1.5c.

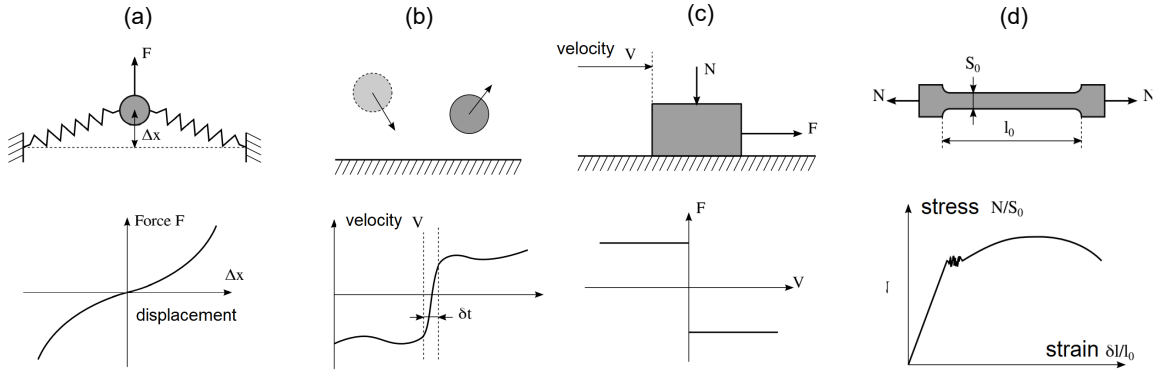

Figure 1.5: Sources of nonlinearity (a) geometric nonlinearity achieved by assembling two springs (b) simplified shock model (c) dry friction (d) material nonlinearity of metal stretching [Gourc, 2013]

- Material nonlinearity

  A classical material nonlinearity appears in the metals. Initially, the metal shows a linear strain/stress relationship. When at the higher strains the material yields, the response becomes nonlinear and irreversible as Fig. 1.5d.

Figure. 1.5c shows a simplified friction law. But in reality, the behavior of friction is very sophisticated. Mastering the friction in the NES design is still a challenge. Moreover, large-scale deformation often implies a failure of the system. NES designs also make little use of material nonlinearity. So mastering the nonlinearity to achieve parameter design mainly relies on the first two kinds of nonlinearities: geometric and impact.

Depending on the source of nonlinearities, various types of NES are realized, for example, a cubic NES, a Vibro-Impact (VI) NES, rotary NES, track NES [Wang *et al.*, 2015] and a piecewise NES [Yao *et al.*, 2018] as Fig. 1.6 shows. Among them, the control of cubic, bistable nonlinearity and impact is the core of this thesis.

1.2.2 Geometric nonlinearity configuration

Cubic nonlinearity contributes significantly to the construction of NES. In the early stage, Roberson constructed a nonlinear component by means of a spring whose load-deflection characteristic is the sum of a linear and cubic term [Roberson, 1952].

The conical spring and variable pitch spring can provide desirable cubic nonlinearity by the proper design of its diameter of the biggest/smallest coils and the pitch distribution [Qiu *et al.*, 2018b ; Qiu *et al.*, 2019a]. The negative stiffness mechanism is required to counterbalance the linear terms in nonlinear force-displacement phase to obtain the pure cubic nonlinearity so-called quasi-zero stiffness mechanism as Fig. 1.7a shows.

Permanent magnets can also form nonlinear restoring forces. The permanent magnet is connected to the end of a small horizontal beam to provide the repulsive force or attractive force in the vertical direction, caused by the other fixed magnets [Fang *et al.*, 2017] as Fig. 1.7b shows. If a tuning piezoelectric beam with a movable tip magnet substitutes the fixed magnet, a tuned bistable NES is constructed [Fang *et al.*, 2021]. Both vibration suppression and energy harvesting can be simultaneously improved by the

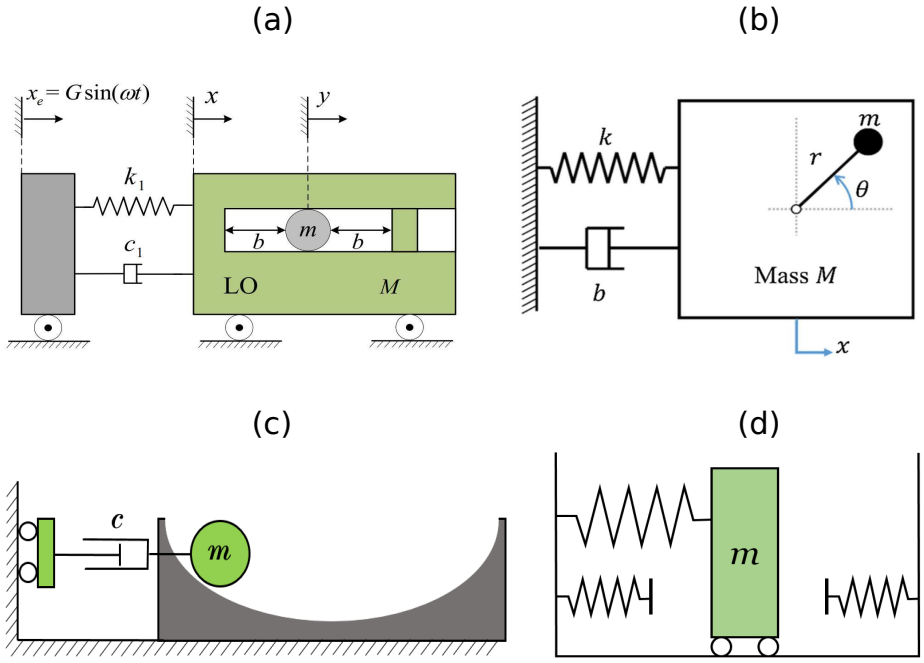

Figure 1.6: Schematic of representation of various NES (a) VI NES [Qiu, 2018] (b) rotary NES [Saeed *et al.*, 2020] (c) track NES (d) piecewise NES

optimal implementation of the mechanical damping ratio, the resistance of the piezoelectric element, the thickness of the beam, etc.

A permanent magnet is placed vertically inside a tube as Fig. 1.7c shows. Two magnets are fixed at both ends of the generator tube housing. By varying the distance between the bottom and center magnet, magnetic restoring forces are calibrated [Mann et Sims, 2009 ; Saha *et al.*, 2008]. When other magnets are placed symmetrically around the midpoint of the tube, the center magnet is repelled away from the midpoint and produces a bistable nonlinearity [Saha *et al.*, 2008]. Another oblique-magnet configuration consists of two symmetric pairs of oblique magnets to produce vertical direction force without horizon forces [Robertson *et al.*, 2012].

In the acoustic system, a thin visco-elastic membrane performs much larger amplitude oscillations than membrane thickness under pressure in the coupling box, as Fig. 1.7d shows. The nonlinear behaviors can be defined as the ratio of pressure and transversal displacement of the center of the membrane [Bellet *et al.*, 2010 ; Bellet *et al.*, 2012]. The nonlinearity of the acoustic membrane depends on the thickness of the film and the square of the radius.

By analogy with the symmetry membrane structure, a thin rod, such as a piano wire in Fig. 1.7e, with no pretension, clamped at both of its ends, can also perform a transverse vibration at its center [McFarland *et al.*, 2005a]. This geometrically nonlinear spring can achieve a cubic nonlinearity. In [Wierschem *et al.*, 2012], a broadband passive damping effect responding to impulsive excitations was proved experimentally.

The above studies show several methods to construct the cubic nonlinearity. However, a pure cubic nonlinearity without other linear stiffness components is still a challenge. So it's necessary to consider the dynamic behaviors coupled with both cubic NES and other stiffness component. An essential type of stiffness perturbation is negative stiffness. It

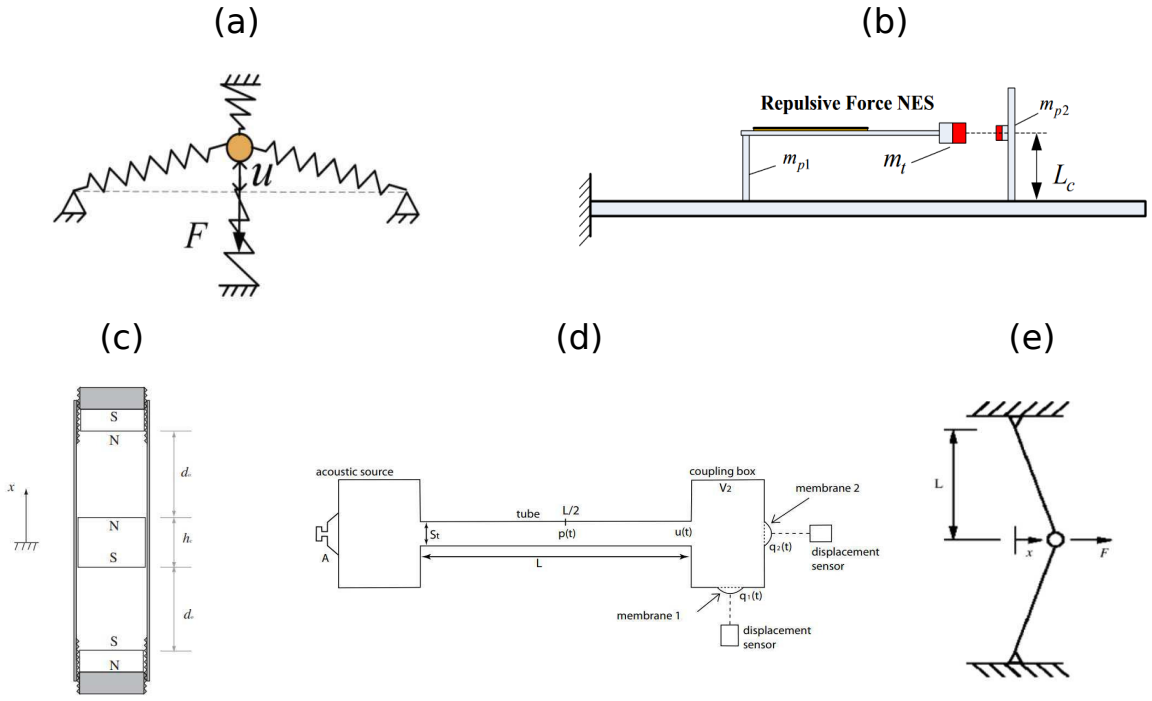

Figure 1.7: Realization of nonlinearity by (a) spring system [Qiu *et al.*, 2018b] (c) permanent magnet [Mann et Sims, 2009] (b) magnet coupled to an elastic beam [Fang *et al.*, 2017] (d) membrance in acoustic system [Bellet *et al.*, 2012] (e) wire [McFarland *et al.*, 2005a]

can be realized by a larger pre-compression linear spring [Johnson *et al.*, 2013], buckled beam fixed on a support [Mattei *et al.*, 2016] and the magnetic attraction (repulsion), [Erturk et Inman, 2011]. The analytical modeling of bistable NES has been carried out by Menivitch through the complexification-averaging analysis [Manevitch *et al.*, 2014] so that it can achieve a predictive design of bistable NES for optimal TET. The mechanism of 1:1 and 1:3 internal resonances is revealed. Romeo identified the rate of overall energy dissipation of bistable NES under various energy inputs by means of Frequency-Energy Plots (FEP) [Romeo *et al.*, 2015b]. The experimental bistable NES device, based on the transverse displacement of the center of a composite bistable plate [Shaw *et al.*, 2013] is carried out. It shows a greater isolation region and a lower peak response to base excitation than the equivalent linear system. Increasing the knowledge related to the bistable NES is another objective in this thesis.

1.2.3 Impact configuration

Another important family of NES is associated with impact. Due to the existence of assembly errors, there can be clearance between the components, such as loosening joints. The components then collide with each other in the presence of vibration. When two objects collide for a short period of time, the instantaneous velocity magnitude and direction change due to the presence of the recovery factor. This implies a loss of energy. This useful phenomenon is applied efficiently for energy absorption or harvesting. This kind of absorber is named Vibro-Impact (VI) NES as Fig. 1.6a shows. The asymptotically

stable motion of two rigid masses in VI NES dates from the 1980s to provide a basis for detecting progressive wear in mechanisms [Bapat *et al.*, 1983]. And the experimental results confirm the parameters influence of mass ratio, coefficient of restitution, and gap size on the free vibrations [Bapat et Sankar, 1985]. Bapat also developed a general analytical method to describe multiple stable impacts per period of motion. The model considered an inclined impact damper with friction and collision on either one or both sides of the main mass with identical and non-identical coefficients of restitution [Bapat, 1995]. VI NES shows its potential in seismic mitigation of structures [Nucera *et al.*, 2007]. A three-story shear-frame system, coupled with VI NES to the top floor, was well protected under seismic excitation [Nucera *et al.*, 2008]. Other applications of VI NES are presented [Babitsky, 2013].

VI NES is also referred to as an impact damper, and its behaviors under different energy inputs have been extensively studied [Li *et al.*, 2017c ; Gendelman, 2012]. The NES ball, which vibrates in a cavity with a pre-designed gap, causes rapid decrease of the amplitude of the primary mass. Similar to the cubic NES, VI NES can also perform a TET. The mechanism of TET and its complicated dynamics have been further studied [Lee *et al.*, 2009] by means of frequency-energy plot.

Inspired by the VI NES concept, other similar NES improvements have been proposed, such as multiple balls in parallel [Li *et al.*, 2017a]. If multiple balls exist in the cavity to absorb energy, it's a so-called particle damper [Lu *et al.*, 2014]. When the excitation frequency is low, lacking relative motion between the particles and enclosure lead to a low damping effect. The chaos region, which causes damping performance to degrade, exists below and above the resonance frequency. When the LO performs a periodic motion near the resonance frequency of the LO, maximum granular damping is achieved. [Sánchez et Carlevaro, 2013].

1.3 Dynamic of linear oscillator coupled with NES

The Linear Oscillator (LO) coupled with NES implies several dynamic behaviors, which can be generally categorised into the following three types:

- (1) Periodic response

  The periodic response is a fundamental phenomenon, where the amplitude of LO and NES is kept constant as Fig. 1.8a shows. The NES is capable of absorbing energy from the LO by a steady-state vibration. The large amplitude of displacement between LO and NES is directly related to the efficiency of steady-state energy absorbing. However, the steady response is might be unstable facing the force perturbation [Jiang *et al.*, 2003] or even in different initial conditions [Gendelman et Starosvetsky, 2006].

- (2) Quasi-periodic response

  When the amplitude of the system is modulated and presents a periodicity, it is termed as the quasi-periodic response. Quasi-periodic responses arise from various nonlinear dynamic systems under a single-frequency excitation. In the close vicinity of the main resonance system with NES, quasi-periodic oscillation is more obvious than the steady-state. According to modulation of quasi-periodic response, it can

be described as weakly (Fig. 1.8b) and strongly (Fig. 1.8c). *This strongly quasi-periodic response is termed as Strongly Modulated Response (SMR). The modulation of the oscillations is very deep and its amplitude is comparable to the amplitude of the response itself* [Starosvetsky et Gendelman, 2008]. The enormous variation of SMR in amplitude allows it to be distinguished from steady-state or weak quasi-periodicity.

- (3) Chaotic response

  Chaos is an essential characteristic of a nonlinear system. It can be witnessed not only in the bistable NES system (Fig. 1.8d) during the transition from an intra-well oscillation to a cross-well oscillation but also in the VI NES case as a result from impact. The slight perturbation of system parameters will result in a significant change of regime from a steady response to chaotic motion [Zang et Chen, 2017]. This process is termed as bifurcation. The bifurcation, route to chaos and dynamic response regimes with the variation of damping parameters and mass ratio has been investigated [Li *et al.*, 2017c]. To indicate the occurrence of chaotic motion, the Lyapunov exponent can be applied as a numerical method [Grinberg *et al.*, 2012]. A positive exponent means chaos. Melnikov method provides the analytical parameter boundary to predict and control the chaos [Savadkoohi *et al.*, 2011].

When the LO and NES oscillate at the same frequency, 1:1 resonance, it triggers an efficient way to dissipate the energy of LO. This efficient energy transfer is referred to as Targeted Energy Transfer (TET). This process is the mechanism that *the energy of some form is directed from a source (donor) to a receiver (recipient) in a one-way irreversible fashion, it governs a broad range of physical phenomena* [Vakakis *et al.*, 2008]. In the context of NES, TET describes procedures in which the LO's energy is irreversibly transferred into NES mass and finally dissipated by the NES damping through resonance capture. This type of efficient vibration mitigation phenomenon has been observed in various types of NES, for example, piecewise NES [Lamarque *et al.*, 2011], VI NES [Li *et al.*, 2017a], bistable NES [Habib et Romeo, 2017].

1.3.1 Hamiltonian system

To realize the effect of TET, damping is necessary to dissipate the energy. However, the dynamic of TET in weak damping cases can be explained in terms of the periodic orbits of the Hamiltonian system. The relationship between response regime and energy can also be illustrated by the frequency-energy plot.

It is found that there exist three kinds of branches in the frequency-energy plot in Fig. 1.9: (1) two main backbone branches (2) subharmonic branches (3) special branches.

The main backbone branches are marked as $S11+$ and $S11-$, which indicate the NES and LO oscillate in the same dominant frequency. +/- means that NES and LO vibrate in-phase or out-phase, respectively. The two main backbone branches are divided by the natural frequency of LO ($\omega = 1$). 1: 1 orbit requires a specific value of the initial energy level (amplitude of the excitation) to be activated. A more detailed introduction of excitation threshold can be referred to [Lee *et al.*, 2008]. This concept of threshold energy is the most important difference compared to the traditional TMD.

The subharmonic branches are the horizontal branches along the main branch. Those orbits are marked as the tongues curves, which are separated from the main branches

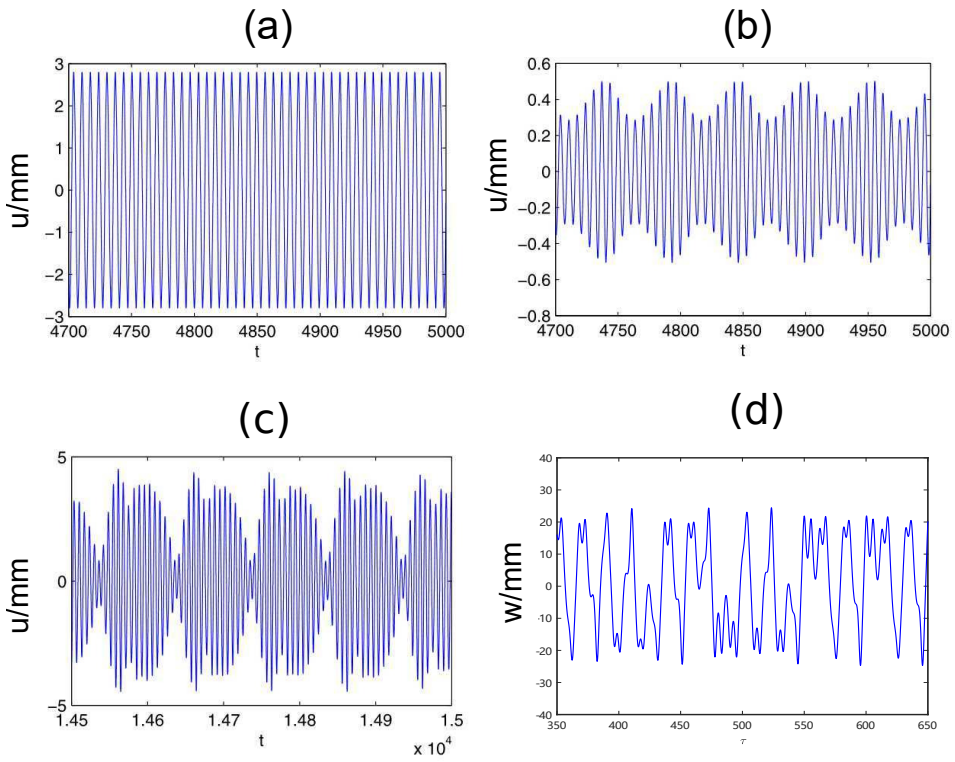

Figure 1.8: Examples of dynamic behaviors in NES. (a) periodic response, (b) weakly quasi-periodic response, (c) strongly quasi-periodic response of LO in 2-degrees-of-freedom NES system under harmonic force, respectively. u represents the absolute displacement of LO [Grinberg *et al.*, 2012] (d) Chaos motion in 1-degree-of-freedom bistable NES system under harmonic force [Qiu *et al.*, 2018a]. w is the relative displacement between LO and NES

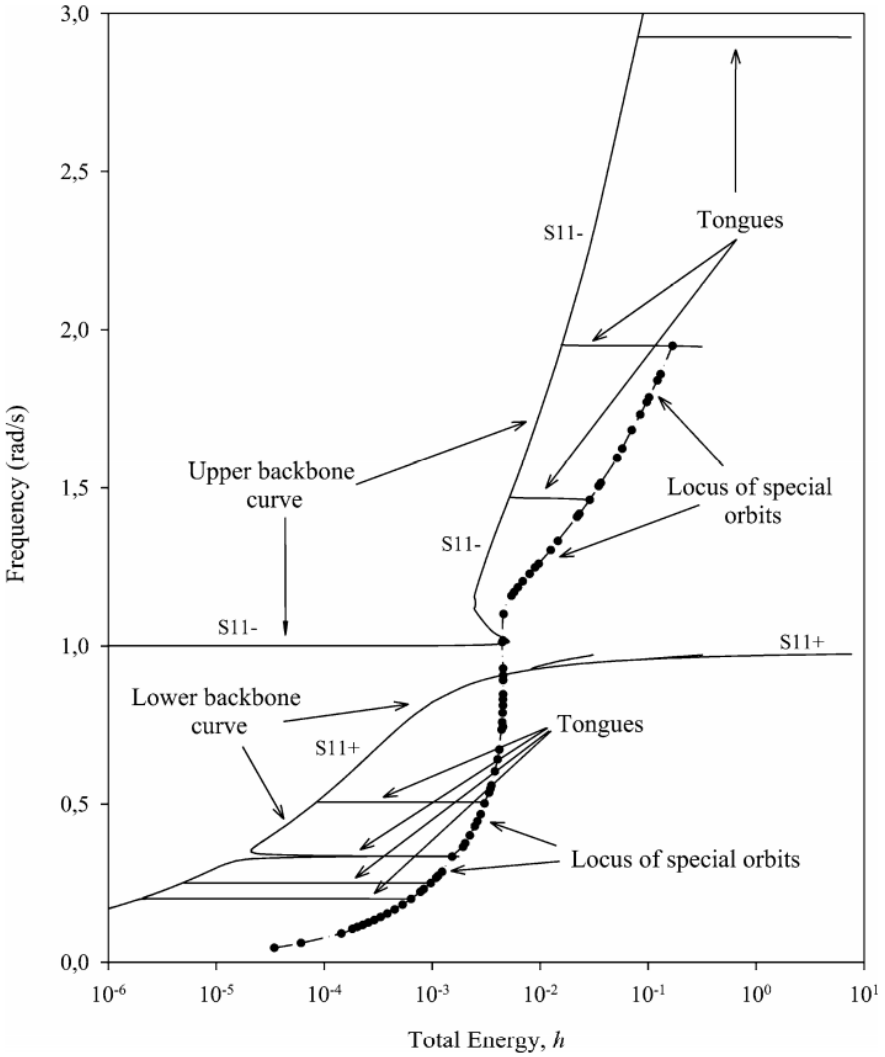

Figure 1.9: Frequency-energy plot of a linear oscillator coupled to a NES [Kerschen *et al.*, 2007]

in Fig. 1.9. The subharmonic branches $S13\pm$ mean that the LO oscillates 'three times faster' than the nonlinear attachment. The calculation of subharmonic orbits is carried out [Lee *et al.*, 2005a]. The horizontal subharmonic orbits locate in a lower energy region means that LO oscillates in a faster way with respect to NES.

The special branches are marked by black circles in Fig. 1.9. Those special orbits play the role of connecting the main $S11\pm$ branches and other subharmonic orbits. Those moderate energy level orbits are considered as nonlinear beats, which occur in the initial phase of 1:1 resonance. Those special orbits have been studied analytically using the complexification-averaging method first introduced by Manevitch [Manevitch, 1999].

Another crucial feature of the branches of the nonlinear Hamiltonian system is frequency-energy dependence. With increasing energy, the frequency of the oscillator possesses a higher frequency. Those three kinds of branches correspond to the three types of TET in a weak damping system: (1) fundamental TET through 1:1 resonance (2) subharmonic TET through subharmonic orbits (3) TET initiated by nonlinear beats. These three essential response regimes can be better interpreted by the Wavelet Transform (WT).

The undamped backbone is superimposing the WT analysis of NES sytem in a transient response [Lee *et al.*, 2005a]. The initial motion locates on the upper high energy tongues in Fig. 1.9. It produces an initial nonlinear beat that channels a major portion of energy to NES in a fast time scale to trigger efficient TET [Kerschen *et al.*, 2005 ; Sigalov *et al.*, 2012]. The WT shows this nonlinear beat corresponds to vertical special orbits that connect $S11-$ branch and $S11+$ branch in Fig. 1.9. Both amplitudes of LO and NES drop through dissipation of damping. When the nonlinear beat vanishes, the system engages in 1:1 resonance capture. As energy further decreases, the heavy shaded moves down along the $S11+$ backbone. In the above three mechanisms of TET, the 1:1 resonance has the most efficiency to transfer almost 100% instantaneous energy of LO to NES. Meanwhile, nonlinear beats only achieve 55% [Kerschen *et al.*, 2008].

The overlapping of the WT shaded area and the backbone curve fully illustrate the underlying hamiltonian system dominating the relatively small damping system dynamics substantially. So, the Hamiltonian system can be a good reference for the corresponding system with weak damping through the frequency-energy analysis. Essential orbits, for example, fundamental 1:1 resonance, subharmonic orbits and the special orbits explain the features of TET, the states of the system and transitions between different energy levels.

1.3.2 Nonlinear normal mode

Nonlinear Normal Mode (NNM) can be considered as an extension of linear normal mode. In nonlinear systems, the modes of the system are related to the energy level and do not have modal superposition properties. So to overcome this disadvantage in a nonlinear system, Rosenberg proposed that *NNM requires that all material points of the system reach their extreme values and pass through zero simultaneously and allows all displacements to be expressed in terms of a single reference displacement* [Rosenberg, 1960]. Shaw and Pierre extend this concept to the damping system that NNM is a two-dimensional invariant manifold in phase space, so the orbits that start out in the manifold remain in it for all time [Shaw et Pierre, 1991 ; Shaw et Pierre, 1994].

The relationship between NNMs and backbone curves in frequency-energy plot is that every point of undamped backbone represents a minimal period of periodic motion (NNMs) and conserved energy, which contains the potential and kinetic energies.

Another difference from the linear modes is that the nonlinear modes interact via internal resonance. So the number of nonlinear model modes can exceed the degree of freedom of the system due to the mode bifurcation [Vakakis, 1997]. More modes are produced through internal resonance, which is more easily triggered in a higher energy level.

NNMs of 2-DOFs mass-spring system with cubic nonlinearities are investigated [Jiang *et al.*, 2005] as well as NNMs of piecewise system with shock absorbers [Mikhlin et Perepelkin, 2011]. The NNMs of a continual mechanical system are analyzed [Avramov et Mikhlin, 2010].

1.4 Analytical methods

Numerous analytical techniques exist to predict the response of NES system. Generally, the Harmonic Balance Method (HBM) and Multiple Scales Method (MSM) are widely used to investigate the 1:1 resonance capture so as to guide the design of the NES system.

1.4.1 Perturbation method

An exact analytical solution can be hardly obtained when the system involves nonlinear components. So, the perturbation method is used to find an approximate solution by starting from the exact solution of related, simpler problems [Nayfeh *et al.*, 1980 ; Neyfeh et Balachandran, 1995]. In the perturbation method, a small parameter ϵ, which is always relative to the mass ratio in NES system, is introduced to express the solution into power series, like $A = A_0 + \epsilon^1 A_1 + \epsilon^2 A_2 + ...$ The A_0 is the known solution to the solvable problem. A_1 and A_2 represent the first-order, second-order terms. In the successive term, a higher power of ϵ results in less important but necessary correcting terms. Usually, only the first two terms are kept by truncating the higher series.

The HBM is an alternative approximate method to calculate the steady-state response of a nonlinear system. The initial idea for HBM is that the steady-state response can be viewed as a quasi-sinusoidal, despite the fact that the nonlinear influence exists in the system. Compared with the perturbation method, the application of HBM can not only be restricted in a weakly nonlinear system but also be adapted in a strong nonlinear system. The potential application of HBM in the NES problem has been implementing [Malatkar et Nayfeh, 2007]. If the system possesses the cubic nonlinearity, only odd harmonic terms have been included in the Fourier expansion.

The order of the Fourier expansion terms dominates the accuracy solution in HBM. A higher order of harmonic terms requires a higher order equation, which leads difficulty to solve the equation. When the order of expansion is too small, it can converge fast but causes a relatively large error. So to address this drawback, the Incremental Harmonic Balance Method (IHBM) has been proposed. And the application of IHBM has been implemented in cubic nonlinear system [Cheung *et al.*, 1990] to trace the frequency response curve automatically, as well as the stability of the periodic solution. The application of IHBM method on the piecewise NES case is also carried out [Wang *et al.*, 2019].

In nonlinear system's response, the variety of amplitude is always slower than the oscillation. So to extract the information of amplitude, the multiple scales method expands the real time into multiple and independent time scales $\tau_k = \epsilon^k \tau, k = 0, 1 \ldots$. Then those time scales are subsitituded into the equation of system. Different scales with the same order of small parameter ϵ are extracted to better explore the dynamic behaviors. The multiple scales method is always introduced by Manevitch variable [Manevitch, 2001]. A single complex variable describes the reduction of variables of displacement and velocity and decomposes the oscillation of the system into slow envelope modulation and another fast oscillation part. This method is also accompanied by the Complexification-Averaging (CX-A) procedure and is also applied in the NES with non-polynomial potential [Gendelman, 2008] and piecewise system [Lamarque *et al.*, 2011].

When the dynamical flow is considered in the vicinity of a 1:1 resonance manifold, only the first harmonic is considered in Manevitch variable. However, some NES, such

as the bistable NES, also contains higher harmonic terms, which is also considered by D.Bitar [Bitar *et al.*, 2020] into classic Manevitch's complex variables to improve the approximation of NES displacement.

1.4.2 Slow invariant manifold

The combination of the multiple scales method and complexification-averaging method can generate a general equation that describes the variation of motion along the Slow Invariant Manifold (SIM). In the context of NES, *SIM is a topologic structure that manifests the quantitative relation between NES and LO motion. It represents an intrinsic characteristic of the system and will not be influenced by external excitations.* Every point in the SIM curve represents a possible periodic solution of LO and NES. It enables to explain the main dynamic regimes characterizing the nonlinear response of different types of NESs under either impulsive or harmonic excitation.

According to different characteristics of nonlinearity, various SIM structures exist in different NES like Fig. 1.10. A classic SIM of cubic NES possesses two singularity points corresponding to the points of local maximum and minimum. The stability of the fixed point is evaluated by the introduction of perturbations. The substitution of perturbation term transfers the equation of the system into matrix form. So the root of the characteristic equation indicates the stability of the periodic solution. If one of the roots has no positive part, the fixed point is stable, vice versa. The two singularity points identify the middle curve as an unstable region, for example the dashed curve part in Fig. 1.10a.

In a VI NES, the numerical simulation shows the important role of SIM to identify the period of motion under transient and harmonic periodic force [Li *et al.*, 2016]. The SIM of VI NES possesses a simpler structure that consists of the left unstable branch and partial stable region on the right branch in Fig. 1.10b. The lack of an upper singularity point causes the maximum amplitude of the LO in each SMR cycle to vary. It is seen that the maximum local amplitude of LO is different every time. Meanwhile, in the cubic case, the maximum amplitude of the LO in the SMR is always approximately the same. This response characteristic distinguishes the VI NES from the normal cubic NES.

In a non-smooth system with a piecewise nonlinearity, the SIM structure is presented in Fig. 1.10c. Similar to the cubic nonlinearity case, the unstable region is located in the middle of SIM. The simulation result indicates that the slow flow of dynamic behaviors under the impulse and sinusoidal loading move along the SIM structure [Lamarque *et al.*, 2011]. When the energy of the system is intensive enough, the energy is dissipated effectively until it reaches the down singularity point. During this period, both amplitudes of LO and NES decrease give evidence of TET in a non-smooth nonlinear system.

The rotary NES has a special form of SIM that the left branch maintains all stable, the right branch of SIM indicates unstable in Fig. 1.10d. Linear stability analysis shows that the stability is eliminated by a saddle-node bifurcation. During the regime of resonance capture, the phase trajectory slides down along with the stable branch of the SIM until the LO amplitude reaches the critical threshold where the resonance capture breaks down. The phrase trajectory escapes from the SIM. It signifies the end of the regime of TET [Saeed *et al.*, 2020].

The necessary condition for the existence of TET and SMR can be conducted through SIM. If damping parameters are too large, the two singularity points disappear. The

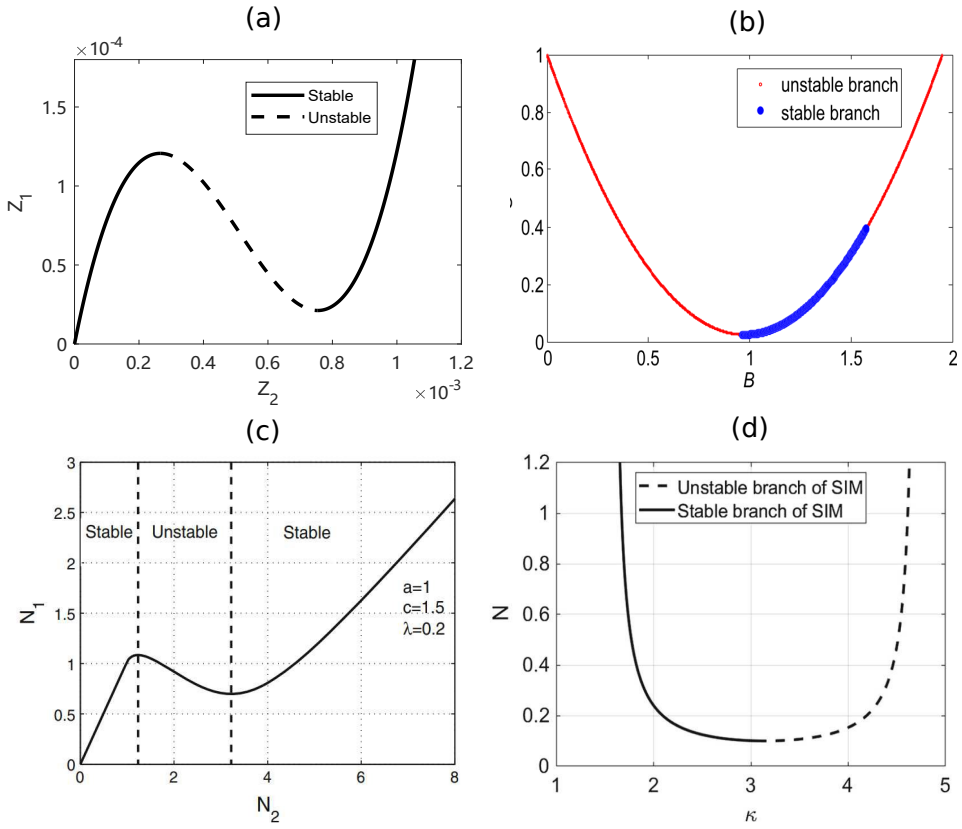

Figure 1.10: (a) SIM structure of cubic NES. The solid curves represent the stable branch, and the dashed line is the unstable branch [Qiu *et al.*, 2018a] (b) SIM of VI NES: one stable branch in bold line and two unstable branches in fine line [Li *et al.*, 2017c] (c) SIM of piecewise NES [Lamarque *et al.*, 2011] (d) SIM of the rotary NES with left stable branch and right unstable branch [Saeed *et al.*, 2020]. The x-axis represents the information of LO motion and the y-axis represents the information of NES motion

damping parameter has to satisfy essential conditions to enable a pair of saddle-node bifurcation to exist [Gourc *et al.*, 2012].

1.4.3 Melnikov method

The Melnikov method can analyze and estimate the occurrence of chaos in a nonlinear dynamic system by measuring the distance between the stable and unstable manifolds of the perturbed system [Zhang *et al.*, 2009]. It offers an analytical process to study the global bifurcation of the system and the transition to chaos.

If the control parameter satisfies the critical condition that the Melnikov function equals simple zero, a global homoclinic bifurcation occurs, a threshold value of the parameter for chaos occurrence is obtained. This method stems from the investigation of proper condition to homoclinic bifurcation, which characterises the dynamic of the bistable system into chaos regimes [Guckenheimer et Holmes, 2013].

Due to the standard process of Melnikov analysis, it has been applied in various domains. The threshold values of a homoclinic bifurcation are estimated in parameter space. Those predictions are verified through numerical simulations [Farshidianfar et

Saghafi, 2014a ; Farshidianfar et Saghafi, 2014b]. Zhang used an extended Melnikov method to indicate that the multi-pulse jumping of heteroclinic orbits, which also verified by the numerical simulation [Zhang *et al.*, 2009]. For the bistable piezoelectric energy harvest [Stanton *et al.*, 2012], Melnikov theory was derived to find an equivalent damping condition, dimensionless frequency threshold for which the Melnikov function has simple zero. It has cautioned that it is more suitable for a weak excitation case. So the Melnikov method is found and demonstrated to be a useful tool for analysing the appearance of chaos.

1.5 Numerical methods

1.5.1 Lyapunov exponent

In addition to the Melnikov method, the Lyapunov Exponent (LE) can be used to quantitatively evaluate chaos behaviors through calculating the average exponential growth or decay of nearby orbits [Strogatz, 2018]. The definition of the Lyapunov exponent (λ_{LE}) is given:

$$\lambda_{\mathrm{LE}} = \lim_{d(0)\to 0, t\to\infty} \frac{1}{t} \ln\left(\frac{d(t)}{d(0)}\right) \tag{1.1}$$

where $d(t)$ is the distance in phase space between a given orbit and a test orbit, initially starting infinitesimally close with initial distance $d(0)$.

For a periodic solution (orbit), λ_{LE} reduces to be negative when the calculation time tends to be infinity. As for a chaotic solution, the Lyapunov characteristic exponents approaches a positive value as time increases. Further on, only the maximal component should be considered as an indication of chaos.

For a given ordinary differential equation, Wolf created a toolbox in Matlab to calculate LEs, where the algorithm employed for determining the exponent was proposed [Wolf *et al.*, 1985]. In a single DOF system, this method is applied to investigate the low energy chaotic transition [Romeo *et al.*, 2015a]. The lower and upper energy threshold can be identified for a different magnitude of harmonic excitation. The result of the lower threshold shows a good agreement with the Melnikov approximation. The initial velocity condition of triggering chaotic motion has been verified by LE method [Dekemele *et al.*, 2019]. Calculation of LE can also guide the design of bistable NES so that the negative LE of equivalent Duffing oscillator indicates the non-chaotic motion.

In the non-smooth system, the estimation of LEs is not direct. The numerical tools to handle those discontinuities and plenty of calculation methods are applied [Müller, 1995 ; Stefanski, 2000 ; Stefański et Kapitaniak, 2003 ; De Souza et Caldas, 2004]. Li proposes an approach to calculate LEs based on the experimental data for VI NES [Li *et al.*, 2018]. The maximal positive LE decreases gradually in a non-chaotic response within a limited time. As for the SMR period, the LEs remain steady positive. So the estimation of LEs can help to distinguish the response regimes of VI NES.

1.5.2 Wavelet transforms

Complex frequency distribution in NES vibration behaviors requires some signal processing method, such as Wavelet Transforms (WT). WT can extract the frequency distribution

information of the system response over time.

The concept of WT is proposed by the geophysicist Jean Morlet [Morlet *et al.*, 1982b]. It uses a finite set of wavelets, which are modulated by a Gaussian envelope to compute the wave propagation using complex functions [Morlet *et al.*, 1982a].

WT is a fundamental technique for non-stationary time-frequency analysis. It applies variable-size regions, which is named as the windowing technique to detect various frequency components. For a higher frequency part, small-time intervals are considered, while the size of the window (time interval) increases for the lower-frequency component. The characteristics of this variable interval distinguish the Fast Fourier Transform (FFT), which assesses stationary. The WT extends the 'static' FFT. Instead of using a fixed cosine and sine trigonometric function, WT alters simple families of orthogonal functions to localize frequency and time. The heavy shadow region means the area where the main frequency components concentrate. And the light shaded region corresponds to a region with lower WT amplitude. The amplitude of WT is the function of frequency and time. The signal decomposition technique enables us to deduce the temporal evaluation of dominant frequency components of signals analyzed. However, signals could be too small to be analyzed by the particular windows using in the WT.

Lee used the numerical WT to study the time evaluation of harmonic components over the entire time window of simulation [Lee *et al.*, 2005a]. Kerschen concluded that the 1:1 resonance capture is responsible for energy pumping by observing the frequency component distribution in the time domain [Kerschen *et al.*, 2005]. The WT helps to explain that the NES can tune itself with the aim of engaging in a 1:1 resonance interaction. Combining with the frequency-energy plot, a transition of two predominant frequency components also appears as energy decreases. The plot of WT is calculated to differentiate high and low WT amplitudes [Li *et al.*, 2017d]. The time histories of the main frequency component of the signals illustrate that the nonlinear beats phenomenon initiates the energy transition between the NES and LO under transient excitation and 1:1 resonance.

1.6 Experimental tests

The effect of TET and the feasibility of NES has been realized by various experiments implementations [Gendelman, 2011 ; McFarland *et al.*, 2005b ; Jiang *et al.*, 2003]. McFarland firstly examines the nonlinear energy pumping by an experimental fixture [McFarland *et al.*, 2005b]. The NES mass and LO mass are aluminium angle stocks, which move along a straight air track. Various connecting hardwares and transducers are connecting to it. The LO is grounded through a linear spring. Meanwhile, a cubic nonlinearity, which is constructed by a thin rod (piano wire) with no pretension, clamped at both of its ends, ground the NES mass. A long-stroke electrodynamic shake provides excitation to LO by a rod, which contacts the force transducer. Broadband, single, brief transient excitations are achieved by a manual switching arrangement. The experimental device is shown in Fig. 1.11a. The experiments confirm the analytical prediction of the nonlinear energy pumping phenomenon at a single fast frequency in the vicinity of the natural frequency of LO. The NES can dissipate the maximum portion of energy.

For an acoustic system in Fig. 1.11b, the TET also appears between the acoustic medium and visco-elastic membrane [Bellet *et al.*, 2012 ; Bellet *et al.*, 2010]. The U-

shape tube, which possesses an adjustable length, is the linear system so that the first resonance frequency can be tuned by adjusting this length. The sliding system can produce the pre-stress to the membrane, which is clamped to the supporting device. The center of the membrane performs a large amplitude oscillation. This displacement of the membrane center is governed by 1-DOF differential equation. Due to the pre-stress in the membrane, the nonlinear absorber does not perform a pure cubic nonlinearity but with a linear stiffness. A loudspeaker and a coupling box provide the acoustic source. This experimental device constitutes an analogy of a 2-DOFs mechanical spring-mass system. The experiment concludes that TET exists between a primary acoustic medium and a nonlinear membrane absorber. By adjusting the membrane radius and pre-stress, the various acoustic system is tuned on their different resonance frequencies.

The mass-spring mechanism is also presented in Fig. 1.11c [Dekemele *et al.*, 2020]. The mass is restricted and moves along the rail. Two linear springs attach to the NES and the other end of linear springs moves along a special track with designed curve. When the mass moves, the mass is pushed back with an equivalent force and provided by a nonlinear track through rolling bearing connecting to linear springs. Because of the symmetry of linear springs, the total force in the direction perpendicular to the rail is counterbalanced. The force parallel to the rail is conserved. This track ensured a purely cubic nonlinearity characteristic, which was verified by the identification of the NES. This spring-mass system is installed on a two-frame structure. Effective vibration mitigation has been observed under a transient impact. The NES engaged in resonance capture cascade, and the corresponding pumping time prediction technique is verified.

The magnetic force can also construct either cubic or a bistable nonlinearity. The Magnetic-Strung Nonlinear Energy Sink (MS-NES) [Pennisi *et al.*, 2018] is presented in Fig. 1.11d. The core component is the string that provides the coupling force between LO and NES. The function of force and displacement contains a term proportional to the cube of displacement without considering the higher-order terms and linear stiffness term. The two additional magnets locate a certain distance away to provide a repulsive force and balance the linear stiffness of mechanical component. The energy of LO is transferred into the NES. Then the NES oscillates in the coils and the kinetic energy of NES is converted into electrical energy by means of an electromagnetic transducer. The result of the experiment successfully shows that the linear stiffness terms, which can radically change the response of the system, has been cancelled out. The SMR can be a valid option for energy absorption, and the bistable configuration shows an advantage to improve the energy harvesting aspect.

In addition to the damping effect, energy can also be absorbed through collisions such as Fig. 1.11e. So a VI NES consists of a mass that impacts the two sides and moves freely in a cavity of LO. An embedded VI NES is installed to the LO [Li *et al.*, 2016 ; Gourc *et al.*, 2015a]. The ball and the closed cavity is made of the same material of hardened steel. The NES ball is free to move inside a rigid barrier. The contact-less laser measures the displacement of LO as well as the displacement of 10 kN electrodynamic shake. The experimental SMR zone is similar to the numerical simulation. A more realistic model of impact and friction inside the cylinder should be considered to improve the correspondence between theoretical and experimental results. The system in 1:1 resonance is judged from the impact directly.

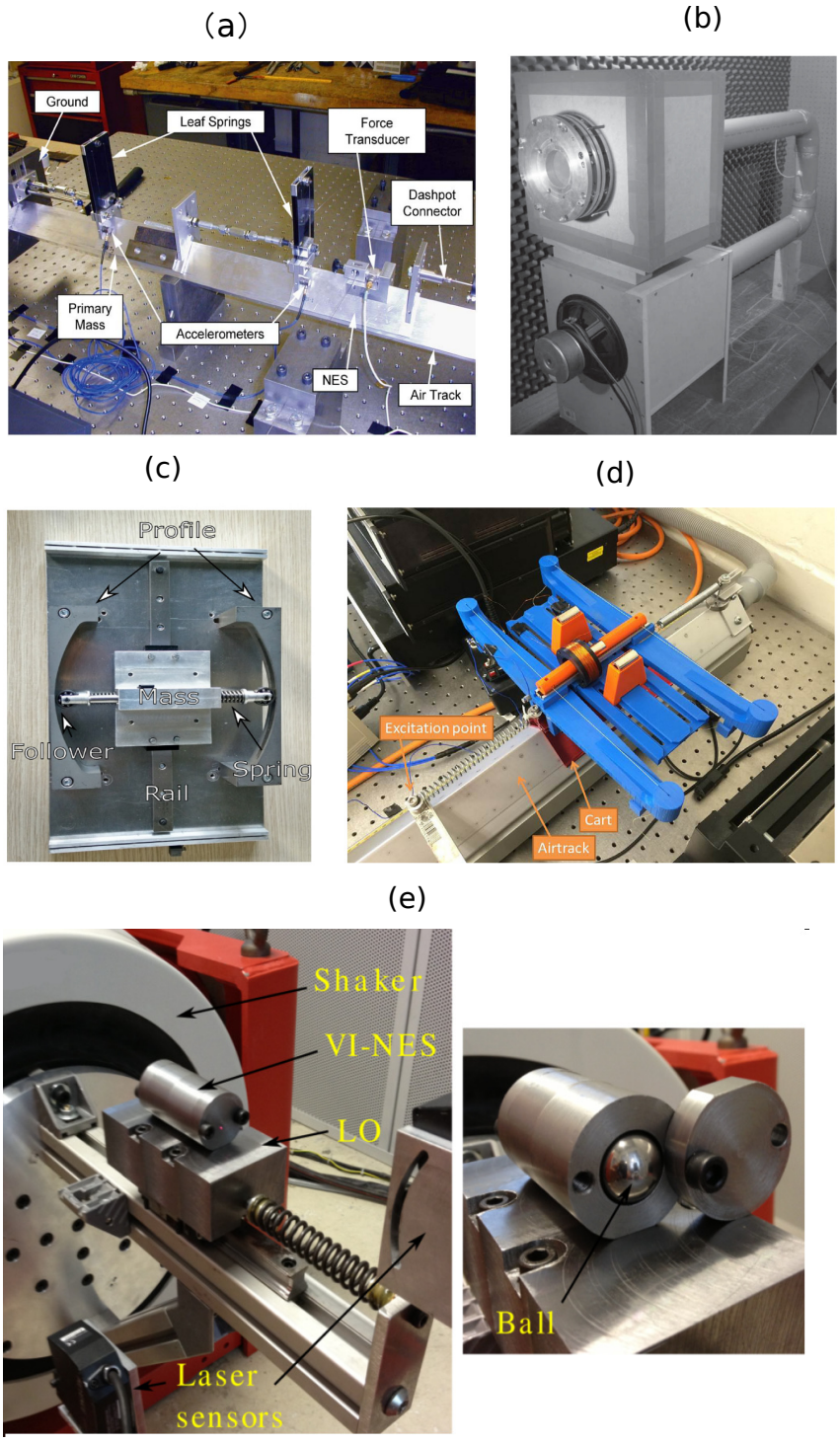

Figure 1.11: (a) Leaf springs type of NES [McFarland *et al.*, 2005a] (b) membrane absorbers in acoustic system [Bellet *et al.*, 2010] (c) realization of track NES design [Dekemele *et al.*, 2020] (d) mechanical NES with an electric circuit, a coil, and additional magnets [Pennisi *et al.*, 2018] (e) VI NES [Gourc *et al.*, 2015a]

1.7 Applications

1.7.1 Vibration mitigation

A direct application for NES in vibration mitigation is chatter control as chatter increases surface roughness and damages the spindle. A VI NES is embedded in cutting tool of lathe. The result shows that the VI NES offers a significant vibration mitigation effect and passively controls the chatter instability in the turning process [Gourc *et al.*, 2015b]. In the aspect of mitigation of vibration in pipes conveying fluid, an enhanced NES system is implemented on the pipe [Yang *et al.*, 2019] As a result of a strong fluid pipe interaction, this kind of flow-induced vibration and noise is inevitable. An optimal design can realize a maximum efficiency of 98%. A similar investigation of global stability analysis of pipes conveying fluid is carried on under the framework of Lyapunov stability theory [Duan *et al.*, 2021a ; Duan *et al.*, 2021b].

In the aircraft flying at transonic speeds condition, the structure is prone to instabilities, for example, Limit Cycle Oscillation (LCO). A potential **definition** of LCO in the context of aeroelastic is that *the instability causes diverging responses (Note that these are unstable, oscillatory responses of which amplitude becomes exponentially growing). It is, however, due to structural or damping nonlinearities that such responses can be limited. This kind of self-sustaining response is termed as LCO* [Lee *et al.*, 2005b].

In the early stage, a wind-tunnel model of 2-DOFs rigid wing model is investigated to avoid LCO [Lee *et al.*, 2007b]. The role of NES to mitigate aeroelastic instability partially or even completely is confirmed through passively transferring the energy of the wing to NES irreversibly. Three main mechanisms for suppressing aeroelastic instability have been identified through numerical study: recurring burst out and suppression, intermediate suppression, and complete elimination. Based on the analytical prediction, experiments validate several aspects of the theory. The introduction of NES induces other branches that are responsible for the three LO suppression. The interaction strongly with the aeroelastic modes through 1:1 resonance captures is the key to LCO suppression with the NES [Lee *et al.*, 2007a].

The interaction of air and panel causes the panel flutter, which is considered as a self-excitation and maintains a limited amplitude. This kind of panel fatigue may damage the structure of the flight vehicle, so the NES is attached to laminated panels to investigate its dynamic behaviors in supersonic airflow. It concludes that a relatively heavy mass is required to be efficient. It functions in a specific range of nonlinearity coefficients and degrees of damping. The most effective installation position of a NES is in a region behind the center line of the panel in the direction of the airflow through the finite element method [Jian *et al.*, 2021]. The 2-DOFs rigid wing is coupled to two NES, which are located in the two ends of the wing. The several typical cases with interesting dynamics are analyzed in detail. 1:1 resonance captures is accompanied by the high efficiency of TET. It's also possible to transfer the energy of LO to some specific targets, which is different to the traditional TET mechanism [Zhang *et al.*, 2017]. The result shows that the NES could enhance the critical velocity of the freestream under which the vibration of the wing can be mitigated. A 3-D trapezoidal wing coupled with a NES in hypersonic flow is investigated [Tian *et al.*, 2019]. In another air-solid interaction condition, a rotary NES is attached to the square prism model. Various influence parameters (ball mass, NES track radius, ball friction, and radial clearance between NES track walls and the rotating ball)

are verified in their roles in vibration mitigation. It demonstrates that NES is amenable to mitigate flow-induced vibration successfully [Selwanis *et al.*, 2021]. An adaptive and passive galloping suppression of a suspended linear cable is investigated. The LCO of the cable due to nonlinear wind loading is effectively eliminated by a lightweight, easy-to-make attachment [Guo *et al.*, 2017].

The helicopter suffers from ground resonance. This kind of dynamic instability comes from the coupling of the motion of the blades in the rotational plane and the motion of the fuselage. So the potential NES is attached on the fuselage and an ungrounded configuration is performed [Bergeot *et al.*, 2016], where the prediction of steady-state response regimes is also proposed. Ground resonance instability can be fully suppressed under the suitable conditions and partially suppressed through the periodic response or SMR [Bergeot *et al.*, 2017].

A linear piecewise NES is introduced to suppress the vibration rotor and blade, which is mainly responsible for the failure of the rotating machine [Cao *et al.*, 2020]. A beam connects LO and NES disk. The one end of other beams is installed to LO, and the other end is in the hole of the NES disk. The radius of the hole is different, so the beams contact the NES one by one as the rotation speed becomes faster. It concludes that the vibration suppression capability of NES for a rotor-blade system, in which the inhibitions of NES upon the steady resonance of the rotor can reach 93% and 88%.

In the field of civil engineering, the damping of buildings is particularly important when the system is exposed to natural disasters as well as to fatigue and ageing of its own structure. A 9-story structure equipped with a NES system has been implemented. The experiment includes two types of NES: A smooth cubic NES and a single side impact NES. And the NES is mounted on the 8t/9th floor. The experimental result shows a strong capability of NES to reduce the global response of the structure due to the blast loading in a large scale structure. A significant transfer of energy from the lower modes of the structure to its higher modes is observed [Wierschem *et al.*, 2013]. Another absorbing capability of track NES, which is installed on the top of the 2-story structure, is also studied [Wang *et al.*, 2015]. A five-story steel frame coupled with track NES has gained good protection under five earthquake waves with different frequency spectrums [Lu *et al.*, 2017]. The ratio of the peak response is reduced up to 50%, while for root mean square response is up to 80%.

1.7.2 Energy harvesting

Another essential applied field for NES, is the energy harvesting [Harne et Wang, 2013]. It has been proved that the energy of LO can be pumped into NES with high efficiency over broadband frequency ranges. So this part of kinetic energy could be useful to convert into an electrical source and supply some sensors. The possible energy transfer mechanism in the combination of NES and piezoelectric energy harvest is investigated [Li *et al.*, 2017d].

A spring with bistable nonlinearity and a hardening-type stiffness element provide a wider bandwidth over which the energy can be harvested. The study also reveals that the amount of power harvested by a bistable NES device is at most $4/\pi$ greater than that of the tuned linear device provided. The device produces a square wave output under harmonic excitation. The hardening stiffness system provides the same maximum harvested power as a linear system, ideally [Ramlan *et al.*, 2010]. And a low amplitude excitation reduces harvested power [Quinn *et al.*, 2011]. Kremer investigates the performance of energy

harvesting using NES under harmonic and transient response [Kremer et Liu, 2014]. Experiment shows the capability of energy localization as well as broadband vibration absorption. An initial energy threshold is required to enable dominated energy to locate in NES. A nonlinear beat and TET are the symbol of the best energy harvesting. Two different electromechanical configurations, composed of NES and piezoelectric elements, are investigated under various parameter influences [Ahmadabadi et Khadem, 2014]. Both optimal designs have been achieved to maximize the dissipated energy by the NES and increase the harvested energy by the piezoelectric element.

1.8 Nonlinear spring design

Spring elements are widely used in the engineering sector due to their high reliability, simplicity and low cost. A common cylinder spring is viewed as a linear spring because of its constant pitch, cylinder wire, closed and ground end. The compression length of linear spring is proportional to the force value, so-called linear stiffness.

A nonlinear spring possess a nonlinear load-displacement function, which is also referred as its strain energy absorption rate [Jutte et Kota, 2008]. The nonlinear spring can be constructed by designing the geometry characteristic of spring. The generation of nonlinearity is due to the number of active coils decreases or increases with various compression or tension. Nowadays, it exists three main parameters to achieve nonlinear nonlinearity (1) mean diameter, (2) pitch, (3) coil diameter. However, in the current production process, the third parameter can be hardly realized to be variable. The control of the first parameter corresponds to the conical spring. The second type of control parameter corresponds to cylindrical variable pitch spring. Besides them, the piecewise springs and free-edge spherical shells can also privide a piecewise nonlinearity and other nonlinearity [Jazar *et al.*, 2007 ; Touzé et Thomas, 2006].

The objective of providing variable spring rates can be achieved by designing a mean diameter with the constant pitch and constant coil diameter. For the conical spring with constant pitch, there are two types of spring, solid and telescope. The latter one can be fully compressed as a plan. The conical springs possess a lower solid height than a normal spring while maintaining a close spring rate [Paredes et Rodriguez, 2009]. Regardless of the type of conical spring, the force-displacement curve can be divided into a linear and a nonlinear part. The point T in Fig. 1.12a is the transition point that separates the linear and nonlinear regimes.

In the second regime (T-C period), maximum deflexion of the largest coils has been reached. The end coil has contacted with the ground, and the base coils also start to collide so that the number of active coils decreases continuously. The variety of active coil numbers determines the nonlinear force-displacement $(F - u)$ relationship of the second period.

The detailed description of the above equation is mentioned [Rodriguez *et al.*, 2005]. The accuracy of theoretical prediction was verified by experimental tests [Paredes, 2013]. The conical spring can provide a strong nonlinear force (store more energy) with little displacement at its maximum compression. The conical spring is characterised by its small upper coil diameter and large lower coil diameter so that it shows more lateral stability and avoids buckling greatly [Patil *et al.*, 2015].

The load-displacement relation of variable pitch spring also has two phases in Fig. 1.12b.

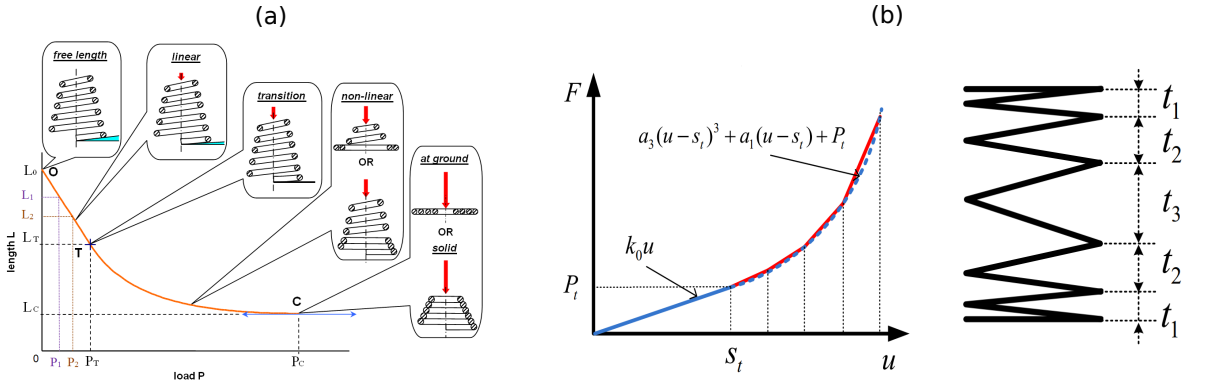

Figure 1.12: (a) Load-displacement curve of conical spring with constant pitch corresponding to the compression phase [Paredes et Rodriguez, 2009] (b) $F-u$ relation of cylindrical variable pitch spring and the pitch distribution in a variable pitch spring [Qiu *et al.*, 2019a]

In the very beginning, the space between the coil is compressed, but the number of active springs is constant. So during this period, the restoring force is proportional to displacement. Due to its variable pitch characteristic, some of the coils will close up (have contact with other coils) faster than other coils, so the number of active coils decreases resulting in an increase of spring rate. By designing the pitch, or the center distance between the coils, particular force-displacement relationship can be constructed. The main idea of designing the pitch is to divide the nonlinear phase into serval pieces and calculate the average stiffness of every part. According to that local stiffness, the residual active coils can be calculated. Technically, the actual force-displacement curve of variable pitch spring is piecewise. Qiu has proposed asymmetrical distribution of pitch to smooth and better fit the target force-displacement curve [Qiu *et al.*, 2019a]. While designing the variable pitch spring, the buckling condition should be avoided [Patil *et al.*, 2014], the maximum acceptable stress in the spring body [Paredes, 2000], and other constraints, for example stability of the spring [Trabelsi, 2014], should be taken into consideration.

Both variable pitch spring and conical spring perform a linear stiffness phase, which prevents them from directly applying to a pure cubic mechanism. Pre-compression strategies and an extra negative stiffness mechanism should be added to counterbalance the linear phase and linear component in the nonlinear phase.

1.9 Optimal design for NES

The mistuned NES may result in significant drawbacks, such as a relatively high mass ratio or a risk of detached resonance tongue that is easily triggered. So to avoid the above disadvantages, Gourc plots a narrow region of amplitude-frequency $F-\sigma$ of harmonic excitation, where the three solutions of fixed points do not exist [Gourc *et al.*, 2014]. An optimal cubic nonlinearity should satisfy that the target excitation is not located in the three solutions region to obtain a broadband with no detached resonance tongue. Even a small mass ratio (1%) can also achieve an efficient performance of vibration mitigation.

In a base-excited viscoelastic isolation system with an attached NES, the criteria for deriving the optimal parameters is assumed as the smaller value of the maximum

amplitude of the LO and the narrower frequency band for the region with multiple solutions. So the optimal parameter of larger cubic nonlinearity, a modest viscoelastic damping parameter, mass ratio are selected through the amplitude-frequency plot [Huang *et al.*, 2019]. The role of the damping parameter to attenuate the amplitude of frequency response has been confirmed numerically.

Another criterion for optimization is the rate of amplitude degradation. For the optimal mitigation of impulsive response of system through TET, the amplitude of the impulse should close to a critical value [Vakakis *et al.*, 2008]. Tuan gives a clear insight to practically design optimal cubic nonlinearity under transient excitation [Nguyen et Pernot, 2012]. It gives a critical amplitude condition, above which the system leads to the occurrence of an efficient dissipation of energy. Optimal design criterion can be described as the initial impulsive amplitude of LO should locate in the vicinity of singularity point in the SIM structure, so that the cubic nonlinearity value shall be chosen greater than the optimal value computed for minimal initial energy.

SIM offers us a fundamental basis for the dynamic behavior of NES, and it can also help us to guide the optimal design. The optimal point is selected in the singularity point to achieve minimal amplitude of LO under the harmonic force. In the VI-NES, the SIM is applied to explain the different response regimes [Qiu *et al.*, 2019b ; Qiu *et al.*, 2018a]. The critical value of the cavity length is obtained. Both analytical prediction of efficient TET at the resonance frequency and optimal performance to protect the LO are achieved by the experiment. Based on response regimes, Chavarette applied an optimal control strategy to transforme chaotic and periodic motions of the nonideal and ideal systems into stable orbits. The periodic or controlled behaviors possess a less energy consumption of structure coupled to an essentially nonlinear oscillator than that of chaotic behavior [Chavarette *et al.*, 2010].

The target of most of NES optimal designs is under transient impulsive or harmonic excitation. Oliva investigates the performance of the NES under random Gaussian white noise base excitations in a numerical method [Oliva *et al.*, 2017]. The work contains the use of statistical linearization techniques and an accurate empirical formulation to guide the NES optimal parameters. The target of minimizing the dynamic response in terms of both displacements and accelerations is verified by using Monte Carlo Simulations. In addition to the excitation uncertainty, the parameter uncertainty of the NES system should also be considered. So the discontinuities of parallel NESs are considered random design variables, which are optimized for cases multiple NESs in parallel [Boroson *et al.*, 2017]. Numerical simulation indicates that a larger number of parallel NESs leads to efficiency increases.

1.10 Objectives of thesis

The literature review provides the necessary concept to access the Targeted Energy Transfer (TET) mechanism in Nonlinear Energy Sink (NES). It demonstrates a broader brand of absorbing frequency than traditional Tuned Mass Damper (TMD). So to design a NES with an optimal state, absorbing in a maximal efficiency or causing Linear Oscillator (LO) to possess a minimal amplitude, an optimal design criterion based on response regimes has to be established. The bistable NES, which is appropriately designed, can be more efficient than a pure cubic NES. The optimal region for cubic nonlinearity and

negative stiffness requires to be further revealed. In a real application environment, the NES involves other nonlinearity, for example, impact, which is inevitable. So a couple of those characteristics leads to novel type NES, Vibro-Impact Cubic (VIC) NES. It widens the way for the practical application of NES.

The second chapter focuses on the optimal design of cubic and bistable NES. The response regime of cubic NES and analytical optimal nonlinearity design are given and verified by the numerical simulation. Both for cubic and bistable NES, the optimal state is defined as the moment when the Strongly Modulated Response (SMR) disappears and turns to be a stable response. The parameters, which governs the ceiling of maximal efficiency are revealed to guide the NES design. The bistable NES has more complex behaviors than cubic NES. The relationship between the target excitation and the optimal cubic nonlinearity parameter is found. Its robustness is also examined. An adjustable four springs device is tuned to transfer the cubic nonlinearity into bistable nonlinearity. So it can achieve the optimal design for various target excitations.

The third chapter focuses on the characteristic response regimes of bistable NES, the intra-well oscillation and chaos. An adapted complex variables method, which considers the initial equilibrium as the original point, investigates the intra-well oscillation amplitude. This amplitude can give the threshold of triggering chaos with the simplified circle expansion model within the separatrix. The impact of negative stiffness is reflected in two main aspects, (1) changing the Slow Invariant Manifold (SIM) structure (2) introducing attraction points and chaotic regions. The chaotic region and the unstable region in the SIM gradually overlap as the negative stiffness increases. The disappearance of response regimes with increasing absolute negative stiffness value can be explained by the level of overlap of chaos region and unstable region in the SIM structure. The characteristic regimes of different negative stiffness designs are observed in the experiments, which confirms the numerical simulation results.

The fourth chapter aims to estimate the energy pumping time in both transient response and harmonic excitation. The amplitude decay rate of LO is revealed by the multiple scales method. The conservative system is considered first to obtain a particular state integration. Then, the equivalent points are expressed to measure the average decay rate during the energy pumping time in transient response. The previous two steps are necessary to perform a semi-analytical method to estimate the energy pumping time under harmonic excitation. A particular integration term is assumed as a simplified term, which involves the external excitation term. The simulations under various damping, harmonic excitation amplitude conditions have confirmed the robustness of prediction. The semi-analytical method also gives the same level of prediction as to the experimental results.

The last chapter introduces a novel NES: the impact has been considered into cubic NES and it turns to be a Vibro-Impact Cubic (VIC) NES. The clearance length can classify the VIC NES into three types: narrow, modest, large clearance cases, according to the location of extra singularity line. The response regimes of VIC NES are classified. When the system does not possess a collision, the cubic nonlinearity mainly governs its fixed point. Once the impacts occur, the simplified Vibro-Impact (VI) NES model can describe the stable response of VIC NES well. The VIC NES can be tuned to adapt to the different energy inputs by changing the length of clearance which is not accessible for cubic NES. The optimal analytical curve is given and is verified by the numerical and experimental way.

CHAPTER 2

Optimization design for cubic NES and bistable NES

Abstract

This chapter mainly concentrates on optimizing cubic Nonlinear Energy Sink (NES) and bistable NES to find the maximum efficiency point under harmonic excitation. The dynamic model of cubic NES is also analyzed to obtain the fixed point of the system. Then the response regimes are presented to find the maximum efficiency point, where the Strongly Modulated Response (SMR) disappears for both the cubic and bistable NES. With the help of analytical predictions, the proper cubic nonlinearity is determined for particular harmonic excitation. Then experimental device confirmers the optimal design for particular excitation. The robustness of optimal design is also verified numerically and experimentally.

Contents

2.1 Optimal design criteria for cubic NES

The basic cubic NES is a fundamental research target. The first objective is to carry out its dynamic modeling and analytical treatment. By the demonstration of the response regime under various energy inputs, the optimal criterion of cubic NES is created. The existing experiment device can turn the cubic NES into bistable NES. So second objective is to optimize the bistable NES. The cubic NES and bistable NES share some similarities, for example, the efficient Targeted Energy Transfer (TET). The research approach to the cubic model facilitates the optimization of the bistable NES. Finally, the experimental results confirm the optimal designs for various target excitations.

2.1.1 Dynamic modeling

The target system is described schematically in Fig. 2.1, which is also adressed in [Gourc, 2013 ; Gendelman, 2008]. The equation of motion is:

$$\begin{aligned} &m_1\ddot{x} + k_1 x + c_1\dot{x} + c_2(\dot{x}-\dot{y}) + k_2(x-y)^3 = k_1 x_e + c_1\dot{x}_e \\ &m_2\ddot{y} + c_2(\dot{y}-\dot{x}) + k_2(y-x)^3 = 0 \end{aligned} \tag{2.1}$$

where m_1, c_1 and m_2, c_2, are the mass, damping of Linear Oscillator (LO) and NES, respectively. k_1 is a linear stiffness between LO and base. A cubic nonlinearity k_2 connects the LO and NES. x and y are the absolute displacements of m_1 and m_2. And the dots denote differentiation with respect to real time t. The imposed harmonic displacement excitation is expressed as $x_e = Gcos(\omega t)$

Introducing the following variables into Eq. (2.1):

$$\begin{aligned} &\epsilon = \frac{m_2}{m_1}, \omega_0^2 = \frac{k_1}{m_1}, K = \frac{k_2}{m_2\omega_0^2}, \lambda_1 = \frac{c_1}{m_2\omega_0}, \\ &\lambda_2 = \frac{c_2}{m_2\omega_0}, F = \frac{G}{\epsilon}, \Omega = \frac{\omega}{\omega_0}, \tau = \omega_0 t \end{aligned} \tag{2.2}$$

The governed equation of the cubic NES system can be reduced to a dimensionless form:

$$\begin{aligned} &\ddot{x} + x + \epsilon\lambda_1\dot{x} + \epsilon\lambda_2(\dot{x}-\dot{y}) + \epsilon K(x-y)^3 = \epsilon F\cos\Omega\tau - \epsilon^2 F\lambda_1\Omega\sin\Omega\tau \\ &\epsilon\ddot{y} + \epsilon\lambda_2(\dot{y}-\dot{x}) + \epsilon K(y-x)^3 = 0 \end{aligned} \tag{2.3}$$

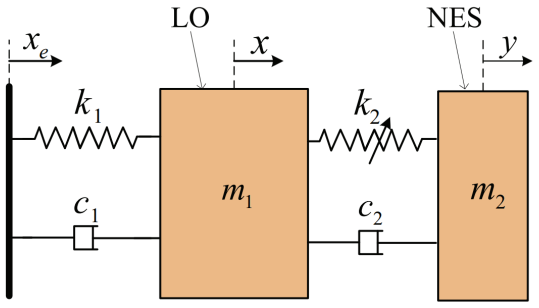

Figure 2.1: Schematic of linear oscillator and cubic NES system.

where the ϵ is the mass ratio and K is the cubic nonlinearity parameter in a dimensionless form. λ_1 and λ_2 are the dimensionless damping parameters of LO and NES, respectively. F is the dimensionless excitation amplitude. And the dots in Eq. (2.3) denote differentiation with respect to τ time scale. Since the mass ratio ϵ is a small parameter, the term containing ϵ^2 in Eq. (2.3) can be eliminated. So it gives:

$$\begin{aligned} &\ddot{x} + x + \epsilon\lambda_1\dot{x} + \epsilon\lambda_2(\dot{x} - \dot{y}) + \epsilon K(x-y)^3 = \epsilon F\cos\Omega\tau \\ &\epsilon\ddot{y} + \epsilon\lambda_2(\dot{y} - \dot{x}) + \epsilon K(y-x)^3 = 0 \end{aligned} \tag{2.4}$$

To calculate the fixed point of the system, the barycentric coordinates are introduced in the following forms:

$$v = x + \epsilon y, w = x - y \tag{2.5}$$

where v means the mass center of system, w means the relative displacement between LO and NES. Substituting above expression into Eq. (2.4) gives:

$$\begin{aligned} &\ddot{v} + \epsilon\lambda_1\frac{\dot{v} + \epsilon\dot{w}}{1+\epsilon} + \frac{v + \epsilon w}{1+\epsilon} = \epsilon F\cos\Omega\tau \\ &\ddot{w} + \epsilon\lambda_1\frac{\dot{v} + \epsilon\dot{w}}{1+\epsilon} + \frac{v + \epsilon w}{1+\epsilon} + \lambda_2(1+\epsilon)\dot{w} + K(1+\epsilon) = \epsilon F\cos\Omega t \end{aligned} \tag{2.6}$$

Under the assumption of 1:1 resonance, the following Manevitch complex variables are introduced [Manevitch, 2001]:

$$\phi_1 e^{i\Omega\tau} = \dot{v} + i\Omega v,\ \phi_2 e^{i\Omega\tau} = \dot{w} + i\Omega w \tag{2.7}$$

The role of Manevitch complex variables is to separate the rapid oscillation part of the system at frequency Ω and slow modulation of complex amplitude $\phi_j, j = 1, 2$. $\overline{\phi_j}$ means its conjugate. After the introduction of Manevitch complex variables into Eq. (2.6), only terms containing $e^{i\Omega\tau}$ are reserved:

$$\begin{aligned} &\dot{\phi}_1 + \frac{i\Omega}{2}\phi_1 + \frac{\epsilon\lambda_1(\phi_1 + \epsilon\phi_2)}{2(1+\epsilon)} - \frac{i(\phi_1 + \epsilon\phi_2)}{2\Omega(1+\epsilon)} - \frac{\epsilon F}{2} = 0 \\ &\dot{\phi}_2 + \frac{i\Omega}{2}\phi_2 + \frac{\epsilon\lambda_1(\phi_1 + \epsilon\phi_2)}{2(1+\epsilon)} - \frac{i(\phi_1 + \varepsilon\phi_2)}{2\Omega(1+\epsilon)} + \frac{\lambda_2(1+\epsilon)\phi_2}{2} - \frac{3iK(1+\epsilon)\phi_2^2\overline{\phi}_2}{8\Omega^3} - \frac{\epsilon F}{2} = 0 \end{aligned} \tag{2.8}$$

NES can present a strongly quasi-periodic oscillation, which is termed as Strongly Modulated Response (SMR). This type of motion can be interpreted by the study of the fixed point. To obtain the analytical threshold value for SMR, a perturbation method and the multiple scales method are used with respect to the small parameter $\epsilon \approx 1\%$:

$$\begin{aligned} &\phi_j = \phi_j(\tau_0, \tau_1, \ldots), \frac{\mathrm{d}}{\mathrm{d}\tau} = \frac{\partial}{\partial\tau_0} + \epsilon\frac{\partial}{\partial\tau_1} + \cdots \\ &\tau_k = \epsilon^k\tau, \quad k = 0, 1, \ldots \end{aligned} \tag{2.9}$$

When LO and NES oscillate near 1:1 resonance, the frequency term of excitation Ω is close to the reduced natural frequency of LO. A new detuning parameter σ is defined as:

$$\Omega = 1 + \epsilon\sigma \tag{2.10}$$

Substituting Eq. (2.9) into Eq. (2.8), terms that contain a coefficient of ϵ^0 give:

$$\begin{aligned}&\frac{\mathrm{d}}{\mathrm{d}\tau_0}\phi_1 = 0\\&\frac{\mathrm{d}}{\mathrm{d}\tau_0}\phi_2 + \frac{1}{2}i\left(\phi_2-\phi_1\right) + \frac{1}{2}\phi_2\lambda_2 - \frac{3}{8}iK\phi_2^2\overline{\phi}_2 = 0\end{aligned} \tag{2.11}$$

Order ϵ^1

$$\begin{aligned}&\frac{\mathrm{d}}{\mathrm{d}\tau_1}\phi_1 + \frac{1}{2}\lambda_1\phi_1 + \frac{1}{2}i\left(\phi_1-\phi_2\right) + i\sigma\phi_1 - \frac{1}{2}F = 0\\&\frac{\mathrm{d}}{\mathrm{d}\tau_1}\phi_2 + \frac{1}{2}\lambda_1\phi_1 + \frac{1}{2}\phi_2\lambda_2 + \frac{1}{2}i\sigma\left(\phi_1+\phi_2\right) + \frac{1}{2}i\left(\phi_1-\phi_2\right) - \frac{3}{8}iK(1-3\sigma)\phi_2^2\overline{\phi}_2 - \frac{1}{2}F = 0\end{aligned} \tag{2.12}$$

To study the stable amplitude of LO and NES, the derivative term is set to zero. The new variables are introduced into Eq. (2.11) as follows:

$$\phi_1\left(\tau_1\right) = N_1 e^{i\delta_1}, \quad \phi_2\left(\tau_1\right) = N_2 e^{i\delta_2} \tag{2.13}$$

The stable solutions of N_1 and N_2 are given by N_{10} and N_{20} in the ϵ^0 order of equation. The expression that describes the topological structure of the Slow Invariant Manifold (SIM) of cubic NES system is obtained in the following form:

$$\begin{aligned}&Z_1 = \lambda_2^2 Z_2 + Z_2 - \frac{3K}{2}Z_2^2 + \frac{9K^2}{16}Z_2^3\\&Z_1 = N_{10}^2, \quad Z_2 = N_{20}^2\end{aligned} \tag{2.14}$$

The position of two extrama of SIM are described as:

$$\begin{aligned}&Z_{2,j} = N_{2,j}^2 = \frac{4}{9}\frac{2 \mp \sqrt{-3\lambda_2^2+1}}{K}\\&Z_{1,j} = N_{1,j}^2 = \frac{8}{81}\frac{\pm\sqrt{(1-3\lambda_2^2)^3}+9\lambda_2^2+1}{K}, j = 1,2\end{aligned} \tag{2.15}$$

The SIM is shown in the blue curve in Fig. 2.2. It represents the intrinsic property of the system and its independence with respect to external excitation. The $Z_{2,1}$ and $Z_{2,2}$ are the values of Z_2 at singularity points, which are marked in red in Fig. 2.2. The $Z_{1,1}$ and $Z_{1,2}$ are the values of Z_1 at singularity points, respectively. The two singularity points divide the SIM into two stable branches and an unstable region, which is responsible for the possible occurrence of energy pumping.

2.1.2 Cubic NES response regimes

This kind of SMR can be analyzed in the order of ϵ. The fixed points of the second equation of Eq. (2.11) mean the periodic response. When $\tau_0 \to 0$, the solution of stable branch can be written as $\Phi\left(\tau_1\right) = \lim_{\tau_0\to\infty}\phi_2\left(\tau_0,\tau_1\right)$. When the SMR occurs, the stability of fixed point chnages. This asymptotic stability of the fixed points can expressed by substituting the second equation of Eq. (2.11) into the first equation of Eq. (2.12) with respect to time scale τ_1, then it gives:

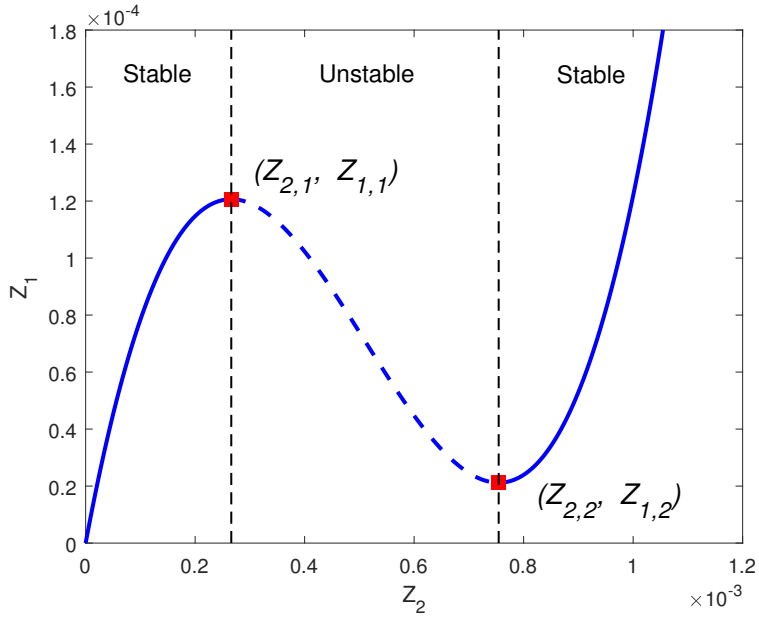

Figure 2.2: The SIM structure of cubic NES. Two folded singularity points separate the SIM into the stable region (blue solid line) and unstable region (dashed line).

$$\begin{aligned}&\frac{\partial}{\partial\tau_1}\left[2i\left(-\frac{\lambda_2}{2}\Phi-\frac{i}{2}\Phi+\frac{3iK}{8}\Phi^2\overline{\Phi}\right)\right]\\&+2i\left(\frac{i}{2}+\sigma i+\frac{\lambda_1}{2}\right)\left(-\frac{\lambda_2}{2}\Phi-\frac{i}{2}\Phi+\frac{3iK}{8}\Phi^2\overline{\Phi}\right)-\frac{i}{2}\Phi-\frac{F}{2}=0\end{aligned}\tag{2.16}$$

Since the $\Phi(\tau_1)$ is solution of ϕ_2 in particular condition $\tau_0 \to \infty$, the polar form in Eq. (2.13) is applied in the above equation. The equations that govern the evaluation of amplitude N_2 and phase δ_2 are obtained after separation of the real and imaginary parts.

$$\frac{\partial N_2}{\partial\tau_1}=\frac{f_1\left(N_2,\delta_2\right)}{g\left(N_2\right)},\quad \frac{\partial\delta_2}{\partial\tau_1}=\frac{f_2\left(N_2,\delta_2\right)}{g\left(N_2\right)}\tag{2.17}$$

with

$$\begin{cases}f_1\left(N_2,\delta_2\right)=-9\lambda_1K^2N_2^5+24\lambda_1KN_2^3-12FKN_2^2\cos\delta_2-16\left(\lambda_2+\lambda_1+\lambda_2^2\lambda_1\right)\\+16F\cos\delta_2+16\lambda_2F\sin\delta_2)\\f_2\left(N_2,\delta_2\right)=\left(-54K^2\sigma-27K^2\right)N_2^4+\left(96K\sigma+12K-24\lambda_2\lambda_1K\right)N_2^2\\+36KFN_2\sin\delta_2-12\lambda_2^2-32\sigma-32\sigma\lambda_2^2+\dfrac{16\lambda_2F\cos\delta_2-16F\sin\delta_2}{N_2}\\g\left(N_2\right)=54K^2N_2^4-96KN_2^2+32+32\lambda_2^2\end{cases}\tag{2.18}$$

Starosvetsky indicated that it exists two kinds of fixed points (1) ordinary fixed points (2) folded singularity points in the Eq. (2.17) [Starosvetsky et Gendelman, 2008]. The first type of fixed points has to satisfy the the condtion $f_1 = f_2 = 0$ and $g \neq 0$. The second one corresponds to the condition $f_1 = f_2 = g = 0$. The system with $f_1 = f_2 = 0$ can be rewritten in the follwing matrix form:

$$\begin{bmatrix} a_{11} & a_{12} \\ a_{21} & a_{22} \end{bmatrix} \begin{bmatrix} \sin\delta_2 \\ \cos\delta_2 \end{bmatrix} = \begin{bmatrix} b_1 \\ b_2 \end{bmatrix} \tag{2.19}$$

with

$$\begin{aligned} &a_{11} = 16\lambda_2 F, \quad a_{12} = -12FKN_2^2 + 16F, \quad a_{21} = \frac{36FKN_2^2 - 16F}{N_2}, \quad a_{22} = \frac{16\lambda_2 F}{N_2} \\ &b_1 = 9\lambda_1 K^2 N_2^5 - 24\lambda_1 K N_2^3 + 16N_2\left(\lambda_1 + \lambda_2 + \lambda_2^2\lambda_1\right), \\ &b_2 = \left[27K^2N_2^5(1+2\sigma) - 12KN_2^3\left(1 - 2\lambda_1\lambda_2 + 8\sigma\right) + 16N_2\left(\lambda_2^2 + 2\sigma\lambda_2^2 + 2\sigma\right)\right]/N_2 \end{aligned} \tag{2.20}$$

The determinant should not vanish, so that the phase of ordinary points δ_2 can be calculated. As for the singularity point, the determinant of matrix is simplified as $det(a) = 8F^2g/N$. So when the system of $g = 0$ and $f_1 = 0$, the f_2 condition can be satisfied automatically. So only $f_1 = 0$ is under the consideration. The expression of f_1 contains the $sin(\delta_2)$ and $cos(\delta_2)$ terms, so it can be transfered into a cos form as:

$$\cos(\delta_2 - \eta) = \frac{b_1}{\sqrt{a_{11}^2 + a_{12}^2}}, \tan(\eta) = \frac{a_{11}}{a_{12}} \tag{2.21}$$

and the δ_2 can be solved as:

$$\delta_2 = \arcsin\left(\frac{a_{11}}{\sqrt{a_{11}^2 + a_{12}^2}}\right) + \arccos\left(\frac{b_1}{\sqrt{a_{11}^2 + a_{12}^2}}\right) \tag{2.22}$$

So the expression of singularity points ($N_2 = N_{2,j}, j = 1, 2$) is given:

$$\Delta_{2,j} = \gamma_j \pm \arccos\left(\frac{N_{2,j}\left(16\lambda_1 - 24\lambda_1 K N_{2,j}^2 + 9\lambda_1 K^2 N_{2,j}^4 + 16\lambda_2 + 16\lambda_1\lambda_2^2\right)}{4F\sqrt{9K^2N_{2,j}^4 - 24KN_{2,j}^2 + 16 + 16\lambda_2^2}}\right) \tag{2.23}$$

with

$$\gamma_j = \arcsin\left(\frac{4\lambda_2}{\sqrt{9K^2N_{2,j}^4 - 24KN_{2,j}^2 + 16 + 16\lambda_2^2}}\right) \tag{2.24}$$

The expression of (2.23) inside the $arccos$ should be less than or equal to 1. So the excitation thresholds G_jc are given by:

$$G_jc = \epsilon F_jc = \frac{\varepsilon N_{2,j}\left(9\lambda_1 K^2 N_{2,j}^4 - 24\lambda_1 K N_{2,j}^2 + 16\left(\lambda_1 + \lambda_2 + \lambda_1\lambda_2^2\right)\right)}{4\sqrt{9K^2N_{2,j}^4 - 24KN_{2,j}^2 + 16 + 16\lambda_2^2}}, j = 1, 2 \tag{2.25}$$

The excitation thresholds G_jc divide the response regimes for each level of energy. In the following numerical simulation, the parameters of cubic NES case are fixed as: $\epsilon = 0.01$, $\lambda_1 = 1.67$, $\lambda_2 = 0.167$, $K = 1742$. As the amplitude of displacement excitation increases, the three types of dynamic behaviors occur:

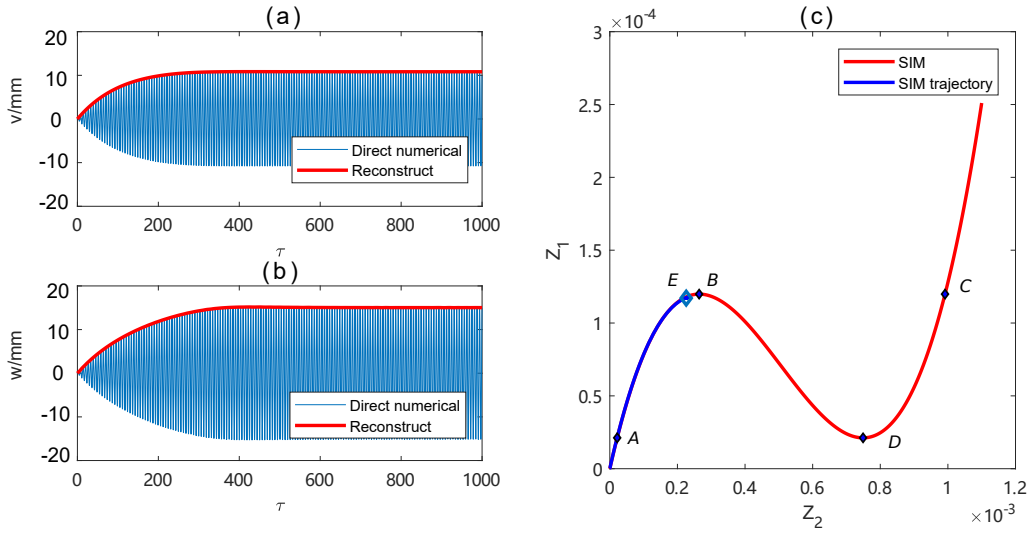

Figure 2.3: Stable response: cubic NES response under low energy input (G = 0.22mm with initial condition: $v(0) = \dot{v}(0) = w(0) = \dot{w}(0) = 0$). Subplots (a) and (b) represent the time-displacement response of v and w, the red curve is the reconstructed envelope amplitude (c) reconstructed trajectory projection (blue) in SIM structure (red).

(a) Stable response

When the harmonic excitation is lower than G_1c, the efficient energy pumping is not activated. The response of LO and NES appears to be a periodic response with constant amplitude as in Fig. 2.3a. The reconstructed envelope is obtained by solving the complex equation (2.8). The blue trajectory of amplitude rises along with the SIM over time in Fig. 2.3c. Its final point E is located on the left SIM stable branch. With the increasing harmonic excitation amplitude, the final stable position E is closer to the singularity point B, before snap-through. Point A is located on the left branch with the same Z_1 value as singularity point D. Point C has the same Z_1 height as singularity point B but is located on the right branch.

(b) SMR

When the excitation amplitude exceeds the critical value of excitation G_1c but is lower than G_2c, a saddle-node bifurcation occurs. The existence of folded singularity results in the relaxation-type oscillation phenomenon like Fig. 2.4b. The trajectory of the system in Fig. 2.4c has a snap-through motion between the two stable branches. A complete SMR cycle consists of a trajectory $A - B - C - D - A$ of 4 steps on the SIM branch. In the first $A - B$ stage, the NES amplitude is low and TET is not activated. The growth of LO amplitude is observed. The snap-through motion appears in the second $B - C$ stage. This snap-through motion of phase trajectory implies a sudden increase of NES amplitude. In the third $C - D$ stage, the resonance capture results in a fast decrease of LO amplitude. Phase trajectory moves down along the SIM right branch. After most of LO energy is dissipated, the trajectory returns to point A in the fourth $D - A$ stage. It also brings a sudden decrease in NES amplitude. A new SMR cycle starts. The trajectory on the stable branch for the stage $A - B$ and $C - D$ coincide closely with the backbone of the

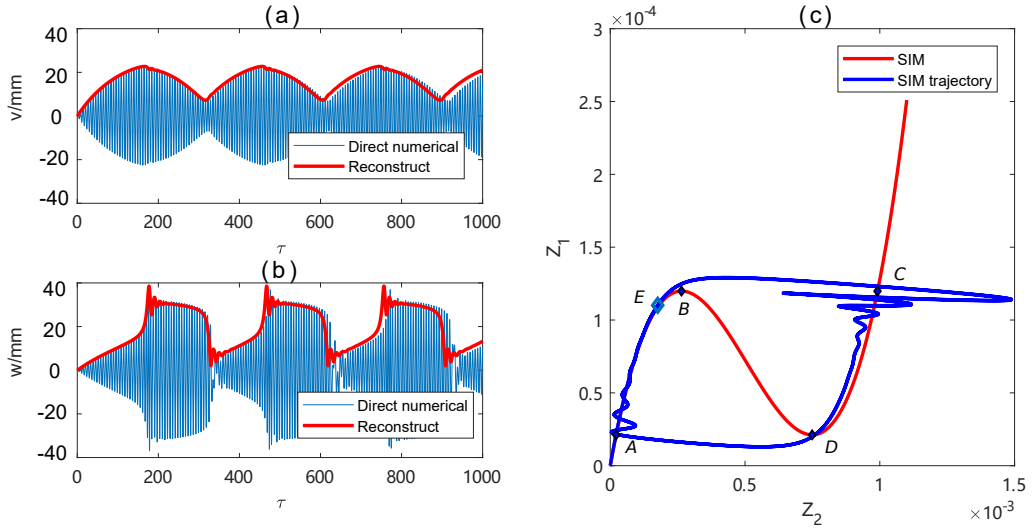

Figure 2.4: SMR: cubic NES response under moderate energy input (G = 0.28mm with initial condition: $v(0) = \dot{v}(0) = w(0) = \dot{w}(0) = 0$). Subplots (a) and (b) represent the time-displacement response of v and w, the red curve is the reconstructed envelope amplitude (c) reconstructed trajectory projection (blue) in SIM structure (red).

SIM. So SIM is an efficient tool to describe the SMR motion.

(c) Post stable response

If the excitation amplitude continues to grow and surpasses the upper boundary G_2c of SMR interval, the SMR disappears and an ordinary fixed point E occurs on the phase portrait of the SIM. The ordinary fixed point corresponds to a periodic response in Fig. 2.5a. The trajectory of the system in Fig. 2.5c arrives at the final stable point, E, located on the SIM stable branch, close to the singularity point D of the right branch.

2.1.3 Efficiency analysis of cubic NES

To better understand the efficiency with which the input energy is absorbed during the different stages, the energy dissipation ratio is defined in the time interval $[\tau_0, \tau]$ as:

$$\begin{aligned} E_{\mathrm{LO}}(\tau) &= \int_{\tau_0}^{\tau} \epsilon\lambda_1 \dot{x}^2 \mathrm{d}\tau \\ E_{\mathrm{NES}}(\tau) &= \int_{\tau_0}^{\tau} \epsilon\lambda_2 (\dot{x}-\dot{y})^2 \mathrm{d}\tau \\ r_{NES} &= \frac{E_{NES}}{E_{NES}+E_{LO}} 100\% \end{aligned} \tag{2.26}$$

Figure. 2.6 shows that the 3 response stages are divided by the analytical SMR interval $[G_1c, G_2c]$. When the input energy ($G < G_1c$) is too weak to activate the SMR, the average LO amplitude and maximal LO amplitude coincide and increase linearly as the excitation amplitude increases. Once the harmonic excitation is strong enough to activate the SMR, the difference between average and maximal LO amplitude reveals that the amplitude of the NES is no longer stable. In comparison with the previous stage, the NES possesses more energy. Even though the external excitation is increasing, the maximal amplitude of LO remains almost constant. When the excitation amplitude achieves the G_2c threshold

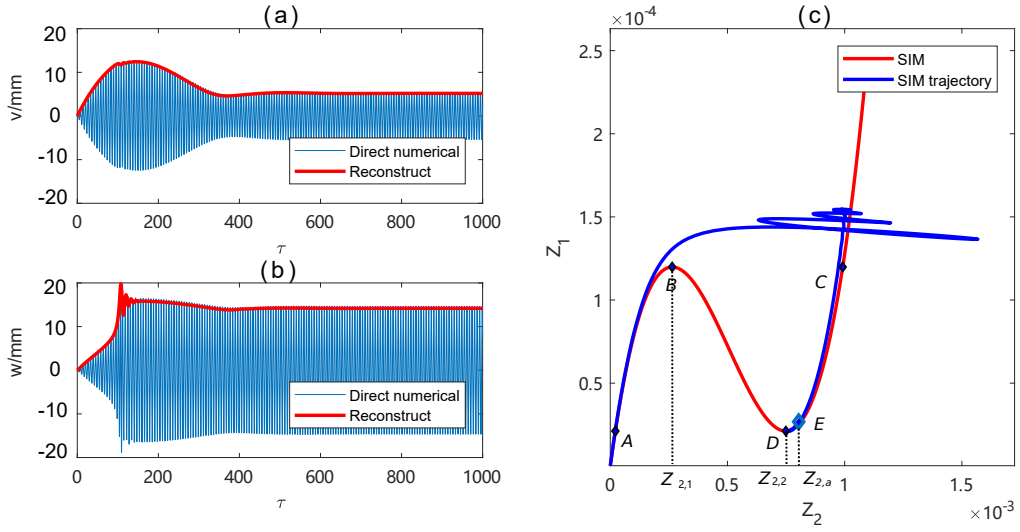

Figure 2.5: Post stable response: cubic NES response under intense energy input (G = 0.38mm with initial condition: $v(0) = \dot{v}(0) = w(0) = \dot{w}(0) = 0$), where SMR just disappears. Subplots (a) and (b) represent the time-displacement response of v and w, the red curve is the reconstructed envelope amplitude (c) reconstructed trajectory projection (blue) in SIM structure (red).

value, the curves of average and maximal LO amplitude coalesce again and NES motion becomes stable. With a slight increase in excitation amplitude, the system arrives at its maximum efficiency point and the amplitude of LO is a local minimum. That means that the full potential of absorbing energy has been explored.

Through the efficiency distribution, the maximal efficiency point and the local lowest LO amplitude appear when the excitation amplitude is slightly above the threshold G_2c. In this optimal state, the system performs a stable response and phase trajectory is locates at the singularity point D in the SIM structure.

When the system achieves a stable optimal state, the periodic solution of Eq. (2.8) can be expressed under the assumption that the derivative is zero.

$$\dot{\phi}_1 = \dot{\phi}_2 = 0, \phi_1 = \phi_{10}, \phi_2 = \phi_{20} \tag{2.27}$$

Introducing them into the second equation of (2.8), a more convenient expression is deduced for the 1:1 resonance condition ($\Omega = 1$):

$$\alpha_3 K^2 Z_{20}^3 + \alpha_2 K Z_{20}^2 + \alpha_1 Z_{20} + \alpha_0 F^2 = 0, \quad Z_{20} = |\phi_{20}|^2 \tag{2.28}$$

where

$$\begin{aligned} \alpha_0 &= -\frac{1}{4}\frac{(\varepsilon^2\lambda_1^2 + 1)(1+\varepsilon)^2}{(\lambda_1^2+1)} \\ \alpha_1 &= \frac{1}{4}\frac{(\lambda_1^2\lambda_2^2 + \lambda_1^2 + 2\lambda_1\lambda_2 + \lambda_2^2)(1+\varepsilon)^2}{\lambda_1^2+1}, \\ \alpha_2 &= -\frac{3}{8}\frac{(1+\varepsilon)^2\lambda_1^2}{\lambda_1^2+1}, \alpha_3 = \frac{9}{64}(1+\varepsilon)^2 \end{aligned} \tag{2.29}$$

The above equation manifests the relationship between the excitation amplitude G ($G = \epsilon F$) and stable NES amplitude in the function of cubic nonlinearity parameter K.

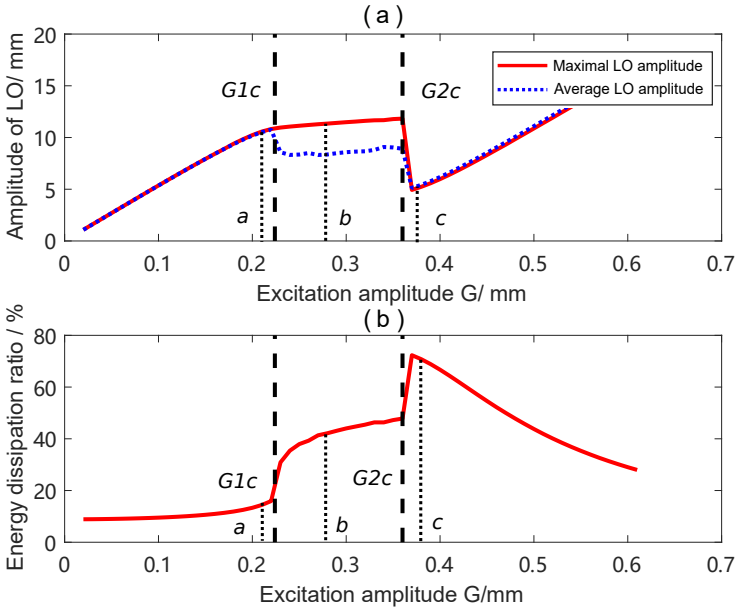

Figure 2.6: Response of cubic NES under the increasing excitation amplitudes, $\sigma = 0$ (a) the maximal amplitude and average amplitude of LO, (b) energy dissipation ratio of NES. Dotted lines a, b and c in figures represent condition in Fig. 2.3, 2.4 and 2.5.

Once the target excitation amplitude is fixed, the optimal K value can be calculated by setting critical condition $Z_{20} = Z_{2,2}$ into Eq. (2.28). So the optimal K design function is expressed:

$$K = -\frac{4}{729}\frac{1}{\alpha_0 F^2}(16\sqrt{(-3\lambda_2^2+1)^3}\alpha_3 - 108\lambda_2^2\alpha_2 - 288\lambda_2^2\alpha_3 + 81\sqrt{-3\lambda_2^2+1}\alpha_1 + 144\alpha_2\sqrt{-3\lambda_2^2+1} + 192\sqrt{-3\lambda_2^2+1}\alpha_3 + 162\alpha_1 + 180\alpha_2 + 224\alpha_3) \tag{2.30}$$

The amplitudes of LO under different cubic nonlinearity parameters K and various harmonic excitation amplitudes are presented in Fig. 2.7 to check the accuracy of the predictions. The various cubic nonlinearity parameters are tested under a certain excitation to find an optimal K value.

The thick red line corresponds to the numerical optimal K design curve. It represents the projection of the minimal amplitude that LO can have for a certain excitation in the $K - G$ plane. The thin red and thin dotted blue lines are the maximal and average amplitudes of LO respectively. The SMR occurs in the region, where these lines do not coincide. The dotted and dashed thick blue lines represent the analytical optimal K design with and without correction coefficient ξ respectively.

An obvious trend is observed: a larger imposed excitation amplitudes leads to a smaller designed cubic nonlinearity parameter. There is a distance between the real and predicted curves. The distance can be interpreted by the errors between the analytical arrival point D and real arrival point E in Fig. 2.5c.

Ideally, once the SMR vanishes, the final stable solution should be located at singularity point D. In fact, the simulation demonstrates that the real final stable point does not coincide with point D, but is slightly higher on the SIM. The theoretical amplitude

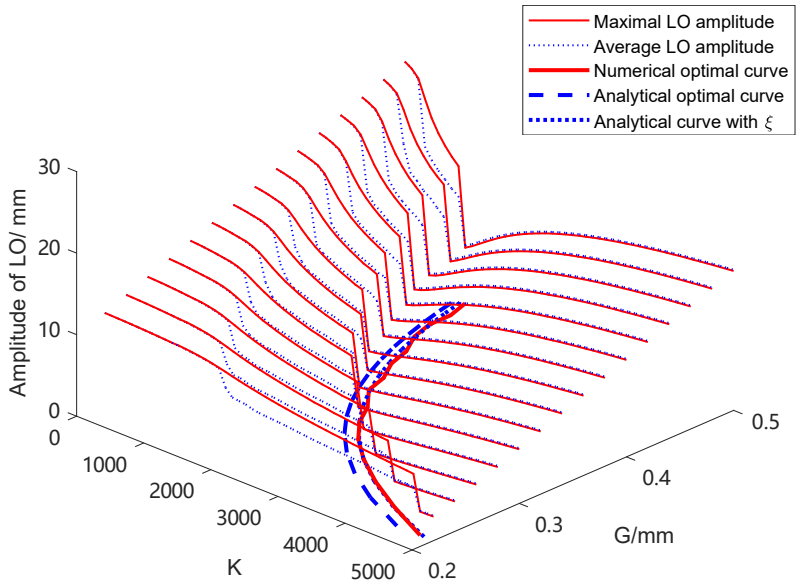

Figure 2.7: Distribution of the LO amplitude with the variation of excitation amplitudes G and cubic nonlinearity parameters K under the damping condition $\lambda_1 = 1.67$, $\lambda_2 = 0.167$.

threshold $Z_{2,2}$ may be smaller than the simulated value $Z_{2,a}$, leading to errors between the analytical and numerical $K - G$ curves.

The correction coefficient ξ is defined as $Z_{2,a} = \xi Z_{2,2}$ to describe the distance between the analytical arrival point $Z_{2,2}$ and simulated arrival point $Z_{2,a}$. $\xi = 1.07$ is given by the measurement in Fig. 2.5 and then it is introduced into Eq. (2.28) to calculate K. The corrected predicted curve (thick blue dotted line in Fig. 2.7) almost coincides with the real optimal $K - G$ curve.

The correction coefficient ξ helps improve the accuracy in the prediction of the optimal K value. If the cubic nonlinearity parameter of the system exceeds the optimal value, then the response of the system will remain stable. For example, the cubic nonlinearity parameter must be tuned to 1500 in order to minimise the LO amplitude (5.3mm) under excitation (G = 0.4mm) (Fig. 2.7). When the K value is extended to 3400, the LO possesses a minimal stable amplitude of 10.2mm, which is smaller than the average amplitude of the LO during SMR (10.26mm). Thus, in the K value range [1500, 3400], cubic NES can achieve a better absorption performance than SMR. A vast range of K can be chosen. When the system faces uncertainties in the K value, it shows a strong robustness. The absorption efficiency can be maintained at a relatively high level if the K value is slightly larger than the optimal value. Even if the K value is lower than the optimal value, the response is SMR, which is still considered to be highly efficient.

When phase trajectory reaches its ideal maximum efficiency point D in SIM structure, the system has a periodic response. So the constant amplitude of NES and LO is marked as $N_{2,2}$ and $N_{1,2}$. The response of w can be expressed as $w = N_{2,2}cos(\tau+\delta_1)$ approximately. In the whole period (τ to $\tau + 2\pi$), the energy dissipated by NES can be rewritten as:

$$\int_{\tau}^{\tau+2\pi} \varepsilon\lambda_2 \dot{w}^2 d\tau = \int_{\tau}^{\tau+2\pi} \varepsilon\lambda_2 \left(-N_{2,2}\sin\left(\tau+\delta_1\right)\right)^2 d\tau = \varepsilon\lambda_2 N_{2,2}^2 \pi \tag{2.31}$$

As for the energy dissipated by the LO, the velocity $\dot{x}$, the x can be expressed as $x = v + \epsilon y$, where the ϵ is an extremely small parameter and leads to $x \approx v$. So, at the maximum efficiency point, x is $N_{1,2}cos(\tau + \delta_2)$. Similarly to Eq. (2.31), the energy dissipated by the LO in the whole period is $\varepsilon\lambda_1 N_{1,2}^2\pi$. So the maximum efficiency point during one period is

$$r_{NES} = \frac{\lambda_2 N_{2,2}^2}{\lambda_1 N_{1,2}^2 + \lambda_2 N_{2,2}^2} \tag{2.32}$$

According to the Eq. (2.15), from a theoretical point of view, the above equation is finally turned into the following form with $N_{2,2} = \sqrt{Z_{2,2}}$ and $N_{1,2} = \sqrt{Z_{1,2}}$, where $Z_{1,2}$ is the value of Z_1 at singularity point D:

$$r_{NES} = \frac{9\lambda_2}{6\lambda_1\lambda_2^2 - 2\lambda_1\sqrt{-3\lambda_2^2 + 1} + 2\lambda_1 + 9\lambda_2} \tag{2.33}$$

This equation shows that the ceiling of maximum theoretical efficiency is determined only by the damping λ_1 and λ_2. Fig. 2.8a depicts its maximum theoretical efficiency values for different damping conditions. In fact, the ideal amplitude of NES and LO for the instant the SMR disappears shows some differences with simulation, which leads to the error between the analytical maximum efficiency value and the simulated value.

The distribution of parameters ξ in the λ_1, λ_2 plane can be used to correct predicted maximum efficiency, shown in Fig. 2.8b. The analytical value $Z_{2,2}$ produces greater errors than the simulated value $Z_{2,a}$ in the lower λ_1, λ_2 values. In contrast, the analytical value $Z_{2,2}$ can better describe the arrival point $Z_{2,a}$ for a relatively high damping parameter. So the maximum efficiency value when considering the correction coefficient ξ can be rewritten as:

$$r_{NES} = \frac{9\lambda_2}{(4\xi^2 - 6\xi)\lambda_1\sqrt{-3\lambda_2 + 1} + (-3\xi^2 + 9)\lambda_1\lambda_2^2 + \lambda_1(5\xi^2 - 12\xi) + 9(\lambda_1 + \lambda_2)} \tag{2.34}$$

The distribution of maximum efficiency based on Eq. (2.34) is illustrated in Fig. 2.8c. It demonstrates that for certain fixed λ_1, an optimal damping value λ_2 exists to promote the energy-absorbing performance. Reducing the damping on the preliminary structure λ_1 can enhance the maximum absorbing efficiency value.

The three different damping conditions, labelled in Fig. 2.8c as condition 1, 2 and 3, are used to verify the analytical prediction of maximum efficiency. The predicted values for conditions 1, 2 and 3, are obtained directly by Eq. (2.34) with different correction coefficients $\xi = 1.12, 1.06, 1.13$ from Fig. 2.8b, are 77%, 71% and 53% respectively. The direct calculations of maximum efficiency of 76%, 68% and 52%, which are very close to the predicted values. A simpler way to estimate maximum efficiency value has been found.

To verify that the maximum absorbing efficiency values are independent of the optimal cubic nonlinearity parameter design, various simulations are performed in the different damping environments, as shown in Fig. 2.9. Each point on the excitation-efficiency line represents the maximum efficiency value achievable for the corresponding optimal cubic nonlinearity parameter design with correction coefficients from Eq. (2.30). For the brown line in Fig. 2.9, when excitation amplitude changes from 0.1mm to 1mm, the optimal K design changes according to Fig. 2.7 but the maximum efficiency value is almost constant.

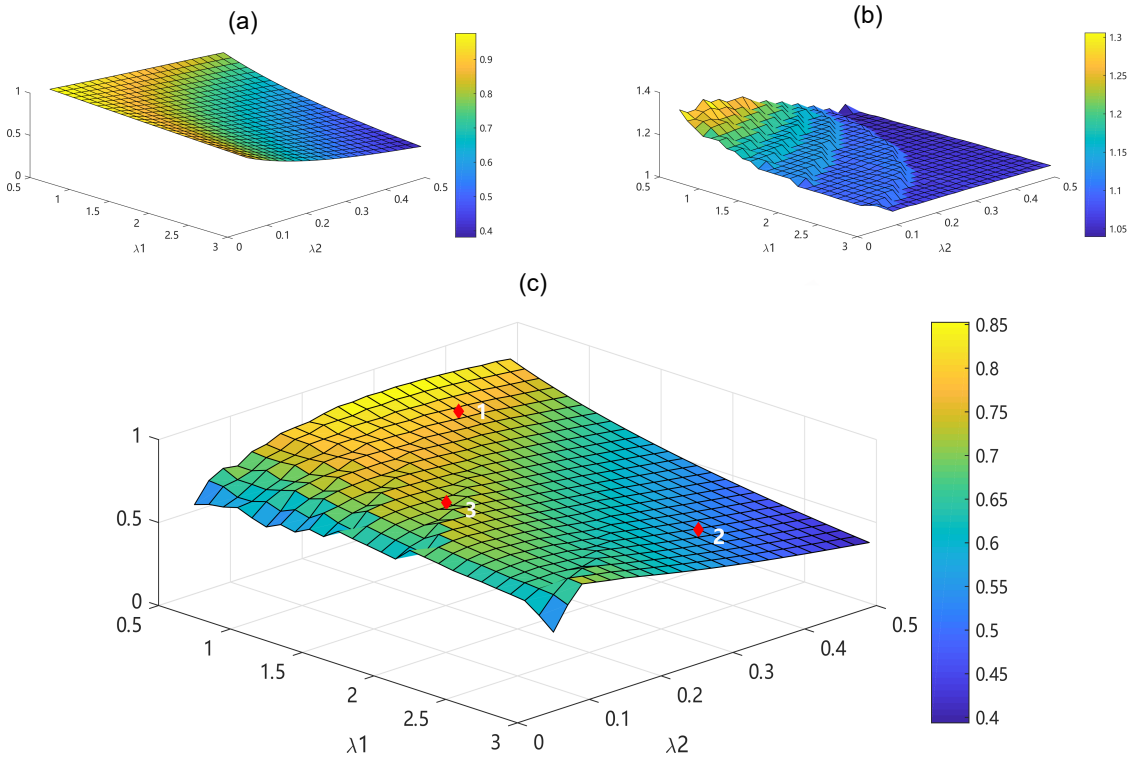

Figure 2.8: Maximum efficiency values and correction coefficient ξ in the function of λ_1 and λ_2 in case $K = 1742$ and $\epsilon = 0.01$. (a) ideal maximum efficiency estimated by Eq. (2.33) (b) correction coefficient ξ distribution (c) maximum efficiency values with ξ corrected by Eq. (2.34), point 1, 2 and 3 are the 3 conditions to be verified.

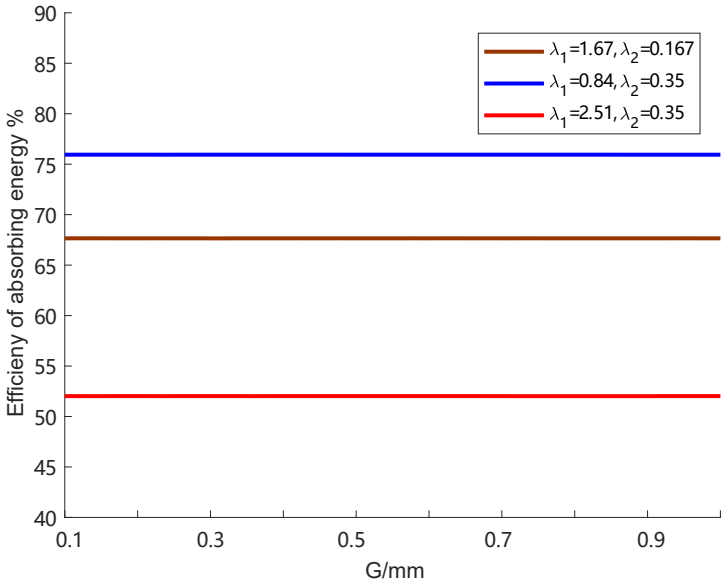

Figure 2.9: Maximum energy dissipation ratio that a best tuned K system for certain excitation G can achieve under the different damping parameters conditions.

This phenomenon indicates that the maximum ability to absorb energy is independent of the K design. The cubic nonlinearity parameter design can only adopt a certain excitation input and its maximum efficiency level is determined by the damping conditions.

According to Eq. (2.33), the cubic nonlinearity parameter K and mass ratio ϵ do not influence the limit of maximum efficiency. Combining a lower damping of a main structure $\lambda_1 = 0.5$ and a relative lower damping of NES system $\lambda_2 = 0.33$ can improve the maximal efficiency level to 85%. So, the maximal absorbing efficiency can be enhanced by selecting the proper damping condition. Because the prerequisite of the above result is the existence of SMR, the restrict of $\lambda_2 < 1/\sqrt{3}$, and not too high a mass ratio ϵ is still necessary [Starosvetsky et Gendelman, 2010].

2.2 Experimental study of cubic NES

To obtain the strong nonlinearity, the four springs device is constructed by Qiu [Qiu *et al.*, 2019a]. The whole system is consists of two nonlinear springs and two linear springs. According to the characteristic of nonlinearity that is provided by different parts of the device, the cubic NES device is classified into two parts: (1) conical springs mechanism, (2) linear springs mechanism

(a) Conical springs mechanism

The conical springs are adapted because of their advantages in anti-buckle at large deflection. The single conical spring presents a piecewise force-displacement curve as Fig. 1.12a shows. Once the deflection of spring crosses the transition point, the nonlinear behaviors start. So to overcome the linear stiffness phase, a symmetrical connection type is proposed as Fig. 2.10a. The two conical springs are pre-compressed

Table 2.1: Experimental parameters of NES system

k_0	a_1	a_3	k_l	l_{0l}	l_c
187N/m	280N/m	3.4e5N/m^3	1100N/m	50mm	14.3mm

at the transition point. When the center mass moves along the axis of conical spring, the composed force-displacement curve is smooth and no longer piecewise. The new force-displacement relation is written as:

$$F = (k_0 + a_1) \cdot u + a_3 \cdot u^3 \tag{2.35}$$

where k_0 are linear phase stiffness. a_1 and a_3 are the linear stiffness and cubic nonlinearity value in the nonlinear phase of conical spring. Although it exists the square term in the combined curve, its contribution can be maintained within a small value and negligible by optimization of the mean diameters of the biggest and smallest coils of conical spring [Qiu *et al.*, 2018b].

(b) Linear springs mechanism

The composed force-displacement curve of conical springs contains a linear stiffness part $k_0 + a_1$ that prevents the direct application of two conical springs systems. To construct a pure cubic nonlinearity without a linear part, a negative stiffness is implemented through two cylindrical compression springs as Fig. 2.10b. The cylindrical spring can rotate with the other end fixed. The direction of movement is perpendicular to its axis. Based on the Taylor expansion, the force-displacement in the function of pre-compression length (l_p) can be expressed as:

$$F = (-2k_l \frac{l_p}{l_{0l} + 2l_c - l_p}) \cdot u + (k_l \frac{l_{0l} + 2l_c}{(l_{0l} + 2l_c - l_p)^3}) \cdot u^3 \tag{2.36}$$

where l_{0l} and l_c are the free lengths of linear spring and connector respectively. k_l is the stiffness of linear spring.

By combining the conical springs and linear springs, the composed system is presented as Fig. 2.10c and the corresponding force-displacement relationship is obtained:

$$F = k_2 u + k_3 u^3, k_2 = \left(a_1 + k_0 - 2k_l \frac{l_p}{l_{0l} + 2l_c - l_p}\right), k_3 = \left(a_3 + k_l \frac{l_{0l} + 2l_c}{(l_{0l} + 2l_c - l_p)^3}\right) \tag{2.37}$$

The linear stiffness of four springs device k_2 can be totally counterbalanced through tuning the proper pre-compression length l_p. To verify the analytical prediction and optimal design, an adjustable four springs device is constructed and is presented in Fig. 2.11. The parameter of the four springs system is given in Tab.2.1.

A linear oscillator is connected to a 10kN electrodynamics shaker and is excited by a harmonic excitation with its natural frequency. The NES mass is embedded through a track and a four springs device. The latter prived the cubic nonlinearity parameter and negative stiffness through adjusting pre-compression length of linear springs. The two contactless displacement sensors are installed vertically to measure absolute displacement of LO and NES. An accelerometer is also installed to the shaker to measure its acceleration.

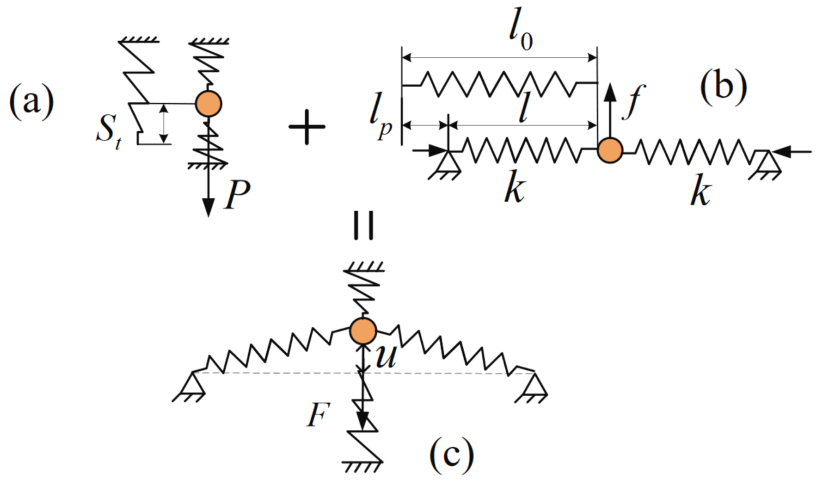

Figure 2.10: Detailed diagram of the NES system: (a) conical springs mechanism, (b) linear springs mechanism, (c) combining system.

Table 2.2: Environmental parameters of the experiment

Physical parameters	m_1	m_2	c_1	c_2	k_1
	5.5kg	0.065kg	5N·s/m	0.5N·s/m	1.145e4N/m
Reduced parameters	ϵ	λ_1	λ_2	f_0	
	1.18%	1.69	0.169	7.3Hz	

The extra digital oscilloscope and a bandpass filter can correct bias and attenuate high frequency noise. The LO mass, NES mass and their corresponding damping are presented in Tab. 2.2. The dimensionless parameters (mass ratio, damping, natural frequency) are fixed to design the optimal K.

When the length of pre-compression l_p is about 14mm, the calculated cubic nonlinearity value k_2 is 6.61e5 N/m^3 (K = 4.86e3), the linear part k_3 equal to -9 N/m. The value of linear part is very small compared to the strong nonlinearity ($\delta = 0$). So in this case, the four springs device is tuned as a cubic NES. The experiment measurement of cubic nonlinearity value is presented in Fig. 2.12. Although some distributions exist in the vicinity of zero position, the prediction of force-displacement relationship is close to the experimental result, especially in a large displacement.

In this parameter condition, the analytical prediction of Eq. (2.25) indicates that this state is designed for target excitation G = 0.26mm. So the system can have a minimal stable amplitude. To verify the optimal design for G = 0.26mm, two different excitation amplitudes G = 0.25mm and G = 0.28mm are examined. As the previous response regime analysis, if the input amplitude is lower than the critical value, the system still performs the SMR. So time-displacement response in the blue curve shows a classic SMR in Fig. 2.13. The LO oscillates in a stable response with minimal amplitude if the excitation slightly exceeds the target excitation. When G = 0.28mm, the stable response occurs as the red curve in Fig. 2.13. So an optimal design for the target excitation is achieved in the cubic NES case.

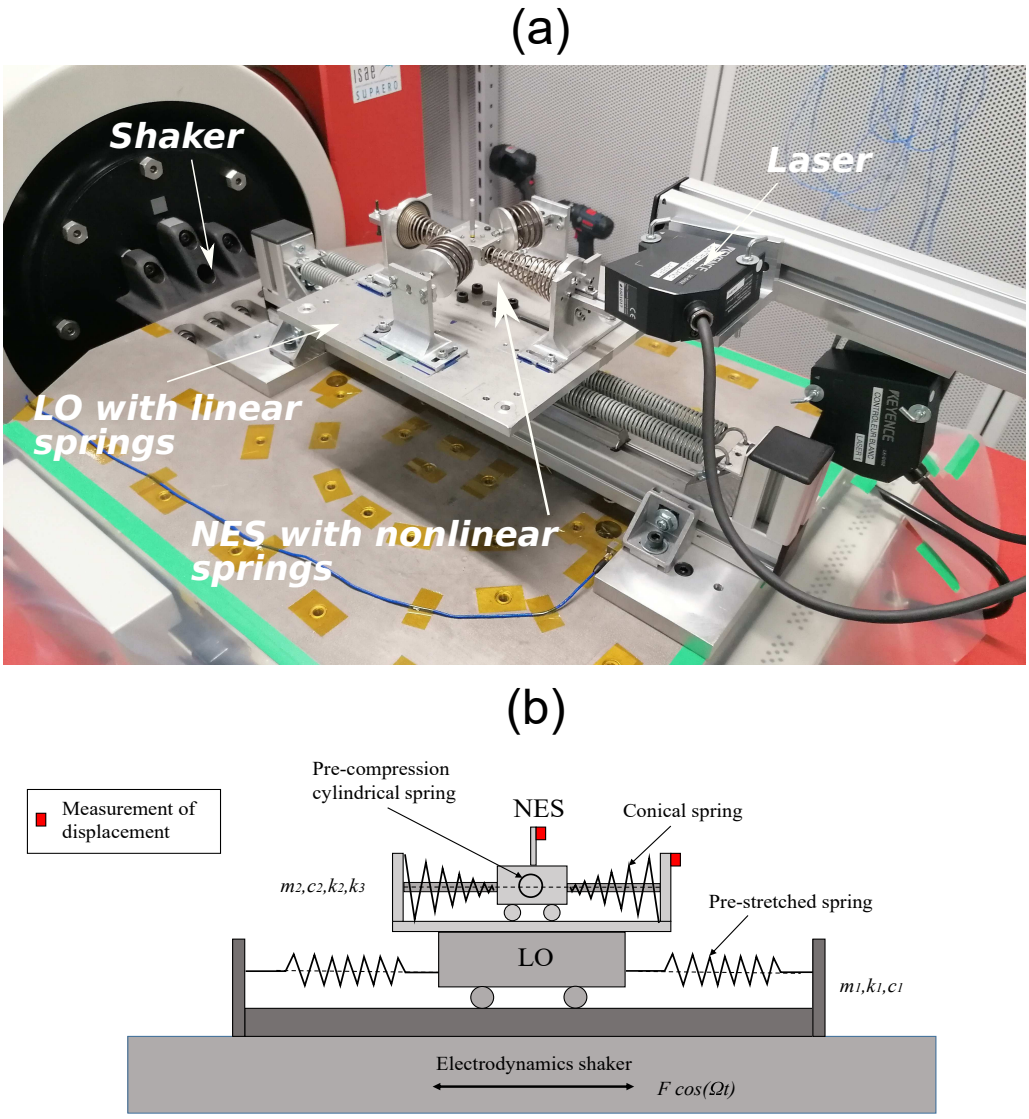

Figure 2.11: (a) Detailed view of experimental setup (b) Scheme of system.

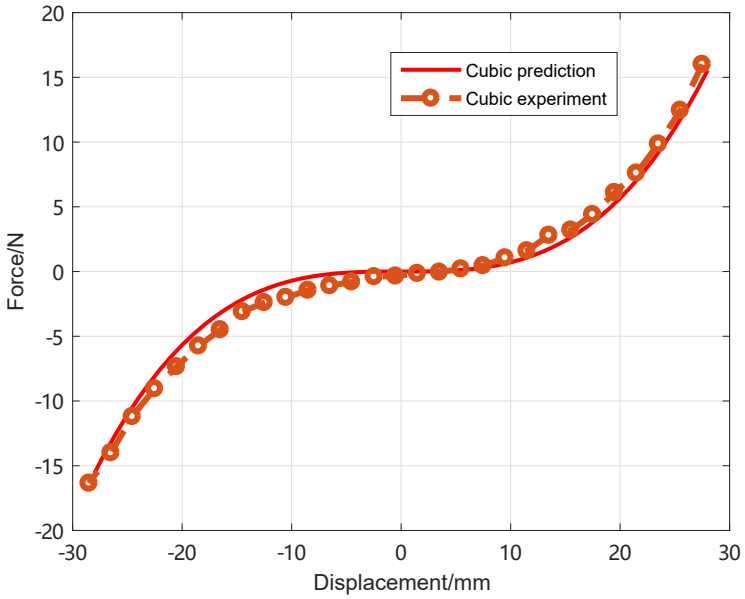

Figure 2.12: Experimental measurement of cubic force-displacement curve.

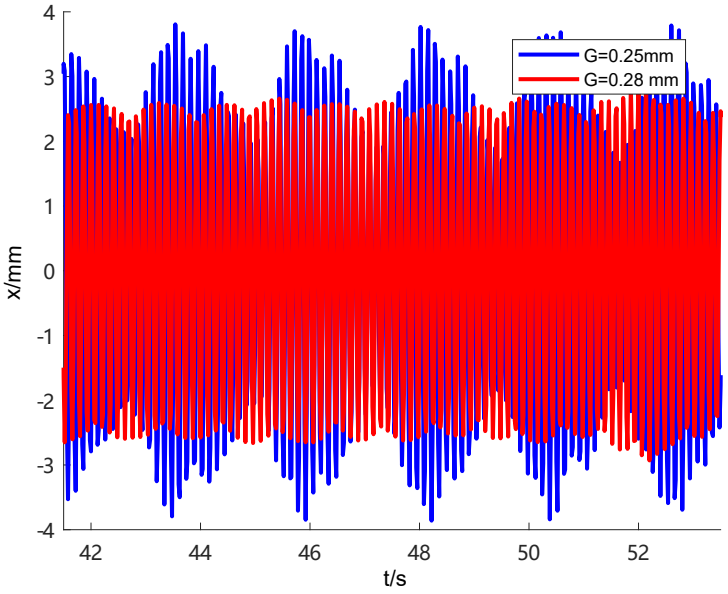

Figure 2.13: Experimental result of time displacement for optimal cubic NES design for target excitation G = 0.26mm. Blue curve is the response of LO under G = 0.25mm. Red curve is the response of LO under G = 0.28mm.

2.3 Optimal design criteria for bistable NES

Through the Eq. (2.37), a large pre-compressed length l_p will cause the negative stiffness becomes significant. It is inappropriate to ignore them in the analytical process. So the cubic NES will turn into a bistable NES configuration as Fig. 2.14 illustrates.

The introduction of negative stiffness in the experimental device will produce two equilibrium points, one on either side of the original coordinate. And the dynamic behavior of bistable NES shows some different features, for example, chaos motion and intra-well oscillation. The original motion equation has to add the negative stiffness term k_3 in Eq. (2.1), it gives:

$$\begin{aligned} &m_1\ddot{x} + k_1 x + c_1\dot{x} + c_2(\dot{x}-\dot{y}) + k_2(x-y)^3 + k_3(x-y) = k_1 x_e + c_1\dot{x}_e \\ &m_2\ddot{y} + c_2(\dot{y}-\dot{x}) + k_2(y-x)^3 + k_3(y-x) = 0 \end{aligned} \tag{2.38}$$

With the similar treatment procedure in the cubic NES case and a new variable $\delta = k_3/m_2\omega_0^2$, the systems equations can reproduce a demensionless form:

$$\begin{aligned} &\ddot{v} + \epsilon\lambda_1\frac{\dot{v}+\epsilon\dot{w}}{1+\epsilon} + \frac{v+\epsilon w}{1+\epsilon} = \epsilon F\cos\Omega\tau \\ &\ddot{w} + \epsilon\lambda_1\frac{\dot{v}+\epsilon\dot{w}}{1+\epsilon} + \frac{v+\epsilon w}{1+\epsilon} + \lambda_2(1+\epsilon)\dot{w} + K(1+\epsilon)w^3 + \delta(1+\epsilon)w = \epsilon F\cos\Omega t \end{aligned} \tag{2.39}$$

By appling the complexification-averaging method and multiple scales method, the ϵ^0 order of bistable system is extracted as:

$$\begin{aligned} &\frac{\mathrm{d}}{\mathrm{d}\tau_0}\phi_1 = 0 \\ &\frac{\mathrm{d}}{\mathrm{d}\tau_0}\phi_2 + \frac{1}{2}i\left(\phi_2-\phi_1\right) + \frac{1}{2}\phi_2\lambda_2 - \frac{3}{8}iK\phi_2^2\overline{\phi}_2 - \frac{1}{2}i\delta\phi_2 = 0 \end{aligned} \tag{2.40}$$

the ϵ^1 order

$$\begin{aligned} &\frac{d}{d\tau_1}\phi_1 + \frac{1}{2}\lambda_1\phi_1 + \frac{1}{2}i\left(\phi_1-\phi_2\right) + i\sigma\phi_1 - \frac{1}{2}F = 0 \\ &\frac{d}{d\tau_1}\phi_2 + \frac{1}{2}\lambda_1\phi_1 + \frac{1}{2}\phi_2\lambda_2 + \frac{1}{2}i\sigma\left(\phi_1+\phi_2\right) + \frac{1}{2}i\left(\phi_1-\phi_2\right) \\ &-\frac{3}{8}iK(1-3\sigma)\phi_2^2\overline{\phi}_2 - \frac{1}{2}F + \frac{1}{2}i\delta(\sigma-1)\phi_2 = 0 \end{aligned} \tag{2.41}$$

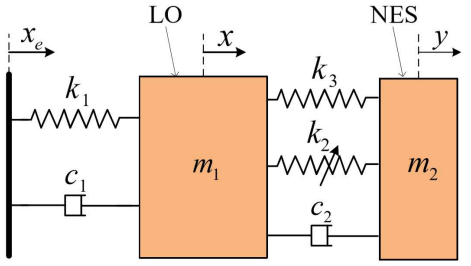

Figure 2.14: Schematic of linear oscillator and bistable NES system

Another aspect of the introduction of the negative stiffness parameter δ is the deformation of SIM structure, which is expressed:

$$\begin{aligned} Z_1 &= \lambda_2^2 Z_2 + (\delta-1)^2 Z_2 + \frac{3K}{2}(\delta-1)Z_2^2 + \frac{9K^2}{16}Z_2^3 \\ Z_1 &= N_1^2, \quad Z_2 = N_2^2 \end{aligned} \tag{2.42}$$

with corresponding singularity points

$$Z_{2,j} = N_{2,j}^2 = \frac{4\left(2(1-\delta) \mp \sqrt{(1-\delta)^2 - 3\lambda_2^2}\right)}{9K}, j = 1,2 \tag{2.43}$$

2.3.1 Bistable NES response regimes

When the motion of NES is between two equilibrium, the dynamic transition is rapid and sweeps out a large stroke due to the negative stiffness. Thus, the viscous damping can realize a highly efficient energy dissipation. A double-wells restoring force potential can better manifest the four different response regimes.

The second equation of Eq. (2.38) is equivalent to: $\ddot{w} + \lambda_2\dot{w} + Kw^3 + \delta w = \ddot{x}$ with the definition $\lambda_2 = \epsilon\hat{\lambda}_2, \ddot{x} = \epsilon\hat{x}, u_1 = w, u_2 = \dot{w}$. It is necessary to consider the acceleration term and damping term as small perturbations to the Hamiltonian system.

$$\begin{cases} \dot{u}_1 = u_2 \\ \dot{u}_2 = -\delta u_1 - K u_1^3 + \epsilon\left(\hat{x} - \hat{\lambda}_2 u_2\right) \end{cases} \tag{2.44}$$

The Hamiltonian of system without perturbation ($H(u_1, u_2)$) and its potential function ($U(u_1, u_2)$) can be written as:

$$\begin{aligned} H(u_1, u_2) &= \frac{u_2^2}{2} + \delta\frac{u_1^2}{2} + K\frac{u_1^4}{4} \\ U(u_1) &= \delta\frac{u_1^2}{2} + K\frac{u_1^4}{4} \end{aligned} \tag{2.45}$$

In the bistable case, the system is characterized by a double-well potential energy surface. Three equilibrium points exist: $(u_1, u_2) = (0,0)$ and $(u_1, u_2) = (\pm\sqrt{-\delta/K}, 0)$. The K governs the span of two wells $2\sqrt{-\delta/K}$ (the distance between two equilibra) and the depth of well $\Delta w = -\delta^2/4K$. When the potential energy of the NES is lower than Δw, it will be trapped in one of the two wells. So K and δ determine the lower boundary of energy above which bistable NES performs a cross-well oscillation. In contrast to the influence of K, larger values of $|\delta|$ increase the span and depth of the potential well. The parameters of this bistable NES case are fixed as: $\epsilon = 0.01$, $\lambda_1 = 1.67$, $\lambda_2 = 0.167$, $K = 1742$, $\delta =$ -0.44. According to the location of potential energy surface of bistable NES, its response regimes can be classified in four following stages.

(a) Intra-well oscillation

It exists two attrctor points at $w = \pm x_0 = \pm\sqrt{-\delta/K}$ in the potential function, where NES possesses the lowest potential energy and is called potential well. The critical LO amplitude for NES escaping from the well and chaos occurrence is obtained by the Melnikov analysis [Qiu *et al.*, 2019a]. When the LO amplitude is lower than the

critical value, the NES potential energy is in one of the wells. The NES oscillates around the stable equilibrium ($w = x_0$) as time displacement in Fig. 2.15, it is termed as intra-well oscillation. Since the cubic nonlinearity parameter is far larger than that of cubic NES near the stable equilibrium, relatively high efficiency can be produced for low energy input.

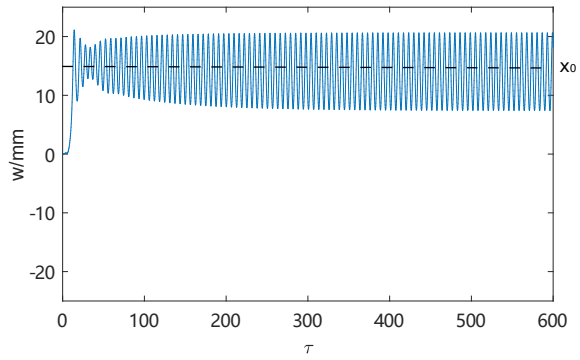

Figure 2.15: Time-displacement of bistable NES for intra-well oscillation with G = 0.05mm, $\sigma = 0$.

(b) Chaotic motion

Once the input energy increases, the trajectory will oscillate between two wells. So the displacement of NES can cross the two equilibrium with the occurance of chaos in Fig. 2.16. The chaotic motion is identified by the calculation of Lyapunov exponents, which is positive [Romeo *et al.*, 2015b]. The chaotic motion possesses higher energy than intra-well oscillation. In this stage, with increasing energy, 1: 3 subharmonic oscillation is also confirmed and brings a relatively low efficiency.

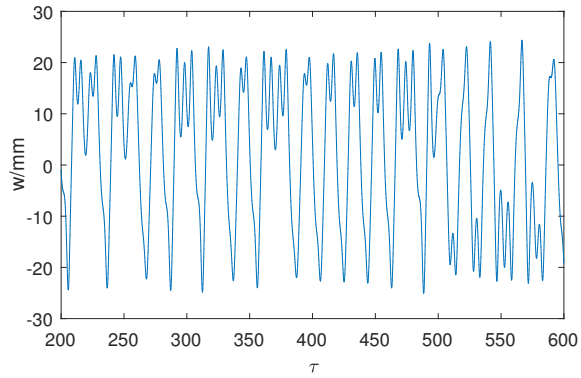

Figure 2.16: Time-displacement of bistable NES for chaotic motion with $G = 0.08$mm, $\sigma = 0$.

(c) SMR

When NES amplitude continues to grow, the cubic nonlinearity parameter has a larger effect on the response behaviour. In Fig. 2.17, the 1:1 resonance is mixed

with temporary chaotic motion. In the time domain, the chaotic motion connects two adjacent cycles of SMR. The boundary of the SMR stage and chaotic motion stage is hard to identify. With the increasing excitation amplitude, the time interval of chaotic motion will be compressed.

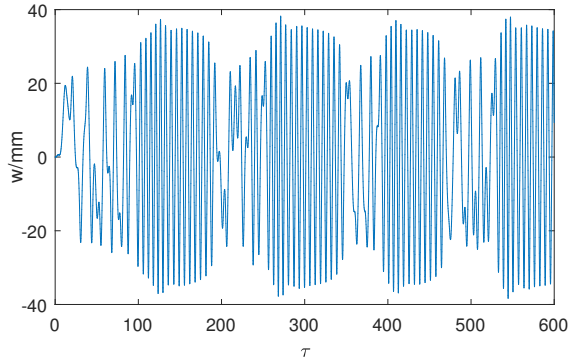

Figure 2.17: Time-displacement of bistable NES for SMR stage with $G = 0.3$mm, $\sigma = 0$.

(d) Periodic response

The system reaches a periodic response, and the SMR disappears in Fig. 2.18. The efficiency of the NES reaches its maximum value between the transition from the SMR stage to the stable response stage.

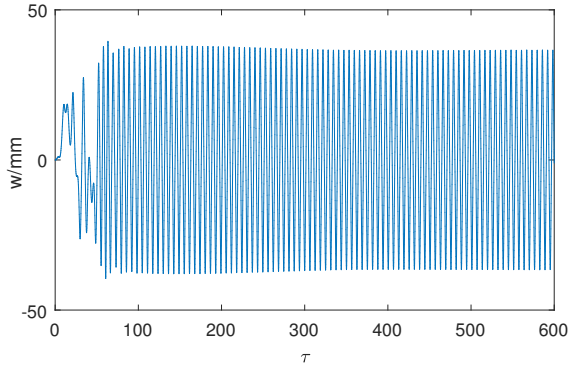

Figure 2.18: Time-displacement of bistable NES for stable response with $G = 0.5$mm, $\sigma = 0$.

2.3.2 Efficiency analysis of bistable NES

Fig. 2.19 illustrates the performance of bistable NES and its various stages with increasing excitation. G_0c is the boundary of chaos. Due to the mixture of chaos stage and beginning SMR, the analytical expression G_1c can not describe the occurrence of SMR. But the threshold excitation (G_2c) is still helpful for predicting the disappearance of SMR [Qiu *et al.*, 2018b], which gives:

$$
\begin{aligned}
&G_jc = \epsilon\frac{N_{2,j}}{4}\frac{F_1}{F_2}, j = 1, 2\\
&F_1 = 9K^2N_{2,j}^4\lambda_1 + 24KN_{2,j}^2\delta\lambda_1 - 24KN_{2,j}^2\lambda_1 + 16\delta^2\lambda_1 + 16\lambda_1\lambda_2^2 - 32\delta\lambda_1 + 16\lambda_1 + 16\lambda_2\\
&F_2 = \sqrt{9K^2N_{2,j}^4 + 24KN_{2,j}^2\delta - 24KN_{2,j}^2 + 16\lambda_2^2 + 16(\delta^2-1)^2}
\end{aligned}
\tag{2.46}
$$

The response regimes in Fig. 2.19 show the intra-welland inter-well oscillations, which are divided by G_0c. Before it enters the chaos stage, the NES exhibits a small amplitude response of oscillation around one of the equilibria. In this stage, the LO amplitude increases almost linearly and the curves of average and maximal LO amplitude coincide. However, the efficiency decreases rapidly with increasing excitation.

In the second stage, the displacement of NES starts to pass the two equilibria. The curves of average and maximal LO amplitude separate in Fig. 2.19, and the distance becomes larger, which means that the amplitude is not constant.

With the introduction of SMR, the distance between the average and maximal LO amplitude becomes constant. Moreover, the bistable NES performs a higher efficiency than that of cubic NES because of higher speed, and more significant stroke swept in the dynamic transition of negative stiffness.

Once the SMR disappears, the curves of the average and maximal LO amplitude coincide again. The efficiency of the NES reaches its maximum value, where the LO amplitude starts to increase with the growth of excitation amplitude. It is reasonable to believe that the energy-absorbing capability is saturated.

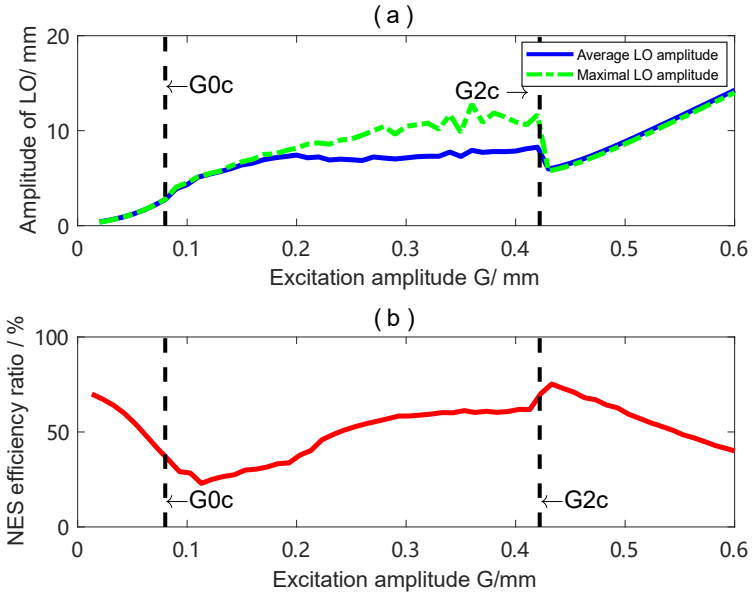

Figure 2.19: Response of bistable NES under the increasing excitation amplitudes, $\sigma = 0$ (a) the maximal amplitude and average amplitude of LO for different excitation G (b) energy dissipation ratio of bistable NES. G_0c is the excitation threshold for chaos occurrence, G_2c is the excitation threshold for SMR disappear.

For a given excitation amplitude G, it can be considered an upper threshold of excitation $G_2c = G$ to achieve maximum efficiency. Then, the optimal expression K_m

is determined by solving the first equation of Eq. (2.46):

$$\begin{aligned}K_m = \frac{2}{81}\,(&\varepsilon^2\,(-144\delta\lambda_1^2\lambda_2^4 + 72\delta^2\lambda_1^2\lambda_2^2 - 36\delta^3\lambda_1\lambda_2\\ &-72\delta\lambda_1^2\lambda_2^2 - 324\delta\lambda_1\lambda_2^3) + 108\delta^2\lambda_1\lambda_2 - 108\delta\lambda_1\lambda_2\\ &-24\delta^3\lambda_1^2\lambda_2^2 + 48\mu\delta\lambda_1^2 + 108\mu\lambda_1\lambda_2^3 - 12\mu\delta^4\lambda_1^2\\ &-36\mu\lambda_1\lambda_2 + 48\mu\delta^3\lambda_1^2 - 24\mu\lambda_1^2\lambda_2^2 - 72\mu\delta^2\lambda_1^2\\ &-8\delta^5\lambda_1^2 + 40\delta^4\lambda_1^2 + 144\lambda_1^2\lambda_2^4 - 80\delta^3\lambda_1^2\\ &+80\delta^2\lambda_1^2 + 24\lambda_1^2\lambda_2^2 + 324\lambda_1\lambda_2^3 - 40\delta\lambda_1^2 - 162\delta\lambda_2^2\\ &+36\lambda_1\lambda_2 + 8\lambda_1^2 + 36\mu\lambda_1^2\lambda_2^4 + 162\lambda_2^2 - 12\mu\lambda_1^2 + 81\mu\lambda_2^2\\ &+4\mu^3\lambda_1^2 - 24\mu\delta^2\lambda_1^2\lambda_2^2 + 48\mu\delta\lambda_1^2\lambda_2^2 - 36\mu\delta^2\lambda_1\lambda_2\\ &+72\mu\delta\lambda_1\lambda_2 + 4\mu^3\delta^2\lambda_1^2 - 8\mu^3\delta\lambda_1^2)^2\,/\,(G^2\,(\delta^2 + \delta\mu\\ &+3\lambda_2^2 - 2\delta - \mu + 1))\end{aligned} \tag{2.47}$$

where $\mu^2 = \delta^2 - 3\lambda_2^2 - 2\delta + 1$

In order to compare the numerical optimal design with the analytical prediction (2.47) under the given fixed excitation, various cubic nonlinearity parameters K are fully tested, and the results are presented in Fig. 2.20. The thick red line is the projection of minimal LO amplitude in the $K - G$ plane. The thick blue line is the analytical prediction of K. The Fig. 2.20 illustrates an evident tendance that smaller cubic nonlinearity parameter K can bear larger excitation better. Without introducing the coefficient of correction, ξ, the analytical prediction can still describe the optimal $K - G$ curve with sufficient accuracy.

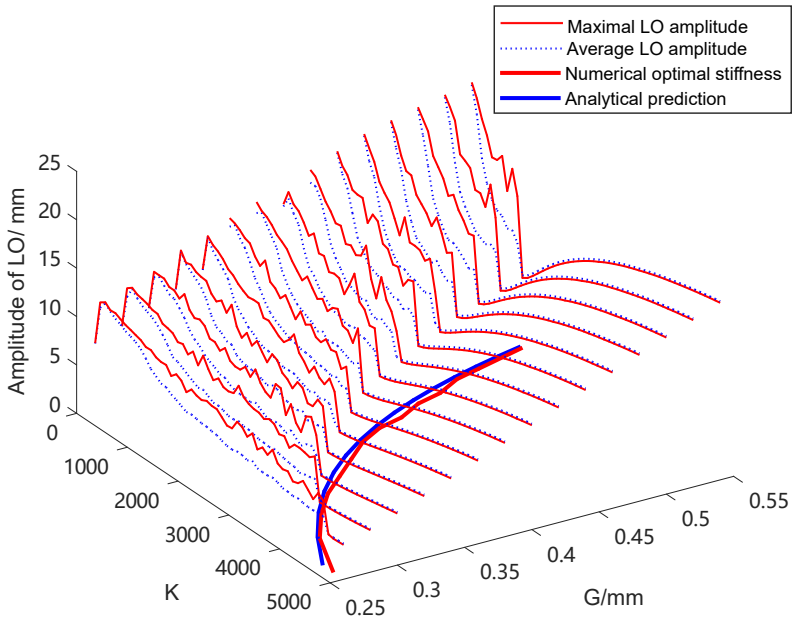

Figure 2.20: Distribution of the optimal design of K of bistable NES with the variation of harmonic excitation amplitudes G under the damping condition $\lambda_1 = 1.67$, $\lambda_2 = 0.167$ and fixed δ = -0.44.

As with the efficiency analysis in the cubic case, the optimal point occurs in the stable response phase, where the SMR vanishes. The limit efficiency of the optimal point can be obtained from Eq. (2.32), where the expressions of $Z_{1,2}$ and $Z_{2,2}$ are replaced by Eq. (2.43). The following expression is the estimation of maximum efficiency for bistable NES.

$$r_{bis-NES} = \frac{9\lambda_2}{2\lambda_1\mu(\delta - 1 + \mu) + 12\lambda_1\lambda_2^2 + 9\lambda_2} \tag{2.48}$$

where $\mu^2 = \delta^2 - 3\lambda_2^2 - 2\delta + 1$.

Eq. (2.48) becomes the same as Eq. (2.33), if $\delta = 0$. Unlike Eq. (2.33), the efficiency of bistable NES involves the negative stiffness. Without introduction of correction coefficient ξ, the real arrival point is already close to the folded point $Z_{2,2}$, which leads to enough accurate estimation of the maximal efficiency. For example, the predicted value of maximum efficiency is 78% in Fig. 2.19. The maximum efficiency value obtained by direct calculation is 75%. So Eq. (2.48) provides a simpler way to to estimate the maximum efficiency of bistable NES.

2.3.3 Robustness analysis of optimal design

In order to apply the optimal design in practice, it is essential to consider the effect of uncertainties of design parameters on the system response. This kind of uncertainties may come from the material properties and assembly errors of the system. The impact of these uncertainties on the performance of energy absorption, as well as on the reliability and robustness of the spring NES device are investigated [Braydi *et al.*, 2020]. Under transient vibrations, the bistable NES has better robustness compared to tuned TMD [Dekemele *et al.*, 2019].

The value of K is chosen from 1250 to 2750, and δ varies from -0.56 to -0.3. Let the target harmonic excitation be fixed at G = 0.4mm. According to the optimal cubic nonlinearity parameter K function Eq. (2.47), an optimal value is obtained (K = 2000, δ = -0.43), where the system has achieved the maximum efficiency of 75%. In the vicinity of the optimal design, an obvious dividing line is observed. The efficiency distribution shows a cut off on both sides of the separatrix (dashed line in Fig. 2.21).

For quantitative analysis of the stiffness uncertainties, the responses of two other parameters combinations on each side (case A: K = 1750, δ = -0.5 and case B: K = 2200, δ = -0.41) are also compared with the optimal design, which is presented in Fig. 2.21. In the left half part of the parameters plane, the designed system performs a SMR such as case A in Fig. 2.22. Although the LO has an unstable amplitude, it can be considered as efficient energy-absorbing, and the average efficiency can be 62%. In this region, the optimal design of the bistable NES shows strong robustness.

If the system parameters are located on the right side of the dividing line, the capacity to absorb energy is saturated, and the response turns to be a periodic oscillation. The stable LO amplitude is 5.9mm in case B and it is slightly larger than 5.4mm under optimal design in Fig. 2.22. In case B, the efficiency of NES is still considerably high. The system's efficiency is more sensitive to variation in K. So the contour map of the efficiency distribution shows a striped form on the right part. In this region, the system's periodic response always possesses a higher efficiency than that of SMR. Once the optimal design is fixed, the chosen K (of the real system) should be slightlys larger than the calculated value, in order to ensure a stable response. A descent of $|\delta|$ also helps stabilise the response and achieve high efficiency in the vicinity of the optimal design. Our optimal method allows to determine the minimal but optimal K required for certain excitations.

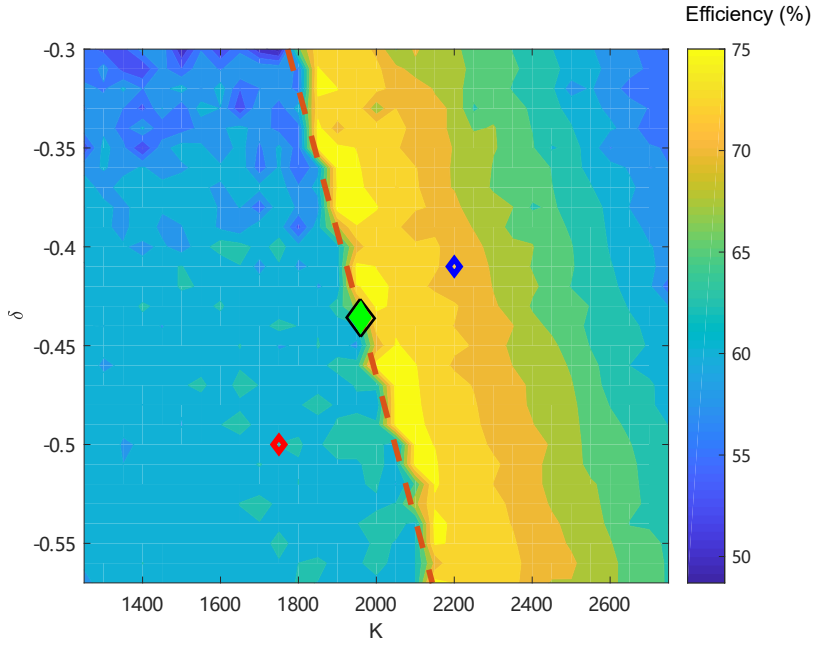

Figure 2.21: Influence of design paramters K - δ on efficiency for excitation G = 0.4mm, $\sigma = 0$. The green diamond corresponds to the optimal design with $K = 2000$, δ = -0.43. Case A (red diamond): $K = 1750$, δ = -0.5 and case B (blue diamond): $K = 2200$, δ = -0.41.

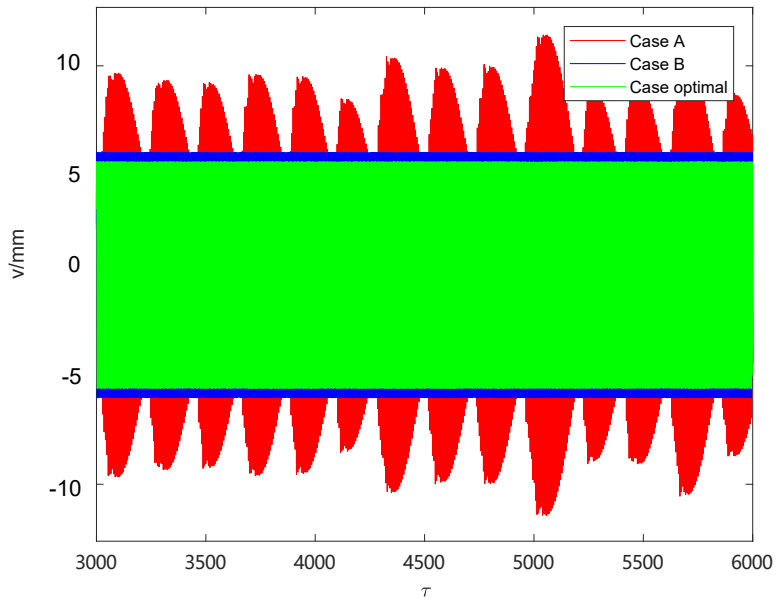

Figure 2.22: Time-displacement of optimal case (K = 1958, δ = -0.44), case A (K = 1750, δ = -0.5) and case B (K=2200, δ = -0.41) for excitation G = 0.4mm, $\sigma = 0$.

2.4 Experimental study of bistable NES

In subsection 2.2, a pure cubic nonlinearity mechanism is constructed and the optimal design of cubic NES for the target excitation is validated.

In the experiment of cubic NES, two axial compression conical springs and linear springs are constructed. It demonstrates that the two linear springs can also be pre-compressed to provide the extra negative stiffness to counterbalance linear stiffness and achieve bistable nonlinearity. The increasing pre-compression length of linear spring l_p leads the system to possess different values of k_3 and k_2. So the system can shift from the cubic NES to the bistable NES and adapt various amplitudes excitations in the optimal state.

In the perspective of the optimal excitation amplitude G_2c that can be absorbed, a high K value results in a lower G_2c and a low $|\delta|$ value shows the same effect of decreasing G_2c. However, increasing the pre-compression length leads to an increase in both K and $|\delta|$. In Fig. 2.23a, the thick blue curve indicates that a bistable NES with higher pre-compression length can achieve larger G_2c. It means the threshold excitation amplitude G_2c is mainly governed by the negative stiffness.

The dash lines in Fig. 2.23b clearly present that the NES can be tuned to absorb target excitation ranging from [0.26, 0.41]mm based on the environmental parameters of the experiment. The left red endpoint of this thick curve, where δ almost equals 0, represents a system possessing pure cubic nonlinearity. The points in the rest of the curve represent bistable NES designs with higher $|\delta|$ values in the more right side. In the contour plot of Fig. 2.23b, G_2c at the same height shows a near-vertical relationship with the δ axis, which indicates that G_2c is more sensitive to changes in negative stiffness. In other words, adjusting the negative stiffness can more obviously regulate larger target excitation G_2c.

When the l_p rises to 17.5mm, the cubic nonlinearity value becomes k_2 = 7.1e5 N/m^3 and the negative stiffness increases to k_3 = -159 N/m. The corresponding reduced parameters are K = 5.3e3 and δ = -1.2. The parameters of the system are the same with Tab.2.1. The experimental bistable nonlinearity is realized in Fig. 2.24. Two equilibrium positions are observed in ± 13mm. Globally, the experimental bistable nonlinearity is close to the analytical description.

In this condition, the numerical simulation indicates the system is designed for the target excitation G = 0.37mm as the red point of the bistable case in Fig. 2.23b. So two excitation cases (0.36mm and 0.40mm), which are selected on each side of 0.37mm, are examined. In a lower input energy case, the bistable NES still performs the SMR like the red curve in Fig. 2.25. In the higher excitation amplitude case 0.4mm, which is slightly larger than the target excitation, the system turns to be a stable response with minimal amplitude. In practice, it is possible to set the target excitation somewhat smaller than the actual required excitation to obtain a greater cubic nonlinearity parameter or less negative stiffness. Since the negative stiffness plays a significant role in the compression process, the required pre-compression length of the linear spring can be reduced slightly to regulate the requirements more precisely.

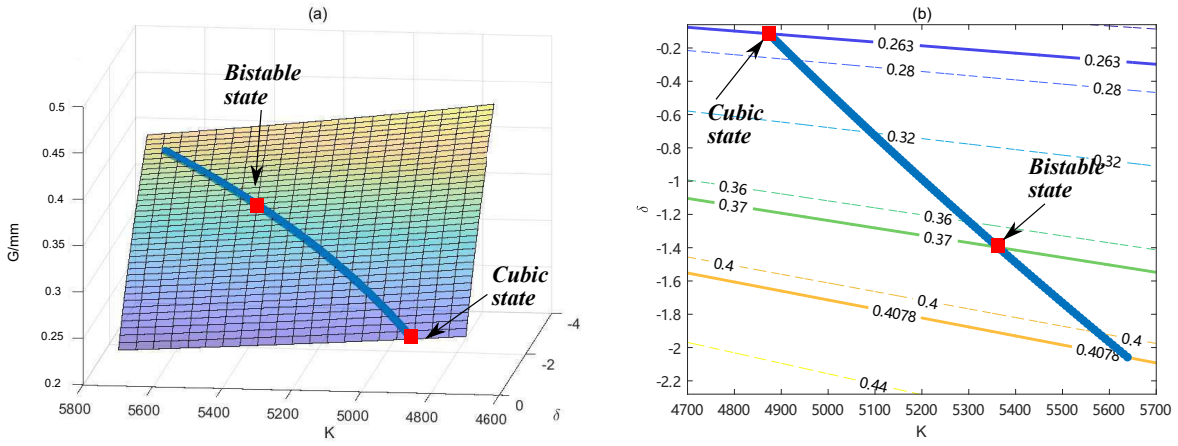

Figure 2.23: (a) Numerical optimal amplitude surface G_2c based on environmental parameters of the experiment in Tab. 2.2. Blue curve represents the G_2c, K and δ that the experimental mechanical NES system can achieve (b) optimization criteria curve. Solid green line represents the optimal δ-K combination set to absorb the target excitation G = 0.37mm with maximum efficiency. Blue curve represents the mechanical parameters that the spring NES system can achieve with various pre-compression lengths.

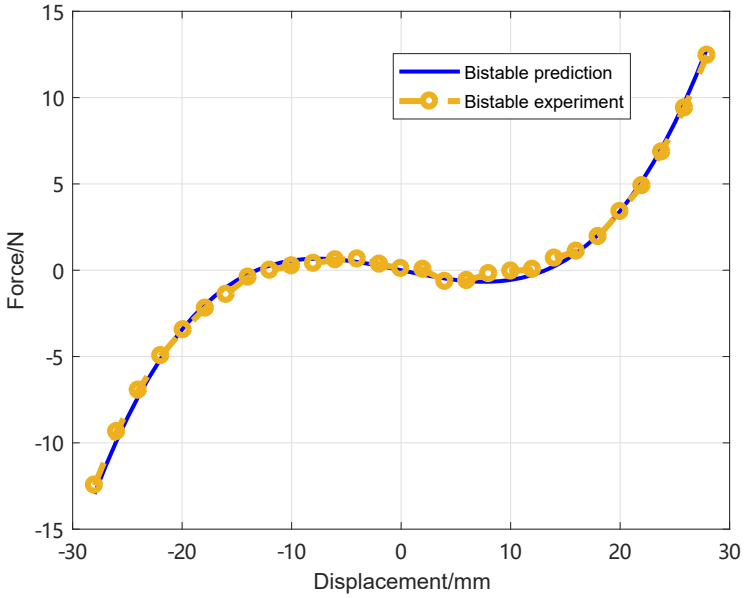

Figure 2.24: Experimental measurement of bistable force-displacement curve.

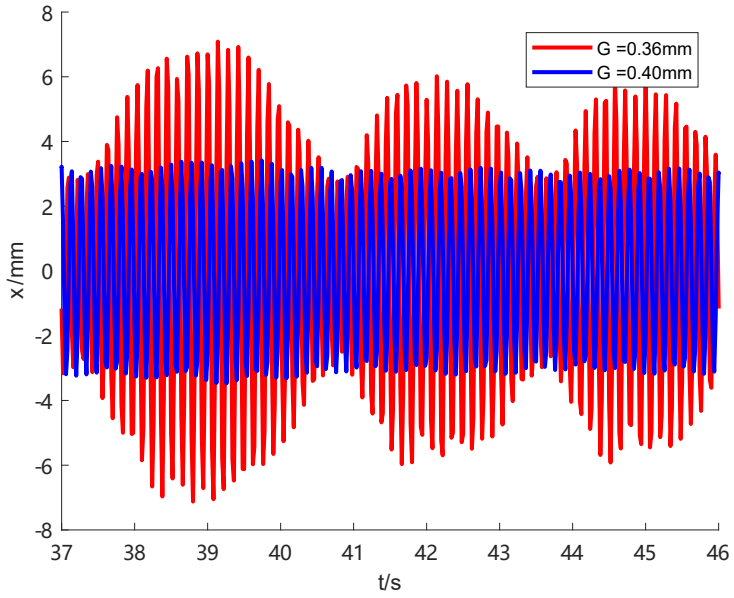

Figure 2.25: Experimental result of time displacement for optimal bistable NES design for target excitation G = 0.37mm. Blue curve is the response of LO under G = 0.40mm. Red curve is the response of LO under G = 0.36mm.

2.5 Conclusions

The current study investigates the fundamental influence of the design parameters on the maximum absorbing efficiency limit for the optimization of both cubic and bistable NES. Based on the response regimes, the optimal point is selected in the transition of SMR and stable response. The numerical method indicates the feasibility of the nonlinearity control strategy, and the experiment is realized to obtain the optimal design. Several main conclusions can be drawn:

1. The emergence of the maximum efficiency point is similar in the response regimes of both cubic and bistable NES. It appears during the transition from the SMR to the stable response. The expression of the maximum efficiency is found. The maximum efficiency level only depends on the damping parameters λ_1 and λ_2 in cubic case. The negative stiffness can improve the maximum efficiency level in a bistable NES.

2. The analytical relationship between the optimal cubic nonlinearity parameter value and a target excitation has been given and verified by simulation for both cubic and bistable NES. The error between the analytical optimal cubic nonlinearity parameter designs and the numerical results can be reduced by introducing a correction coefficient ξ in the cubic case. The bistable NES, meanwhile, does not require such processing. A proper damping combination is helpful to improve the maximal efficiency level that the system can achieve.

3. The performances of bistable NES cases, whose parameters are in the vicinity of optimal combination, are compared to verify their robustness. A slightly larger value of cubic nonlinearity parameter than the calculated value can help the system

achieve its target excitation for cubic and bistable NES designs. The experiment confirms that by adjusting the pre-compression length of linear spring, the force-displacement curve of four springs device can shift from the cubic NES into a bistable NES and absorb the various target excitations in the optimal state.

CHAPTER 3

Identification of chaos and qualitative analysis in bistable NES

Abstract

This chapter focuses on the development of an adapted complex variables method in the vicinity of equilibrium in bistable Nonlinear Energy Sink (NES). A simplified chaos trigger model is established to describe the distance between the stable phase cycle and the pseudo-separatrix. An analytical expression can predict the excitation threshold for chaos occurrence. The damping parameters boundary for chaos is identified by the Melnikov analysis. A qualitative analysis method based on the relative positions between the chaos trigger threshold line and the Slow Invariant Manifold (SIM) unstable region is proposed. This degeneration of the response regimes can be interpreted by the qualitative analysis method, which helps to classify the bistable NES. The experiment confirms the analytical result of intra-well oscillation in the frequency domain. The characteristic response regimes of weak, modest and strong bistable NES are identified by the experimental results.

Contents

3.1 Adapted complex variables method for intra-well oscillation

There are various dynamic behaviors of bistable NES. In a low energy case, subharmonic resonances and chaotic cross-well oscillations are excited. In a higher energy case, the fundamental 1:1 resonance mainly governs the dynamic behavior. If the bistable NES system is under harmonic excitation input, four typical response regimes at different energy levels appear in turn: (1) intra-well oscillation, (2) chaotic inter-well oscillation, (3) Strongly Modulated Response (SMR), (4) stable periodic response, as mentioned in the previous section.

Intra-well oscillation relates to a low energy motion that is restricted to one of the potential wells. It will become chaotic with increasing energy. An exact method to describe the intra-well oscillation is necessary to divide the regimes. There are currently two effective methods to identify potential chaos oscillation. First, the Lyapunov Exponent (LE) measures the degree of stochasticity of a trajectory by defining a relative distance in phase space between a given orbit and a test orbit beginning with a nearby initial condition. An LE approaching a positive value implies a chaotic orbit [Romeo *et al.*, 2015a]. However, the LEs are difficult to calculate analytically. The numerical calculation is also restricted by an infinitesimal initial distance and an infinite time horizon. So a practical Wolf's algorithm is applied [Romeo *et al.*, 2015a ; Dekemele *et al.*, 2019]. The Melnikov method is another of the few analytical ways to obtain an approximate criterion for chaos. According to the Melnikov theory, the chaos and transverse interaction over the separatrix in the phase plane occur simultaneously. The threshold values of damping and other control parameters for the occurrence of homoclinic bifurcation are presented [Al-Shudeifat *et al.*, 2013 ; Farshidianfar et Saghafi, 2014a]. Both ways can hardly predict the harmonic excitation amplitude threshold for the occurrence of chaos.

A definition of the amplitude of the NES is necessary to predict the threshold of harmonic excitation amplitude for chaotic motion. The traditional treatment of w defines it as the relative distance between Linear Oscillator (LO) and NES. However, the negative stiffness generates one equilibrium on either side of the origin of the coordinates. The small oscillation around equilibrium will be described as a large amplitude. The phase trajectory at a low energy level will not fit alongside a classic SIM structure. It also generates a massive error in the analytical calculation of NES amplitude. So it is necessary to consider the position of equilibrium and define the distance between the NES and the equilibrium point as a relative displacement.

The target bistable system is illustrated in Fig. 2.14. After the substitution of variables, a dimensionless form of equation is extracted as Eq. (2.39). The system is investigated in the vicinity of 1:1 resonance where LO and NES oscillate at the identical frequency Ω. Two adapted complex variables describing the neighbourhood of positive stable equilibrium point $x_0 = \sqrt{-\delta/K}$ are given by

$$\begin{aligned} \phi_1(\tau)e^{i\Omega\tau} &= \frac{d}{d\tau}v(\tau) + i\Omega(v(\tau) + \epsilon x_0) \\ \phi_2(\tau)e^{i\Omega\tau} &= \frac{d}{d\tau}w(\tau) + i\Omega(w(\tau) - x_0) \end{aligned} \tag{3.1}$$

with $i = \sqrt{-1}$ the imaginary unit. A minus sign should be added to before x_0 in Eq. (3.1) in order to study the local dynamics near the negative stable equilibrium $-x_0$. For

the sake of symmetry, only intra-well oscillation on the positive side falls within the scope of our present considerations. Unlike the definitions of ϕ_1 and ϕ_2 in the previous section, the amplitude with respect to the stable equilibrium point on one side ($w = x_0$) is described here instead of the amplitude with respect to the unstable equilibrium point ($w = 0$). In a low energy intra-well oscillation case, the NES vibrates symmetrically near the positive equilibrium as a center. However, the numerical simulation confirms that the LO amplitude is also slightly asymmetrical. The center of LO oscillation approximately locates at $-\epsilon x_0$. The initial adapted complex variables assumption fits well the simulation result.

Introducing Eq. (3.1) into Eq. (2.39), and keeping only terms containing $e^{i\Omega\tau}$ yields the following slow modulated system:

$$\begin{aligned}
&\dot{\phi}_1 + \frac{i\Omega}{2}\phi_1 + \frac{\epsilon\lambda_1(\phi_1+\epsilon\phi_2)}{2(1+\epsilon)} - \frac{i(\phi_1+\epsilon\phi_2)}{2\Omega(1+\epsilon)} - \frac{\epsilon F}{2} = 0 \\
&\dot{\phi}_2 + \frac{i\Omega}{2}\phi_2 + \frac{\epsilon\lambda_1(\phi_1+\epsilon\phi_2)}{2(1+\epsilon)} - \frac{i(\phi_1+\varepsilon\phi_2)}{2\Omega(1+\epsilon)} + \frac{\lambda_2(1+\epsilon)\phi_2}{2} - \frac{3iK(1+\epsilon)\phi_2^2\overline{\phi}_2}{8\Omega^3} \\
&-\frac{\epsilon F}{2} - \frac{i\phi_2\delta(1+\epsilon)}{2\Omega} - \frac{3iK(1+\epsilon)\phi_2{x_0}^2}{2\Omega} = 0
\end{aligned} \tag{3.2}$$

The stable response of intra-well oscillation corresponds to the fixed point of Eq. (3.2) when the derivative equals zero, it gives:

$$\dot{\phi}_1 = \dot{\phi}_2 = 0 \Rightarrow \phi_1(\tau) = \phi_{10}, \phi_2(\tau) = \phi_{20} \tag{3.3}$$

After the substitution of above variables into Eq. (3.2), the analytical amplitude of the system can be expressed in a more convenient form. Coefficients β_i (i = 1..3) are not given here due to their lengths.

$$\begin{aligned}
\phi_{10} &= \frac{\dfrac{i\epsilon\phi_{20}}{\Omega(1+\varepsilon)} - \dfrac{\varepsilon^2\lambda_1\phi_{20}}{1+\varepsilon} + \varepsilon F + i\varepsilon^2\lambda_1 F\Omega}{i\Omega + \dfrac{\varepsilon\lambda_1}{1+\varepsilon} - \dfrac{i}{\Omega(1+\varepsilon)}} \\
&\beta_3 Z_{20}^3 + \beta_2 Z_{20}^2 + \beta_1 Z_{20} + \beta_0 F^2 = 0, \quad Z_{20} = |\phi_{20}|^2
\end{aligned} \tag{3.4}$$

The small detuning parameter σ is applied to measure how near the excitation frequency is to the natural frequency of LO. It gives $\Omega = 1+\epsilon\sigma$. The stability of intra-well oscillation is studied by introducing a small perturbation ρ_j and its complex conjugate $\overline{\rho_j}, j = 1, 2$ into the fixed point equation Eq. (3.2).

$$\phi_1 = \phi_{10} + \rho_1, \quad \phi_2 = \phi_{20} + \rho_2, \overline{\phi_1} = \overline{\phi_{10}} + \overline{\rho_1}, \overline{\phi_2} = \overline{\phi_{20}} + \overline{\rho_2} \tag{3.5}$$

Extracting the perturbation terms gives the characteristic matrix.

$$\begin{bmatrix} \dot{\rho}_1 \\ \dot{\rho}_2 \\ \dot{\overline{\rho}}_1 \\ \dot{\overline{\rho}}_2 \end{bmatrix} = \begin{bmatrix} M_{11} & \epsilon M_{21} & 0 & 0 \\ M_{21} & M_{22} & 0 & M_{24} \\ 0 & 0 & \overline{M}_{11} & \epsilon\overline{M}_{21} \\ 0 & \overline{M}_{24} & \overline{M}_{21} & \overline{M}_{22} \end{bmatrix} \begin{bmatrix} \rho_1 \\ \rho_2 \\ \overline{\rho}_1 \\ \overline{\rho}_2 \end{bmatrix} \tag{3.6}$$

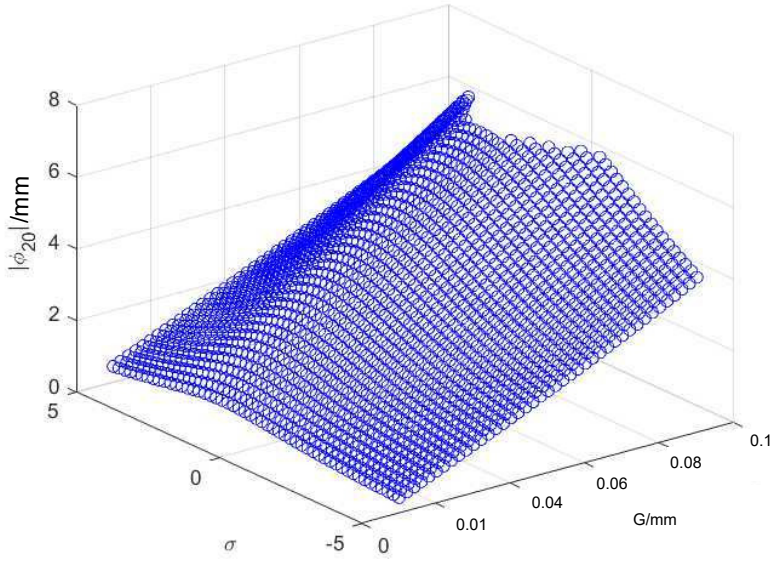

Figure 3.1: NES amplitude of intra-well oscillation in the frequency domain with system parameters: $\epsilon = 0.01$, $\lambda_1 = 1.67$, $\lambda_2 = 0.167$, K = 1742, δ = -0.44. Blue points indicate that the solutions of intra-well oscillation are all stable.

where

$$\begin{cases} M_{11} = -\dfrac{i(1+\epsilon)}{2} - \dfrac{\epsilon\lambda_1}{2(1+\epsilon)} + \dfrac{i}{2(1+\epsilon)(1+\epsilon\sigma)} \\ M_{21} = -\dfrac{\epsilon\lambda_1}{2(1+\epsilon)} + \dfrac{i}{2(1+\epsilon)(1+\epsilon\sigma)} \\ M_{22} = \dfrac{3i(1+\epsilon)K\phi_{20}\bar{\phi}_{20}}{2(1+\epsilon)(1+\epsilon\sigma)} - \dfrac{\lambda_2(1+\epsilon)}{2} + \dfrac{i\epsilon}{2(1+\epsilon)(1+\epsilon\sigma)} \\ -\dfrac{i(1+\epsilon\sigma)}{2} - \dfrac{\epsilon^2\lambda_1}{2(1+\epsilon)} + \dfrac{i(1+\epsilon)(3Kx_0^2+\delta)}{2(1+\epsilon\sigma)} \\ M_{24} = \dfrac{3i(1+\epsilon)K\phi_{20}^2}{8(1+\epsilon\sigma)^3} \end{cases} \tag{3.7}$$

The existence of a root of the characteristic equation with a positive real part implies the instability of periodic intra-well oscillation, and vice versa. The stability of intra-well oscillation around equilibrium is deduced and presented in Fig. 3.1 in the frequency domain. All blue points mean that all the real roots of matrix (3.6) are located in the left-half complex plane. The motion within the well is naturally stable in our case. $|\phi_{20}|$ is lower than the chaos threshold. It ensures that the local dynamics is restricted to within the well. If the value of $|\phi_{20}|$ exceeds the chaos threshold, it is beyond the scope of our present section, and results in truncation in the vicinity of the natural frequency in Fig. 3.1.

3.1.1 Asymptotic analysis of local SIM

Since the intra-well vibration is away from the unbalance point $w = 0$. So the conventional SIM is not applicable in this low energy state. The local SIM structure is reconstructed

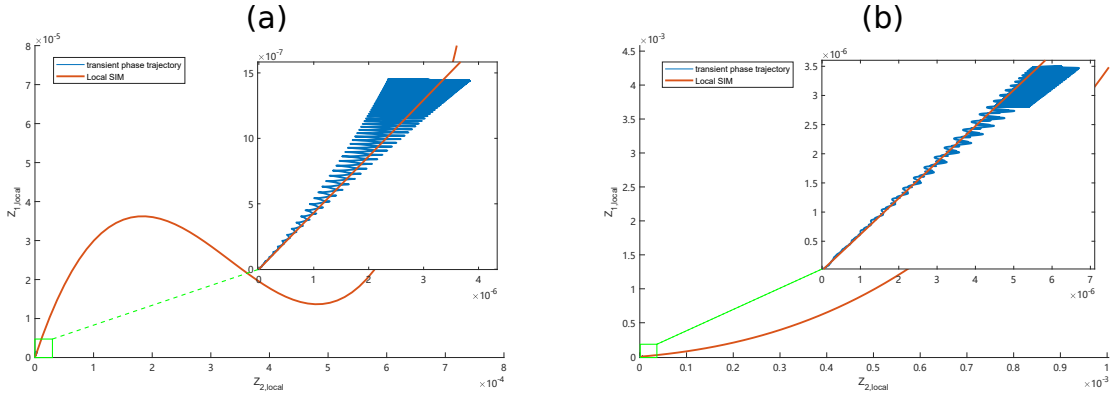

Figure 3.2: Local SIM and local phase trajectory for (a) k_3 = -20 N/m (δ = -0.174), (b) k_3 = -100N/m (δ = -0.871). Zoomed insert represents the detailed phase trajectory of intra-well oscillation defined by Eq. (3.1) in the green frame

by the adapted complex variables method.

The dynamic behavior is considered to involve motion on various times scales. By substituting Eq. (2.9) into Eq. (3.2), the terms involving the same power of ϵ^0, are selected:

$$\begin{aligned} &\frac{\partial}{\partial \tau_0}\phi_1 = 0, \\ &\frac{\partial}{\partial \tau_0}\phi_2 + \frac{1}{2}\lambda_2\phi_2 + \frac{1}{2}i(\phi_2 - \phi_1) - \frac{1}{2}i\delta\phi_2 - \frac{3}{2}iK\phi_2{x_0}^2 - \frac{3}{8}iK\overline{\phi}_2\phi_2^2 = 0 \end{aligned} \tag{3.8}$$

The first equation in Eq. (3.8) indicates that the modulation of ϕ_1 is independent of τ_0. Fixed point $\Phi = \lim_{\tau_0 \to \infty} \phi_2$ obeys the algebraic equation:

$$\frac{1}{2}\lambda_2\Phi + \frac{1}{2}i(\Phi - \phi_1) - \frac{1}{2}i\delta\Phi - \frac{3}{2}iK\Phi{x_0}^2 - \frac{3}{8}iK\overline{\Phi}\Phi^2 = 0 \tag{3.9}$$

Taking $\phi_1(\tau_1) = N_1 e^{i\delta_1}$ and $\Phi(\tau_1) = N_2 e^{i\delta_2}$ and then solving the above equation gives:

$$\begin{aligned} &Z_1 = \left(\lambda_2^2 + (\delta - 1)\left(\delta - 1 + 6Kx_0^2 + \frac{3}{2}KZ_2\right) + 9K^2\left(x_0^2 + \frac{Z_2}{4}\right)^2\right)Z_2 \\ &Z_1 = N_1^2, Z_2 = N_2^2 \end{aligned} \tag{3.10}$$

An illustration of the modified local SIM is given in Fig. 3.2 under the different negative stiffnesses where $\epsilon = 0.01, \lambda_1 = 1.67, \lambda_2 = 0.167, K = 1742$.

In a cases of small negative stiffness, the modified SIM possesses a characteristic similar to the classic cubic SIM curve, which has two singularity points like Fig. 3.2a. Although most part of the SIM curve is beyond the scope of this application, the zoomed insert part in the vicinity of point (0,0) shows that the phase trajectory rises along with the SIM. In a more significant negative stiffness case, in Fig. 3.2b, the modified local SIM becomes a monotonically increasing curve. The phase trajectory of the zoomed insert part still oscillates around the SIM, which shows that it is correct for low energy input case.

Unlike the traditional description method, where the phase trajectory has fully separated itself from the SIM in low energy case, the modified SIM describes intra-well motion more accurately. This modified local SIM structure is developed based on the adapted complex variables method and its application scope is restricted to an intra-well oscillation. So,

the modified SIM is termed as a local SIM that describes its dynamic behaviors with sufficient accuracy only in a low energy input case. A more significant energy input will result in its failure.

In order to distinguish two different SIM structures, the SIM structure (Eq. (3.10)) obtained by the method of adapted complex variables is called local SIM. the SIM structure (Eq. (3.19)) obtained by the classical Manivitch variables is called global SIM. The former describes the intra-well oscillation at low energy states with more accuracy. The latter describes SMR and stable periodic motion at high energy states more accurately

3.1.2 Performance verification

The validity of the adapted complex method can be verified by comparing it with numerical simulations. The difference between amplitudes of w and v calculated by Eq. (3.4), which is indicated by the red line with red dots at both ends above or below the surface, and direct numerical calculation (surface) is presented in Fig. 3.3 for the various negative stiffness cases (k_3 = -20N/m and k_3 = -100N/m) with system parameters: ϵ = 0.01, λ_1 = 1.67, λ_2 = 0.167, K = 1742. These parameters were kept constant in the following numerical simulation.

The adapted method generates errors mainly in the vicinity of $\sigma = 0$ in Fig. 3.3. What can be observed is the growth of accuracy away from natural frequency. The amplitude of w and v steady rises with the augment of excitation amplitude G, resulting in NES oscillating in a more significant span and even finally exceeding the potential well. This kind of error can be understood by the dissatisfying of the initial low energy assumption.

In a weak negative stiffness case, the analytical NES amplitude is always more significant than the numerical result as in Fig. 3.3a. The LO amplitude shows a good fit result compared with direct numerical simulation in Fig. 3.3b.

In a more intense $|\delta|$ case, the adapted complex variables method generates smaller NES amplitudes in Fig. 3.3c, where the red lines with red dots are still below the amplitude surface. As for the accuracy of LO amplitudes calculation, Fig. 3.3d shows the larger analytical results in the vicinity of $\sigma = 0$. The absolute maximum errors of NES amplitude calculations are 1.2% and 2.5% in low and high $|\delta|$ cases, respectively, which are acceptable for our future study.

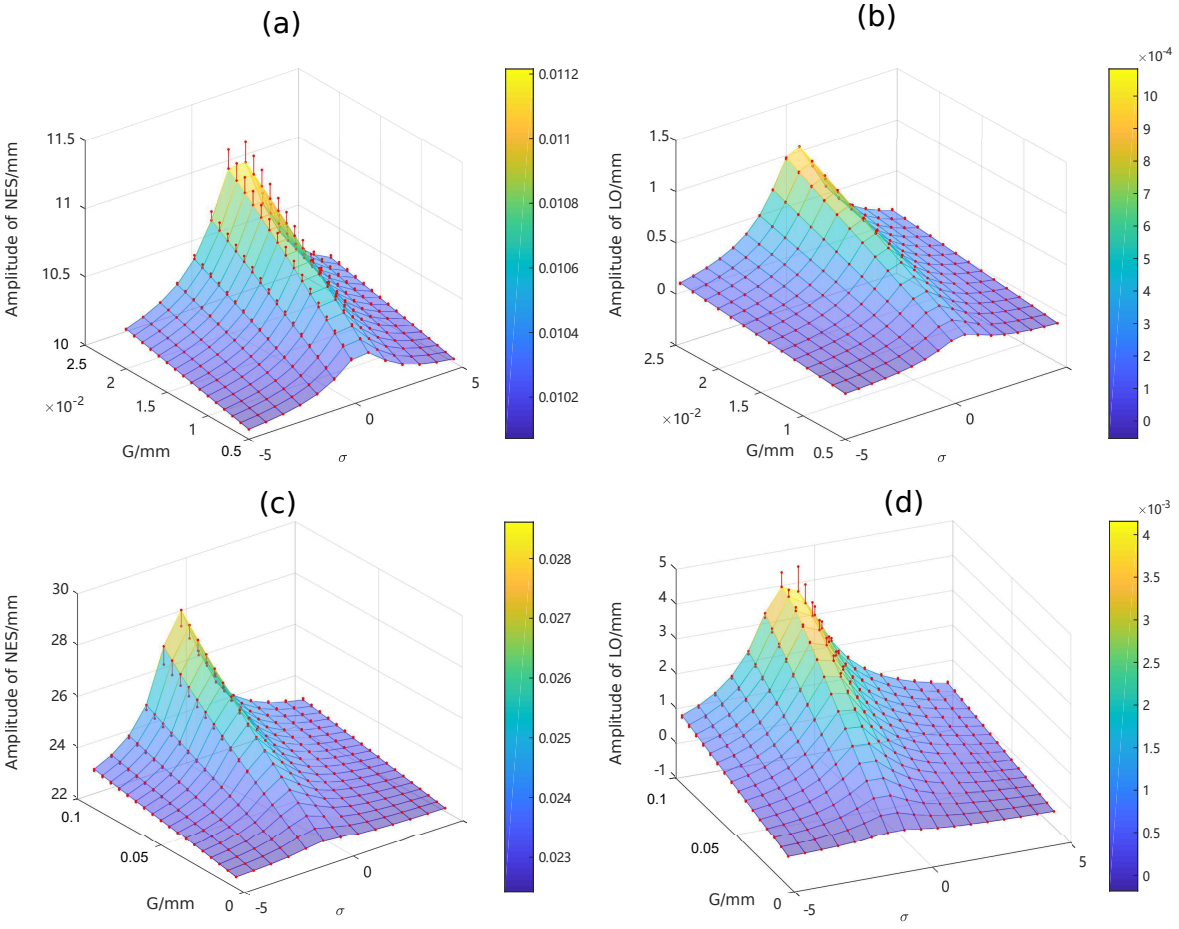

Figure 3.3: Comparison of numerical calculation and analytical result of LO and NES amplitudes. (a), (b) are the amplitudes of NES and LO in a weak negative stiffness case, k_3 = -20N/m (δ = -0.174). (c), (d) are the amplitudes of NES and LO in a strong negative stiffness case, k_3 = -100N/m (δ = -0.871). The surface is the direct numerical result from the ODE45 function in Matlab. Red lines with red dots at both ends represent the difference between the analytical and numerical results

3.2 Analytical prediction of chaotic motion

3.2.1 Simplified model for chaos occurrence

Chaos always occurs in the transition from intra-well oscillation to inter-well oscillation. The Melnikov method is one of the few effective methods for finding the necessary condition for homoclinic bifurcation and predicting chaotic motion. According to [Vakakis *et al.*, 2008 ; Qiu *et al.*, 2018a], the unperturbed homoclinic orbit of bistable NES that connects the saddle points is shown as the red curves in Fig. 3.4. Its expression is given by:

$$\begin{aligned} q_+^0(\tau) &= (R \cdot sech(S\tau), -RS \cdot sech(S\tau)\tanh(S\tau)) \\ q_-^0(\tau) &= -q_+^0(\tau) \end{aligned} \tag{3.11}$$

where $R = \sqrt{-\delta/K}$, $S = \sqrt{-\delta}$. This orbit is also termed as pseudo-separatrix.

The NES oscillates around the attractor (equilibrium) with a small amplitude, and the circle can describe its corresponding stable phase trajectory with sufficient accuracy in the low energy input condition. The phase trajectory expands in a circle with the its center at the attractor point $(x_0, 0)$. Its intersection with the pseudo-separatrix can be considered as a symbol of the occurrence of chaos. The different values of δ result in the deformation of geometric shapes of pseudo-separatrix, so the trigger conditions are different as shown in Fig. 3.4. The critical δ value divides the trigger conditions into two types: (1) with the contact point located on the pseudo-separatrix or (2) with the contact point located on the extreme right of the pseudo-separatrix.

During the transition from intra-well oscillation to chaotic inter-well oscillation, the phase trajectory will cross the pseudo-separatrix. The trigger condition can be determined by calculating the minimum distance between the point on the pseudo-separatrix and the attractor. The minimal distance D is the minimum radius required for a circle in contact with the pseudo-separatrix, which leads to the critical condition of triggering chaos. The D value, as a function of w, can be defined from Eq. (3.12):

$$D^2 = \left(w - \frac{1}{2}R\sqrt{2}\right)^2 + \frac{S^2w^2\left(R^2 - w^2\right)}{R^2} \tag{3.12}$$

The local minimum distance, which exists only in the following three positions within the interval $[0, R]$, are obtained by taking the derivative of w in the above equation and setting this derivative to zero.

$$w_{1,2,3} = \frac{\left(-\frac{1}{4}\sqrt{2}S + \frac{1}{4}\sqrt{2S^2+8}\right)R}{S}, \frac{R}{\sqrt{2}}, R \tag{3.13}$$

If the negative stiffness $|\delta|$ exceeds the critical value $(2-\sqrt{2})^2$, (critical negative stiffness k_3 = -39.4 N/m in our case), the minimum distance is always equal to $(1-\sqrt{2}/2)R$, which means that the point on the pseudo-separatrix that is closest to the attractor point is always located at the extreme right point, as case (b) in Fig. 3.4 shows.

In a case of relatively greater negative stiffness, it is reasonable to consider the distance between the extreme right point and the attractor as the critical amplitude. If the final stable NES amplitude $|\phi_{20}|$ exceeds the critical amplitude $|\phi_{20c}| = (1-\sqrt{2}/2)R$, chaotic

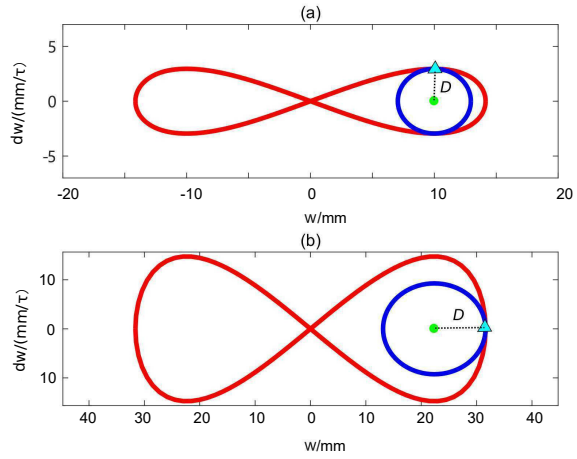

Figure 3.4: Different trigger conditions in (a) small negative stiffness value (k_3 = -20N/m, $\delta = -0.174$), (b) large negative stiffness value (k_3 = -100N/m, $\delta = -0.871$). The red line is the pseudo-separatrix, the blue line is the ideal phase trajectory, the green dot is the attractor center $(x_0, 0)$, and the triangle is the contact point. The radius D gives the critical NES amplitude for chaos occurrence.

behavior appears. And the amplitudes threshold of NES for chaos occurrence, $Z_a = |\phi_{20c}|^2$ can be expressed in Eq. (3.14).

$$Z_a = \begin{cases} (1 - \dfrac{\sqrt{2}}{2})^2 R^2 & |\delta| > (2 - \sqrt{2})^2 \\ \dfrac{R^2 S^2}{4} & |\delta| \leq (2 - \sqrt{2})^2 \end{cases} \tag{3.14}$$

3.2.2 Analytical chaos prediction

The assumption is that the intra-well oscillation expands in a circle and intersects the pseudo-separatrix at critical amplitudes $|\phi_{20c}|$ in various negative stiffness cases. If the system's amplitude increases monotonically before its phase trajectory crosses the pseudo separatrix, the trigger condition Eq. (3.14) can be substituted for the stable solution $Z_{20} = Z_a$ and $G_0 c = \epsilon \cdot F$ in the second equation of Eq. (3.4). So the analytical excitation for chaos occurrence is as follows:

$$G_0 c^2 = -\frac{\epsilon^2 Z_a \left(Z_a^2 \beta_3 + Z_a \beta_2 + \beta_1\right)}{\beta_0} \tag{3.15}$$

A more exact threshold value of excitation calculated by Eq. (3.15) can be compared with the numerical result. The numerical result is obtained through the calculation of the Lyapunov exponent. The exponent measures the average exponential growth or decay of an infinitesimal close state. The definition of Lyapunov exponent is given in Eq. (1.1). When it turns to be positive, there is a chaotic motion in the response. For a given ordinary differential equation fo bistable NES system, the calculation of Lyapunov exponent is numerically determined from Eq. (2.39) with the algorithm described in Wolf [Wolf *et al.*, 1985] with a Matlab implementation.

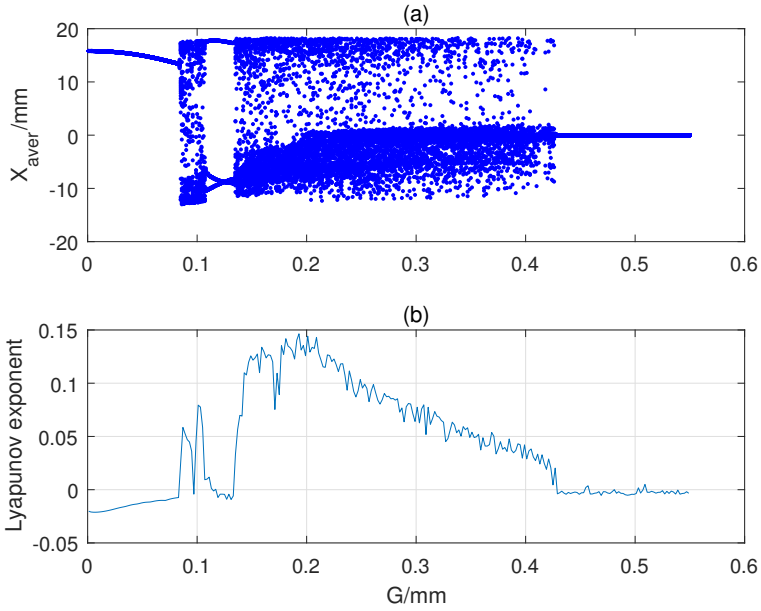

Figure 3.5: (a) Bifurcation of bistable NES (k_3 = -50, δ = -0.44) response under variety of excitation amplitude G, X_{aver} means the average distance of NES with respect to the w = 0 position (b) Lyapunov exponent calculation for variety of excitation amplitude G with condition: $\epsilon = 0.01$, $\lambda_1 = 1.67$, $\lambda_2 = 0.167$, K = 1742, $\sigma = 0$

Through the Fig. 3.5, before excitation amplitude increases to 0.085 mm, the system performs a stable intra-well oscillation, the Lyapunov exponent is negative. Once excitation exceeds the chaos threshold, the exponent turns out to be positive immediately. Even in the 1: 3 subharmonic stage, the Lyapunov exponent appears to be negative again in the range of [0.11mm, 0.14mm]. During the SMR stage (G = [0.2mm, 0.43mm]), chaos motion is mixed with 1:1 resonance, so the Lyapunov exponent is always positive with a decreasing tendency. When excitation exceeds the threshold, the response of the system re-turns to be a stable and optimal state. Lyapunov exponent becomes negative again. The Lyapunov method proves to be efficient enough to determine the chaos threshold. So the chaos threshold G_0c for k_3 = -50N/m is selected as 0.085 mm. So the numerical result of chaos threshold in the function of negative stiffness is marked in the red curve in Fig. 3.6.

The comparison between numerical predictions and analytical predictions reveals a gradual decline in excitation threshold for chaos occurrence as negative stiffness weakens in Fig. 3.6. The more intense negative stiffness results in a deeper well requiring more energy input to escape from it, which leads to a higher excitation threshold to trigger chaos.

The analytical prediction values are close to the numerical results for a large range of negative stiffness in Fig. 3.6. It proves that our analytical method is suitable and accurate enough. According to the performance verification section, the analytical NES amplitude is smaller than the numerical amplitude in the strong negative stiffness case. This implies that the analytical NES amplitude will give a more significant critical trigger excitation.

The accuracy of predictions is changed in strong negative stiffness. The simplified model is less accurate if the phase trajectory is far away from the attractor. At the

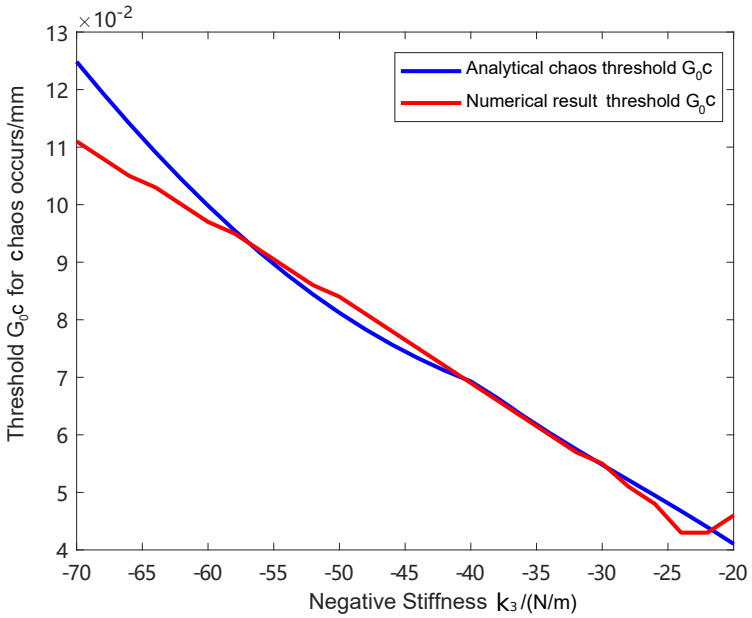

Figure 3.6: Comparison of analytical chaos predictions with numerical results under various negative stiffness designs, with condition: $\epsilon = 0.01$, $\lambda_1 = 1.67$, $\lambda_2 = 0.167$, K $= 1742$, $\sigma = 0$

moment when a trajectory passes the pseudo separatrix, it is always at some distance from the attractor. This distance rises as the value of $|\delta|$ increases.

From another point of view, the adapted complex variables method is based on the stable periodic solution triggering chaos. In a case of much higher negative stiffness, the instantaneous amplitude of the NES exceeds its final stable amplitude, which is inconsistent with the initial assumption that it is the final stable phase trajectory (final periodic solution), rather than the instantaneous amplitude, that triggers the pseudo-separatrix.

In addition, only one side attractor is under consideration. A greater negative stiffness makes the phase trajectory deviate from the ideal circle model. When the phase trajectory passes the mid point between the origin point and the attractor, the other side attractor in the negative side will increase NES amplitude. The asymmetry of amplitude with respect to the attractor renders the prediction results invalid. In the vicinity of the pseudo-separatrix, the intra-well and inter-well subharmonic oscillations are beyond the descriptive capabilities of the adapted complex variables method. The above potential interpretation explains the generation of error in the process of application of the adapted complex variables method in the prediction of chaos.

3.2.3 Damping parameter boundary for chaos

Chaos in bistable NES is a complex behavior. The Melnikov method is one of the few effective ways to analyze homoclinic bifurcation and detect the occurrence of chaos. It describes the distance between stable and unstable manifolds of the perturbed system and can estimate the occurrence of global bifurcation in the parameter space [Guckenheimer et Holmes, 2013]. The homoclinic bifurcation means the transverse insertion of stable and

unstable manifolds of a saddle fixed point. It is an obvious symbol of chaotic behaviors. This pseudo-separatrix distinguishes whether the phase diagram of the system is intra-well oscillation or inter-well oscillation. When the potential energy arrives to its local maximum (displacement equals to zero), the center of the phase trajectory shifts from a center fixed point to a saddle equilibrium, and chaos will occur. This transition is a result of the change of excitation or the inner system parameters. The homoclinic orbit breaks and may cross manifolds when the perturbed terms are considered. For simplicity, the Melnikov function can be expressed and the detailed calculation process can be found in [Qiu, 2018]:

$$M(\tau_0) = \sqrt{\frac{2}{K}}\frac{N_1\pi\Omega^3}{\epsilon}\sin(\Omega\tau_0+\phi)\,sech\left(\frac{\pi\Omega}{2\sqrt{-\delta}}\right)\pm\frac{4\delta\sqrt{-\delta}}{3K}\frac{\lambda_2}{\epsilon} \tag{3.16}$$

where, N_1 is stable LO amplitude ($\phi_1 = N_1 e^{i\delta_1}$). The condition for traversing the intersection of stable and unstable manifolds is satisfied when $M(\tau_0) = 0$.

$$\left|\sqrt{\frac{2}{K}}\frac{N_1\pi\Omega^3}{\epsilon}sech\left(\frac{\pi\Omega}{2\sqrt{-\delta}}\right)\right| > \left|\frac{4\delta\sqrt{-\delta}}{3K}\frac{\lambda_2}{\epsilon}\right| \tag{3.17}$$

$$\begin{aligned}\lambda_2(1) &< \frac{3\sqrt{2K}N_1\pi\Omega^3}{4\delta\sqrt{-\delta}}sech\left(\frac{\pi\Omega}{2\sqrt{-\delta}}\right)\\ \lambda_2(2) &> -\frac{3\sqrt{2K}N_1\pi\Omega^3}{4\delta\sqrt{-\delta}}sech\left(\frac{\pi\Omega}{2\sqrt{-\delta}}\right)\end{aligned} \tag{3.18}$$

In other words, with the above equation, the interval of damping parameter λ_2 required to avoid the occurrence of chaos at the critical amplitude N_1 can be determined. For a designed LO amplitude $N_1 = 3$mm, the threshold curves are shown in Fig. 3.7. The critical value of damping λ_2 equals to 0.266, where the critical excitation amplitude $G = 0.091$mm and the natural frequency $\omega_0 = 7.6$Hz. When the damping value crosses the threshold curves $\lambda_2(1)$ and $\lambda_2(2)$, the Melnikov function changes sign and chaos occurs. Two different damping cases are chosen to visualize the responses and verify the prediction of chaos occurring. Both cases are compared with critical curves in Fig. 3.8.

Case 2 corresponds to the point situated above the threshold value, and the black phase trajectory of w is located around one of the equilibrium points within the pseudo-separatrix in Fig. 3.8. In this stage, the excitation is considered as low energy. As the damping parameter decreases to the chaos region, as in case 1, the displacement of NES crosses the two equilibrium points. The phase trajectory escapes from one potential well to the other, and the chaotic behaviors are identified in Fig. 3.8.

By setting the different N_1 amplitude requirements, the boundary of chaos can vary. It is clear from the Fig. 3.9 that the region of chaotic behavior between the two surfaces becomes larger as N_1 increases. These conditions provide a domain in the parameter spaces, where the Melnikov function changes its sign and the possible chaotic behaviors happen. Meanwhile, the phase trajectory of NES will cross the pseudo-separatrix. According to the LO amplitude, the result can predict and distinguish the formation of chaos and can be used for the optimal design of bistable NES systems.

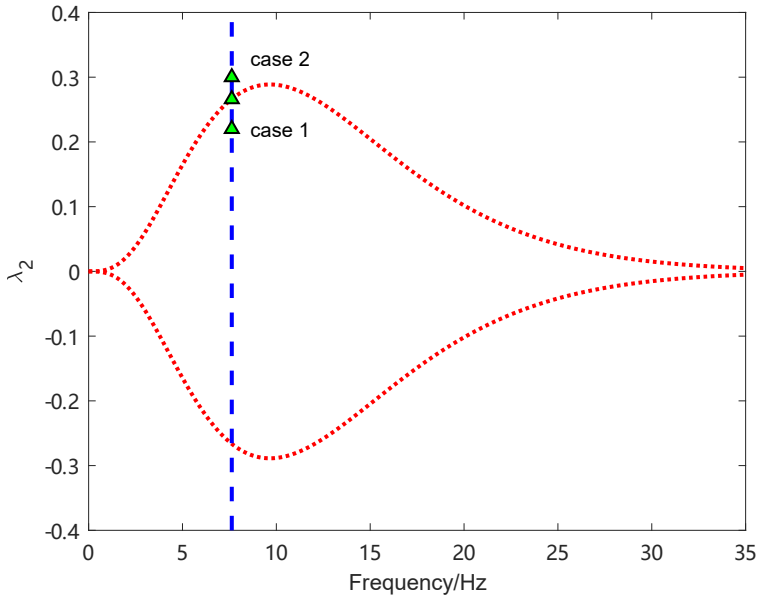

Figure 3.7: Chaos boundary for λ_2 with designed amplitude N_1 = 3mm (ϵ = 0.01,K = 1742, δ = -0.44). The blue dashed line is the natural frequency ω_0 = 7.6Hz of the linear oscillator

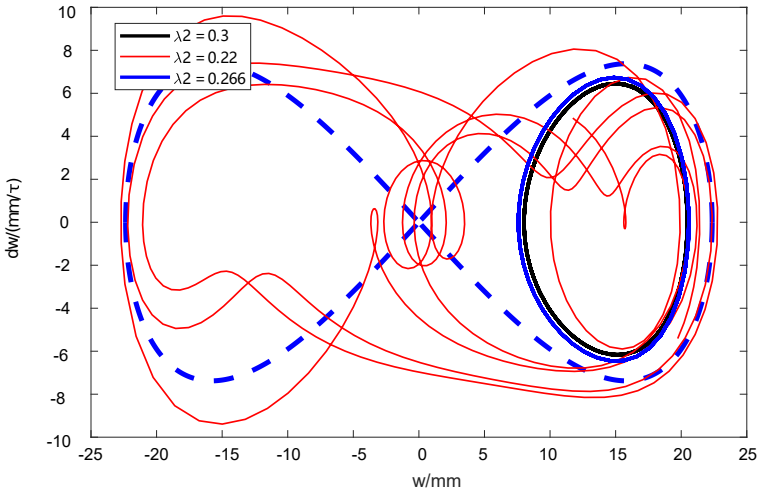

Figure 3.8: Phase trajectory for different damping parameters λ_2, black line: case 2, λ_2 = 0.3, intra-well oscillation; red line: case 1, λ_2 = 0.266, critical value for occurrence of chaos; blue line: λ_2 = 0.22, chaos inter-well oscillation

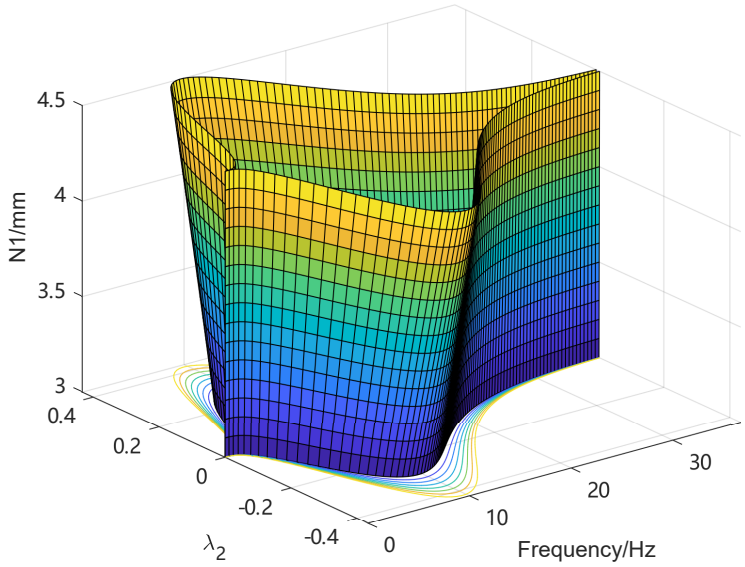

Figure 3.9: Chaos boundary for λ_2 with different designed amplitudes N_1 ($\epsilon = 0.01, K = 1742, \delta = -0.44$)

3.3 Classification and qualitative analysis of response regimes

The presentation of negative stiffness introduces chaotic motion essentially changing the response regimes. Two main characteristics are discussed below to interpret the response regimes in various negative stiffness cases.

First, the pseudo-separatrix governs the low energy behaviors and distinguishes them from chaotic motion. Low energy restricts the NES to oscillation around the attractor $(\sqrt{-\delta/K}, 0)$, and expands in one well with growing energy. If the amplitude of w exceeds the extreme right point $(\sqrt{-2\delta/K}, 0)$ of the separatrix, the inter-well chaotic motion pervades two wells and their vicinity.

Secondly, the classic global SIM branch can better describe the high energy behaviors of bistable NES. The phase trajectory oscillates around the right branch of the global SIM when the system shows SMR or stable periodic response. By applying the classic complex variables $\phi_1 e^{i\Omega\tau} = \dot{v} + i\Omega v, \quad \phi_2 e^{i\Omega\tau} = \dot{w} + i\Omega w$ into and a multiple scales method, the traditional global SIM can be extracted as in Eq. (3.19). Here the ϕ_1 and ϕ_2 represent the amplitude of LO and NES with respect to the original position $v = 0$ and $w = 0$, respectively.

$$\begin{aligned} &Z_1 = \lambda_2^2 Z_2 + (\delta - 1)^2 Z_2 + \frac{3K}{2}(\delta - 1) Z_2^2 + \frac{9K^2}{16} Z_2^3 \\ &Z_1 = N_1^2, \quad Z_2 = N_2^2 \end{aligned} \tag{3.19}$$

with singularity values $Z_{2,j}$:

$$Z_{2,j} = N_{2,j}^2 = \frac{4\left(2(1-\delta) \mp \sqrt{(1-\delta)^2 - 3\lambda_2^2}\right)}{9K}, j = 1, 2 \tag{3.20}$$

In the SIM plane, there are four characteristic lines worth to emphasize:

1. Line A

   This attractor line is located in ($Z_2 = -\delta/K$). The phrase trajectory starts from the attractor line A and oscillates around this axis in the intra-well oscillation stage.

2. Line B

   This chaos threshold line is located in ($Z_2 = -2\delta/K$). It is deduced from the width of the pseudo-separatrix. Once the phase trajectory crosses this line, there is a high possibility to activate chaos. In other words, chaos occurs when the NES amplitude exceeds $\sqrt{-2\delta/K}$ based on the previous simplified chaos trigger model.

3. Line C

   This singularity line C is located in ($Z_2 = Z_{2,1}$). It divides the classic global SIM structure into stable and unstable branches. In the cubic NES case, once the phase trajectory crosses this singularity line, a snap-through motion occurs. However, in an intensive negative stiffness case, this condition does not ensure the occurrence of the jumping phenomenon.

4. Line D

   This singularity line D is located in ($Z_2 = Z_{2,2}$). If the trajectory reaches line D, it jumps definitively to the right stable branch of the global SIM even in a bistable NES with a large $|\delta|$ value.

All the four characteristic lines are parallel to the axis Z_1. So the Z_1, Z_2 plane, is divided into two regions: (1) Chaotic region. It occupies range of $Z_2 = [0\ -2\delta/K]$. When the system performs the chaos, phase trajectory will occupy this range. (2) Unstable region. It occupies range of $Z_2 = [Z_{2,1}, Z_{2,2}]$. This region is associated with the jumping phenomenon of phase trajectory. It is a temporary region before the system reaches at its final state.

3.3.1 Weak bistable NES

For a better comprehension of the distribution of the regimes. Its efficiency ratio is defined as the same with Eq. (2.26)

Initially, a small value of negative stiffness k_3 = -20 N/m (δ = -0.17) is introduced in the following simulation. This bistable NES preserves some original features of the cubic NES. Fig. 3.10 shows that the whole excitation range has five distinct phases. For each phase, the typical behavior of the time domain and its phase trajectory are extracted in Fig. 3.11. The relative positions of four characteristic lines are demonstrated in Fig. 3.12.

When the NES maintains an intra-well oscillation, e.g. case 1 in Fig. 3.11c, this low energy level motion is trapped in one of the wells. Because the NES vibrates in the vicinity of equilibrium, the trajectory is quasi-asymmetric around attractor line A. The adapted complex variables method can describe its behaviors better by the local SIM according to the previous section.

In the second stage of Fig. 3.10, the chaos motion brings a higher efficiency compared to previous stage. And the maximal amplitude and avergae amplitude curves separate

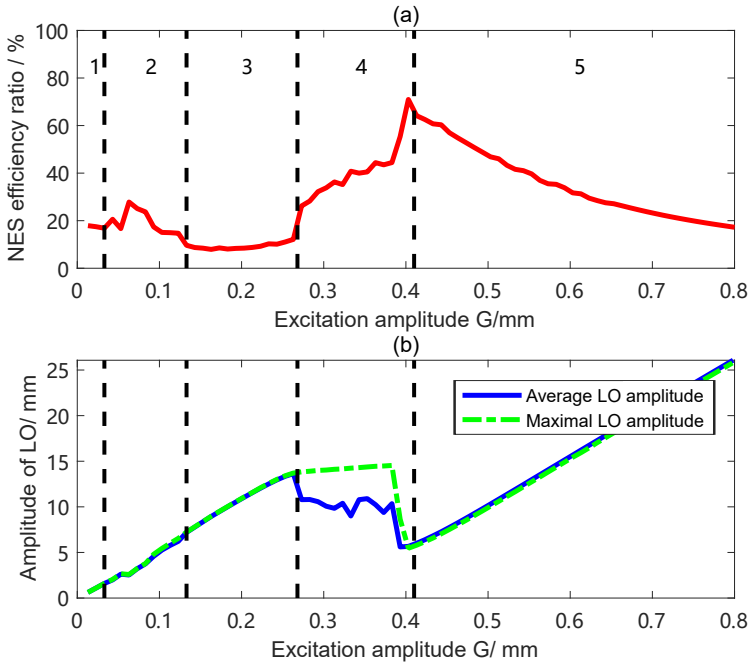

Figure 3.10: (a) Energy dissipation ratio of NES (b) maximal and average LO amplitude in weak bistable NES case with k_3 = -20 N/m (δ = -0.17). The blue line represents the average amplitude in a given time interval, the green dashed line is the maximal amplitude. The black dashed lines divide regimes into five stages.

slightly. Increasing energy input causes the NES amplitude to exceed line B and trigger chaotic motion. However, the small value of δ leads to a significant gap between the chaos threshold line B and singularity line D. The phase trajectory can neither activate SMR nor be attracted to the left global SIM branch, but can only expand and take a position near line B, as in case 2 in Fig. 3.11c.

In the third stage of Fig. 3.10, the LO amplitude increases linearly with increasing G and the corresponding efficiency maintains a low level, which implies that the TET is not activated. After the generation and transient expansion of chaos, the time domain displacement of w is symmetrical to the zero position. The phase trajectory is re-attracted to the left stable global SIM branch as in case 3 in Fig. 3.11c and rises along the left global SIM branch. This attraction motion that results from the phase trajectory increasing in the Z_1 direction affects the left stable global SIM branch more quickly than the expansion of the phase trajectory in Z_2 direction in the initial low energy input stage.

In the fourth stage of Fig. 3.10, a complete SMR emerges. TET is activated, so the NES efficiency arises higher. The separation of the maximal amplitude and average amplitude curves manifests an unstable amplitude motion: SMR. The phase trajectory of weak bistable NES moves along with the global SIM structure. However, once the phase trajectory re-enters the chaos region after the efficient energy dissipation, the motion is chaotic in case 4 of Fig. 3.11, which is different from the cubic NES case.

In the beginning of fifth stage in Fig. 3.10, the efficiency of NES arrives its maximum. The system achieves an optimal state, whcih is stable and periodic. The maximal efficiency of this weak bistable NES in the Fig. 3.10 is about 71%. Due to the large amplitude

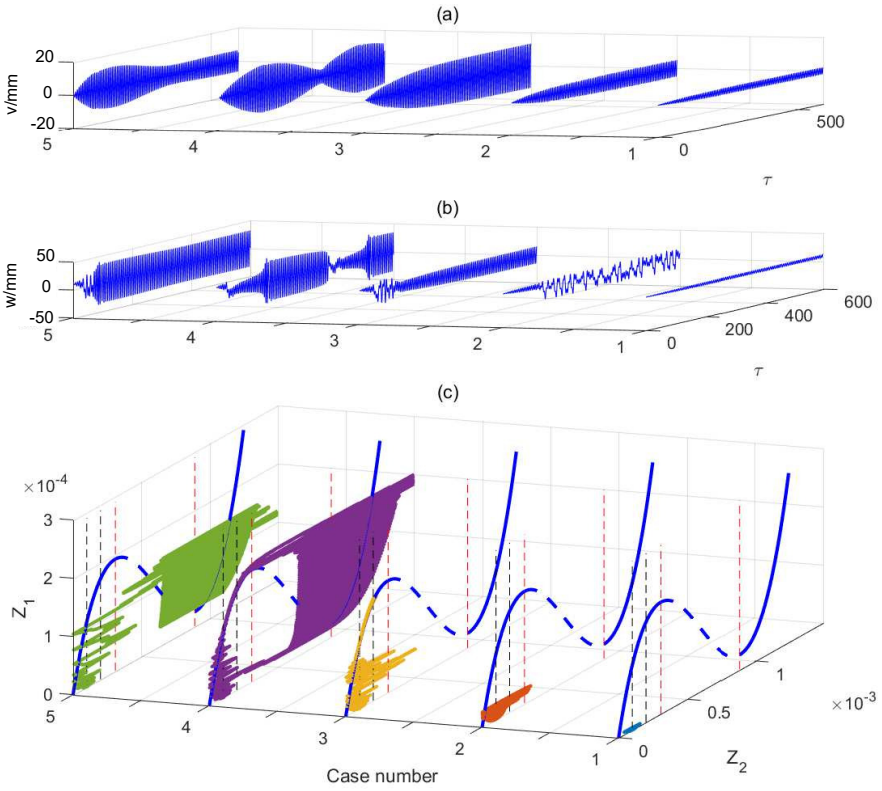

Figure 3.11: Response regimes in weak bistable NES with k_3 = -20 N/m (δ = -0.17) (a) v displacement (b) w displacement (c) phase trajectory of Z_2 and Z_1. The 5 typical responses are chosen at various excitations G = 0.04mm, 0.1mm, 0.25mm, 0.35mm, 0.42mm, with same initial condition ($w(0) = x_0, v(0) = \dot{v}(0) = \dot{w}(0) = 0$), $\sigma = 0$.

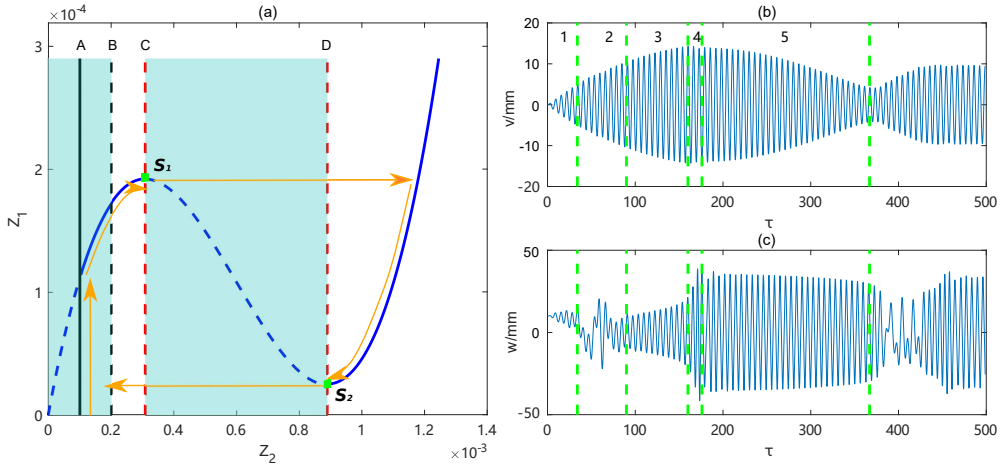

Figure 3.12: Characteristic global SIM of weak bistable NES and SMR in the time domain for exicitation G = 0.35mm, $\sigma = 0$. (a) The global SIM structure with unstable and chaos regions (shaded). Orange arrow line indicates various stages in one SMR cycle. S_1 and S_2 are the singularity points whose locations are defined as $(Z_{2,1}, Z_{1,1})$ and $(Z_{2,2}, Z_{1,2})$. (b) displacement of w, and (c) displacement of v with initial condition $(w(0) = x_0, v(0) = \dot{v}(0) = \dot{w}(0) = 0)$. The green lines divide the SMR into various stages corresponding the global SIM explanation by orange arrow line.

excitaion, the trajectory easily crosses the global SIM unstable region without rising along the left stable branch like case 5 of Fig. 3.11c. Chaos triggers the snap-through motion. The trajectory jumps directly to the right global SIM branch before it crosses the singularity point $S_1 : (Z_{2,1}, Z_{1,1})$. So the maximal LO amplitude at the jump moment is lower than that of the cubic SMR stage. This implies that the LO can be protected better if there is high energy input in a weak bistable NES case. Since the phase trajectory finally arrives at the right branch of the global SIM without jumping back, it indicates saturation of the capability of absorbing energy. The final position of the phase trajectory will be located in a higher position of the right global SIM branch with an excitation of increasing amplitude. The optimal point ideally occurs at the singularity point $S_2 : (Z_{2,2}, Z_{1,2})$ in the global SIM structure.

The negative stiffness can not only affect the stage of response regimes, but also influence the SMR behavior. The time domain of SMR, which is divided by green dashed lines in Fig. 3.12b shows five different parts of a complete SMR: (1) intra-well oscillation, (2) chaos expansion, (3) re-attraction to SIM, (4) jumping motion, (5) Targeted Energy Transfer (TET). Compared with the SMR in the pure cubic case, the SMR starts from the intra-well oscillation, so the orange arrow line represents a trajectory rising along line A in Fig. 3.12a. The initial motion is constrained in the well and increases until the trajectory is re-attracted to the left stable global SIM branch, on which the orange line converges. As the trajectory crosses the singularity line C, it jumps to the right stable branch of the SIM, and moves down to the other singularity point S_2. 1:1 resonance in this period produces an intense TET and leads to effective dissipation by the NES. Once the NES has dissipated most of the energy of the LO, the phase trajectory of the system jumps back to the chaotic region in the vicinity of attractor line A and waits for the charge of energy under harmonic excitation.

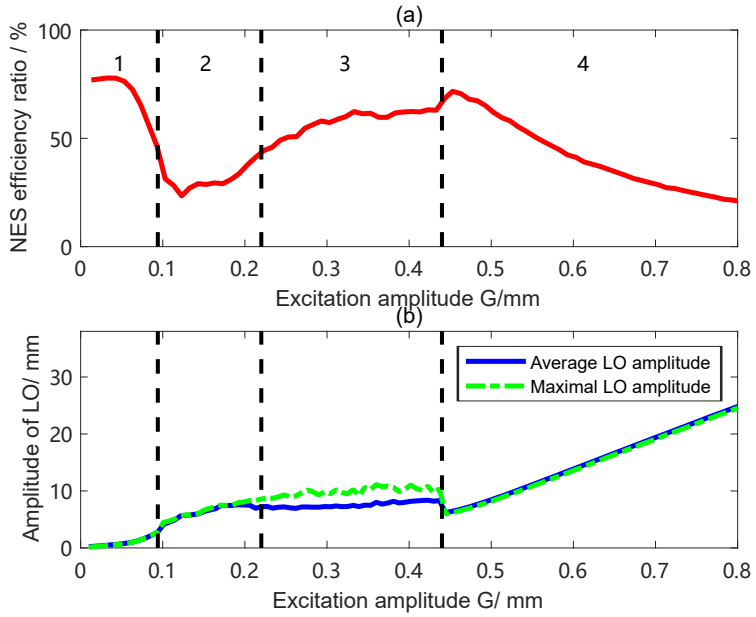

Figure 3.13: (a) Energy dissipation ratio of NES (b) maxiaml and average LO amplitude in modest bistable NES case with k_3 = -60N/m (δ = -0.52). The blue line represents the average amplitude in a given time interval, the green dashed line is the maximal amplitude. The black dashed lines divide regimes into four stages.

3.3.2 Modest bistable NES

The re-attraction to the global SIM mechanism in a weak bistable system becomes delicate when the $|\delta|$ parameter takes a larger value. The mechanism of this attraction back to the left global SIM branch is mainly due to the proximity of the chaos threshold line B to the left global SIM branch. The phase trajectory has a strong possibility of continuing to expand along with line A and being attracted by the left global SIM branch, rather than crossing the unstable region and triggering SMR.

If the negative stiffness is intense enough, the chaos trigger line B will be located in the global SIM unstable region. Therefore, the critical condition for the disappearance of re-attraction can be determined as the overlap of line B and line C. The condition is expressed as follows:

$$\begin{aligned} Z_{2,1} &= \frac{4(2(1-\delta) - \sqrt{(1-\delta)^2 - 3\lambda_2^2})}{9K} = \frac{-2\delta}{K} \\ \delta_{wm} &= -\frac{8}{7} + \frac{2}{7}\sqrt{-7\lambda_2^2 + 9} \end{aligned} \tag{3.21}$$

The damping of the NES system determines the critical value of negative stiffness. If the negative critical value exceeds the critical value -0.295 (when λ_2= 0.167), the re-attraction to the left global SIM branch mechanism is hardly observable. To better prove this point, the efficiency distribution for a larger negative stiffness case is presented in Fig. 3.13 with larger negative stiffness case k_3 = -60N/m (δ = -0.52). The efficiency distribution can be divided into 4 stages in Fig. 3.13 and its characteristic behaviors under inputs of increasing amplitude excitation are presented in Fig. 3.14.

In the first stage of intra-well oscillation, the NES possesses a high absorbing efficiency.

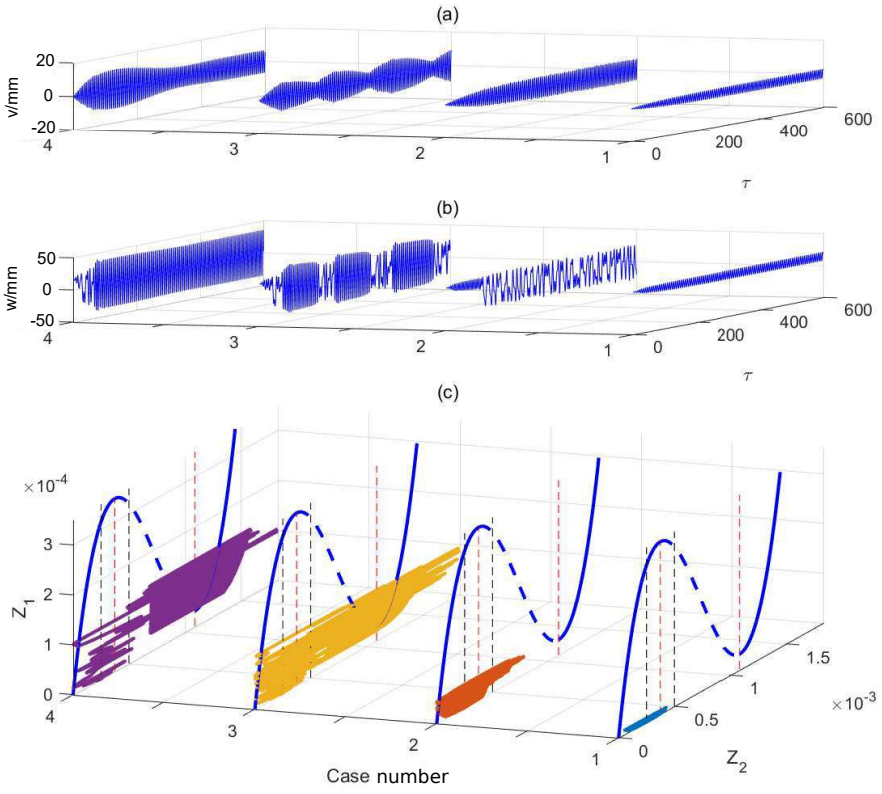

Figure 3.14: Response regimes in modest bistable NES with k_3 = -60N/m (δ = -0.52) (a) v displacement (b) w displacement (c) phase trajectory of Z_2 and Z_1. The 4 typical responses are chosen at various excitations G = 0.08mm, 0.15mm, 0.34mm, 0.45mm, with same initial condition ($w(0) = x_0, v(0) = \dot{v}(0) = \dot{w}(0) = 0$), $\sigma = 0$.

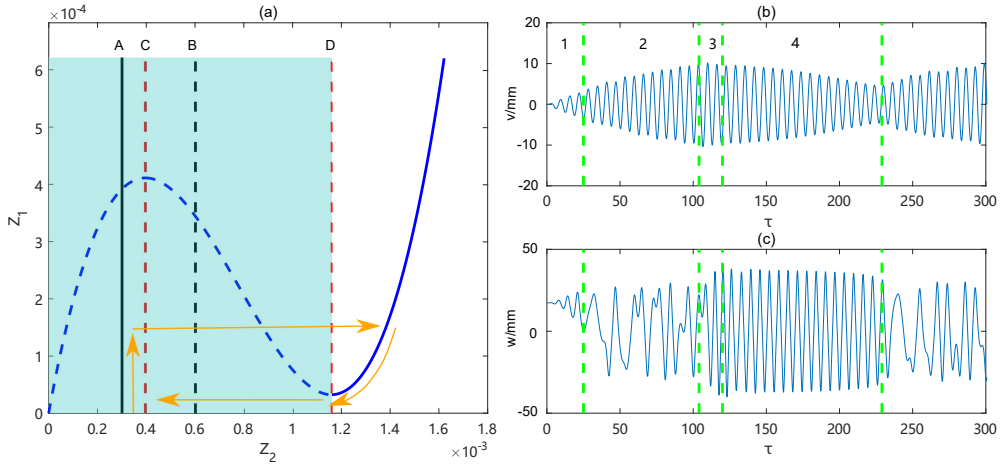

Figure 3.15: Characteristic modest bistable global SIM and SMR in the time domain for excitation G = 0.34 mm, $\sigma = 0$. (a) The global SIM structure with the unstable and chaos regions (shaded). The orange arrow line indicates various stages in one SMR cycle. (b) displacement of w, (c) displacement of v, with initial condition $(w(0) = x_0, v(0) = \dot{v}(0) = \dot{w}(0) = 0)$. The green lines divide the SMR into various stages corresponding to the global SIM explanation by the orange arrow line.

However, as the excitation amplitude increases, its high efficiency is lost and declines drastically.

In the second stage in Fig. 3.13, chaos emerges. When $|\delta|$ increases, the span and depth of potential well become larger, so a larger amplitude excitation is necessary to trigger the chaotic motion. The critical value is G = 0.09mm, while the chaos threshold excitation is G = 0.03mm in a weak bistable case. This threshold value divides the efficiency distribution figure into the chaotic and intra-well region in Fig. 3.13, A coexistence of subharmonic oscillations and chaotic motions can be realised in this stage.

In the third stage, SMR occurs in Fig. 3.13. A greater value of negative stiffness leads to the fact that the chaos trigger line B is located in the global SIM unstable region and is close to the singularity line D in Fig. 3.15a,. It can be deduced that SMR is more early to produce in modest bistable case. As already observed in Fig. 3.13b, the SMR region starts at G = 0.22mm, which is lower than the SMR trigger excitation G = 0.26mm in weak bistable NES.

In the fourth stage, the NES system possesses a stable regime again in Fig. 3.13. The optimal point is generated in this stage. The absorption efficiency of the NES system decreases with increasing external excitation. The maximal efficiency of this modest bistable NES in the Fig. 3.13 is about 72.5%.

The influence of the more significant value of $|\delta|$ in the global SIM and SMR in the time domain is illustrated in Fig. 3.15a. The chaotic region will even overlap the global SIM unstable region partially or entirely if the negative stiffness is increasing. The size of the overlapping parts of the two areas determines the division of the response regimes.

Only four stages have been retained in Fig. 3.15b, 3.15c: (1) intra-well oscillation, (2) chaos expansion, (3) jumping motion, (4) TET. For an SMR cycle of the modest bistable case, the re-attraction to the global SIM part has been completely compressed and replaced by the chaos expansion.

Because the extreme right point in phase trajectory of case 2 is close to singularity line D in Fig. 3.14c, the SMR is trigged by crossing chaotic region and unstable global SIM region in Z_1, Z_2 plane instead of reaching at the singularity point $S_1 : (Z_{2,1}, Z_{1,1})$ and then jumping. It means that the system does not require fully charging the energy to activate SMR. A lower trigger excitation amplitude results in a lower initial Z_1 amplitude, from which the trajectory moves down along the right stable global SIM branch. This shorter path helps NES dissipate energy around the optimal point within a shorter time and higher efficiency. As the case 3 in Fig. 3.14c, the system performs 3 SMR cycles within 600 τ. However, the weak bistable case performs only one complete SMR during the same time. Chaos provides a much faster way to charge and trigger SMR and accelerate every SMR circle. More SMRs in a fixed time interval are observed in Fig. 3.14c. That is why the SMR stage in the modest bistable NES has higher efficiency than that of weak bistable NES. A more efficient way to dissipate energy is generated.

3.3.3 Strong bistable NES

The chaos threshold line B will approach the SMR boundary line D more closely for higher negative stiffness. The critical condition is defined as singularity line C is overlap with attractor line A to ensure the close distance between line B and D in global SIM structure.

$$\begin{aligned} Z_{2,1} &= \frac{4}{9}\frac{2-2\delta-\sqrt{(1-\delta)^2-3\lambda_2^2}}{K} = -\frac{\delta}{K} \\ \delta_{ms} &= -\frac{8}{5}-\frac{4}{5}\sqrt{5\lambda_2^2+9} \end{aligned} \tag{3.22}$$

In the condition of $\lambda_2 = 0.167$, the critical δ value that classifies the modest NES and strong NES is -0.82.

A larger negative stiffness case with $k_3 = 150$ N/m (δ = -1.3) is selected in the strong bistable NES simulation. The expansion of the chaos regime will disappear in effeciency distribution Fig. 3.16. The trajectory will cross the singularity line D and directly start to jump and perform an SMR. Case 2 in Fig. 3.17 shows that the snap-through phenomenon occurs at the instant when phase trajectory crosses the chaos region, if the distance between lines B and D is small enough in Fig. 3.18a. The energy dissipation ratio can be classified into 3 stages: (1) intra-well oscillation, (2) SMR, (3) stable stage.

In the first intra-well stage, the NES system possesses a low efficiency. It implies that the negative stiffness must be tuned to a modest bistable configuration in order to maintain high efficiency even at low energy input. Too large or too small a negative stiffness will lead to a decrease in efficiency. The energy is mainly localized in the LO, the amplitude of which mainly increases linearly in Fig. 3.16b.

In the second SMR stage, the maximal amplitude and average amplitude curves separate drastically in a large distance. Meanwhile, in the modest NES case, both curves separate gradually. It implies that chaos motion is not involved in the SMR stage of strong bistable NES case. It makes the SMR stage of strong bistable NES performs similar to an SMR stage of cubic NES, where the chaos can be hardly observed. Compared with the SMR stage in weak bistable NES case, the duration of energy pumping in Fig. 3.17b is longer and it has a less absorbing cycle within the same time interval.

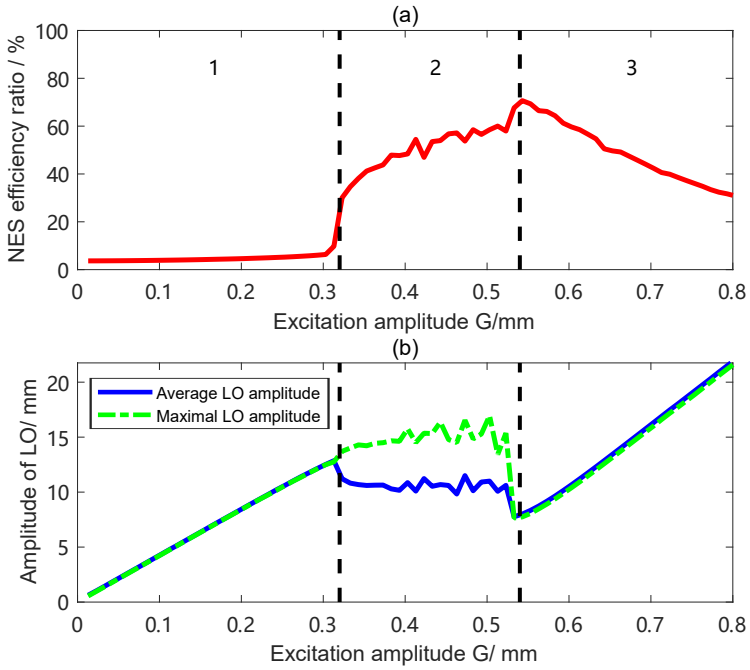

Figure 3.16: (a) Energy dissipation ratio of NES (b) maximal and average LO amplitude in strong bistable NES case. The blue line represents the average amplitude in a given time interval, the green dashed line is the maximal amplitude. The black dashed lines divide regimes into three stages.

In the third stable periodic response stage, the large negative stiffness value increases the excitation amplitude threshold for SMR disappearance, about G = 0.54mm. Meanwhile, the excitation amplitude thresholds for SMR disappearance are G = 0.44mm and G =0.4mm in the modest and weak bistable NES design, respectively. A high $|\delta|$ value can help the system to achieve an optimal state in a higher energy input case. The attractor line A restricts the motion inside of potential well before it jumps out. The maximal efficiency of this strong bistable NES in the Fig. 3.16 is about 70.5%.

In the strong bistable NES case, the increasing $|\delta|$ results in a simpler form of SMR. The motion of SMR is either in a potential well or in the right stable global SIM branch. The chaotic motion becomes weak and transient. Only 3 parts: (1) intra-well oscillation, (2) snap-through, and (3) TET are classified as in Fig. 3.18b, 3.18c. In the second SMR stage, once the phase trajectory crosses the chaos trigger line B, the right stable branch of the global SIM attracts the phase trajectory.

3.3.4 Abnormal bistable NES

If the negative stiffness is extremely large, another critical condition can be achieved, where the chaos threshold line B coincides with the singularity line D, and the following equation can be derived:

$$\begin{aligned} Z_{2,2} &= \frac{4}{9}\frac{2-2\delta+\sqrt{(1-\delta)^2-3\lambda_2^2}}{K} = -\frac{2\delta}{K} \\ \delta_{sa} &= -\frac{8}{7}-\frac{2}{7}\sqrt{-7\lambda_2^2+9} \end{aligned} \tag{3.23}$$

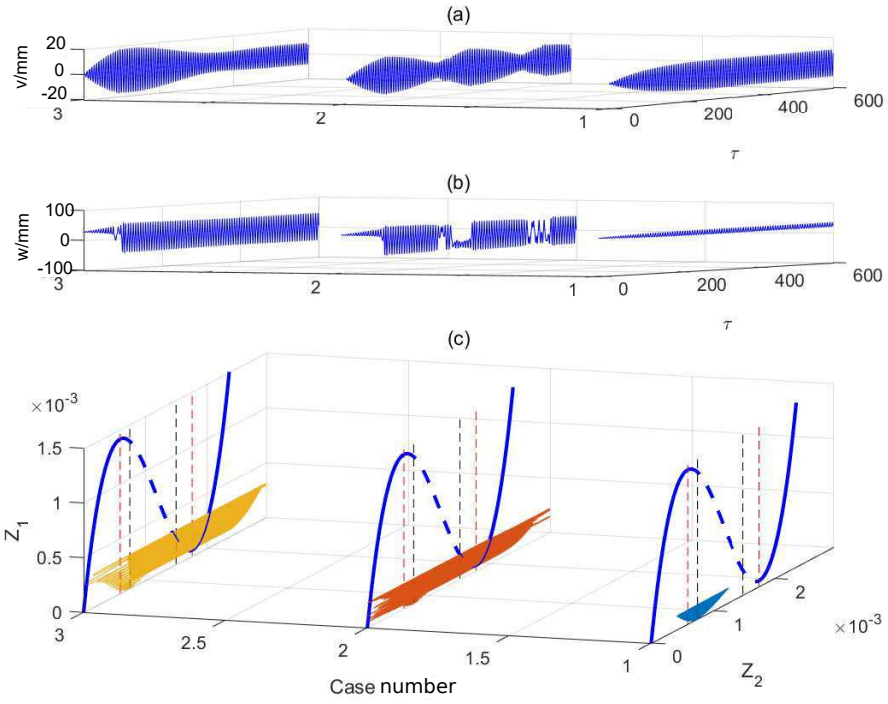

Figure 3.17: Response regimes in strong bistable NES with k_3 = -150 N/m (δ = -1.3) (a) v displacement (b) w displacement (c) phase trajectory of Z_2 and Z_1. The 3 typical responses are chosen at various excitations G = 0.25mm, 0.45mm, 0.55mm, with same initial condition ($w(0) = x_0, v(0) = \dot{v}(0) = \dot{w}(0) = 0$), $\sigma = 0$

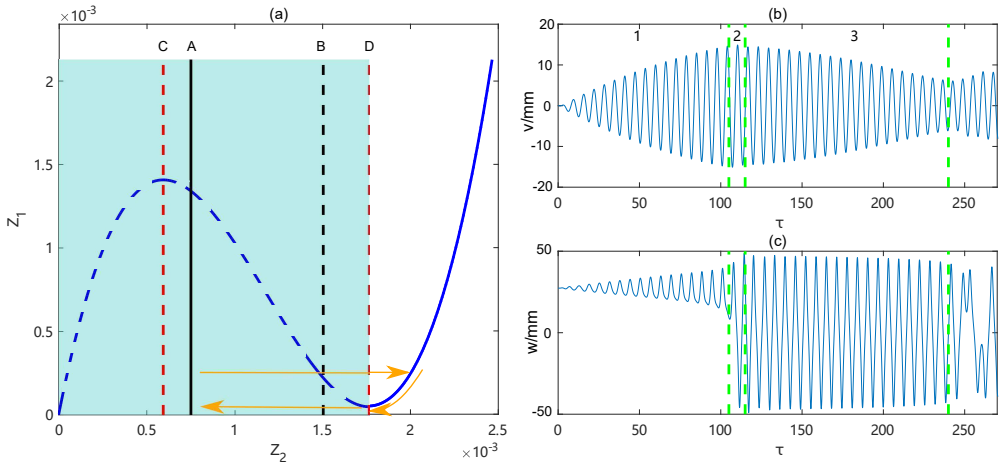

Figure 3.18: Characteristic strong bistable global SIM and SMR in the time domain for excitation G = 0.45mm, $\sigma = 0$. (a) The global SIM structure with the unstable and chaos region (shaded). The orange arrow line indicates various stages in one SMR cycle. (b) displacement of w, (c) displacement of v, with initial condition ($w(0) = x_0, v(0) = \dot{v}(0) = \dot{w}(0) = 0$). The green lines divide the SMR into various stages corresponding to the global SIM explanation indicated by the orange arrow line

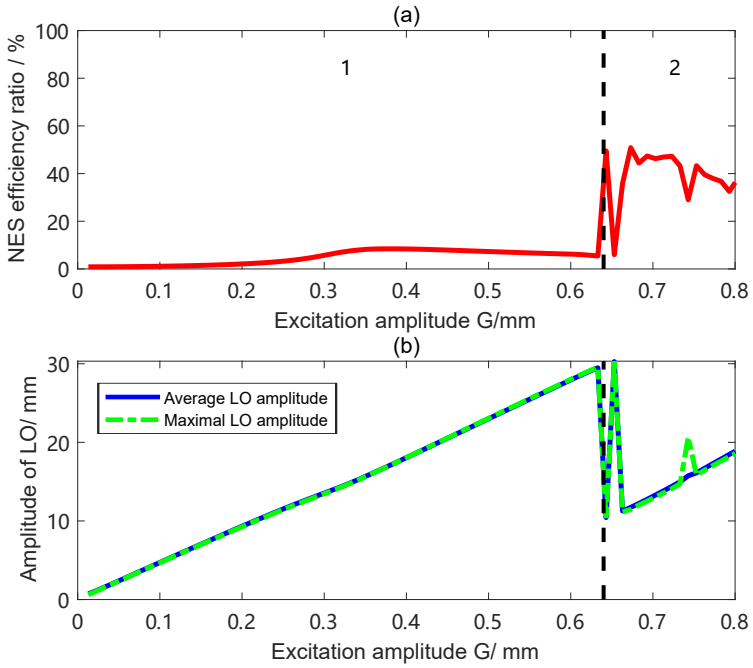

Figure 3.19: (a) Energy dissipation ratio of NES (b) maximal and average LO amplitude in abnormal bistable NES case. The blue line represents the average amplitude, the green dashed line is the maximal amplitude. The black dashed lines divide regimes into two stages.

Solving the above equation gives a critical negative stiffness of δ_{sa} = -2, above which, bistable NES is classified as an abnormal case. In this abnormal case, the simulation of negative stiffness case k_3 = -250 (δ = -2.2) is carried out.

In this case, the trajectory exceeds the chaos threshold and becomes a stable inter-well oscillation. Because the interaction of chaos threshold line B and the right global SIM branch, the SMR vanishes. Only two regimes persist in the efficiency distribution and LO amplitude in Fig. 3.19 : (1) intra-well oscillation, and (2) stable periodic response. In contrast to the previous model, the SMR stage is compressed and vanishes, leading to a so-called abnormal bistable NES.

The chaos trigger line B has exceeded on the right side of singularity line D, so the optimal point (maximum efficiency) is not lying on the singular point S_2. The maximal efficiency that an abnormal NES can achieve is much lower than in previous cases, about 50%.

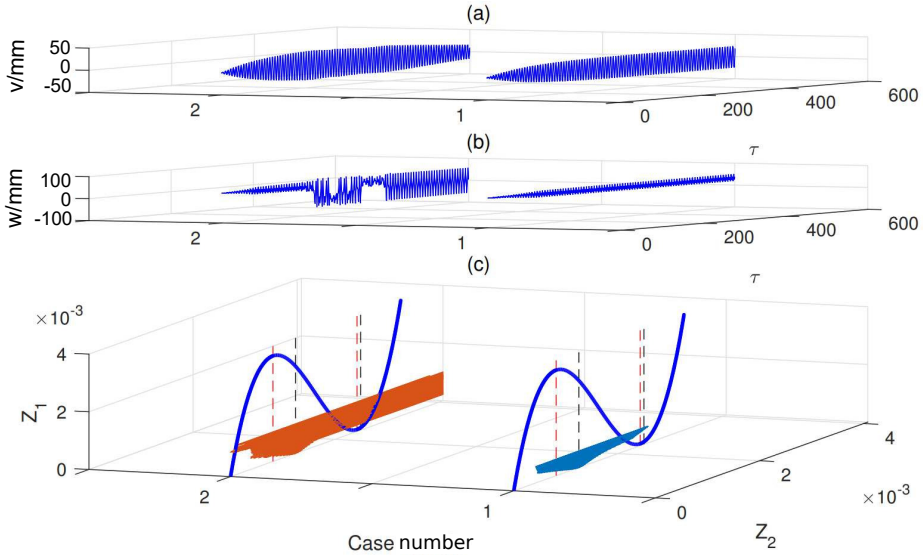

Figure 3.20: Response regimes in abnormal bistable NES with k_3 = -250 (δ = -2.2) (a) v displacement, (b) w displacement, (c) phase trajectory of Z_2 and Z_1. The 2 typical responses are chosen at various excitations G = 0.5mm, 0.7mm, σ = 0.

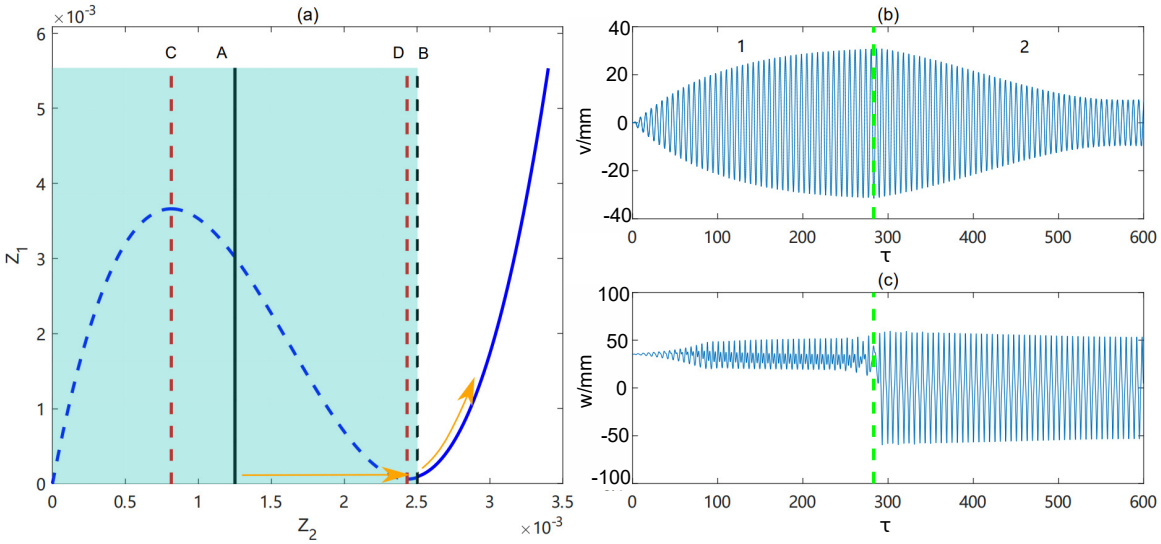

Figure 3.21: Characteristic abnormal bistable global SIM and response in the time domain at excitation G = 0.65 mm, σ = 0. (a) The global SIM structure with unstable region (shaded). The orange arrow line indicates various stages in one SMR cycle. (b) displacement of w; (c) displacement of v. The green lines divide the SMR into various stages corresponding the global SIM explanation by the orange arrow line.

3.4 Experimental study

There are two goals for the experimental study: (1) verify the feasibility of the intra-well adapted complex variables method in the frequency domain. (2) observe the characteristic response regimes of different bistable NES designs under increasing excitation amplitude inputs. Various negative stiffnesses were constructed by adjusting the pre-compression length of the linear spring in the bistable NES. A diagram of the bistable NES is presented in Fig. 2.10.

3.4.1 Static tests

The bistable nonlinearity is constructed by combining 2 linear springs and 2 conical springs that mainly provide the bistable force-displacement relationship. The conical spring presents two phases: (a) linear phase, (b) nonlinear phase during the compression [Qiu *et al.*, 2018b]. When the coils of a conical spring come into contact with each other due to compression, a transition step occurs that divides the linear and nonlinear phases. So the two conical springs are pre-compressed at the transition point to eliminate the linear phase, as in (a) of Fig. 2.10. The two linear springs, whose role is to counterbalance the linear stiffness in the nonlinear phase, are installed perpendicular to the conical springs like (b) in Fig. 2.10. The force-displacement relation of combining system can be expressed as Eq. (2.37). The detailed parameters and 3 initial pre-compression lengths (l_{p1} l_{p2} and l_{p3}) for 3 different bistable NES cases are presented in Tab. 3.1.

The corresponding static force-displacement figures for each case are presented in Fig. 3.22. In each case, the theoretical results provide sufficient accuracy to describe the experimental results and two equilibria (F = 0). The distance between the equilibrium points becomes greater when l_p increases. So it can be concluded that the control strategy of changing the length of pre-compression to produce desirable bistable nonlinearity is feasible. However, increasing l_p will increase not only the $|\delta|$ value but also K value, which is different from the idea of purely introducing δ and keeping K constant used in the previous bistable NES classification. However, the negative stiffness δ presents a more significant role in determining the bistable NES behaviors. The change in pre-compression length results in a major change in δ values. So the experiment of different pre-compression length designs can demonstrate the influence of δ.

3.4.2 Dynamic tests for intra-well oscillation

The testing system consisted of a NES embedded with a LO. A 10 kN electrodynamic shaker provided the excitation at a variable frequency. The absolute displacements of NES and LO were measured by two laser systems installed vertically. The bandpass

Table 3.1: Experimental parameters of NES system

k_0	a_1	a_3	k_l	l_{0l}
187N/m	280N/m	3.6e5N/m^3	1060N/m	50mm
	l_c	l_{p1}	l_{p2}	l_{p3}
	14.5mm	16mm	17.5mm	21mm

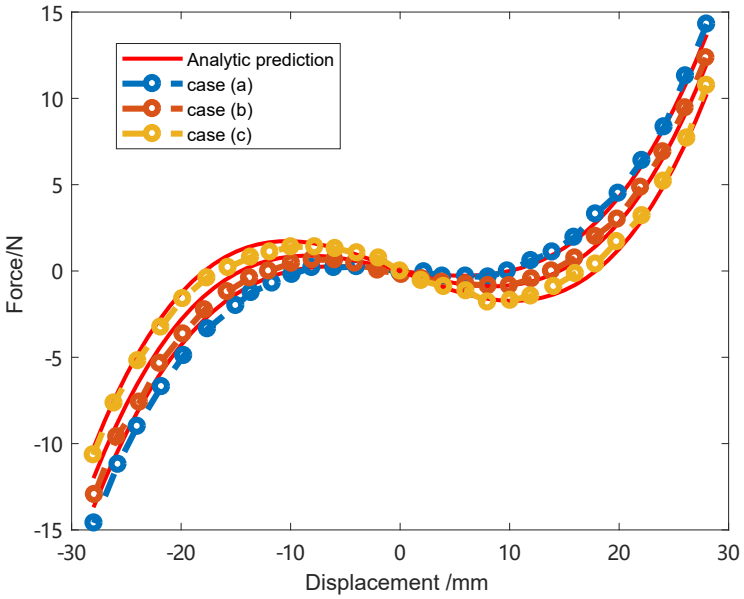

Figure 3.22: Force displacement of different experiment tests with parameters in Tab. 3.3.

Table 3.2: Experimental parameters of system

Physical parameters	m_1	m_2	c_1	c_2	k_1
	5.5kg	0.05kg	5N·s/m	0.5N·s/m	1.148e4N/m
Reduced parameters	ϵ	λ_1	λ_2	f_0	
	0.91%	2.19	0.22	7.27Hz	

filter filtered the high-frequency noise, thus correcting the raw signal and the biases. The amplitude of excitation was 0.08mm, which was the minimum value that the shaker could apply. Its frequency was varied from 7Hz to 7.6Hz at a sweep velocity of 0.01Hz/s. The physical parameters of experiment are summarized in Tab. 3.2. The different negative stiffnesses caused by various pre-compression lengths are presented in Tab. 3.3.

Fig. 3.23 shows the experimentally obtained frequency response function for the small amplitude excitation G = 0.08mm, where 3 cases perform intra-well oscillation. The analytical result was obtained by substituting the reduced parameters in Tab. 3.2 and 3.3 into Eq. (3.4) and resolving the LO amplitude $|\phi_{10}|$.

When a natural frequency excitation is applied in LO, the resonance phenomenon is activated. The LO possesses the largest amplitude, of 7.23Hz, close to the predicted

Table 3.3: Experimental cubic nonlinearity parameters and negative stiffness parameters

	case (a)	case (b)	case (c)
$k_3(N/m)$	-71.4	-136.3	-300.1
$k_2(N/m^3)$	6.95e5	7.2e5	7.89e5
δ	-0.68	-1.31	-2.89
K	6.59e3e5	6.90e3	7.58e3

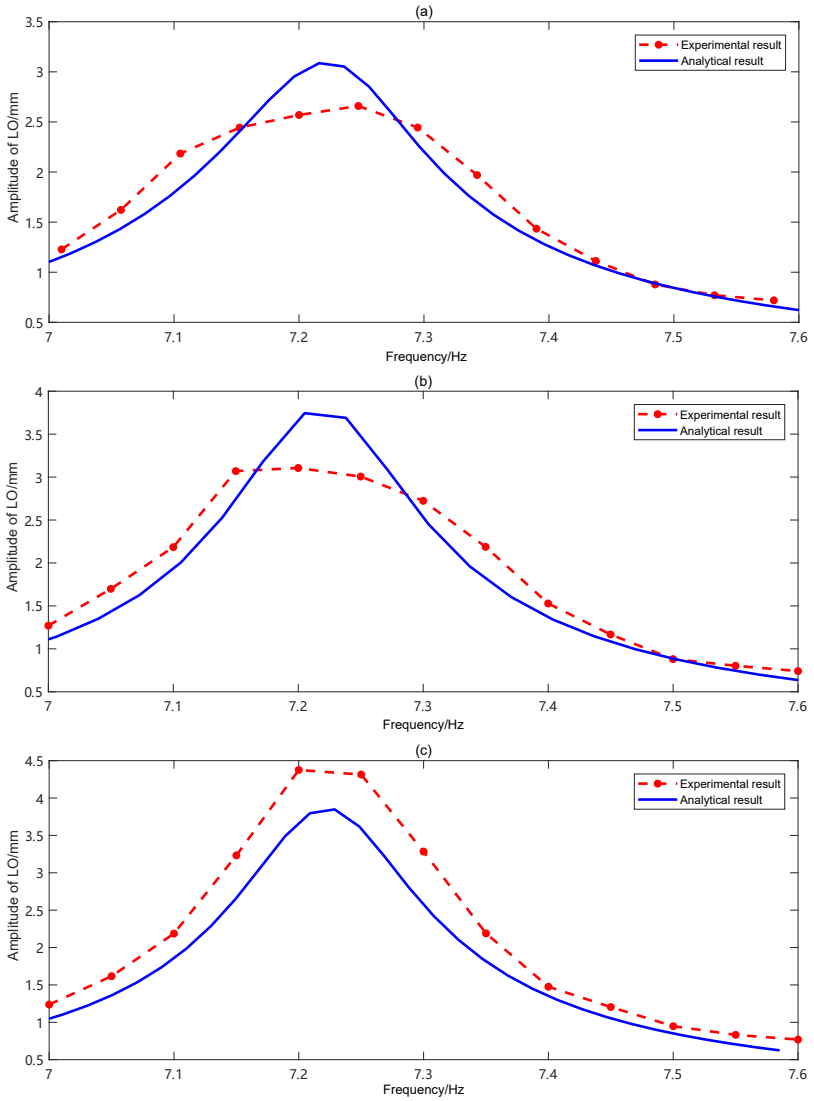

Figure 3.23: Experimental and analytical frequency response curve of LO for different pre-compression length cases at excitation amplitude G = 0.08mm. The parameters of the 3 cases are presented in Tab. 3.3.

value of 7.26Hz. In general, the analytical method described the intra-well oscillation correctly under various δ cases as shown in Fig. 3.23. The analytical amplitude, which is compared with the experimental result, had the same error distribution under different negative stiffnesses. On the two sides of the natural frequency, the analytical result was usually lower than the experimental result. In the vicinity of the natural frequency, the analytical result had a higher amplitude in Fig. 3.23a,b. This error distribution is the same as the numerical test of Fig. 3.3d, where the analytical method possesses a larger result near $\sigma = 0$. In the most intensive δ case in Fig. 3.23c, the calculation method gave a lower analytical result. This confirms the previous conclusion that the adapted complex variables method leads to minor error in the modest bistable case under small excitation. This is due to the fact that the negative stiffness value is too large to cause deformation of the real phase trajectory near the equilibrium point (which does not conform to the assumption of a circle).

3.4.3 Dynamic tests in various energy levels

The previous section confirms the feasibility of the adapted complex variables method in the frequency domain. However, the advantage of the bistable NES in absorbing energy is more apparent in other higher energy levels. In this section, the response of the bistable NES is investigated experimentally in various energy input levels.

The three different compression cases, having parameters that were identical to those of the previous intra-well experimental validation, were tested under a frequency sweeping excitation from 7Hz to 7.6Hz. The same frequency sweeping process with different excitation amplitudes was repeated to record the responses of the LO and NES.

3.4.3.1 Experiments under case (a) configuration parameters

11 sets of excitation amplitudes, from small to large values: 0.08mm, 0.10mm, 0.12mm, 0.15mm, 0.18mm, 0.21mm, 0.25mm, 0.28mm, 0.32mm, 0.36mm, and 0.4mm, were tested for case (a). To help distinguish them, the adjacent time-displacement curves are marked with different colours.

In Fig. 3.24, the black diamond points distinguish the SMR region and resonance peak (potential risk case), where the amplitude of the LO is enormous, and the efficiency of absorbing energy fails for the NES.

In the first case (G = 0.08mm), the stable response was the primary behavior. Intra-well oscillation appeared during the whole frequency domain. The NES oscillated around the equilibria.

In the vicinity of the natural frequency, 7.26Hz, 1: 3 subharmonic oscillation occurred first at low energy input (G = 0.1mm) and became more obvious at G = 0.12mm.

After the external excitation reached a threshold (G = 0.18mm), the region of 1: 3 subharmonic resonance broke and expanded to higher and lower frequency sides with increasing external excitation amplitude. In the neighbourhood of the natural frequency, the response reverted to a 1: 1 resonance. It also implies that the phase trajectory is re-attracted to the left branch of global SIM as case 3 in weak bistable NES simulation of Fig. 3.11c. In the simulation, the system returns from a chaotic motion into periodic motion with increase of excitation amplitude. In the experiment, the NES system turned from subharmonic oscillation into periodic motion. This may be because of the property

of shift-frequency excitation. The 1:3 subharmonic was activated in low frequency. When the frequency of excitation was tuned to f_0, the previous 1:3 subharmonic oscillation was kept. The stability of subharmonic oscillation was better than the chaos behavior, which did not occur as predicted by the traditional analysis framework. So characteristic response of weak bistable NES (re-attraction stage) was observed.

Once G = 0.21mm was applied in case (a), SMR cycles appeared in the frequency interval [7.27Hz, 7.38Hz], which is marked by two black diamond points. The first snap-through motion and last jump-back motion of NES define the interval of SMR in Fig. 3.24b. For the left boundary, at 7.27Hz, the LO always had the maximal amplitude. For the right boundary, at 7.38Hz, the LO possessed minimal local amplitude after several cycles of SMR. This indicated the effect of absorbing the energy of the SMR. The chaotic motion occupied two adjacent efficient TET, which resulted in the augmentation of LO amplitude in Fig. 3.24a.

The SMR interval expanded to [7.21Hz, 7.47Hz] under greater excitation, G = 0.25mm. Then G continued to increase to 0.32mm, the interval of SMR became broader [7.15Hz, 7.47Hz]. As G increased from 0.21 to 0.32mm, the left boundary, where SMR appeared, decreased from 7.23Hz to 7.15Hz, while the right boundary, where SMR vanished, expanded from 7.38Hz to 7.47Hz accordingly. This demonstrates a broader efficient range for performing TET for a higher energy input before the resonance peak occurs.

In G = 0.36mm, the duration of amplitude decline of SMR has extended irregularly and caused a potential risk region near the left interval boundary. Meanwhile, the frequency range of SMR has achieved the maximum of [7.13Hz, 7.54Hz]. The case (a) design has the best robustness facing the uncertainty of excitation frequency under G = 0.36mm. The 1: 3 subharmonic oscillation appeared in the low-frequency region. Then the SMR occurred in the vicinity of natural frequency. The systems returned to a stable response if frequency continued to increase.

When G = 0.4mm, the resonance peak appeared between 7.05Hz and 7.25Hz. Within the resonance interval, the LO amplitude significantly exceeded the other cases, the NES lost its ability to absorb energy, and the system was at risk. A resonance peak occurred due to the existence of three solutions in the singularity equation in the low-frequency region, one of which had a large stable amplitude. However, in the vicinity of the natural frequency, 7.26Hz, the LO had a stable minimal amplitude of 2.8mm, which represents the singularity point of the right global SIM branch. So there is a trade-off relationship between the co-existence of the best performance of NES and the worst resonance peak at the amplitude of G = 0.4mm for case (a) design. The best design also provided a possibility of worse behavior at low frequency. So the feasibility of optimal design case (a) depended on the perturbation of harmonic excitation frequency.

When the excitation increased from 0.08mm to 0.4mm, in the vicinity of natural frequency of LO, there are five stages that appeared in turn: (1) intra-well oscillation stage, (2) 1:3 subharmonic oscillation stage, (3) re-attraction stage, (4) SMR, (5) stable response. Those five stage are marked in Fig. 3.24b with the green dashed boxes. Those response regimes are similar to the weak bistable NES classification based on the numerical response regimes.

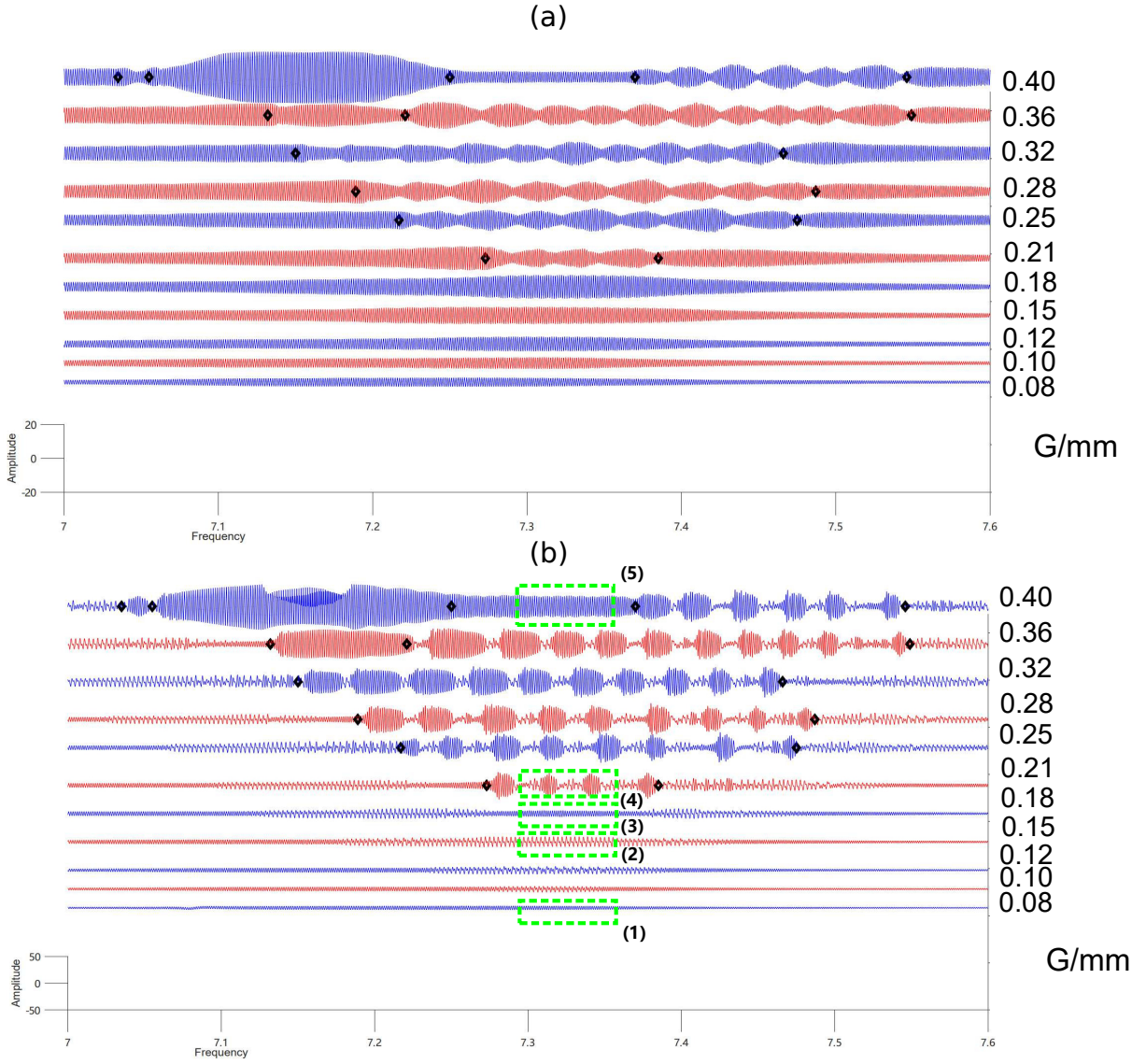

Figure 3.24: (a) Frequency response of LO (b) frequency response of NES for case (a). The amplitudes of excitation are selected as 0.08mm, 0.10mm, 0.12mm, 0.15mm, 0.18mm, 0.21mm, 0.25mm, 0.28mm, 0.32mm, 0.36mm, 0.4mm. The black diamond distinguishes the SMR region from the resonance peak region. The green boxes indicate the characteristic regimes.

3.4.3.2 Experiments under case (b) configuration parameters

Then the pre-compression length was increased to 17.5mm, case (b) possessed larger negative stiffness $|\delta|$ and cubic nonlinearity parameters K. Similarly to case (a), the system (b) was also used with 12 sets of sweeping frequency excitations of different amplitudes: 0.08mm, 0.10mm, 0.12mm, 0.15mm, 0.18mm, 0.21mm, 0.25mm, 0.28mm, 0.32mm, 0.36mm, 0.40mm, 0.44mm. Frequency varied from 7Hz to 7.6Hz.

An essential characteristic of case (b) was the extensive range of apparent chaotic motion, which replaced the subharmonic motion of case (a). A larger depth value of potential well $\delta^2/4K$ enhanced the stability of intra-well oscillation.

In the first three cases (0.08mm, 0.10mm, 0.12mm), the system oscillated in one of the wells over the frequency.

The chaos motion occurred first for G = 0.15mm. A single and weak SMR was also observed for G = 0.18mm, which is lower than the SMR occurrence threshold of case (a) (G = 0.21mm) in Fig. 3.25. The SMR was generated near the natural frequency and divided the chaotic region. The chaos frequency range expanded toward lower and higher frequency sides as the excitation increased.

For excitation G from 0.21mm to 0.32mm, the frequency interval for SMR occurrence expanded from a narrow range [7.29Hz, 7.31Hz] to [7.18Hz, 7.47Hz].

When G became 0.36mm, a potential resonance peak also occurred. However, the frequency range of resonance peak [7.13Hz, 7.18Hz] was narrower than that of case (a). This tendency was more obvious in the response of NES under G = 0.4mm, where the resonance peak region was [7.10Hz, 7.23Hz]. This range was narrower than the [7.05Hz, 7.25Hz] of case (a). The resonance peak occurred when the system did not give a stable response at 7.26Hz. At the same time, the interval in which SMR occurred widened to [7.23Hz, 7.56Hz].

At the amplitude G = 0.44mm, the first signs of the steady-state response of LO at the natural frequency of 7.25Hz appeared, where the LO amplitude in Fig. 3.25 tended to be stable and locally minimal between the SMR and resonance peak. SMR range still dominated the extensive range [7.25Hz, 7.58Hz] and moved to a higher frequency side. An effective SMR range was also enhanced in a high energy input case. A larger compression length can reinforce the amplitude threshold required for the emergence of an optimal stable periodic response (saturation of absorbing energy).

When the excitation increased from 0.08mm to 0.44mm, in the vicinity of the natural frequency of LO, there were four stages that appeared in turn: (1) intra-well oscillation stage, (2) chaotic motion, (3) SMR, (4) stable periodic response (sign appeared). Those four stages are marked in Fig. 3.25b with the green dashed boxes. The re-attraction stage disappears as a prediction of the numerical simulation: the overlap of unstable region and chaos region prevents the phase trajectory jump back to the left global SIM branch. So re-attraction motion disappeared. The characteristic of modest bistable NES: the expansion of chaotic motion was observed.

3.4.3.3 Experiments under case (c) configuration parameters

Case (c) could be achieved by continuing to modify the pre-compression length to 21mm. Case (c) was used with the same amplitude condition as case (b), except for the 0.15mm and 0.44mm cases. The negative stiffness continued to be enhanced.

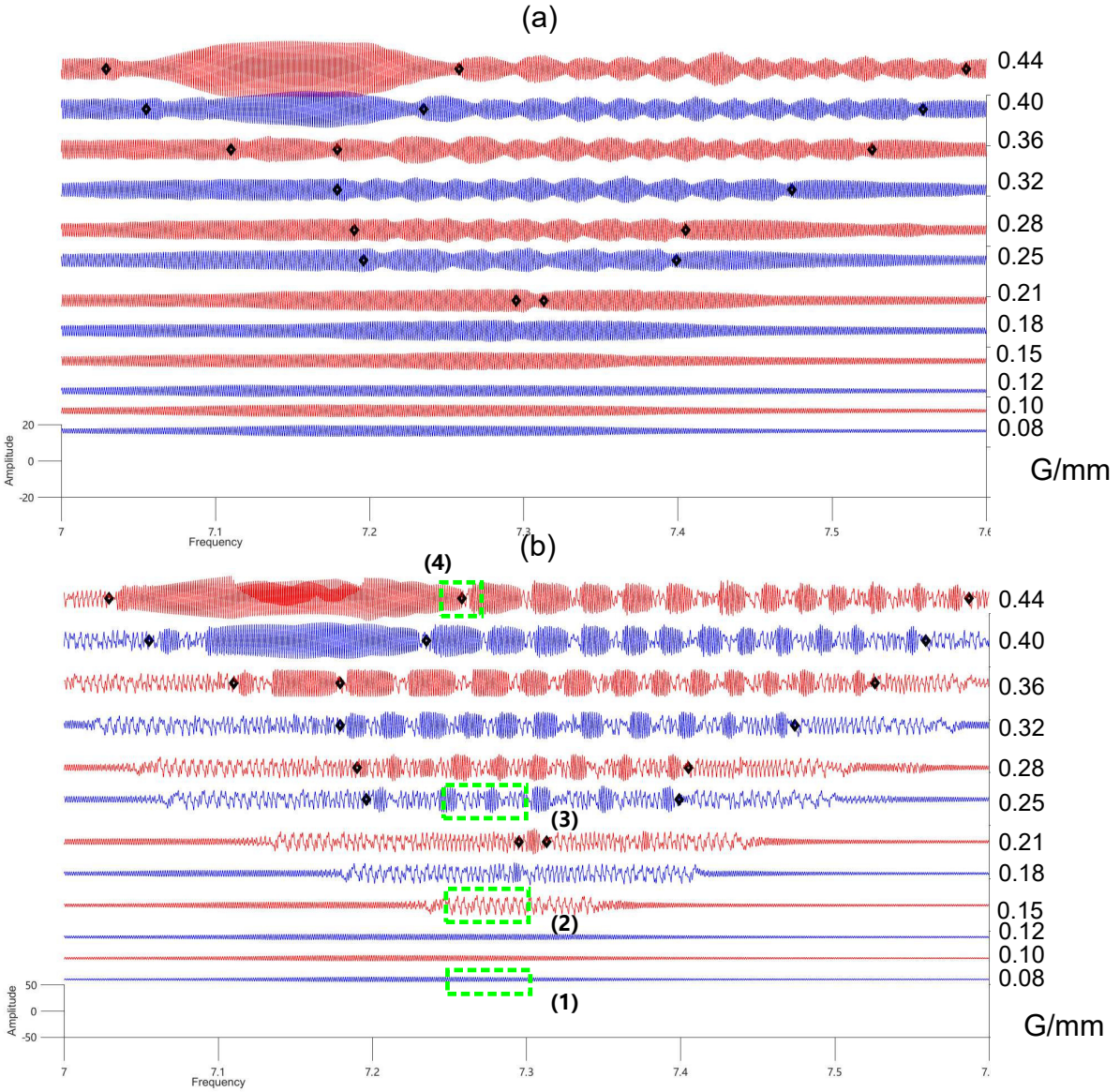

Figure 3.25: (a) Frequency response of LO (b) frequency response of NES for case (b). The amplitudes of excitation are selected as 0.08mm, 0.10mm, 0.12mm, 0.15mm, 0.18mm, 0.21mm, 0.25mm, 0.28mm, 0.32mm, 0.36mm, 0.40mm, 0.44mm. The black diamond distinguishes the SMR region from the resonance peak region. The green boxes indicate the characteristic regimes.

Neither chaotic motion nor subharmonic motion is observed in Fig. 3.26. It can be interpreted as a model of strong bistable NES that the narrow distance between trigger line B and singularity line D causes the phase trajectory to start snap-through motion and jump to the right branch of the global SIM as soon as it comes out of the well. So, before the system oscillates around the right branch of the SIM, the chaos motion is replaced by the 1:1 resonance.

This first SMR appeared at G = 0.18mm, which is the same as case (b) in Fig. 3.26. The frequency range of SMR increased from [7.18Hz, 7.20Hz] to [7.05Hz, 7.41Hz], as the excitation amplitude rose from 0.18mm to 0.36mm. The SMR range expanded to a lower and higher frequency sides. In case (a) and case (b), there was a significant chaotic motion between the two adjacent SMR cycles. In case (c), this chaotic phenomenon is not obvious.

The range of potential resonance peak is [7.07Hz, 7.19Hz] for G = 0.4mm. Compared with the resonance peak in case (b) for G = 0.36mm, the excitation threshold for the occurrence of resonance increased and its appearance was delayed. The resonance situation was improved. Although, the stable periodic response (optimal state) is not observed because of the limitation of the laser displacement sensors. It can be inferred that his optimal state occurs above excitation amplitude of 0.4mm.

When the excitation increased from 0.08mm to 0.4mm, in the vicinity of the natural frequency of LO, there were two stages that appeared in turn: (1) intra-well oscillation stage, (2) SMR, The third stage stable response can be inferred by the numerical simulation. Those two stages are marked in Fig. 3.26b with the green dashed boxes. The disappearance of chaotic motion is the characteristic symbol of a strong bistable NES.

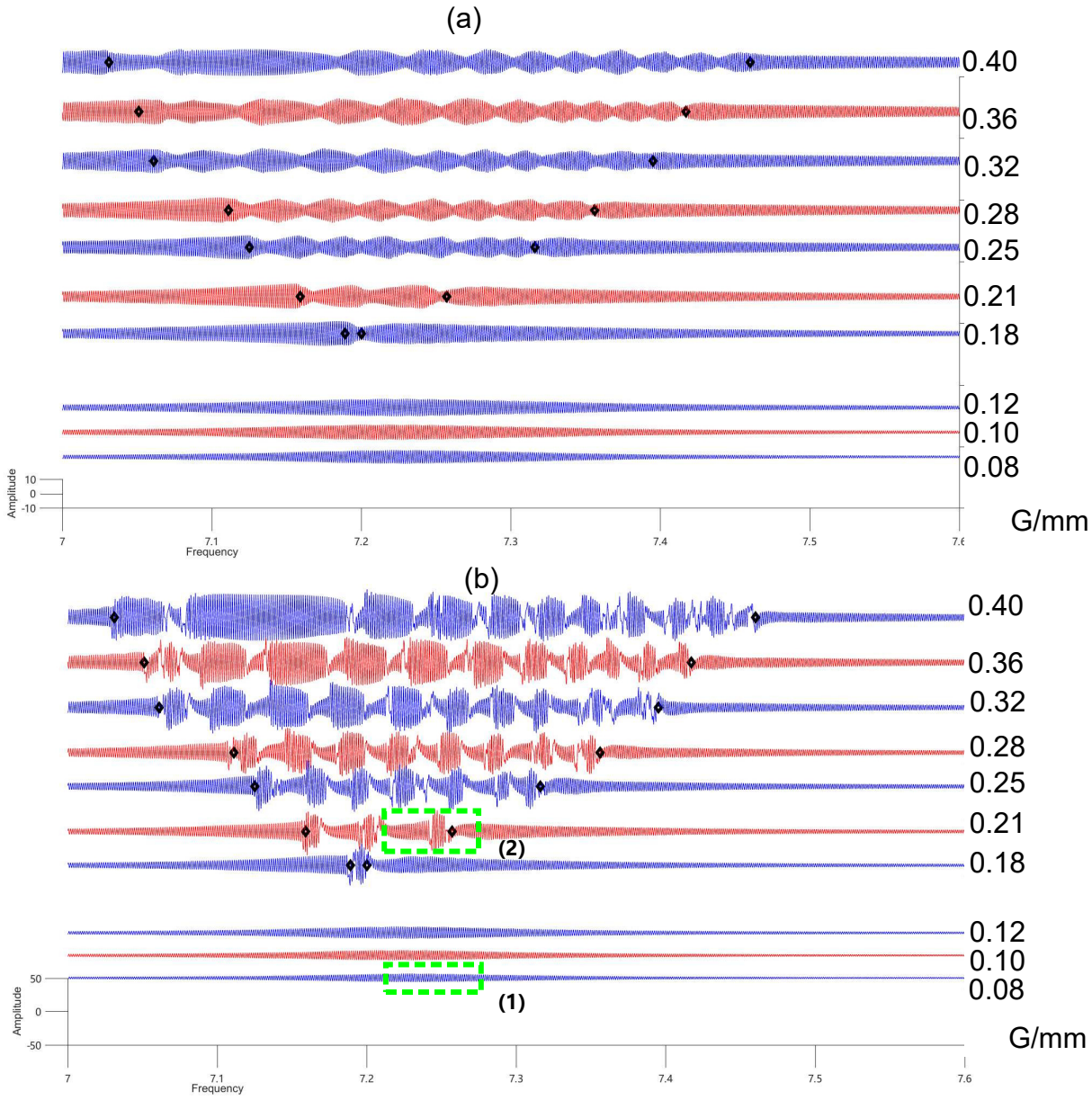

Figure 3.26: (a) Frequency response of LO (b) frequency response of NES for case (c). The amplitude of excitation are selected as 0.08mm, 0.10mm, 0.12mm, 0.18mm, 0.21mm, 0.25mm, 0.28mm, 0.32mm, 0.36mm, 0.40mm. The black diamond distinguishes the SMR region and resonance peak region. The green boxes indicate the characteristic regimes.

3.5 Conclusions

The study focuses on the qualitative analysis of response regimes in bistable NES. Several main conclusions can be drawn:

1. The adapted complex variables method, which defines the equilibrium point as an original coordinate, performs better to approach the dynamic behaviors of intra-well oscillation. The numerical investigation reveals its natural stability of intra-well oscillation. This method gives a good fitting result and has been compared with the numerical results in the frequency domain. The actual phase trajectory of intra-well oscillates along with the constructed local Slow Invariant Manifold (SIM), which describes the low energy behaviors better than the classic method. But the local SIM's reliability is constrained to intra-well oscillation stage.

2. A simplified model of triggering chaos has showed that the phase trajectory expands in a circular form with the equilibrium point as the center within the pseudo-separatrix. Despite being simple, the chosen approach enabled us to predict the analytical harmonic excitation amplitude for chaos occurrence. The numerical chaos boundary has proved the reliability of its analytical prediction in weak negative stiffness cases. The Melnikov method enables the calculation of the critical damping of the NES for triggering chaos and is validated by numerical simulations.

3. The relative position between the chaos trigger line and the global SIM structure has been proposed to illustrate the variation of the triggering Strong Modulated Response (SMR) condition. The variety in relative position of those lines enables us to explain the disappearence of response stages with larger negative stiffness value $|\delta|$ cases and for various energy levels. On the other hand, the location of chaos trigger line B in the global SIM structure classifies the bistable NES as a weak, modest, strong or abnormal bistable NES. A more efficient way to dissipate energy has been found in the modest bistable case, due to the small distance between the chaos trigger line and the singularity line in the global SIM structure.

4. The frequency-response experiment of Linear Oscillator (LO) amplitude was carried out to validate the feasibility of the adapted variables complex method. Good agreement between the theoretical and experimental results of intra-well oscillation under different negative stiffnesses was observed. Experiment confirms that the number of response regimes in the vicinity of LO natural frequency will reduce with a more significant value of $|\delta|$, which is predicted in the numerical simulation. The design of a modest bistable NES provides the broadest frequency range of SMR for the same excitation input and helps to reduce the risk of the resonance peak in the frequency domain.

CHAPTER 4

Estimation of energy pumping time in bistable NES

Abstract

This chapter presents a novel method to measure the energy pumping time of bistable Nonlinear Energy Sink (NES) under a harmonic excitation case based on a particular integration assumption. An equivalent point in the Slow Invariant Manifold (SIM) structure can represent the average variation of amplitudes of Linear Oscillator (LO) and NES during the energy pumping. The strong robustness of this semi-analytical prediction method under parameter perturbation is investigated numerically. The parameters influence on the amplitude declining rate are investigated for both impulsive and harmonic excitation. The validation of energy pumping time estimation is verified in the experimental test.

Contents

4.1 Estimation of energy pumping time

When the Targeted Energy Transfer (TET) is activated in the bistable Nonlinear Energy Sink (NES), it results in a decline process of Linear Oscillator (LO) amplitude. The energy of LO is transferred into NES and dissipated by NES damping through 1:1 resonance. The energy pumping time is defined as the duration of this decline process.

The bistable NES model is the same as the previous section. With the application of multiple scales method and complexification-averaging method, the governed equation can be transfered into several time scales. The first equation in Eq. (2.40) indicates that the ϕ_1 is independent of the τ_0 time scale. It can be demonstrated that ϕ_1 and ϕ_2 evolve toward an equilibrium state for $\tau_0 \to \infty$. Setting the derivative with respect to τ_0, the second equation in Eq. (2.40) and the first equation in Eq. (2.41) yield:

$$\begin{aligned} &\frac{1}{2}i\left(\phi_2-\phi_1\right)+\frac{1}{2}\phi_2\lambda_2-\frac{3}{8}iK\phi_2^2\overline{\phi}_2-\frac{1}{2}i\delta\phi_2=0 \\ &\frac{\mathrm{d}}{\mathrm{d}\tau_1}\phi_1+\frac{1}{2}\lambda_1\phi_1+\frac{1}{2}i\left(\phi_1-\phi_2\right)+i\sigma\phi_1-\frac{1}{2}F=0 \end{aligned} \tag{4.1}$$

The above equation can only behave on the slow time scale τ_1. The complex variables with polar notation of Eq. (2.13) are substituted in Eq. (4.1). N_1 and N_2 modulate the amplitude envelopes of LO and NES. δ_1 and δ_2 are phases of N_1 and N_2. By separating the real and imaginary terms, the following set of equations Eq. (4.2) is obtained after simple algebraical manipulation.

$$\begin{aligned} &\frac{\partial}{\partial T_1}N_1-\frac{1}{2}N_2\sin(\delta_1-\delta_2)+\frac{1}{2}\lambda_1N_1-\frac{1}{2}\cos(\delta_1)F=0 \\ &N_1(\frac{\partial}{\partial T_1}\delta_1)+\frac{1}{2}N_1-\frac{1}{2}N_2\cos(\delta_1-\delta_2)+\sigma N_1+\frac{1}{2}\sin(\delta_1)F=0 \\ &(\frac{1}{2}N_2-\frac{1}{2}\delta N_2-\frac{3}{8}KN_2^3)\sin(\delta_1-\delta_2)+\frac{1}{2}N_2\lambda_2\cos(\delta_1-\delta_2)=0 \\ &\frac{1}{2}N_1+(\frac{3}{8}KN_2^3+\frac{1}{2}\delta N_2-\frac{1}{2}N_2)\cos(\delta_1-\delta_2)+\frac{1}{2}N_2\lambda_2\sin(\delta_1-\delta_2)=0 \end{aligned} \tag{4.2}$$

Resolving the third and fourth equation in Eq. (4.2), the expression of $\cos(\delta_1-\delta_2)$ and $\sin(\delta_1-\delta_2)$ can be expressed as

$$\begin{aligned} \cos(\delta_1-\delta_2)&=-\frac{4(3KN_2^2+4\delta-4)N_1}{N_2((3KZ_2+4\delta-4)^2+16\lambda_2^2)} \\ \sin(\delta_1-\delta_2)&=-\frac{16\lambda_2N_1}{N_2((3KZ_2+4\delta-4)^2+16\lambda_2^2)} \end{aligned} \tag{4.3}$$

The above expression satisfies the relation $cos(x)^2+sin(x)^2=1$ and shows an intrinsic property of bistable NES system. Substituting (4.3) into the first two equations in (4.2), the variation of LO amplitude is presented as follows in Eq. (4.4), with $Z_1=N_1^2$ and $Z_2=N_2^2$.

$$\begin{aligned} &Z_1=Z_2((\delta+\frac{3}{4}KZ_2-1)^2+\lambda_2^2) \\ &\frac{\partial}{\partial\tau_1}Z_1(\tau_1)=-\lambda_2Z_2-\lambda_1Z_1+N_1\cos(\delta_1)F \end{aligned} \tag{4.4}$$

The first equation of Eq. (4.4) is also known as the Slow Invariant Manifold (SIM). Every point in the SIM branch indicates a potential steady response solution, the stability of which can be determined by applying the perturbation method and observing whether the roots of its characteristic equation lie on the left half of the complex plane.

The right-hand side of the second equation of Eq. (4.4) indicates that the LO amplitude is naturally decreasing because its derivation is always negative if there is no external excitation (F = 0). A Hamiltonian system indicates that Z_1 has a derivative of zero and the LO amplitude remains constant. It results in the energy exchange without dissipation in the Hamiltonian system. The energy transfer from LO to NES is an inherent property of the system in the presence of damping. With the existence of the term $\cos(\delta_1)F$, whose positivity or negativity is not fixed. This gives rise to a relaxation-type oscillation.

4.1.1 Transient response

For the sake of simplicity, the response of transient excitation (F = 0, $\dot{v}(0) \neq 0$) is considered first. In this case, the right-hand side of the second equation of Eq. (4.4) is always negative, and the energy localized in LO decreases continuously. The derivation of Z_2 with respect to τ_1 is obtained by deriving the SIM function with respect to Z_2 and then combining it with the second equation of Eq. (4.4).

$$\frac{\partial}{\partial \tau_1} Z_2 = \frac{-\lambda_1 Z_1 - \lambda_2 Z_2}{\frac{27}{16} K^2 Z_2^2 + 3K Z_2(\delta - 1) + (\delta - 1)^2 + \lambda_2^2} \tag{4.5}$$

It is difficult to separate the variables and integrate the Eq. (4.5). However, if the damping of the LO is neglected ($\lambda_1 = 0$), the separation of variables leads to a possible integration, as follows:

$$\begin{aligned} C + \lambda_2 \tau_1 &= \frac{27}{32} K^2 Z_2^2 + 3K Z_2(\delta - 1) + \ln(Z_2)\left((\delta - 1)^2 + \lambda_2^2\right) \\ \tau_{1,p} &= \frac{\mathcal{I}(Z_2(1)) - \mathcal{I}(Z_2(0))}{\lambda_2} \end{aligned} \tag{4.6}$$

The right-hand side of the first equation of Eq. (4.6) is marked as $\mathcal{I}(Z_2)$, describing the state of the systems. When the initial $Z_2(0)$ decreases to $Z_2(1)$, the slow time interval, $\tau_{1,p}$, of this process can be obtained by calculating the state variables $\mathcal{I}(Z_2(0))$ and $\mathcal{I}(Z_2(1))$ from initial state to end state. This process is visualized with the red dashed line in the SIM structure in Fig. 4.1.

For the condition that $\lambda_1 \neq 0$, the pumping time $\tau_{1,p}$ from initial state and end state can be solved according to the following equation.

$$\begin{aligned} &\int_0^{\tau_{1,p}} \left(-\frac{9}{16}\lambda_1 K^2 Z_2^2 + \frac{3}{2}\lambda_1 K(1-\delta) Z_2\right) d\tau_1 \\ &-(\lambda_1(1-\delta)^2 + \lambda_1\lambda_2^2 + \lambda_2)\tau_1 = \mathcal{I}(Z_2(0)) - \mathcal{I}(Z_2(1)) \end{aligned} \tag{4.7}$$

While the trajectory descends from $Z_2(0)$ to $Z_2(1)$, Z_2 is the function of τ_1, which is hard to express in an explicit form. However, Z_2, which represents the NES amplitude, is almost constant during the energy pumping. This assumption that Z_2 remains constant during the TET has been verified numerically [Dekemele *et al.*, 2019]. So, in the integration term in Eq. (4.7), Z_2 is assumed to be a constant $Z_{2,c}$. $Z_{2,c}$ measures the average value

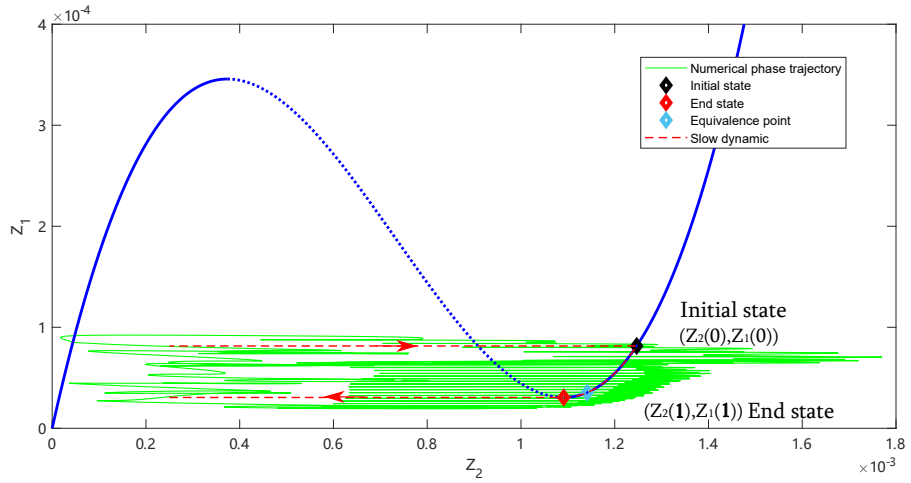

Figure 4.1: The SIM structure (blue line) and transient phase trajectory (green line), which describes the descending motion from initial state ($[Z_2(0), Z_1(0)]$) to end state ($[Z_2(1), Z_1(1)]$). The red dashed line with the arrow means the equivalent ideal slow flow motion.

of Z_2 during TET. It is determined by slow flow dynamics in the undamped condition $\lambda_1 = 0$.

$$\begin{aligned} Z_{2,c} &= \frac{\int_0^{\tau_1} Z_2 d\tau_1}{\tau_{1,p}} \\ &= \frac{\int_{Z_2(1)}^{Z_2(0)} (\frac{27}{16} K^2 Z_2^2 + 3KZ_2(\delta - 1) + (\delta - 1)^2 + \lambda_2^2) dZ_2}{\lambda_2 \tau_{1,p}} \\ &= \frac{[\frac{9}{16} K^2 Z_2^3 + \frac{3}{2} K(\delta - 1) Z_2^2 + (\delta - 1)^2 Z_2 + \lambda_2^2 Z_2]|_{Z_2(1)}^{Z_2(0)}}{\lambda_2 \tau_{1,p}} \end{aligned} \tag{4.8}$$

Finally, the energy pumping time $\tau_{1,p}$ between two states from $Z_2(0)$ to $Z_2(1)$ is found by solving the following equation.

$$\tau_{1,p} = \frac{\mathcal{I}(Z_2(0)) - \mathcal{I}(Z_2(1))}{-(\frac{9}{16}\lambda_1 K^2 Z_{2,c}^2 - \frac{3}{2}\lambda_1 K(1 - \delta) Z_{2,c} + \lambda_1 (1 - \delta)^2 + \lambda_1 \lambda_2^2 + \lambda_2)} \tag{4.9}$$

4.1.2 Harmonic excitation response

The integration of second equation of Eq. (4.4) involves complex terms in which the expressions for the phase $\delta_1(\tau_1)$ and the amplitude $N_1(\tau_1)$ are hard to describe analytically, when harmonic excitation F exists. It causes the integral $F \int_0^{\tau_{1,p}} N_1(\tau_1) \cos(\delta_1(\tau_1)) d(\tau_1)$ to fail. The terms $N_1 \cos(\delta_1)$ represent the real part of ϕ_1. From an engineering interpretation point of view, $Re(\phi_1)$ is considered as amplitude information of LO. Based on this concept, an essential assumption is proposed as $N_1(\tau_1)\cos(\delta_1(\tau_1)) = \sqrt{Z_1}$. This assumption will be verified numerically in the following subsection. So the energy dissipation ratio in the harmonic excitation case is expressed as:

$$\frac{\partial}{\partial \tau_1} Z_2 = \frac{-\lambda_1 Z_1 - \lambda_2 Z_2 + F\sqrt{Z_1}}{\frac{27}{16} K^2 Z_2^2 + 3K Z_2(\delta - 1) + (\delta - 1)^2 + \lambda_2^2} \tag{4.10}$$

Substituting the first equation of Eq. (4.4), the Z_1 in the above equation and separating the special integrals $\mathcal{I}(Z_2(0))$ and $\mathcal{I}(Z_2(1))$, it gives:

$$\int_0^{\tau_{1,F}} (-\lambda_1 \frac{Z_1}{Z_2} - \lambda_2 + F\frac{\sqrt{Z_1}}{Z_2}) d\tau_1 = \mathcal{I}(Z_2(0)) - \mathcal{I}(Z_2(1)) \tag{4.11}$$

Z_1 can be expressed with respect to Z_2 according to the SIM function. If $Z_2(\tau_1)$ is treated as a time variable, it leads to failure to integrate the right side of Eq. (4.10), However, the case of damping without excitation provides a simpler way to calculate this hardly-separate integral term, if $Z_2(\tau_1)$ is equal to a constant, $Z_{2,c}$. The subsequent numerical calculation results will verify the validity of this hypothesis. Although the energy pumping time of the transient response and harmonic excitation cases are not the same, the average value of Z_2 is almost identical. ($Z_{2,c}$, $Z_{1,c}$) represents the equivalent point (state) in the amplitude decline process along with the SIM. So the energy pumping time for the harmonic excitation case $\tau_{1,F}$ can be obtained as

$$\tau_{1,F} = \frac{Z_{2,c}(\mathcal{I}(Z_2(0)) - \mathcal{I}(Z_2(1)))}{-\lambda_1 Z_{1,c} - \lambda_2 Z_{2,c} + F\sqrt{Z_{1,c}}} \tag{4.12}$$

Figure. 4.2 is presented to better understand the calculation procedure of energy pumping time for a harmonic excitation case. Firstly, the parameters of the system, for example, ϵ, λ_1, λ_2 and K and δ, are required for the determination of the geometry of the SIM. The height of initial state is chosen by the usually maximum absolute value of Z_1 of phase trajectory in a given SMR cycle. Meanwhile, end state is referred to as a singularity of the right stable branch of the SIM, which is already fixed in the first step ($Z_2(1) = Z_{2,2}, Z_1(1) = Z_{1,2}$). So, in the second step, the difference between initial state and end state is decided. $Z_{2,c}$, and special state integral terms $\mathcal{I}(Z_2(0))$ and $\mathcal{I}(Z_2(1))$ for the transient response case are still the foundation of the estimation of pumping time with harmonic excitation in the third step. In the fourth step, the average value $Z_{2,c}$ and $Z_{1,c}$ and the other two state integrals are re-substituted into Eq. (4.12) to finally solve $\tau_{1,F}$.

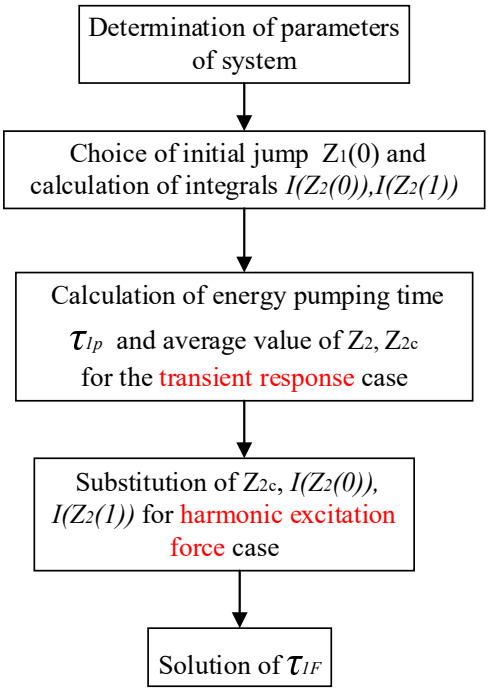

Figure 4.2: Flow diagram of the calculation of energy pumping times for harmonic excitations

4.2 Influence of parameters on transient response

From Eq. (4.9), it is clear that the energy pumping time depends on the initial position of the SIM right branch. The pumping time of various energy levels is compared by both numerical and analytical methods to demonstrate the correctness of the analytical prediction. When LO is applied by various but sufficiently intensive impulse excitations, the trajectory has a snap-through motion and immediately jumps to the right stable branch of the SIM, where NES is governed by 1:1 resonance and vibrates in the vicinity of the natural frequency of LO. The initial quantitative conditions of Z_1 needed to trigger an efficient dissipation of energy have been discussed [Nguyen et Pernot, 2012]. The influence of damping λ_2, cubic nonlinearity parameter K and negative stiffness δ are considered in the following subsection in order to optimize the energy dissipation rate. The whole of the following simulation development is based on parameter sets for $\epsilon = 0.01, \lambda_1 = 1.67, \lambda_2 = 0.167, \delta = -0.44, K = 1742$. And the parameters to be studied can be varied.

4.2.1 Influence of initial heights

Figure. 4.3 presents two typical examples of energy pumping from LO to NES. The Wavelet transform (WT) results show that the dominant frequency equals the natural frequency of the LO. The NES performs 1:1 resonance occupying the whole TET period. So the energy pumping time is defined as the moment that the yellow bar disappears, which means that the trajectory crosses the end state $(Z_2(1), Z_1(1))$ in Fig. 4.1.

Considering the variety of initial heights $Z_1(0)$, a new variable is proposed to measure the velocity of descent, which is shown in Fig. 4.4b. The trajectory oscillates and slips along the right branch; $V_{\tau p}$ shows the average velocity of slow flow descent.

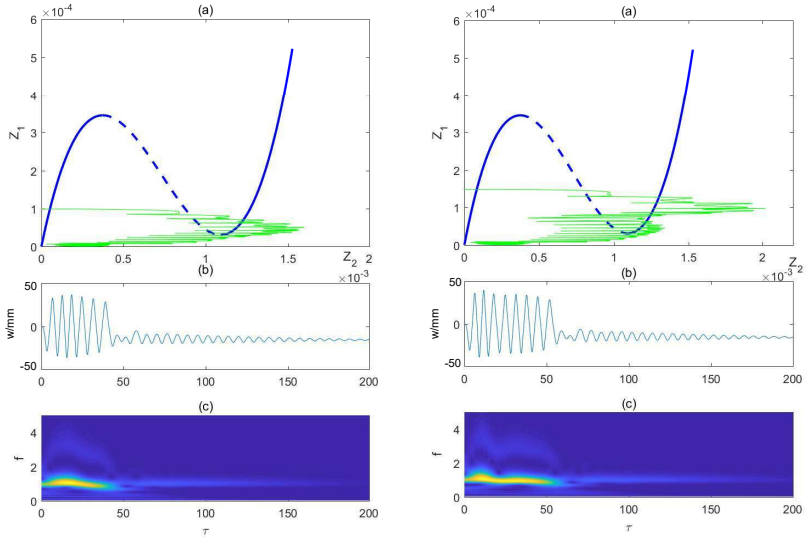

Figure 4.3: Transient TET of different input energies. left: $Z_1(0) = 1e-4$, right: $Z_1(0) = 1.75e-4$ (a) phase trajectory (green) together with SIM (blue), (b) time-domain displacement of NES, (c) frequency distribution of NES vibration, for $\epsilon = 0.01, \lambda_1 = 1.67, \lambda_2 = 0.167, \delta = -0.44, K = 1742$

$$V_{\tau p} = \frac{Z_1(0) - Z_1(1)}{\tau_p} \tag{4.13}$$

The energy pumping time by simulation is presented in line with dots in Fig. 4.4a. As the initial height $Z_1(0)$ increases while the end state $((Z_2(1), Z_1(1)) = (1.09\text{e-}3, 3.052\text{e-}5))$ keeps constant, the time that it requires for the system's trajectory to reach the end state also rises. The relatively high energy input case simulation always causes a more significant value than the analytical prediction. The time required to descend is proportional to the difference between the initial state and end state in Z_1 direction, which explains the phenomenon that the rate of descent remains essentially constant for different energy inputs in Fig. 4.4b. So it is concluded that the rate of decline of Z_1 is mainly determined by the system parameters and is independent of the impulsive input energy value (above the threshold energy for triggering the TET).

4.2.2 Influence of damping

The previous subsection briefly revealed that λ_2 has an essential impact on $V_{\tau p}$. However, the modification of λ_2 also results in a change of shape of the SIM, which is presented in Fig. 4.5a. An impact $Z_1(0) = 1.5e-4$ is assumed to be applied to the system so that this mid-energy maintains the error of analytical prediction at an acceptable level in different damping conditions.

As λ_2 increases, the end state, moves upwards. This implies that the system possesses a higher critical LO amplitude when the TET disappears. The path between the initial height $Z_1(0)$ and the end height $Z_1(1)$ decreases, which helps systems to terminate TET in a shorter time. In addition to the shortening of the path, damping affects the duration

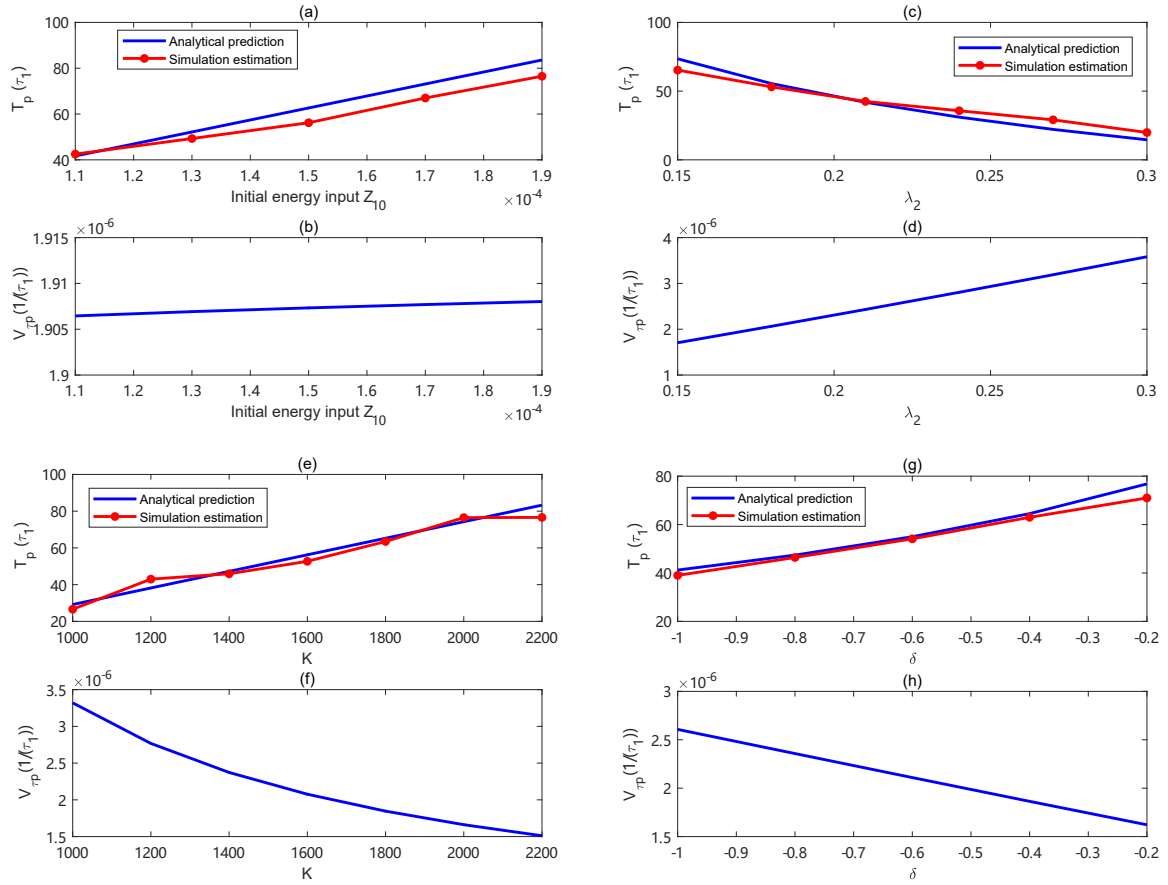

Figure 4.4: Influence of parameters on the energy pumping time and the velocity of descent. (a, c, e, g) analytical prediction and simulation results, (b, d, f, h) descent rate.

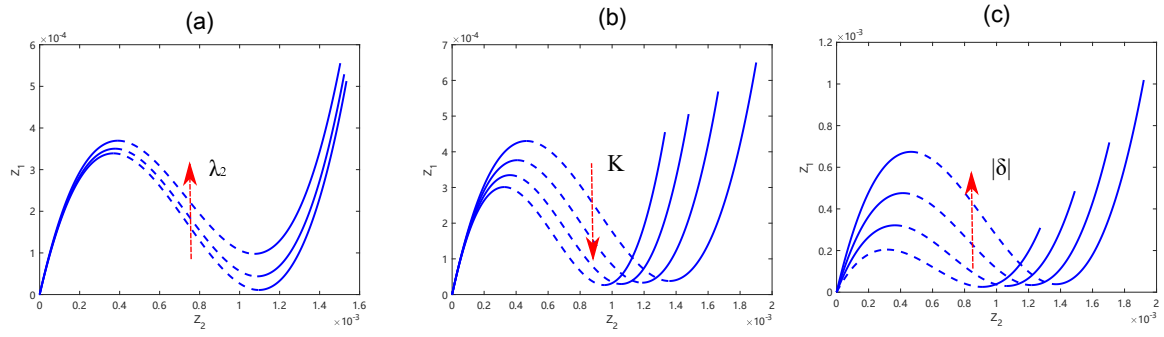

Figure 4.5: Modification of SIM shape under various (a) λ_2 (0.1, 0.2, 0.3) (b) K ([1400, 1600, 1800, 2000]) (c) δ ([-0.05 -0.3 -0.55 -0.8]). Arrow indicates the case with the largest (absolute) values of corresponding parameters.

of the TET. According to Eq. (4.4), a higher value of λ_2 enhances the rate of descent. With shorter paths and greater damping value, the energy pumping time is apparently reduced in Fig. 4.4c, and the average descent rate increases linearly with higher λ_2 in Fig. 4.4d.

Through the second equation of Eq. (4.4), the both parts $\lambda_1 Z_1$ and $\lambda_2 Z_2$ contribute to the descent rate. When the Z_{2c} is selected, whose values are almost constant during the different descent process, about 1.14e-3, for case $\lambda_2 = 0.167$ and initial state $Z_1(0) = 1.5$e-4. The corresponding Z_1 value in SIM right branch is 3.55e-5. The different contribution of damping part is calculated that $\lambda_1 Z_1 = 0.6$e-4 and $\lambda_2 Z_2 = 1.9$e-4. The latter component governs mainly the decent rate value due to its larger value. To maximise the descent rate in transient response, increasing the λ_2 value can be an alternate and effective way. However, it also causes the LO optimal design to have a larger stable response amplitude in harmonic excitation.

4.2.3 Influence of cubic nonlinearity parameter and negative stiffness

To investigate the role of cubic nonlinearity parameter K and negative stiffness δ, the energy pumping times and corresponding descent rates are presented in Fig. 4.4(e-h). The system has the same initial impact as in the previous investigation $Z_1(0) = 1.5$e-4. Firstly, increasing the value of the cubic nonlinearity parameter and negative stiffness causes the SIM to change shape in the direction of the arrow in Fig. 4.5b,c. The final state rises, reaching a larger value of $Z_1(1)$, which means a shorter path to cross. So the energy pumping time is shorter in the case of smaller cubic nonlinearity parameter K. According to the previous description, the equivalence point is located near the end state, and an increase in K allows the equivalence point to have a smaller $Z_{1,c}, Z_{2,c}$. Equation. (4.4) indicates that the smaller $Z_{1,c}, Z_{2,c}$ values lead to a decrease in instantaneous velocity. So the decrease in average velocity with increasing K design can be explained.

When the absolute value of δ rises while the value of K remains constant, the final state, in the SIM structure moves in the direction of a higher $Z_2(1)$ value. Meanwhile, $Z_1(1)$ slightly increases while δ varies in Fig. 4.5c. The decrease in the average descent rate is due to the smaller $Z_2(1)$ value of the end state. So, systems with smaller absolute δ values take a longer time to dissipate energy in Fig. 4.5g. The variation in the descent rate is almost linearly related to the change in δ in Fig. 4.4h. This feature is not the same as the quadratic decrease in decay rate as K increases. The analytical prediction shows a good fit of results in the middle interval of the δ range. In a small negative stiffness case, the analytical result is larger than the simulated value.

It can be concluded that the energy pumping time depends on the modification of the SIM shape. The rate of decline of the system is mainly due to the effect of K, δ on the position of the end state (singularity point) of the SIM, which causes the average Z_1, Z_2 values to ultimately change the average velocity.

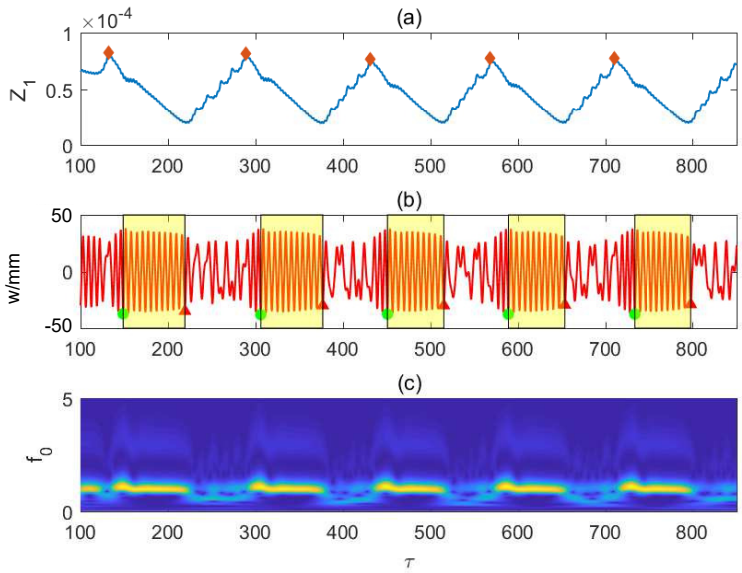

Figure 4.6: Time-displacement of (a) Z_1, (b) w and (c) WT for w. The intervals of energy pumping time are identified and marked in yellow shaded areas

4.3 Influence of parameters on harmonic excitation response

4.3.1 Various initial heights

The parameters of a bistable NES for the numerical simulation are classified as modest ones. The negative stiffness introduces chaos behaviours and the snap-through motion is triggered by the chaos. The initial height $Z_1(0)$ at which the phase trajectory begins to descend is different and unpredictable for each complete SMR cycle. The various maximum local values of Z_1 are marked with the diamond dots in Fig. 4.6a. These different Z_1 values are used as the initial height $Z_1(0)$ of descent to predict the energy pumping time for each SMR cycle.

The energy pumping process describes how the energy of LO is transferred into NES and dissipated by the damping. Energy pumping is referred to as the phase trajectory descends along the righ SIM stable branch and does not include snap-through motion. So the energy pumping time is counted from the moment the NES amplitude reaches its maximum and ends when the NES re-enters chaos. In other words, it implies a phase in which the amplitudes of LO and NES drop simultaneously. The interval of energy pumping time in each SMR cycle is identified in Fig. 4.6.

Based on the calculation process in the excitation case and initial Z_1 value, the predicted pumping time can be calculated, and is summarized in Tab. 4.1, where the unit of $Z_1(0)$ is 1e-5. $\tau_{0,a}$ are the analytical energy pumping times. $\tau_{0,s}$ are the simulated values, which are calculated by time intervals marked in Fig. 4.6b.

Both $\tau_{0,a}$ and $\tau_{0,s}$ are in the fast time scales τ_0. The expression of energy pumping time gives an estimation in slow time scales τ_1. To convert it into fast time scale τ_0, a simple relationship $\tau_1 = \epsilon\tau_0$ is applied according to the definition in multiple scales method.

Each interval starts with a green dot and ends with a red triangle. E_r means the

Table 4.1: Pumping time estimation for same amplitude input G = 0.3mm

$Z_1(0)$/1e-5	8.22	8.15	7.70	7.73	7.75
$\tau_{0,s}$	70.6	70.7	64.3	64.4	64.7
$\tau_{0,a}$	69.4	68.4	62.6	62.9	63.2
$E_r(\%)$	1.73	3.36	2.72	2.38	2.37

Table 4.2: Average pumping time estimation for various energy inputs

G (mm)	0.25	0.275	0.3	0.325	0.35
$\overline{Z_1(0)}$/1e-5	7.23	8.052	8.04	8.23	8.075
$\overline{\tau_{0,s}}$	39.1	57.35	68.67	83.42	104.64
$\overline{\tau_{0,a}}$	39.8	55.42	67.02	87.58	115.56
$E_r(\%)$	-1.76	3.5	2.46	-4.75	-9.45

relative error between $\tau_{0,s}$ and $\tau_{0,a}$. From an intuitive point of view, a higher initial $Z_1(0)$ causes a greater distance to slide down, when the end state $Z_1(1)$ is fixed by the same SIM structure. So a longer energy pumping time is required for the same energy input level. The analyzed values are smaller than the simulated values. An error of less than 5% between the two values can be accepted. When predicting energy pumping time, this semi-analytical method is robust with respect to the uncertainty of initial height $Z_1(0)$ caused by chaos.

4.3.2 Various excitation amplitudes

The initial height $Z_1(0)$ for each SMR changes as time varies. So, to compare the influence of energy input levels, the average Z_1 value is chosen within a time interval of [0,1000](τ). The excitation interval is selected in the range [0.25mm,0.35mm] to ensure the occurrence of SMR, for which the interval of occurrence is numerically [0.22mm, 0.44mm].

For each excitation case, the initial height $Z_1(0)$ where each SMR starts to descend is different. To calculate the average initial height $Z_1(0)$, a time interval of response, which contains 5 complete SMR cycles, is selected. The upper line of $\overline{Z_1(0)}$, $\overline{\tau_{0,s}}$ and $\overline{\tau_{0,a}}$ in Tab. 4.2 represents the average value of the corresponding parameter in these five SMR cycles. This method of calculating the mean height and the mean time was also applied in the study of the relationship between descent rate and negative stiffness.

Although the perturbation exists in the average initial height (average $Z_1(0)$ does not increase for a higher input energy in the second line of the Tab. 4.2), the extension of the analytical and simulated pumping time shows a strong relationship with increasing excitation. Increasing the amplitude of the excitation leads both the simulated and analytical energy pumping times to show an increasing tendency in Tab. 4.2. When the system is maintained at a low energy input, the error level is perturbed but is acceptable. However, the analytical result is larger than the simulated value in a high energy case, G = 0.35mm. In the transient response, the high energy state also leads to a similar error distribution, i.e., a large analytical value, and a more significant excitation results in failure of the method. So low or modest energy inputs are necessary to ensure the

Table 4.3: Pumping time estimation for various negative stiffness cases

$k_3(N/m^3)$	-25	-50	-75	-100	-125
$\overline{Z_1(0)}$	8.86	8.04	9.34	1.12	1.04
$\overline{\tau_{0,s}}$	108.85	68.67	56.82	53.76	37.84
$\overline{\tau_{0,a}}$	122.5	67.02	58.52	57.74	39.93
$E_r(\%)$	-11.1	2.46	-2.9	-6.9	-5.23

validation of this method.

4.3.3 Various negative stiffness cases

Five cases with different negative stiffness values are examined further to investigate the robustness under various negative stiffness designs under the same amplitude excitation G = 0.3mm. Like various energy input cases, the average energy pumping times, obtained by numerical and semi-analytical methods, are compared in Tab. 4.3. With the variation of δ, the perturbation in average initial height $Z_1(0)$ becomes more severe. As the $|\delta|$ declines, more time is needed to dissipate the same energy input level. In the transient response case, the larger value of $|\delta|$ causes the deformation of the SIM structure, where the end state moves to a position with higher value of $Z_2(1)$ and $Z_1(1)$. So the equivalent point, which is close to the end state in the SIM structure, has a more significant value. This variation significantly improves the decline rate, regardless of the initial height $Z_1(0)$ perturbation by Eq. (4.4).

A bigger value of negative results in a faster dissipation ratio also leads to a larger harmonic excitation amplitude threshold to trigger the SMR. The analytical prediction is always larger than the simulated value. A more significant error is found in a weak bistable NES that still conserves some characteristics of a cubic NES, where the snap-through motion is triggered by crossing the singularity of SIM instead of being triggered by chaos. The modest bistable NES (k_3 = -50N/m or -75N/m) shows the errors below 5% and confirms that this method predicts the energy pumping time more accurately in the modest bistable NES case.

4.3.4 Validation of assumption

During the TET, $Z_{2,c}$ is almost constant, and it can be observed that the NES amplitude remains constant in Fig. 4.6 for each energy pumping period. The initial assumption of $N_1(\tau_1)\cos(\delta_1(\tau_1)) = \sqrt{Z_1}$ is a prerequisite for the semi-analytical method. Acquiring exact expressions of integrals is challenging, but the two sides of the equation are equivalent in the integration process. To better demonstrate this point, a numerical example for case G = 0.3mm ($\sigma = 0$) can provide an explanation.

When the initial maximum $Z_1(0)$ is equal to 8.15e-5, the distance in the Z_1 direction, between initial states and end state, ΔZ_1 is -5.1e-5. The analytical energy pumping time $\tau_1 = \epsilon\tau_0 = 0.684$. The positions of the equivalent points are $Z_{1,c}$ = 3.54e-05, $Z_{2,c}$ = 1.14e-3, which is close to the final state. Substituting these parameters into the second equation of (4.4), the average value of $N_1(\tau_1)\cos(\delta_1(\tau_1))$ during the whole TET equals

5.83e-3, while $\sqrt{Z_{1,c}}$ equals 5.95e-3. The approximation produces an error level on the integral of 2%.

Although the other parameters, for example, excitation amplitude and negative stiffness, also influence the accuracy of integral, the good agreements between simulation results and analytical predictions verify the equivalence of integrals. Thus, the following equation is valid during the energy pumping time.

$$\frac{1}{\tau_1}\int_0^{\tau_1} N_1(\tau_1)\cos(\delta_1(\tau_1))d\tau \approx \sqrt{Z_1}|_{Z_1=Z_{1,c}} \tag{4.14}$$

4.4 Experimental validation

The experiment set-up is the same as the previous study with adjusting the pre-compression length to maintain a new modest bistable NES. The parameters of the system are presented in Tab. 4.4. Since the excitation is provided by 10KN electrodynamic shaker, the frequency of excitation is in the natural frequency (f_0 = 7.27Hz) of the LO.

The system is applied with two low excitations, G = 0.21mm and 0.25mm. In both cases, the bistable NES starts to perform SMR, which is presented in Fig. 4.7. According to the previous definition of energy pumping, which counts from the time the NES reaches its maximal amplitude to when the NES re-enters the chaotic state, the time instants are also marked in the figure. In the numerical simulation, the start point of $Z_1(0)$ is obtained by the time displacement of LO. However, Z_1 is expressed as a real part of complex variable $\phi_1(\tau)$, which cannot be recorded directly. From the perspective of a mechanical interpretation, the Z_1 approximately equals the square of the LO amplitude. So, the initial $Z_1(0)$ in the starting point is selected as the square of maximal LO displacement.

The energy pumping times of both excitation cases are calculated in Tab. 4.5, where $t_{e,p}$ and $t_{a,p}$ are the experimental and analytical energy pumping times. In the lower energy input case (G = 0.21mm), the analytical prediction time is always shorter than the experimental observation. This is also the case for the comparison with simulation, where the analytical value is always lower than the simulated one, for example, G = 0.3mm in Tab. 4.2. The variation of value of the initial height $Z_1(0)$ occurs because chaos motion triggers the snap-through motion, so the maximal LO amplitude is unpredictable and it is hard to reach the same level for each SMR cycle. The analytical prediction can estimate the energy pumping time to the same order of magnitude.

In a higher energy input case (G = 0.25mm), in Fig. 4.7c-d, the initial start point also possesses a higher position than that of lower energy inputs. It also causes a need for longer pumping time to dissipate energy. The overestimation occurs in the case of initial height $Z_1(0)$ = 4.7e-5. This can be considered as the failure of the analytical estimation method. In the high energy input cases of harmonic excitation, for example, G = 0.35mm in Tab. 4.2, a high initial start point causes a larger error. This confirms that our analytical prediction provides a better fit for the low energy level input. If this

Table 4.4: Experimental parameters of environment

Reduced parameters	ϵ	λ_1	λ_2	K	δ
	0.91%	2.18	0.24	6.65e3	-1.05

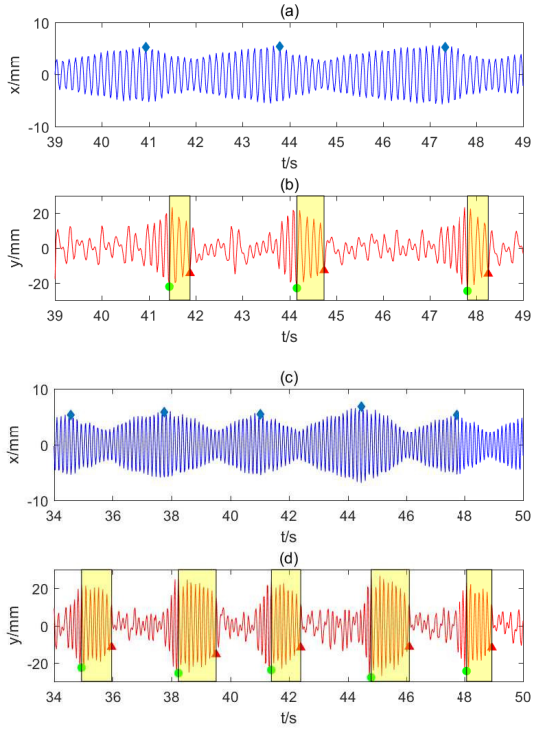

Figure 4.7: Experimental time-displacement result of bistable NES and LO (a) (b) for excitation G = 0.21mm, (c) (d) for G = 0.25mm. The intervals of energy pumping time are identified and marked in yellow shaded areas

Table 4.5: Experimental results of energy pumping time in G = 0.21 and 0.25mm cases.

G (mm)	0.21			0.25				
$Z_1(0)$/1e-5	2.80	3.0	2.76	2.9	3.44	3.01	4.7	2.88
$t_{e,p}$/s	0.44	0.58	0.44	1.02	1.28	1.00	1.30	0.86
$t_{a,p}$/s	0.32	0.44	0.29	0.88	1.6	1.02	3.3	0.84

invalid data is excluded, the remaining mean error on the corresponding predicted values against the experiment is reduced to 4%.

4.5 Conclusions

This study focuses on the adapted method based on the Slow Invariant Manifold (SIM) structure to predict the energy pumping time of a bistable NES under the transient impulsive excitation and harmonic excitation. The calculation process has been presented to examine the robustness of prediction. The factors affecting the rate of amplitude decrease have been analyzed for the transient and harmonic excitation cases. Several main conclusions can be drawn:

1. To estimate the duration of energy pumping time in a damping and harmonic excitation case, the Hamiltonian system is considered first. The equivalent point,

obtained by a damped, transient impulsive system, is essential for energy pumping time calculation under harmonic excitation.

2. The influences of parameters (initial state, cubic nonlinearity parameter, negative stiffness, damping and excitation amplitude) are investigated for both transient response and harmonic excitation. Due to the chaos behaviours, the robustness of the semi-analytical method is tested and proved to be strong enough under parameter perturbation. A larger NES damping λ_2, lower cubic nonlinearity parameter K or larger negative stiffness $|\delta|$ enhance the dissipation rate by modifying the structure of the SIM and the corresponding equivalent point position. Energy input level does not affect the Linear Oscillator (LO) amplitude decay rate in transient case.

3. A particular approximation of complex integration offers the possibility to calculate the energy pumping time for every Strongly Modulated Response (SMR) cycle. Due to the chaos motion, every initial starting point is different. The numerical and experimental results prove the robustness of the calculation method with respect to initial state and excitation. This prediction method shows good potential for predicting the energy pumping time in a low energy state.

CHAPTER 5

Targeted energy transfer in vibro-impact cubic NES

Abstract

This chapter mainly investigates the response regimes of a novel Nonlinear Energy Sink (NES) that couples both nonlinearities: cubic nonlinearity and impact, and gives the optimal criteria. With the non-smooth condition, the conventional Multiple Scales Method (MSM) has to be added impact condition. According to the clearance lengths, three types of Vibro-Impact Cubic (VIC) NES are described. By identifying the occurrence of the collision, the asymptotic analysis of the equivalent cubic NES model and Vibro-Impact (VI) NES model can illustrate the fixed point of VIC NES. The role of clearance length on the response regimes has been given and offers criteria for the optimal design. Combined with the simulation results, the experiment result proves the restraint effect of impact on the emergence of Strongly Modulated Response (SMR).

Contents

5.1 Dynamic modeling

Most current studies primarily consider the single nonlinear component effect. In fact, due to manufacturing and assembly errors, cubic NES devices often introduce other constraints—such as displacement restrictions—which can lead to tight, rigid constraint collisions. The coupling effect of multiple nonlinearities remains a significant challenge. The cubic NES involved in the impact effect has been studied for transient response and is known as Vibro-Impact Cubic (VIC) NES [Wei *et al.*, 2018]. The energy percentage ceases dramatically while energy percentage of normal optimal NES possesses a longer time for resonance capture. Even in a low energy input case, which is not intensive enough to activate the Targeted Energy Transfer (TET) for normal NES, the VIC NES can still dissipate the energy with a very high efficiency. Farid described the VIC NES as a Hybrid Cubic Vibro-Impact (HCVI) NES for harmonic excitation [Farid, 2021], applying a canonical transformation to the Action-Angle (AA) variables to describe the response regimes in VIC NES. Two types of bifurcations were identified, respectively describing the impact boundary and critical maximal transient energy level.

So, to model the cubic NES with impact condition, the diagram of VIC NES is presented in Fig. 5.1. The NES mass m_2 is coupled with a cubic nonlinearity k_2 and linear damping c_2. The NES mass can only move in the cavity. The clearance length on each side of the NES is bilateral and equals b. The m_1, c_1 and k_1 are the mass, viscous damping, and linear stiffness of the Linear Oscillator (LO), respectively. This two-DOFs system is applied by a harmonic excitation $x_e = Gcos(wt)$. The governing equation and impact condition yield:

$$\begin{aligned} &m_1\ddot{x} + k_1 x + c_1\dot{x} + c_2(\dot{x} - \dot{y}) + k_2(x - y)^3 = k_1 x_e + c_1\dot{x}_e \\ &m_2\ddot{y} + c_2(\dot{y} - \dot{x}) + k_2(y - x)^3 = 0 \\ &\forall |x - y| < b \end{aligned} \tag{5.1}$$

where x and y represent the absolute displacement of the LO and NES, respectively. When the impact $|x - y| = b$ occurs, the instant displacements of the LO and NES remain constant, as does the velocity of LO. However, non-smooth dynamics bring about a sudden change in the value of the velocity of NES, as well as its direction before and after impact. This kind of non-smooth behavior entails a loss of energy. The actual velocity loss is more complex; the specific technical tool required to handle this kind of

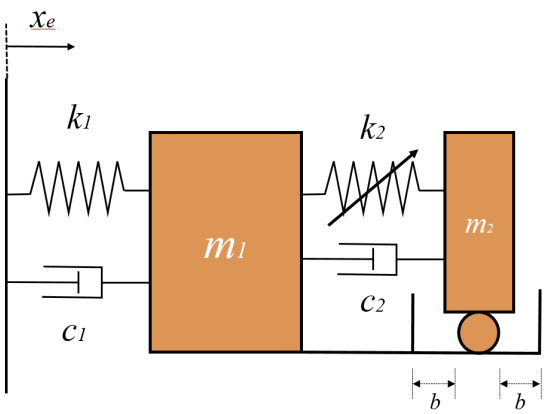

Figure 5.1: Diagram of Linear Oscillator (LO) the Vibro-Impact Cubic (VIC) NES system

inelastic impact is developed [Pilipchuk, 2015] to form closed-form analytical solutions that automatically satisfy collision conditions with the energy loss. However, these simplified shock assumptions have been proven effective and useful in many VI NES problems [Reboucas *et al.*, 2018 ; Li *et al.*, 2017b]. The condition of total momentum conservation gives the following equations for $|x-y|=b$:

$$\begin{aligned} x^+ &= x^-, \dot{x}^+ + \epsilon\dot{x}^+ = \dot{y}^- + \epsilon\dot{y}^- \\ y^+ &= y^-, \dot{x}^+ - \epsilon\dot{x}^+ = -r(\dot{y}^- - \epsilon\dot{y}^-) \end{aligned} \tag{5.2}$$

where r is the restitution coefficient (with a value between 0 and 1). The + and – superscripts represent the system parameter after and before impact. By introducing the rescaled variables Eq. (5.3) and substituting the new variables $v = x + \epsilon y$ and $w = x - y$, the corresponding dimensionless equations are expressed in Eq .(5.4).

$$\begin{aligned} \epsilon &= \frac{m_2}{m_1}, \omega_0^2 = \frac{k_1}{m_1}, K = \frac{k_2}{m_2\omega_0^2}, \lambda_1 = \frac{c_1}{m_2\omega_0}, \\ \lambda_2 &= \frac{c_2}{m_2\omega_0}, F = \frac{G}{\epsilon}, \Omega = \frac{\omega}{\omega_0}, \tau = \omega_0 t \end{aligned} \tag{5.3}$$

$$\begin{aligned} &\ddot{v} + \epsilon\lambda_1\frac{\dot{v}+\epsilon\dot{w}}{1+\epsilon} + \frac{v+\epsilon w}{1+\epsilon} = \epsilon F\cos\Omega\tau \\ &\ddot{w} + \epsilon\lambda_1\frac{\dot{v}+\epsilon\dot{w}}{1+\epsilon} + \frac{v+\epsilon w}{1+\epsilon} + \lambda_2(1+\epsilon)\dot{w} + K(1+\epsilon)w^3 = \epsilon F\cos\Omega t \\ &\forall |w| < b \end{aligned} \tag{5.4}$$

The cavity limits the displacement of the NES with respect to the LO to no more than b. Thus, the impact condition for $|w| = b$ can be re-written as

$$\begin{aligned} v^+ &= v^-, \dot{v}^+ = \dot{v}^- \\ w^+ &= w^-, \dot{w}^+ = -r\dot{w}^- \end{aligned} \tag{5.5}$$

The Manivitch complex variables are presented to separate the fast oscillation components $e^{i\Omega\tau}$ and the slowly invariant amplitude components $\phi_j(\tau), j = 1, 2$, where i is the imaginary unit.

$$\begin{aligned} \phi_1(\tau)e^{i\Omega\tau} &= \frac{d}{d\tau}v(\tau) + i\Omega v(\tau) \\ \phi_2(\tau)e^{i\Omega\tau} &= \frac{d}{d\tau}w(\tau) + i\Omega w(\tau) \end{aligned} \tag{5.6}$$

To avoid secular terms, only terms with $e^{i\Omega\tau}$ are kept. The slow modulated system is obtained in Eq. (5.7).

$$\begin{aligned} &\dot{\phi}_1 + \frac{i\Omega}{2}\phi_1 + \frac{\epsilon\lambda_1(\phi_1+\epsilon\phi_2)}{2(1+\epsilon)} - \frac{i(\phi_1+\epsilon\phi_2)}{2\Omega(1+\epsilon)} - \frac{\epsilon F}{2} = 0 \\ &\dot{\phi}_2 + \frac{i\Omega}{2}\phi_2 + \frac{\epsilon\lambda_1(\phi_1+\epsilon\phi_2)}{2(1+\epsilon)} - \frac{i(\phi_1+\varepsilon\phi_2)}{2\Omega(1+\epsilon)} + \frac{\lambda_2(1+\epsilon)\phi_2}{2} - \frac{3iK(1+\epsilon)\phi_2^2\phi_2}{8\Omega^3} - \frac{\epsilon F}{2} = 0 \\ &\forall |Imag(\phi_2 e^{i\tau})| < \Omega b \end{aligned} \tag{5.7}$$

$\overline{\phi_2}$ is the conjugate value of ϕ_2, while $Imag(\phi_2)$ represents the imaginary part of ϕ_2 (i.e. the displacement component). The impact condition at the moment η is expressed with simple algebraic operations:

$$\begin{aligned}&\phi_1(\eta^-) = \phi_1(\eta^+)\\&\frac{\phi_2(\eta^+)\overline{\phi_2}(\eta^+) - b^2}{\phi_2(\eta^-)\overline{\phi_2}(\eta^-) - b^2} = r^2\end{aligned} \tag{5.8}$$

By applying the multiple scales method, the solution $\phi_j = \phi_j(\tau_0, \tau_1, \ldots)$ is expressed by the fast time scale $\tau_0 = \tau$ and the slow time scale $\tau_1 = \epsilon\tau$. The system of Eq. (5.7) is now examined for different orders of ϵ.

Order ϵ^0:

$$\begin{aligned}&\frac{\mathrm{d}}{\mathrm{d}\tau_0}\phi_1 = 0\\&\frac{\mathrm{d}}{\mathrm{d}\tau_0}\phi_2 + \frac{1}{2}i(\phi_2 - \phi_1) + \frac{1}{2}\phi_2\lambda_2 - \frac{3}{8}iK\phi_2^2\overline{\phi}_2 = 0\\&\forall|Imag(\phi_2 e^{i\tau_0})| < \Omega b\end{aligned} \tag{5.9}$$

Order ϵ^1:

$$\begin{aligned}&\frac{\partial}{\partial\tau_1}\phi_1 + \frac{i}{2}(\phi_1 - \phi_2) + i\sigma\phi_1 + \frac{\lambda_1}{2}\phi_1 - \frac{F}{2} = 0\\&\frac{\partial}{\partial\tau_1}\phi_2 + \frac{i}{2}(\phi_1 - \phi_2) + \frac{i\sigma}{2}(\phi_1 + \phi_2) + \frac{\lambda_1}{2}\phi_1 + \frac{\lambda_2}{2}\phi_2 - \frac{3iK(1-3\sigma)}{8}\phi_2^2\overline{\phi_2} - \frac{F}{2} = 0\end{aligned} \tag{5.10}$$

In the order ϵ^0 equation, ϕ_1 is independent of the slow time scale τ_0 and the excitation terms disappears. The new variables $\phi_1(\tau_1) = N_1 e^{i\delta_1}$ and $\phi_2(\tau_1) = N_2 e^{i\delta_2}$ are introduced to extract its topological structure, known as Slow Invariant Manifold (SIM), yielding:

$$\begin{aligned}&Z_1 = Z_2\lambda_2^2 + Z_2 - \frac{3K}{2}Z_2^2 + \frac{9K}{16}Z_2^3\\&Z_1 = N_{10}^2, Z_2 = N_{20}^2\end{aligned} \tag{5.11}$$

N_{10} and N_{20} are the periodic solution of N_1 and N_2. The two singularity points $Z_{2,j}, j = 1, 2$ divide the SIM into a left–right stable branch and a middle unstable branch in Fig. 5.2.

When displacement constraints are present, the periodic solutions of the system behave differently from the unconstrained case. The extra periodic solution is considered to be introduced by an extra singularity value $Z_{2,e}$. This kind of singularity is independent of $Z_{2,j}$ and is determined by the clearance length. Consequently, it is natural to consider the different $Z_{2,e}$ locations in the SIM structure.

$$\begin{aligned}&Z_{2,j} = N_{2,j}^2 = \frac{4(2 \mp \sqrt{1 - 3\lambda_2^2})}{9K}, j = 1, 2\\&Z_{2,e} = N_{2,e}^2 = b^2\end{aligned} \tag{5.12}$$

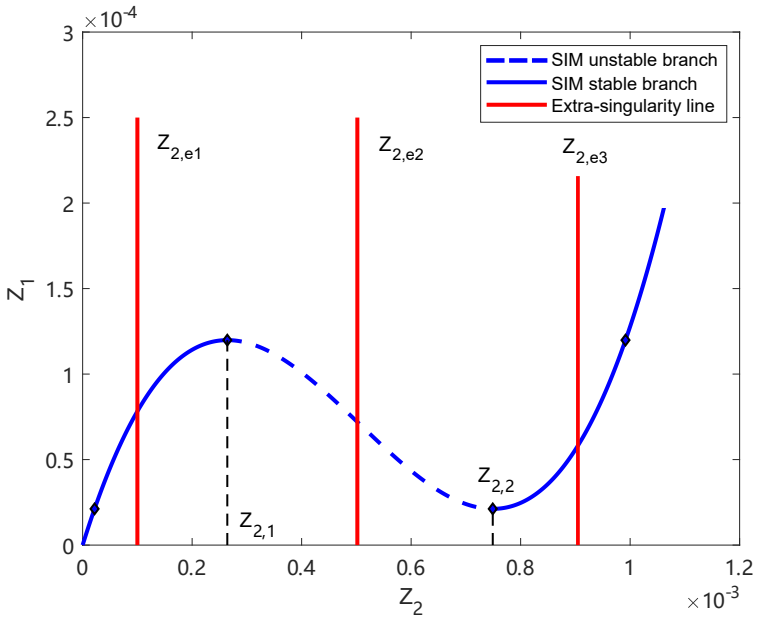

Figure 5.2: SIM of the VIC NES with three extra singularity lines (red) $Z_{2,e1}$ = 0.1e-3, $Z_{2,e2}$ = 0.5e-3, $Z_{2,e3}$ = 0.9e-3. The dashed blue line indicates the unstable region and the solid blue lines indicate the stable branches.

5.2 Response regimes

The location of the extra singularity line in the SIM structure affects the response regimes significantly. The three different clearance lengths are selected so that the $Z_{2,e1}$—possessing a narrow clearance—is located on the left stable branch. In the second case, the $Z_{2,e2}$ value lies within the interval $[Z_{2,1}, Z_{2,2}]$ and the extra singularity line is located in an unstable region. If the clearance length has a larger value, e.g. $Z_{2,e3}$, the extra singularity line will be located on the right stable SIM branch. The analysis of response regimes is developed according to this classification.

5.2.1 Narrow clearance case

If the clearance is relatively narrow (b = 10mm), the extra singularity line crosses the left stable branch at a critical point $(Z_{2,e1}, Z_{1,e1})$; the latter $Z_{1,e1}$ is easily obtained by substituting the $Z_{2,e1}$ into Eq. (5.11). The simulation parameters are fixed for $\epsilon = 0.01, \lambda_1 = 1.67, \lambda_2 = 0.167$ and $K = 1742$. The initial conditions for following simulations are same $v(0) = \dot{v}(0) = w(0) = \dot{w}(0) = 0$. In a low energy input case, the final stable amplitude of the NES is lower than b, which means that the NES oscillates in the cavity. In Fig. 5.3, the amplitude of both the NES and LO increase monotonically and ultimately reach a stable amplitude. In the subplot of Fig. 5.3c, the actual phase trajectory—indicated by the green line—also rises along the left branch SIM monotonically without coming into contact with the extra singularity line $Z_2 = Z_{2,e1}$.

Before the harmonic excitation amplitude causes the collision, the system behaviors can be analyzed with the framework of the cubic system. The fixed points of Eq. (5.7) are expressed as ϕ_{10}, ϕ_{20}. It is assumed that the imaginary part of ϕ_{20} is assumed to satisfy the displacement constraint with a low energy input. Solving the expression of ϕ_{10} in

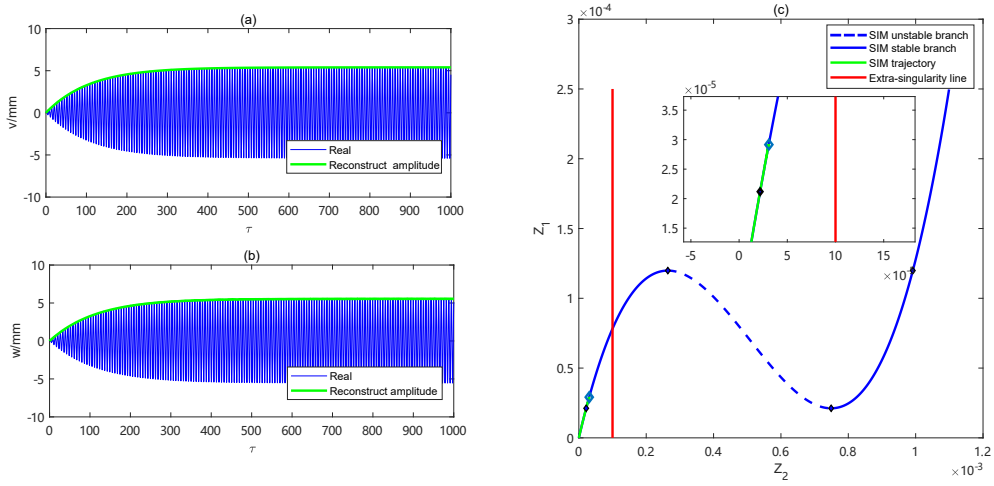

Figure 5.3: (a),(b) Time displacement response of v and w for narrow clearance case G = 0.1mm, $\sigma = 0$. The green envelopes represent the reconstructed amplitude, while the blue curves describe the time response (c) SIM structure. The green line represent the phase trajectory

the first equation of Eq. (5.7) and re-substituting it into the second equation of Eq. (5.7) yields the expression of ϕ_{20}. Simple algebraic operations lead to the more convenient equation, with detune parameter $\Omega = 1 + \epsilon\sigma$:

$$\begin{aligned} &\dot{\phi_1} = \dot{\phi_2} = 0, \rightarrow \phi_1(\tau) = \phi_{10}, \phi_2(\tau) = \phi_{20} \\ &\phi_{10} = \frac{\dfrac{i\epsilon\phi_{20}}{\Omega(1+\epsilon)} - \dfrac{\epsilon^2\lambda_1\phi_{20}}{1+\epsilon} + \epsilon F + i\epsilon^2\lambda_1 F\Omega}{i\Omega + \dfrac{\epsilon\lambda_1}{1+\epsilon} - \dfrac{i}{\Omega(1+\epsilon)}} \\ &\alpha_3 K^2 Z_{20}^3 + \alpha_2 K Z_{20}^2 + \alpha_1 Z_{20} + \alpha_0 F^2 = 0, \quad Z_{20} = |\phi_{20}|^2 \end{aligned} \tag{5.13}$$

The coefficients α_1, α_2 and α_3 are determined by the system parameters, which are same as Eq. (2.29) in the second chapter. When the collision occurs, the Z_{20} reaches the extra singularity line $Z_2 = b^2$. The corresponding threshold excitation G_c can be calculated with the third equation of Eq. (5.13). The excitation amplitude for impact is expressed in Eq. (5.14)

$$G_c = \epsilon F_c = \epsilon\sqrt{\frac{\alpha_3 K^2 b^6 + \alpha_2 K b^4 + \alpha_1 b^2}{-\alpha_0}} \tag{5.14}$$

Figure. 5.4 presents the analytical threshold excitation (surface) for various clearance designs, combined with the numerical calculations (red points). The dotted lines connect the analytical and numerical amplitude threshold and measure their differences.

When the excitation frequency equals the natural frequency of the LO ($\sigma = 0$), the required trigger excitation amplitude increases along with the clearance length design. A critical point $(Z_{2,e1}, Z_{1,e1})$ requires a more significant excitation amplitude—whose frequency is away from $\sigma = 0$—to trigger the collision conditions. When the excitation frequency is in the vicinity of its natural frequency, the resonance phenomenon will amplify the amplitude of the system, facilitating the collision condition for a low excitation

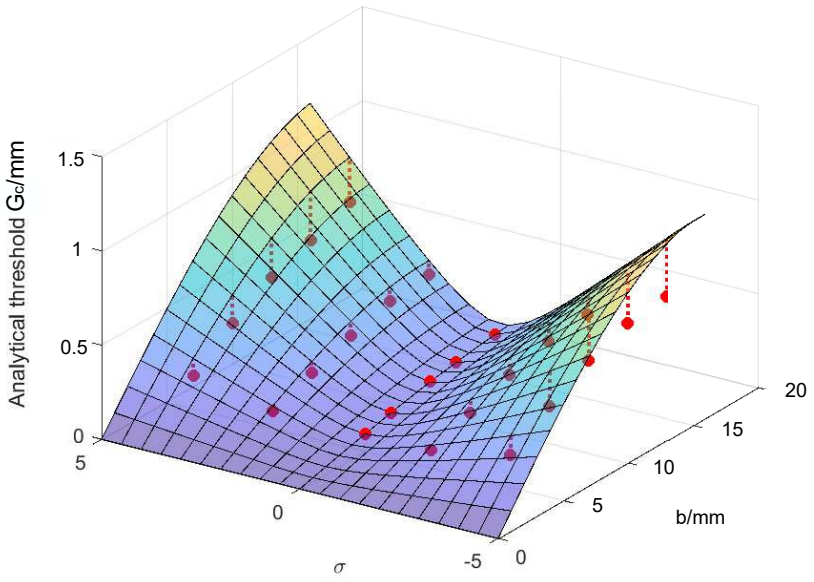

Figure 5.4: Analytical and numerical threshold of excitation for different clearance designs. The surface represents the analytical results. The red points are the numerical results and the red lines are the distance between numerical results and analytical results.

amplitude. The excitation threshold G_c grows significantly when the frequency is away from the $\sigma = 0$. In the vicinity of $\sigma = 0$, the amplitude threshold values predicted by Eq. (5.14) are located exactly on the surface. The error increases along with the lower or higher excitation frequency. A bigger clearance design also causes a larger prediction error (indicated by the longer red dotted line in Fig. 5.4).

It is worth mentioning that all the results resolved in this subsection are restricted to the case of narrow clearance. In this case, no SMR exists, and the impact's triggering is caused by the NES amplitude of a single fixed point exceeding b.

Once the excitation amplitude exceeds the threshold value $G_c = 0.17$mm for case $\sigma = 0$, the impact occurs. In Fig. 5.5, the occurrence of impact divides the response into two parts. At the beginning, the LO and NES oscillate with a continued increasing amplitude until the NES comes into contact the barrier. In this period, the reconstructed amplitude can accurately describe the variation of amplitude. The phase trajectory overlaps with the SIM branch and rises in the direction of the black arrow. Once the phase trajectory reaches the critical point $(Z_{2,e1}, Z_{1,e1})$, it starts oscillating and decreases along an extra singularity line. At this moment, the reconstructed amplitude cannot fit the time response of NES, for the reason that the $\dot{w}$ value can exceed $|b|$ and is not limited by the displacement constraint. The restitution coefficient r indicates the energy loss during the impact. This extra energy dissipation process leads to a decrease in the amplitude of the LO, instead of crossing the critical point $(Z_{2,e1}, Z_{1,e1})$ in a pure cubic case after the impact occurs. This discontinuity in velocity can be observed in Fig. 5.5c; quite similar to the pure VI NES, this discontinuity belongs to the period of two asymmetric impact per cycle.

When the NES oscillates in a small amplitude due to the displacement constraint, the local stiffness becomes extremely low near the equilibrium. The relatively low velocity of the NES also reduces the influence of the damping terms. Therefore, it is reasonable

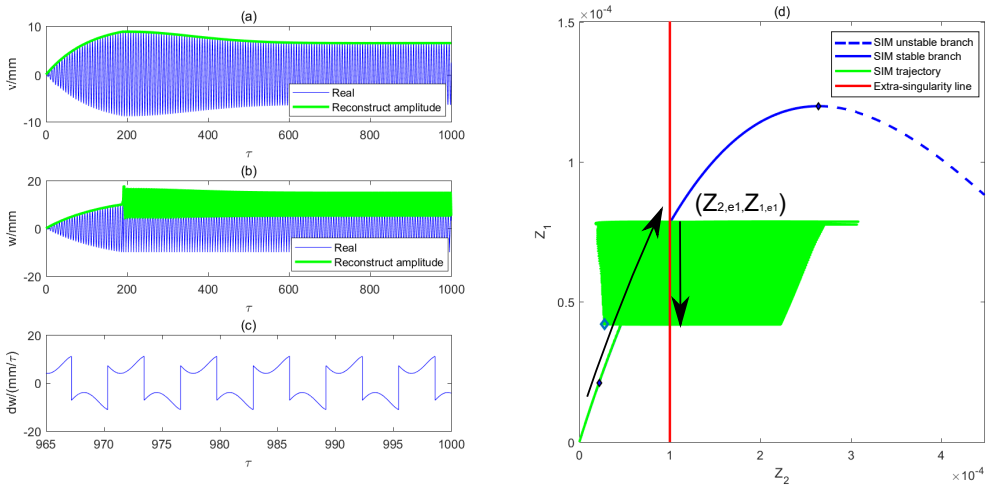

Figure 5.5: (a), (b) Time displacement response of v and w for narrow clearance case G = 0.2mm, $\sigma = 0$. The green envelopes represent the reconstructed amplitude, while the blue curves describe the time response (c) velocity of the NES $\dot{w}$ (d) SIM structure. The green line represents the phase trajectory. The blue solid/dashed line is a stable/unstable branch of SIM. The red straight line is the extra-singularity line. Black arrows indicate the movement of phase trajectory before and after the impact.

to consider the cubic nonlinearity and damping terms $c_2(\dot{y}-\dot{x})+k_2(y-x)^3$ as a small perturbation term $O(\epsilon)$, being actually similar to a pure VI NES:

$$\begin{aligned} &m_1\ddot{x}+k_1x+c_1\dot{x}+O(\epsilon)=k_1x_e+c_1\dot{x}_e \\ &m_2\ddot{y}+O(\epsilon)=0 \\ &\forall|x-y|<b \end{aligned} \tag{5.15}$$

The following changes in variables are introduced:

$$\varepsilon=\frac{m_2}{m_1},\quad \omega_0=\frac{k_1}{m_1},\quad \tau=\omega_0 t,\quad \lambda=\frac{c_1}{m_2\omega_0},\quad \tilde{\Omega}=\frac{\Omega}{\omega_0},\quad \frac{F}{b}=\varepsilon G \tag{5.16}$$

After nondimensionalization, the above equation is simplified with the displacement transfer into $x=Xb, y=Yb$.

$$\begin{aligned} &\ddot{X}+\varepsilon\lambda\dot{X}+X=\varepsilon G\sin\tilde{\Omega}\tau \\ &\varepsilon\ddot{Y}=0 \\ &\forall|X-Y|<1 \end{aligned} \tag{5.17}$$

The impact condition gives:

$$X_+=X_-,\quad Y_+=Y_-,\dot{X}_+-\dot{Y}_+=-R\left(\dot{X}_--\dot{Y}_-\right),\dot{X}_++\varepsilon\dot{Y}_+=\dot{X}_-+\varepsilon\dot{Y}_- \tag{5.18}$$

In the initial time $t=0$, the starting position is assumed to take place in the left side of the barrier. The solution for this kind of two-impacts-per-cycle regime can be expressed as follows :

$$\begin{aligned} &X(t)=\mathrm{e}^{-\frac{\varepsilon\lambda}{2}t}\left(A_1\cos\Delta t+B_1\sin\Delta t\right)+\alpha\cos(\Omega t+\eta)+\beta\sin(\Omega t+\eta) \\ &Y(t)=C_1t+D_1,\quad 0\le t\le t_1 \end{aligned} \tag{5.19}$$

t_1 represents the time of impact on the right side of the barrier, while Δ, α, β are defined as:

$$\Delta = \frac{\sqrt{4-\epsilon^2\lambda^2}}{2}, \alpha = -\frac{\Omega G\lambda\varepsilon^2}{\left(\Omega^2-1\right)^2+\varepsilon^2\lambda^2\Omega^2}, \quad \beta = -\frac{\varepsilon G\left(\Omega^2-1\right)}{\left(\Omega^2-1\right)^2+\varepsilon^2\lambda^2\Omega^2} \tag{5.20}$$

To solve the integration constant A_1, B_1, C_1, D_1, the expressions given in Eq. (5.19) are inserted into the half period condition Eq. (5.23) as solutions with two symmetrical impacts per cycle. The solutions for those integration constants are:

$$\begin{aligned} A_1 &= -2(1+R)\left(-\alpha\sin\left(\tau_0\right)+\beta\cos\tau_0\right)\varepsilon\Omega es/I \\ B_1 &= -\frac{A_1(ec+1)}{es} \\ C_1 &= -\Delta\left(2ec+1+\mathrm{e}^{-\varepsilon\lambda\pi/\Omega}\right)(1+R)\left(-\alpha\sin\left(\tau_0\right)+\beta\cos\tau_0\right) \\ D_1 &= -\frac{C\pi}{2\Omega} \end{aligned} \tag{5.21}$$

with

$$\begin{aligned} &e = e^{-\epsilon\lambda\pi/(2\Omega)}, s = sin(\Delta\pi/\Omega), c = cos(\Delta\pi/\Omega) \\ &I = -\varepsilon^2\lambda(1+R)es + 2R\varepsilon\Delta e(e-c) - 2\Delta\varepsilon(ec+1) \\ &-\Delta\left(1+e^2\right) + 2\Delta ec(R-1) + \Delta R\left(1+e^2\right) \end{aligned} \tag{5.22}$$

As with the solutions with two symmetrical impacts per cycle, we can also consider a half period:

$$\begin{aligned} &X(0) = X_0, X(\pi/\Omega) = -X_0, Y(0) = Y_0, Y(\pi/\Omega) = -Y_0 \\ &\dot{X}_+(0) = \dot{X}_0, \dot{X}_+(\pi/\Omega) = -\dot{X}_0, \dot{Y}_+(0) = \dot{Y}_0, \dot{Y}_+(\pi/\Omega) = -\dot{Y}_0 \end{aligned} \tag{5.23}$$

Re-substituting Eq. (5.21) into the initial condition $|X-Y|=1$ yields the expression of initial time η:

$$\eta = \arctan\frac{b_1}{a_1} \pm \arccos\frac{1}{\sqrt{{a_1}^2+{b_1}^2}} \tag{5.24}$$

where a_1 and b_1 are voluminous and only their appearances are presented.

The η value corresponds to two fixed points, whose stability can be analyzed with the introduction of perturbation into Eq. (5.19) and by verifying the real part of the roots of the characteristic equation. The detailed calculation can be found in [Gourc, 2013]. The analytical solution of the simplified VI NES model for the various excitations case and for a frequency domain is presented in Fig. 5.6a,b, respectively. The parameters of the VI NES are the same as those of the VIC NES.

In Fig. 5.6a, the excitation amplitude starts above the impact threshold (16.7mm) to ensure that the system has a periodic impact solution. In the narrow clearance case, the weak cubic nonlinearity and damping are neglected. The VIC NES is therefore transferred into a simpler and pure VI NES, whose analytical treatment has been well established. When the excitation grows, the analytical amplitude of the simplified model resembles the actual numerical amplitude. However, the analytical curve differs from the numerical curve once the G increases to 0.3 mm. A different response regime occurs according to the classification of Peterka [Peterka, 1996]. In this regime, there are three impacts per cycle (Fig. 5.7, orange curve), while the more conventional two impacts per cycle (Fig. 5.7,

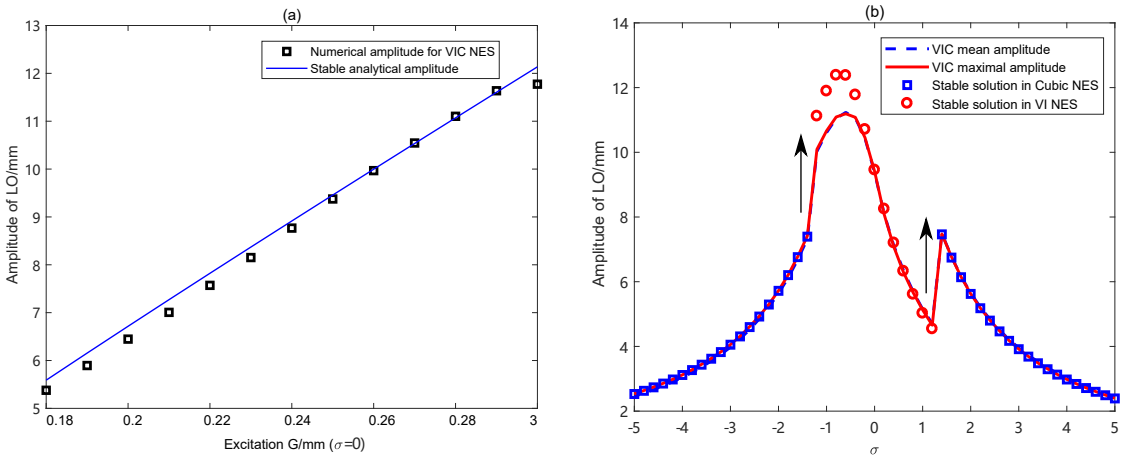

Figure 5.6: Comparison between the numerical response and analytical prediction (a) in growing excitation case for $\sigma = 0$ and (b) in the frequency domain for G = 0.25mm

thick blue line) appear in the case of G = 0.25mm. The reason behind a failed analytical prediction in the form of the hypothetical solution Eq. (5.19) can only represent the regime of two impacts per cycle.

In the frequency domain, the frequency interval σ = [-1.2 1.2] produces a discontinuous numerical curve (Fig. 5.6b). According to Fig. 5.4, when b = 10mm, the excitation for G = 0.25mm can trigger the impact motion from σ = -1 to 1.1. At this stage, the LO amplitude can be accurately predicted by the stable fixed point obtained from the VI NES model near $\sigma = 0$. The overestimations of analytical results are observed in the σ <-0.8. The red circled points in Fig. 5.6b are obtained through asymptotic analysis of the VI NES from Eq. (5.19).

When σ switches from -5 to 0, the regimes shift from the intra-cavity motion into the impact motion, causing a dramatic increase in LO amplitude. The pure cubic model dominates the stable analytical solutions that can appropriately fit the numerical results on both frequency sides of Fig. 5.6b. The stable solutions of the cubic NES indicated by the square are calculated through the asymptotic analysis of Eq. (5.13), whose stability can be determined by examining both positive and negative properties of the real part of the eigenvalue equation roots (once the perturbation is introduced).

On the basis of this discussion, it is feasible to use the VI NES model to calculate the fixed point of the VIC NES in the impact conditions near $\sigma = 0$. This alternative is possible since the VIC NES numerical solution coincides with the VI NES analytical solution. When the impact does not appear, the VIC NES performs as a cubic NES.

5.2.2 Modest clearance case

When the clearance length b is larger than the critical value $N_{2,1}$ = 16.3mm, the extra singularity line $Z_2 = Z_{2,e2}$ will be located on the unstable SIM branch. In a low energy input case (e.g. G = 0.2mm in Fig. 5.8), the displacement has no influence on the regime of the VIC NES and no impact occurs. Therefore, the behavior of the VIC NES is the same as the pure cubic NES for the same parameters in this stage. As the amplitude of the LO and NES increase, the green phase trajectory rises along the stable branch

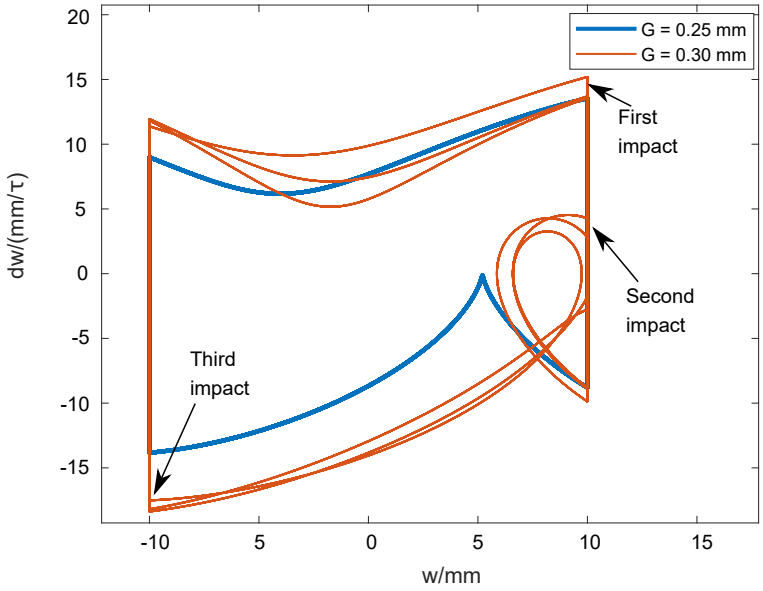

Figure 5.7: Phase trajectory of NES during one cycle for G = 0.25mm, $\sigma = 0$ (two impacts per cycle) and G = 0.3mm, $\sigma = 0$ (three impacts per cycle)

in Fig. 5.8c. The final state of phase trajectory (diamond in Fig. 5.8c) is located at a higher position before it crosses the intrinsic singularity point $(Z_{2,1}, Z_{1,1})$ due to its cubic nonlinearity.

In the pure cubic case, the relaxation-type motion occurs if the amplitude exceeds the threshold. This excitation threshold can also activate the SMR in VIC NES for the same system parameters. The typical SMR motion in a VIC NES can be classified in four stages as shown in Fig. 5.9d:

(1) The phase trajectory rises along with the left SIM branch. It results in both increases of LO and NES amplitudes. In this stage, the displacement constraint does not influence the oscillation in the cavity. The behaviors are the same as the cubic case.

(2) Once the phase trajectory crosses the singularity point $(Z_{2,1}, Z_{1,1})$, it triggers snap-through motion. The amplitude of NES increase dramatically; meanwhile, the LO amplitude is almost constant. The duration of this snap-through motion is short. Compared with the SMR stage of cubic NES, the phase trajectory arrives in the extra-singularity line $Z_2 = Z_{2,e2}$ instead of the right SIM branch.

(3) Due to the displacement restriction, the phase trajectory oscillates around the extra singularity line $Z_2 = Z_{2,e2}$. An efficient TET has been activated, so the LO amplitude decreases during this stage.

(4) After most energy of LO is dissipated. The LO amplitude is reduced. Another snap-through motion occurs. The phase trajectory jumps back to the left SIM branch, and it brings a reduction of NES amplitude. Then a new cycle of SMR start.

The threshold of SMR occurrence $G_{1,c}$ has been deduced and given by Eq. (5.25). From this equation, we can conclude that the SMR trigger conditions are the same for the VIC NES and the cubic NES. Because both cases share the same fold line $N_{2,1}$. However, since the other fold line $N_{2,2}$ is inaccessible in the modest clearance case, which leads to the calculation of G_2c threshold for SMR disappearance can not fit the VIC NES. And the

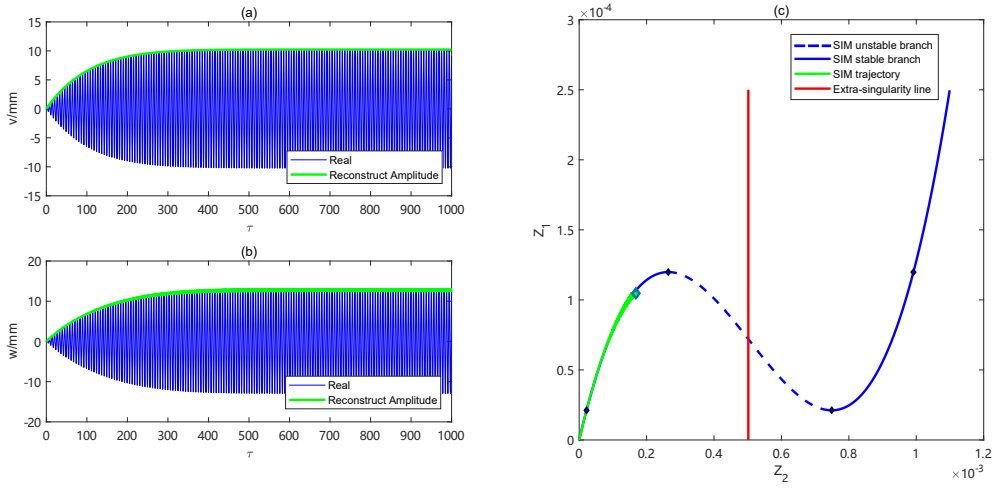

Figure 5.8: (a), (b) Time displacement response of v and w for modest clearance case G = 0.2mm, σ =0. The green envelopes represent the reconstructed amplitude, while the blue curves describe the time response (c) velocity of the NES $\dot{w}$ (d) SIM structure. The green line represents the phase trajectory. The blue solid/dashed line is a stable/unstable branch of SIM. The red straight line is the extra-singularity line.

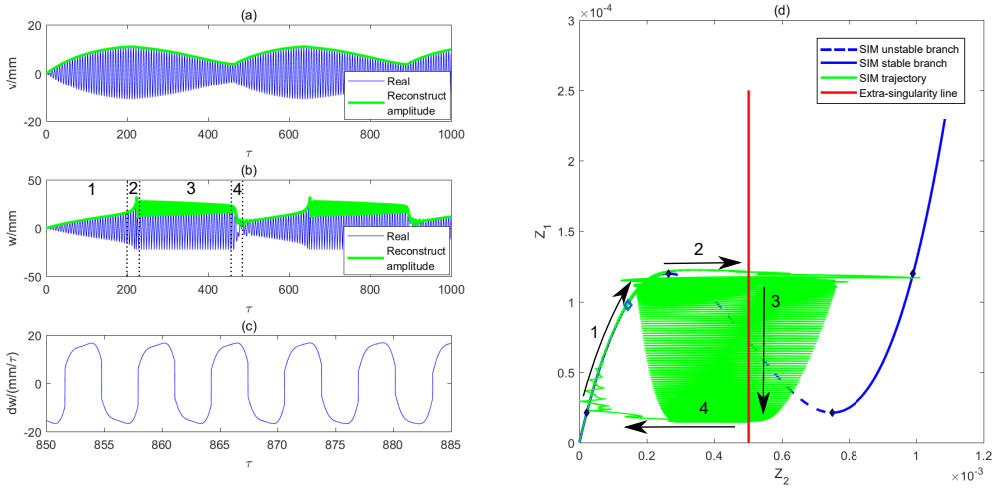

Figure 5.9: (a),(b) Time displacement response of v and w for modest clearance case G = 0.25mm, σ = 0. The green envelopes represent the reconstructed amplitude, while the blue curves describe the time response (c) velocity of the NES $\dot{w}$ (d) SIM structure. The green line represents the phase trajectory. The blue solid/dashed line is a stable/unstable branch of SIM. The red straight line is the extra-singularity line. Black arrows indicate the movement of phase trajectory before and after the impact.

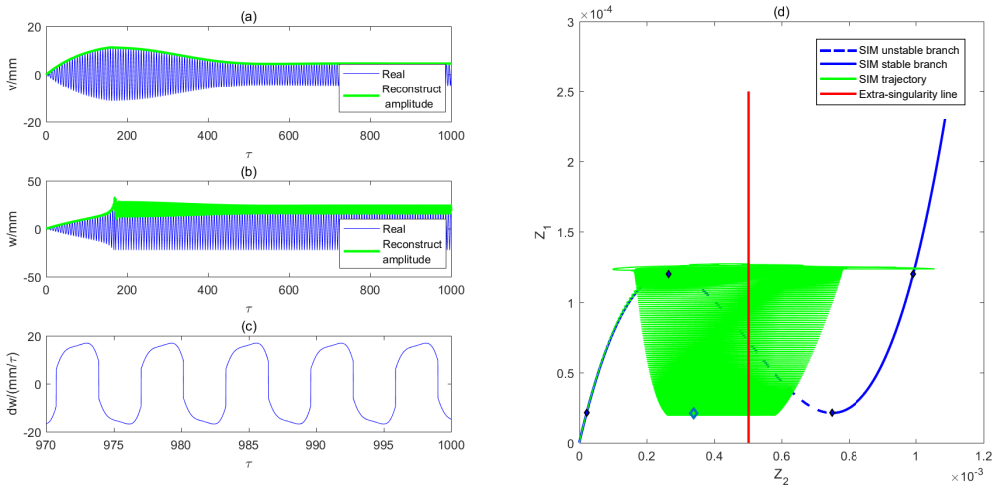

Figure 5.10: (a),(b) Time displacement response of v and w for modest clearance case G = 0.28mm, $\sigma = 0$. The green envelopes represent the reconstructed amplitude, while the blue curves describe the time response (c) velocity of the NES $\dot{w}$ (d) SIM structure. The green line represents the phase trajectory. The blue solid/dashed line is a stable/unstable branch of SIM. The red straight line is the extra-singularity line.

extra singularity value $N_{2,2} = N_{2,e} = b$ is applied in Eq. (2.25) to obatin the threshold in Eq. (5.25).

$$\begin{aligned} G_1 c = \epsilon F_1 c &= \frac{\epsilon N_{2,1}\left(16\lambda_1 - 24\lambda_1 K N_{2,1}^2 + 9\lambda_1 K^2 N_{2,1}^4 + 16\lambda_2 + 16\lambda_1\lambda_2^2\right)}{(4\sqrt{9K^2N_{2,1}^4 - 24KN_{2,1}^2 + 16 + 16\lambda_2^2})} \\ G_e = \epsilon F_e &= \frac{\epsilon b\,(16\lambda_1 - 24\lambda_1 K b^2 + 9\lambda_1 K^2 b^4 + 16\lambda_2 + 16\lambda_1\lambda_2^2)}{(4\sqrt{9K^2b^4 - 24Kb^2 + 16 + 16\lambda_2^2})} \end{aligned} \tag{5.25}$$

In the cubic NES case, the analytical amplitude threshold calculated in Eq. (2.25) for the SMR occurs between [0.22mm, 0.35mm]. The numerical thresholds are [0.24mm, 0.41mm]. In the VIC NES, the analytical result indicates that the SMR starts and ends at [0.22mm, 0.24mm] by Eq. (5.25), while the numerical simulation found that the SMR appears between [0.24mm, 0.28mm]. Numerical and analytical results both confirm that the SMR starts in the same amplitude excitation cases for the VIC NES and cubic NES. The analytical predictions for SMR extinction show some differences with numerical simulation. The displacement constraint results in the SMR of the VIC NES ending at a much lower excitation amplitude case.

Figure. 5.10 shows the stable periodic response of the system when the excitation exceeds the force threshold. The critical force prevents the phase trajectory from jumping back to the left stable branch and being located at a similar height of singularity point $(Z_{2,2}, Z_{1,2})$, having slowly decreased along the extra singularity line $Z_2 = Z_{2,e2}$. In this critical situation, the LO amplitude possesses the minimal stable amplitude, which can only be realized in an optimal cubic NES in the larger energy input case. Thus, the displacement constraint enables the system to enter the optimization state in a lower excitation amplitude case.

As in the previous narrow clearance case, the VI model can accurately predict the fixed point of the VIC NES under impact conditions. In Fig. 5.11a, the system shows a stable response to impact when the excitation amplitude increases beyond 0.28mm. In the relatively low energy case, the analytical prediction has a more significant value than the simulated one. As excitation increases, both results almost overlap.

In the frequency domain (Fig. 5.11b), impact appearance separates the numerical frequency response into two parts. When the VIC NES performs as a cubic NES, the numerical amplitude of the VIC NES coincides with the blue square point on both [-5, -3.2] and [2.8, 5] σ intervals.

Unlike the narrow clearance case, the analytical predictions of pure cubic NES possess two stable fixed points and one unstable fixed point between the σ = [-3, -1.6] and [1.2, 2.6]. The lower stable LO amplitude branch better describes the numerical simulation (blue squares in Fig. 5.11b). In this stage, the NES amplitude tends to have a higher value, which means that more energy of the LO will be transferred into the NES, leading to a lower LO amplitude. Therefore, the numerical results of the LO amplitude are located on the lower stable solution branch. The intervals [-3, -1.6] with three fixed points mean that the NES possesses three potential amplitude cases. The impact is triggered due to the resonance peak, whose appearance does not strictly follow the criteria for the appearance of the three fixed points at σ = -1.6. On the other side, that of interval [1.2, 1.6], the impact is accompanied by a SMR. When the SMR disappears at σ = 1.6, the response becomes an inter-cavity motion again. According to the best of our knowledge, there is no effective theoretical tool to predict the threshold of SMR occurrence and disappearance under non-natural frequency excitation, which means that Eq. (5.25) is only valid for σ =0. When the frequency is away from the natural frequency, the system still performs a stable response without impact. The fixed point of this stable periodic response can be described by the framework of the pure cubic NES model.

The stable analytical branch of the VI NES model (red circles in Fig. 5.11b) also fits well to the VIC NES numerical results in the vicinity of the natural frequency when impact occurs. This interval is distinguished by the drastic increase in LO amplitude between [-1.4, 1]. The overlapping of the maximal and average amplitude curves implies a stable response of the system. The separation of both curves indicates the occurrence of a SMR in the frequency interval [1.2, 1.6]. Compared with the pure cubic NES case, this interval is relatively narrow for SMR occurrence.

5.2.3 Large clearance case

If clearance length b is $>N_{2,2}$ = 27.4mm, this design can be considered as large clearance design. In the simulation, b is fixed for 30 mm so that the extra singularity line $Z_2 = Z_{2,e3}$ is located on the right stable SIM branch (Fig. 5.12d). In the lower energy case, the system performs more like a cubic NES. The phase trajectory rises along the left stable SIM branch until the excitation amplitude exceeds the threshold $G_{1,c}$. A large clearance ensures that the influence of the displacement constraint is validated only for the higher energy input case.

The SMR starts at G = 0.24mm, the same as previous cases since displacement constraint has no impact on the SMR occurrence threshold. Figure. 5.12 presents a classic SMR for G = 0.25mm.

A significant feature of the large clearance case—when compared to the modest case

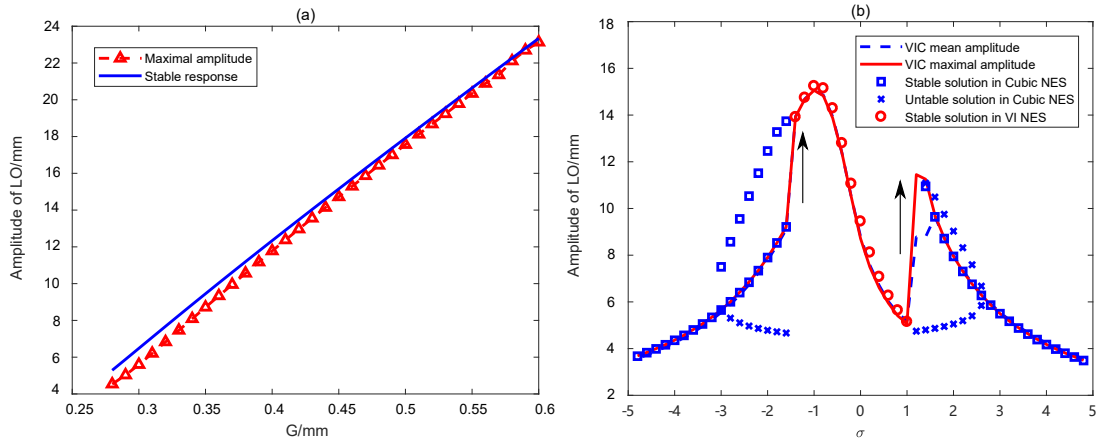

Figure 5.11: Comparison between the numerical response and analytical prediction (a) in the growing excitation case for $\sigma = 0$ and (b) in the frequency domain for G = 0.35mm

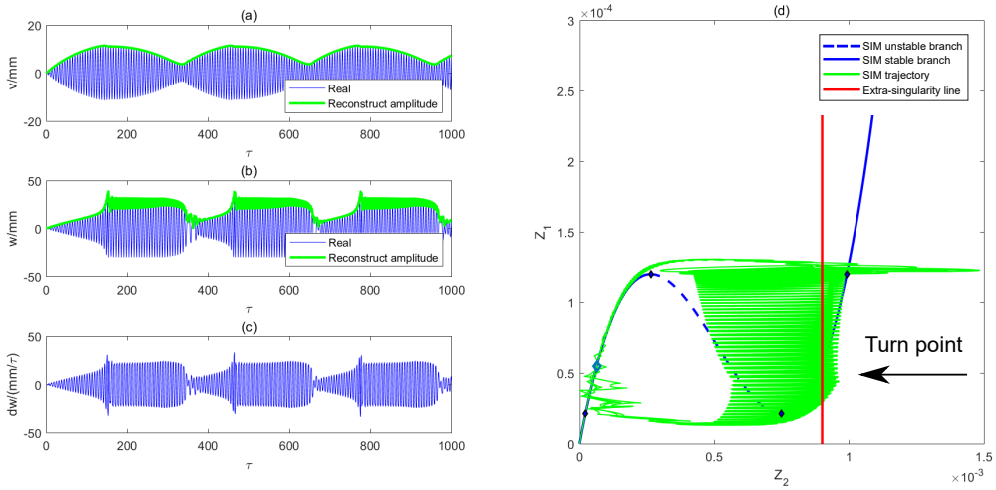

Figure 5.12: (a),(b) Time displacement response of v and w for large clearance case G = 0.25mm, $\sigma = 0$. The green envelopes represent the reconstructed amplitude, while the blue curves describe the time response (c) velocity of the NES $\dot{w}$ (d) SIM structure. The green line represents the phase trajectory. The blue solid/dashed line is a stable/unstable branch of SIM. The red straight line is the extra-singularity line.

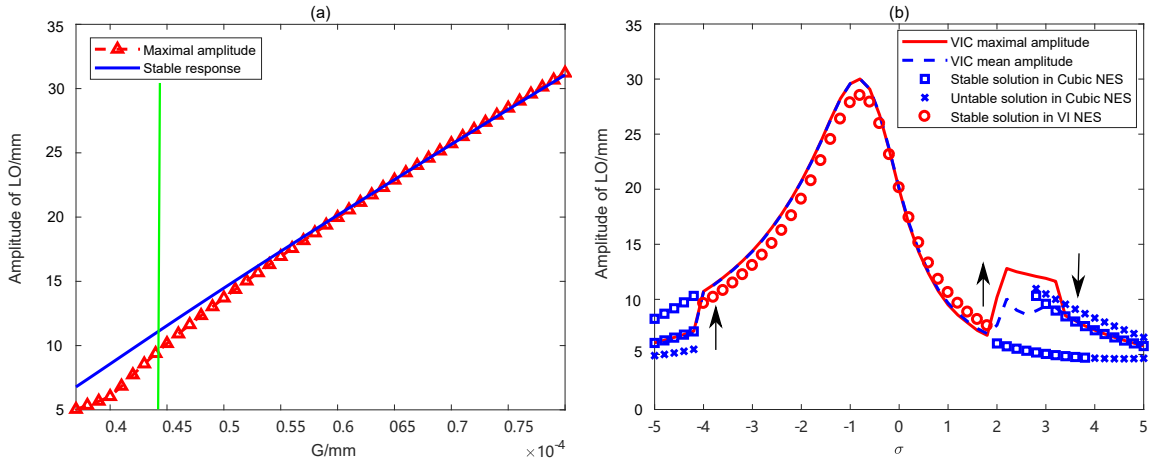

Figure 5.13: Comparison between the numerical response and analytical prediction (a) in growing excitation case for $\sigma = 0$ and (b) in the frequency domain for G = 0.6mm

(Fig. 5.9)—is that the time required for a complete SMR is shorter. The reduction is mainly reflected on the much shorter duration of the 1:1 resonance. An obvious turn point occurs, above which the phase trajectory oscillates along the extra singularity line. Once the phase trajectory descends and crosses the intersection of the extra singularity line and the right SIM branch, the phase trajectory is attracted by the right half-branch of the SIM. In Fig. 5.12d, the direction of the phase trajectory descent changes at the turning point, from vertical descent to descent along the SIM.

When G = 0.44mm, the stable amplitude of NES exceeds the b, which interprets that the red triangle line has the some distance to stable response predicted by the VI NES model in Fig. 5.13a. As excitation increases, the final fixed point is located in the extra singularity line instead of in a small part of the SIM stable branch. In the high energy input case, the VI NES model can better predict the fixed point of the VIC NES, so that the two curves approach each other (Fig. 5.13a).

In the frequency domain, the VI NES model also demonstrates its effectiveness in predicting the fixed point of the VIC NES for G = 0.6mm in Fig. 5.13. Since excitation is larger, the system has a greater frequency range for collisions between [-4, 3.4]. On the lower frequency side of the impact interval, the theoretically predicted values of the red circled points are smaller than the simulated values. On the higher frequency side, theoretical prediction values are larger.

In the large clearance case, collision frequency vanished in the range of [-5, -4.2] and [3.6, 5]. The numerical simulation accurately locates the analytical prediction of the cubic NES model. The SMR frequency is in the range of [1.8,3.4], where the average and maximal amplitude curves start to separate in Fig. 5.13b. Compared with Fig. 5.11, the frequency range of the SMR is more significant in this case. The magnitude of the external excitation does not affect the frequency range of SMR appearance in subsequent studies. Thus, the influence on the frequency range variation of SMR appearance can only be due to the change in clearance length.

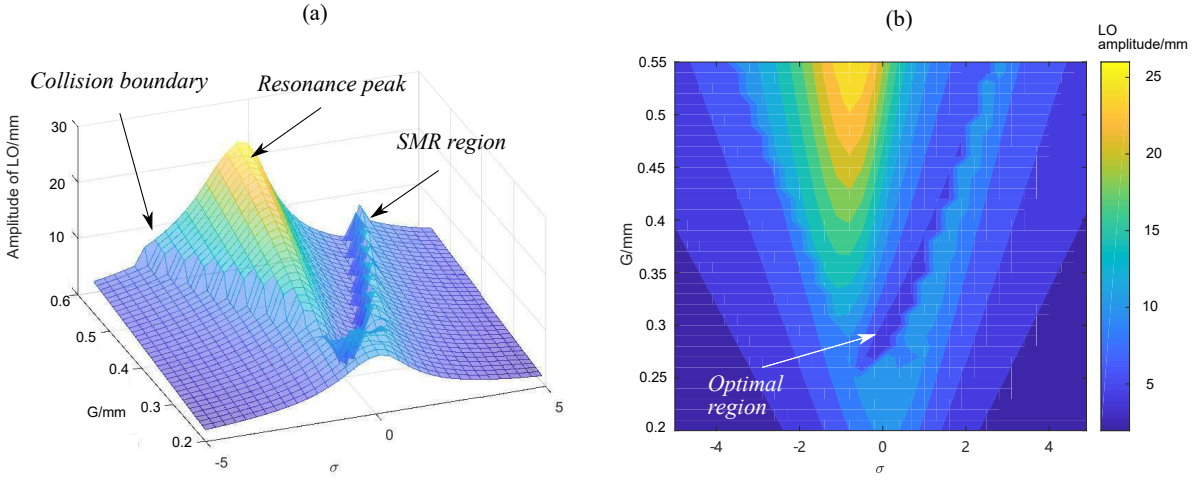

Figure 5.14: Maximal LO amplitude in the frequency domain for the modest clearance case, b = 22.4mm. (a) 3D view (b) contour map of maximal LO amplitude.

5.3 Frequency domain behaviors and optimal design

In the previous section, the frequency distribution of the system under certain excitation conditions was discussed. This section focuses on the frequency distribution of the system under different excitations for modest and large clearance designs.

Figure. 5.14 shows the transform of response regimes along with frequency increase direction: (1) periodic response without impact, (2) resonance peak, (3) optimal region and (4) SMR region, (5) periodic response without impact. On both the low and high frequency sides, the collision is not ensured even in the high excitation amplitude. The collision boundary comprises the left boundary of the resonance peak and the right side of the SMR region. Collision on the low frequency side results in a sudden increase of the maximal LO amplitude. This case, deemed dangerous, is known as resonance peak. According to its interpretation in the cubic NES system [Gourc *et al.*, 2014], the resonance peak results from a saddle-node bifurcation where the three solutions of Eq. (2.12) occur. The optimization interval has a shape akin to a valley and is located in the middle of the resonance and SMR. As the excitation amplitude increases, the frequency required for the optimal point (minimal LO amplitude) increases. Theoretically, the LO amplitude at the optimum point is equal to $N_{1,2} = 4.6$mm at the singularity point, regardless of the amplitude. In the actual numerical simulation, the LO amplitude at the optimum point increases from 4.6mm to 6.2mm as the excitation amplitude increases from 0.25mm to 0.55mm.

The system does not perform a stable amplitude response during the SMR and possesses a large instant amplitude. This region has a narrow width in the frequency domain. The SMR interval shifts to a higher frequency region when a higher excitation amplitude is applied. As the excitation amplitude is constant, the frequency increase causes the system to transition directly from the SMR to the stable response without collision, skipping the stable response phase with collision.

When the clearance is designed to be larger (Fig. 5.15), the same characteristic region appears while the collision boundary remains the same (as indicated in Fig. 5.14). The most dangerous case occurs in $G = 0.55$mm, σ = -0.8, whose LO amplitude is maximal

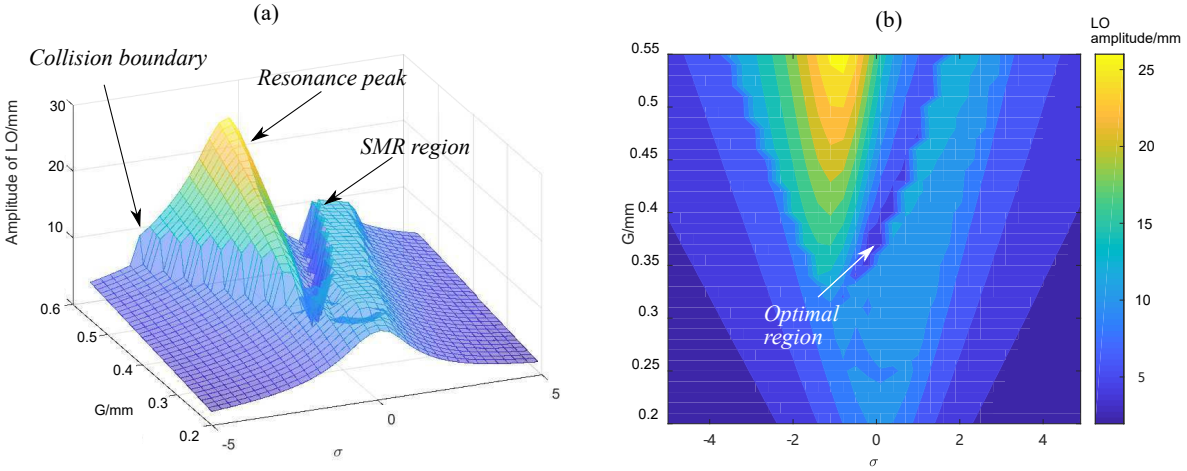

Figure 5.15: Maximal LO amplitude in the frequency domain for the large clearance case, b = 30mm. (a) 3D view (b) contour map of maximal LO amplitude.

(equal to 27.1mm). Under the same condition, the LO reaches 26.1mm in a modest clearance case. The smaller clearance design slightly reduces the resonance peak. The optimal region occupies a higher excitation amplitude region, starting from 0.35mm, while the optimal region in a modest clearance case starts from 0.25mm. The same increasing frequency behavior can be observed for the optimal region when the excitation increases. A platform appears in the SMR region, being much wider than that of a modest clearance case.

The narrow clearance prevents the phase trajectory from crossing the singularity point $(Z_{2,1}, Z_{1,1})$ in the SIM structure, so the SMR cannot appear in this case. The SMR distributions for the modest, large clearance and cubic cases are shown in 5.16; the cubic NES case is considered as an infinite long clearance case.

The maximal and average LO amplitudes (and their difference) are calculated to identify the SMR. When the system performs a stable periodic response, both amplitudes are almost the same. If the error between maximal and average amplitude is larger than 0.15mm, the SMR is identified in this condition. Overall, the area where the SMR appears expands with increasing clearance length. The obstruction effect of the impact on SMR emergence is then confirmed. In Fig. 5.16a, the widest frequency interval is σ = [-0.5, 0.7], when G = 0.265mm. Maximal interval in Fig. 5.16b appears in σ = [-1.1, 1] for G = 0.31mm. The cubic NES case shows the largest SMR interval σ = [-1.7, 2.2] for G = 0.37mm. As can be seen from the maximal frequency range in which the SMR appears, the displacement constraint reduces the frequency robustness, narrowing the range where the SMR appears.

In the higher energy input cases, the SMR appears on the side where σ >0. The frequency range in which SMR appears on this side remains constant as excitation amplitude increases. The width ranges from 0.3 (Fig. 5.16a), to 0.9 (Fig. 5.16b), and then to 2.1 (Fig. 5.16c). Even at high energy inputs, the frequency range in which SMR appears is also limited by the barrier; the smaller the b, the smaller the frequency range.

Although the SMR region is affected by the clearance length, the thresholds at which SMR appears are all the same, i.e. at G = 0.22mm, $\sigma = 0$. This phenomenon is consistent with our previous observation that b does not affect the threshold for SMR appearance.

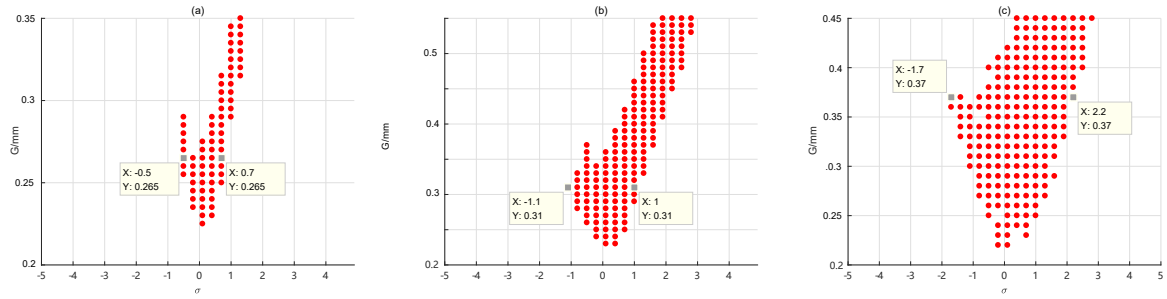

Figure 5.16: SMR distribution for different clearance length cases (a) $b = 22.4$mm (b) 30mm (c) pure cubic case (b$\rightarrow \infty$)

5.3.1 Influence of the restitution coefficient

The restitution coefficient r is only valid when there is a collision in the system. The collision thresholds in the narrow clearance case and the modest/large clearance cases where SMR occurs can be seen as the end of the oscillation within the cavity without collision. Therefore, the restitution coefficient has no effect on the start of the collision threshold and the start of the SMR threshold. The threshold predictions of Eq. (5.14) and Eq. (5.25) are still valid for different restitution coefficients. The collisions occur in the SMR and stable collision stages, so that the restitution coefficient analysis r focuses on the effects in these two stages.

The modest clearance case $b = 22.4$mm under excitation $G = 0.25$mm was selected to investigate the role of r. In Fig. 5.17a, the displacement of three different cases are almost the same due to the absence of collision. At $\tau = 224$, the NES amplitudes for the three cases sharply and simultaneously increase. In the energy pumping period, the three cases with 0.95, 0.65, and 0.35 coefficients take 295, 239, and 195 times on the τ time scale, respectively. A higher value of r means more energy loss for every impact, accelerating the rate of energy dissipation and leading the system amplitude to decrease more rapidly. This faster amplitude reduction rate is also evident in Fig. 5.17b. A smaller r enables the system to have more SMR cycles in the same amount of time.

When the system enters the stable impact response (two impacts per cycle), the LO amplitude is governed by the coefficient A_1, B_1, α, β in Eq. (5.20). The stable analytical amplitude is shown as a blue line in Fig. 5.18. As r increases, the stable amplitude rises slightly. The numerical results (red points in Fig. 5.18) also confirm this tendency. When r varies from 0.8 to 0.3, the stable amplitude is reduced from 12.3mm to 10.8mm. This difference cannot be considered as significant when compared to the wide variation range of r. The system shows low sensitivity to the various values of r.

5.3.2 Clearance design for target excitation

In the previous section, the influence of clearance has on the different response regimes is presented. Every clearance length design corresponds to a target excitation, under which the LO possesses minimal amplitude.

To find out the corresponding target excitation, various amplitude input cases are applied to the different clearance designs. The corresponding results are shown in Fig. 5.19. The thin red lines and thin dashed blue lines are the maximal and average LO amplitudes,

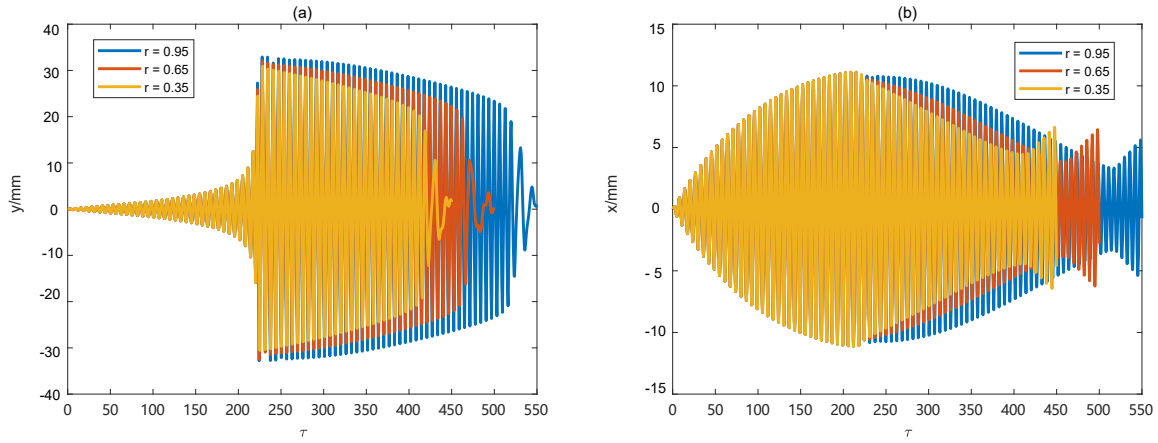

Figure 5.17: Time displacement response of the SMR for different restitution coefficients r: 0.95, 0.65, and 0.35. (a) absolute displacement of the NES (b) absolute displacement of the LO. The excitation amplitude G = 0.25mm, $\sigma = 0$

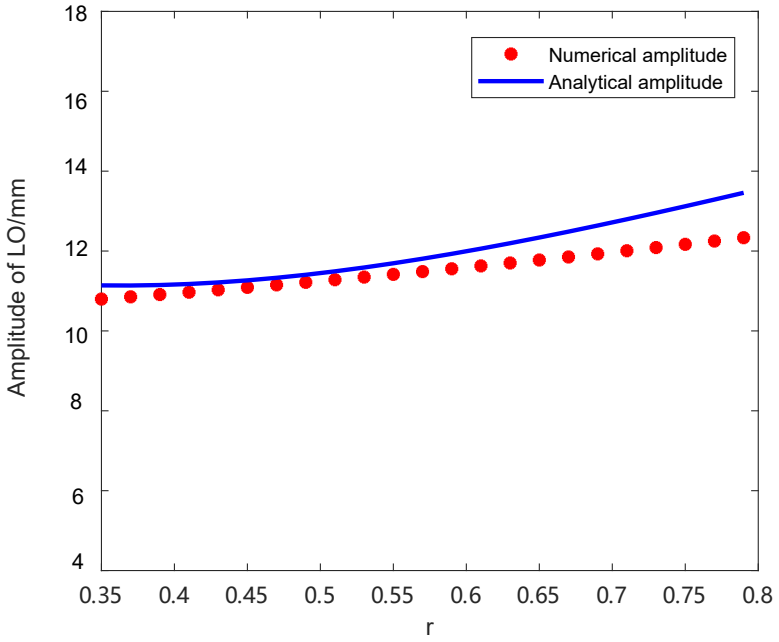

Figure 5.18: Stable LO amplitudes for various restitution coefficients r under harmonic excitation G = 0.4mm, $\sigma = 0$.

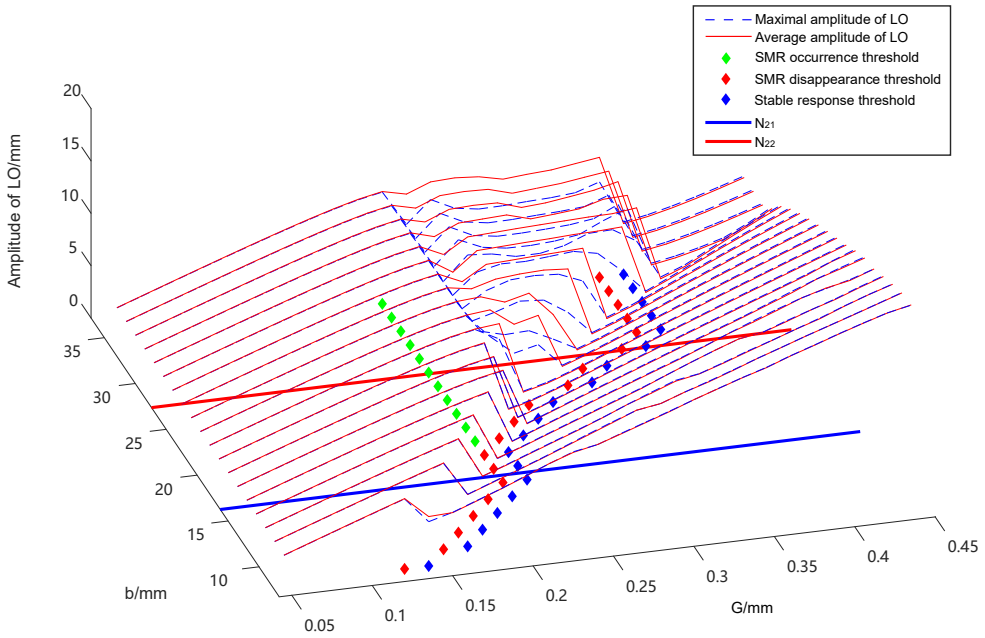

Figure 5.19: The influence of different clearance length b designs on the response regimes. The range of clearance is [8, 9.5, 11, 12.5, 14, 15.5, 17, 18.5, 20, 21.5, 23, 24.5, 26, 27.5, 29, 30.5, 32, 33.5, 35]mm.

respectively. The red and blue diamond-shaped points correspond to the projection of the local maximal and minimal amplitudes on the b–G plane. The green diamond-shaped points indicate the excitation threshold of SMR occurrence for various clearance length designs. The thick blue line A and thick red line B divide the clearance length designs into three categories, which is classified by singularity value $N_{2,1}$, $N_{2,2}$.

If the clearance lengthdesign is $b < N_{2,1} = 16.3$mm, the snap-through motion is prevented, and the SMR cannot be observed in the first five cases. So the green diamond-shaped points do not appear in the region Fig. 5.19. The maximal amplitude curve and average amplitude curves are overlapped, which means that the SMR is not triggered. In those five cases, the response regimes are classified into two types: (1) without impact (2) with impact. In lower energy levels, the NES oscillates within the cavity. The cubic nonlinearity prevents NES mass from contacting the barrier. The threshold of excitation for impact can be calculated by Eq. (5.14). The occurrence of a collision brings about a sharp drop in amplitude, which can be seen as an optimization point. Local maximal and minimal amplitude points are always adjacent to each other. Before and after impact, the LO amplitude increases almost linearly with excitation.

When the clearance length designs are $b > N_{2,1}$, a modest design is considered. The distance between the extra singularity line $Z_2 = Z_{2,e}$ and the singularity point $Z_2 = Z_{2,1}$ in the SIM structure allows the phase trajectory to feature the snap-through motion. However, the extra singularity line prevents the phase trajectory to arrive on the right SIM stable branch. A complete (classic) SMR cannot occur. As the b design increases, the SMR appears in a widened amplitude range. So the distance between green and blue diamond-shaped points enlarge as clearance design increases in Fig. 5.19. The threshold at

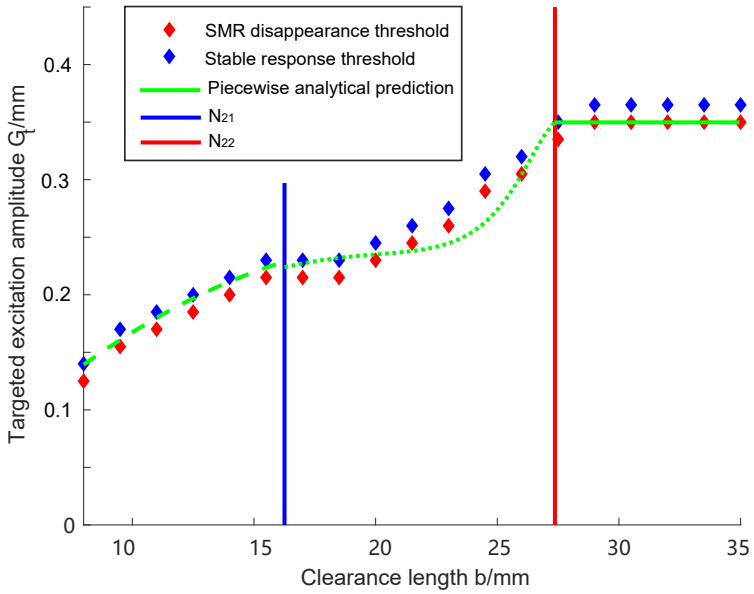

Figure 5.20: Optimal clearance designs for various target excitation amplitudes

which SMR appears (as shown by the green diamond-shaped points) remains unchanged. The system changes from a stable response to a SMR to a stable response with collisions as excitation amplitude increases. The local minimal amplitude point occurs after the SMR disappears. A larger displacement constraint can adjust the VIC NES to optimally adapt to a larger excitation.

Once the clearance is designed to be $b > N_{2,2} = 27.4$mm, continuing to increase the gap length has no effect on the threshold for the appearance and end of the SMR. The excitation interval for the presence of SMR remains unchanged in the last four cases, whose clearance lengths are all larger than the critical value $N_{2,2}$. So the distances between green and blue diamond-shaped points remain constant as clearance design increases in Fig. 5.19. In the third category, the clearance design has no influence on the optimal point, which appears at the singularity point $(Z_{2,2}, Z_{1,2})$ in the SIM structure. The gap-enlarging method to increase the amplitude that can be optimally absorbed by the system thus fails.

The distributions of target excitation for different clearance length b designs are shown in Fig. 5.20 (blue diamond-shaped points). Three types of clearance design are distinguished by thick blue and red lines. If the excitation amplitude is below the critical value $G_{1,c}$, it can be classified as a low energy input. Therefore, the clearance design that should make the extra singularity line $Z_2 = Z_{2,e}$ is located on the left stable SIM branch. Collision occurs and the system achieves the optimal state when the system oscillates in a maximal amplitude and slightly increases its excitation amplitude. The impact condition for a narrow clearance is derived from Eq. (5.14), which leads to the optimal curve (dashed green line to the left of the $N_{2,1}$ line). The optimal clearance length b_o can be solved by setting $G_t = \epsilon F_t$ into Eq. (5.14). The maximal and minimal amplitude points are very close to each other, with the distance being determined by the step size of the excitation amplitude in the numerical simulation. In the ideal case, the maximal and minimal amplitude points are the same and the red and blue diamond-shaped points

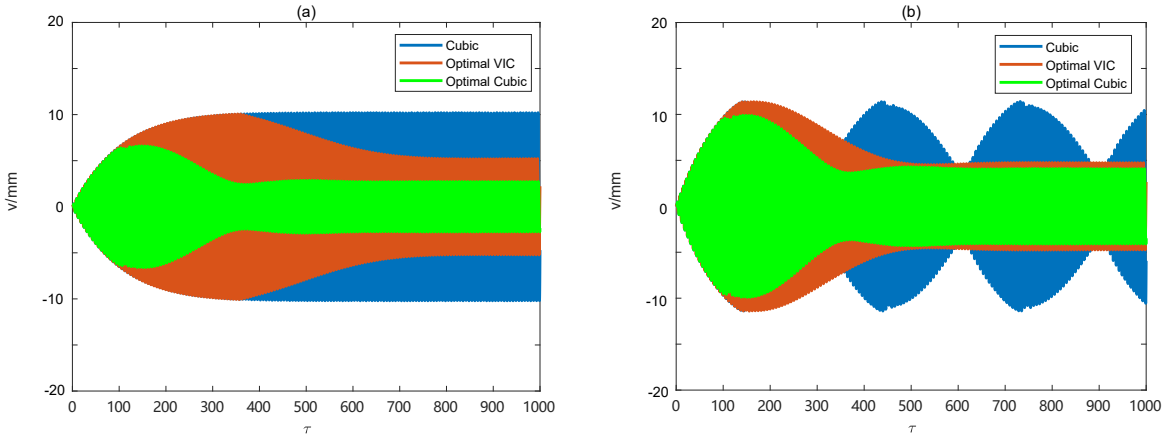

Figure 5.21: Optimal result for (a) target excitation $G_t = 0.2$mm, $\sigma = 0$. The optimal clearance length for VIC NES is $b_o = 12.5$mm, (b) target excitation $G_t = 0.3$mm, $\sigma = 0$. The optimal clearance length for VIC NES is $b_o = 24$mm

overlap. Owing to the step size limitation, the red and blue diamond-shaped points distributed on both sides of the optimal curve validate the optimal design in this case.

If the target excitation is within the interval $[G_{1,c}, G_{2,c}]$, the clearance length b should be within the interval $[N_{2,1}, N_{2,2}]$. The clearance length determines the threshold where the SMR disappears, which is also viewed as an optimal state for the LO. The green dashed curve is plotted by Eq. (5.25), demonstrating the optimal clearance design once the target excitation value has been set. When the target excitation nears $G_{1,c}$, the optimal curve is flat and sensitive to target excitation. A slight variation in target excitation G_t would cause the design value of b to increase significantly. When the target excitation nears $G_{2,c}$, the analytical prediction will produce a larger design value, causing the system to perform the SMR. In this design case, the actual optimal clearance should be slightly smaller than the analytical prediction value. In general, the numerical simulations show a linear relationship and the analytical values reveal a quadratic term relationship. However, the analytical solution is still referable to the optimal curve.

If the target excitation exceeds $G_{2,c}$, adjusting the clearance length would go beyond adapting the increasing excitation. In other words, if the clearance length is $b > N_{2,2} = 27.4$mm, the target excitation that system can absorb remains constant $G_t = 0.35$mm. The final point of phases trajectory will be located at singularity point $(Z_{2,2}, Z_{1,2})$ (optimal state) in the SIM structure, which is independent of the extra singularity line $Z_2 = Z_{2,e}$ (clearance design). On the right side of Fig. 5.20, the red and blue diamond-shaped points are aligned horizontally. The horizontal analytical curve coincides with the point where the SMR ends. Note that the numerical result slightly exceeds the analytical design value.

The results for the different target excitations are presented in Fig. 5.21. The cubic nonlinearity parameter of the optimal cubic NES is determined using the method proposed in [Wu *et al.*, 2021], where the final phase trajectory stays in the singularity point of the SIM.

When $G_t = 0.2$mm, the cubic NES performs a stable periodic response (amplitude = 10.2mm in Fig. 5.21a), whose phase trajectory is finially located on the SIM left branch (as in Fig. 5.5c). However, the optimal VIC NES has a smaller final LO amplitude for the optimal clearance design $b_o = 12.5$mm, about 5.2mm. If the cubic NES is tuned by

substituting the original K value (1.742e3) with an optimal cubic nonlinearity parameter K (6.01e3), the system will hold the minimal LO amplitude (about 2.73mm). So in a low target excitation case ($G_t < G_{1,c}$), the tuning clearance length can lead to an obvious vibration mitigation performance. However, the replacement of cubic nonlinearity parameter can achieve better performance.

In Fig. 5.21b, the target excitation is set to 0.3mm, which is between $[G_{1,c}, G_{2,c}]$. The SMR constitutes the principal motion for the original cubic NES. According to Fig. 5.20, the optimal clearance design b_o = 24mm minimizes the LO amplitude to 4.75mm. The SMR will reappear under the target excitation in a larger clearance design. A clearance design $<b_o$ will increase the final stable LO amplitude. The cubic nonlinearity parameter of the original cubic NES K must be tuned to 2.61e3 to achieve a minimal amplitude of 4.06 mm. The optimal cubic NES with the replacement of K represents a not-so-obvious improvement to the optimal VIC NES.

The cubic NES with fixed cubic nonlinearity can only adapt a single target excitation. If the system is under a smaller excitation, a larger cubic nonlinearity parameter K is required for optimal energy absorption. In the real mechanical environment, the replacement of the spring component has a considerable cost and requires a system redesign. Thus, the VIC NES can provide an alternative approach to adapt a weaker target excitation without changing its spring components.

5.4 Experimental study

The experimental setup was designed to observe the influence that impact has on the behavior of the SMR distribution. Harmonic excitation is initially applied to the LO structure at a specific range of resonance frequency. The threshold value of SMR occurrence and disappearance and the SMR bandwidth in high energy input cases were recorded.

5.4.1 Vibro-impact cubic NES construction

The pure cubic nonlinearity is achieved with a four springs system, which is tuned to a specific pre-compression length to avoid the linear stiffness component in the whole combined force-displacement relationship. The detailed construction process is detailed [Qiu *et al.*, 2018b]. The NES mass is attached to the track through the four springs system, so that it can move along the axis of the conical spring. The whole NES system is connected to the LO, which is embedded on a 10 kN electrodynamic shaker. Two perpendicular countless laser sensors are used to measure the LO and NES, respectively. The experimental device is presented in Fig. 5.22.

The two steel screws with galvanised surface are installed in the hole of the track to stop the relative sliding of the NES into creating displacement constraints (Fig. 5.22b).Due to the design of the track itself, the distance between each hole is 15 mm. By choosing different mounting positions for the screws or by adjusting the position of the rails, we can obtain different clearance configurations. When impact occurs, the side of the NES mass is in contact with the top of the screw on both sides. The stud of the screw was slightly cut down to avoid coming into contact with the conical spring coils and screws, thus ensuring that the impact only occurs between the screws and NES mass. The parameters of the experimental setup and two types of clearance lengths are given in Tab. 5.1. The b_1 and b_2

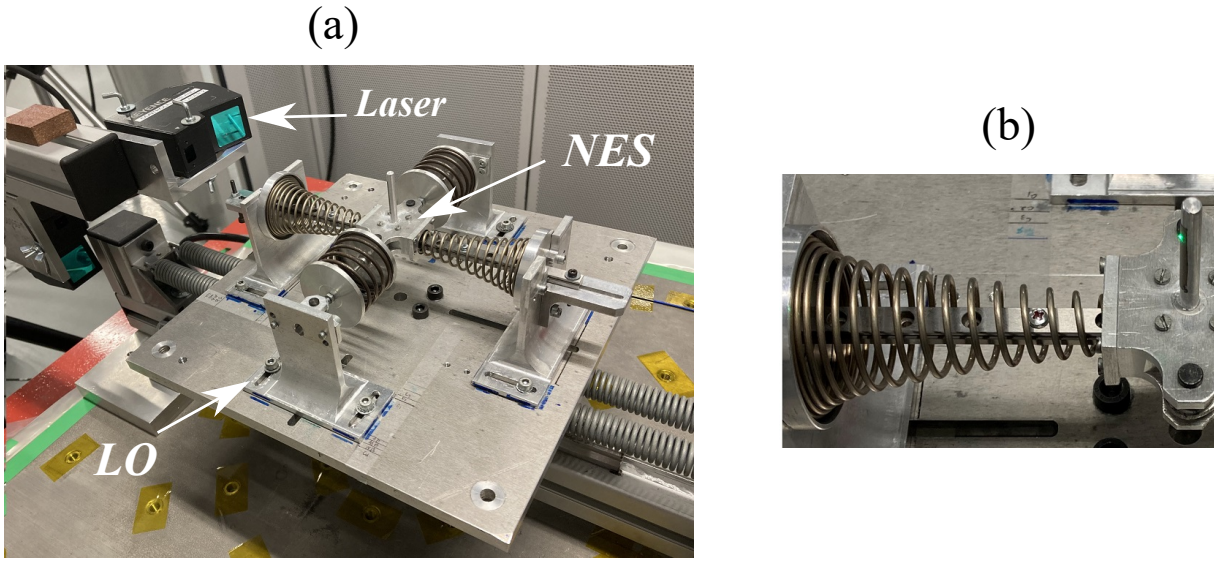

Figure 5.22: Experimental device (a) construction of the NES and LO (b) realization of the displacement constraint

Table 5.1: Experimental parameters of the environment

Reduced parameters	ϵ	λ_1	λ_2	K	r	b_1	b_2
	1.2%	1.67	0.167	4.88e3	0.65	11.5mm	17mm

parameters lie within the unstable SIM branch. The restitution coefficient r is measured by connecting the NES to the ground. All the springs are removed to conserve only the NES mass. An initial NES velocity is applied, so that the NES—the velocity measuring instrument—can measure velocity changes before and after the impact. According to its definition, the average value of r can be calculated through 10 time tests.

5.4.2 Dynamic tests

The amplitude of the harmonic excitation amplitude ranges from 0.18 mm to 0.3 mm, and the difference between the amplitude of adjacent excitation is 0.02mm. The velocity of frequency sweep is 0.01 Hz/s. Three different clearance cases (b = 11.5 mm, b = 17 mm and cubic) were chosen to examine the impact effect. The frequency response for the three clearance cases is shown in Fig. 5.22. The black triangle marks the interval of SMR appearance. The variety of SMR regions according to the clearance changes in Fig. 5.22 shows the same tendency as the numerical simulation in Fig. 5.16. The adjacent responses are marked in different colours to distinguish between them.

In a low energy input case (e.g. G = 0.18 mm), the NES behaviors in Fig. 5.22 show the same SMR extinction. The maximal amplitude occurs at its natural frequency f_0 = 7.3Hz for 7.61mm, 7.68mm and 7.71mm, respectively. The frequency response of the three cases is almost identical, meaning that impact does not occur.

For a higher amplitude excitation G = 0.20 mm, the SMR first occurs in the cubic case (Fig. 5.22c) for [7.28Hz 7.38Hz]. The SMR range is selected by the complete SMR cycle, including the increasing amplitude-phase and decreasing phase. There are no obvious

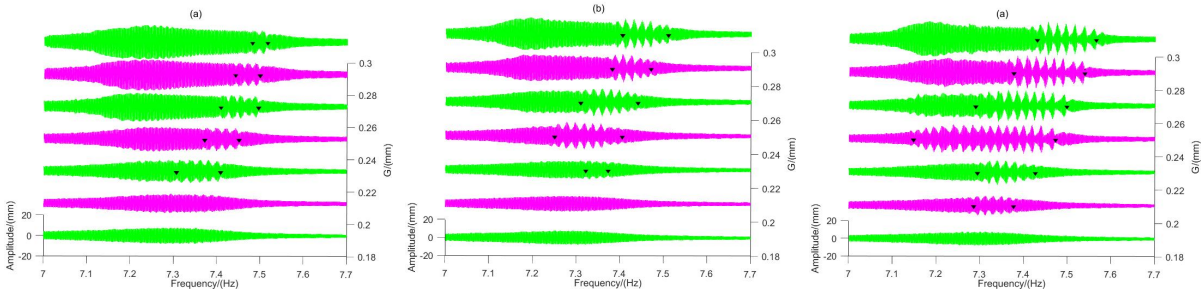

Figure 5.23: Frequency response of the NES for different clearance case (a) $b = 11.5$mm case (b) $b = 17$mm case (c) Cubic NES case. The excitation amplitudes are ranged as 0.18mm 0.2mm, 0.22mm, 0.24mm, 0.26mm 0.28mm and 0.3mm

SMR behaviors that appear in this energy input case for both VIC NES cases.

If the excitation reaches 0.22 mm, the obvious SMR behavior occurs in both cases (Fig. 5.22a-b). In case $b = 11.5$ mm, the SMR appears and reaches its widest frequency bandwidth for [7.31 Hz 7.41 Hz] at the same time. The SMR range of the cubic NES case becomes larger than that of the G = 0.20 mm case.

When G = 0.24mm, the SMR range of Fig. 5.22a remains constant, compared with the previous G = 0.22mm case. In the natural frequency, the response shown in Fig. 5.22a turns into a periodic response, which is considered as the threshold for SMR disappearance for case $b = 11.5$mm. Meanwhile the widest SMR frequency bandwidth in Fig. 5.22b case also reaches at G = 0.24mm for [7.25Hz, 7.41Hz]. In the cubic NES, the SMR range also continues to widen until the excitation amplitude equals 0.24 mm, which is where the cubic NES has the widest SMR bandwidth for [7.147 Hz, 7.473 Hz].

When G = 0.26 mm, the SMR range width remains constant but is located on a higher frequency side of f_0 in (Fig. 5.22a). The SMR disappears at its natural frequency $f_0 = 7.3$Hz in Fig. 5.22b. Therefore, this case is considered as a threshold for SMR disappearance for case $b = 17$mm. The SMR range for cubic NES becomes narrower compared to the previous lower amplitude energy case.

For the higher amplitude inputs (G = 0.28/ 0.30 mm), the SMR intervals of the three cases shift to a higher frequency, and a decrease of the SMR range shown in Fig. 5.22a is observed. In the vicinity of the natural frequency in Fig. 5.22c, the amplitude of the cubic NES tends to become constant. Thus, the excitation amplitude threshold for SMR disappearance for cubic case is recorded as 0.28 mm.

5.4.3 Results analysis

For the sake of simplicity, the results of the target phenomena are summarized in Tab. 5.2. According to the simulation discussed in the previous section, the clearance length b parameter does not influence SMR occurrence. However, an impact observed in our experimental setup leads to the higher required excitation amplitude to trigger the SMR. Our current theoretical tool states that LO and NES amplitudes reach the singularity point $(Z_{2,1}, Z_{1,1})$ of the SIM to satisfy the SMR triggering conditions. From the energy point of view, a loss of energy ensues once the impact occurs, which may prevent the phase trajectory from fully crossing the singularity line $Z_2 = Z_{2,1}$. The system thus requires a larger energy (amplitude) excitation to trigger the SMR. This maght explain

Table 5.2: Effect of clearance length on SMR threshold and distribution.

Case	(a)	(b)	(c)
Threshold for SMR occurrence	0.22mm	0.22mm	0.2mm
Threshold for SMR disappear	0.28mm	0.26mm	0.24mm
Widest SMR interval	0.10Hz	0.16Hz	0.33Hz
SMR interval for G = 0.3mm	0.03Hz	0.106Hz	0.136Hz

the differences in excitation threshold for the SMR. The second row in Tab.5.2 shows an obvious decline in excitation threshold for SMR disappearance. The LO amplitude reaches its local minima when the SMR disappears, which is considered to be an optimal design. By adjusting the clearance length, the VIC NES can be used as an alternative optimal design. The smaller the clearance length, the narrower the widest range of SMR frequency occurrence and the smaller the excitation amplitude threshold value of the SMR disappearance. In the high energy case (G = 0.3mm), the SMR frequency interval is reduced as the clearance length decreases. Compared with the cubic NES case, the SMR bandwidth in case (a) is reduced to 25%, and the case (b) is reduced to 78%. The impact influence on SMR frequency distribution is then essential.

The introduction of impact in the cubic NES damages the robustness of the SMR, as confirmed by both the numerical and experimental tests. If the cubic NES system is well tuned, the impact should be avoided. However, if the cubic NES is not well tuned or is under a weaker excitation amplitude, the displacement constraint (impact) would provide an alternative approach to tune the NES, in order to meet the target excitation without modifying the spring components.

5.5 Conclusions

This current work investigates a novel NES with both cubic nonlinearity and impact conditions using analytical, numerical and experimental methods. According to the clearance length, the Vibro-Impact Cubic (VIC) NES is naturally classified into narrow, modest, and large clearance cases. The corresponding response regimes under various energy input cases were analyzed, leading to the following conclusions:

1. The impact originating from the barrier introduces an extra singularity line in the Slow Invariant Manifold (SIM) structure. When the system is not impacted, the characteristics of the VIC NES are determined by the cubic nonlinearity. The impact threshold is calculated using the asymptotic method. Once the impact occurs, the ensuing response is closer to the conventional Vibro-Impact (VI) NES. The fixed point of the VIC NES at different harmonic excitation amplitudes and frequencies can be accurately predicted using a simplified VI NES model.

2. Some characteristic regions (e.g. the resonance peak, optimal region and Strongly Modulated Response (SMR) regions) are found in the frequency domain. The displacement constraint destroys the robustness of the SMR, resulting in a narrower SMR region. A lower value of the restitution coefficient r accelerates the energy pumping rate during 1:1 resonance. The fixed point of the system is not sensitive to the variation of r.

3. The optimal clearance designs are concentrated. The target excitation must be smaller than $G_{2,c}$ under the framework of the cubic NES in order to make the displacement constraint effective and to absorb energy better than the original design of cubic NES. The piecewise curve of optimal clearance design according to the target excitation is drawn, validated that a lower target excitation requires a narrower clearance length to be tuned as an optimal state.

4. Our experiments confirm the effect that different clearance lengths have on reducing the excitation amplitude threshold for SMR disappearance and on narrowing the SMR frequency interval, which is also obtained by numerical simulation. The target excitation can be adapted optimally by modifying the clearance length. The robustness of the SMR is reduced under the perturbation of the frequency domain for a narrower clearance length.

Conclusions and Perspectives

This thesis is dedicated to passive vibration control via a Nonlinear Energy Sink (NES). NES improves the vibration mitigation effect against the broader frequency excitations, avoiding the occurrence of other resonance peaks, as well as a smaller additional mass, compared to conventional linear absorber. The research contents, no matter analytical, numerical or experimental, are closely focused on the questions proposed in the introduction in order to better understand, design and optimize NES. The responses are almost positive as follows:

- The optimal state is referred to as a stable periodic response after the Strongly Modulated Response (SMR) disappears because of extern energy input saturation both for cubic NES and bistable NES. The damping condition mainly determines the maximal absorbing efficiency in cubic NES. But the bistable NES can overcome this limitation and improve maximal efficiency by introducing the negative stiffness. The experiment proves the feasibility of a tunable cubic nonlinearity strategy for various excitation amplitudes.

- The emergence of chaos and SMR behaviors can be predicted by observing the relative position of trigger lines and unstable regions of SIM. A modest bistable NES design can bring a SMR over the wide frequency range.

- The novel method shows strong robustness to estimate the energy pumping time under the damping, excitation amplitude and cubic nonlinearity distribution. This method can also be extended to the harmonic case.

- The existence of collision compromises the robustness of SMR. The conventional analytical method still possesses the feasibility to describe the response regimes of Vibro Impact Cubic (VIC) NES.

Developed around them, the work of this thesis is structured in five chapters. The first chapter introduces a state of the art of nonlinear absorber. The necessary numerical and analytical tools are presented to access to this thesis. The various sources of nonlinearity classify the NES into two main branches: geometrical nonlinearity configuration and impact configuration, which are the core of our study. The construct method of nonlinearity is presented as well as the presentation of the NES experiment. The final subsection offers the optimal design criteria for NES.

In the second chapter, both response regimes of cubic and bistable NES under various energy levels are manifested. The optimal states for both cubic and bistable NES are identified as a stable periodic motion when the excitation amplitude exceeds the threshold

G_2c. The phase trajectory of the system will eventually arrive at the singularity point of the right stable branch of the Slow Invariant Manifold (SIM). So the maximal efficiency value is extracted as a function of systems parameters. The numerical simulation results in a non-overlap phenomenon of final location of phase trajectory and singularity point. The error of maximal efficiency estimation can be overcome by introducing a correction coefficient in cubic NES. Meanwhile, in the bistable NES, there is no such requirement. The expression of maximal efficiency value indicates that the ceiling of absorption efficiency is independent of the cubic nonlinearity design but is a function of linear oscillator damping and NES damping for cubic NES. Due to the expression for maximum efficiency containing the negative stiffness (δ) in the bistable case, it can have a higher efficiency than cubic NES. The expression of optimal design is given analytically and is verified numerically. The numerical tests show its strong robustness for a higher cubic nonlinearity parameter K design. By adjusting a pre-compression length, the experimental device can realize a tunable negative and cubic nonlinearity parameter to achieve the optimal design facing different excitation amplitudes.

In chapter three, a detailed categorization of bistable NES is addressed. Conventional Manivitch variables can hardly describe the intra-well oscillation of bistable NES. So an adapted complex variables with consideration of equilibria is introduced. The local SIM can describe well this low energy stage. As the excitation amplitude increases, the phase trajectory will expand in the shape of a circle inside the pseudo-separatrix in the phase plane. So a simplified trigger model is proposed to predict the occurrence of chaos when the phase trajectory crosses the pseudo-separatrix. And Melnikov method also provides a parameter boundary to control the occurrence of chaos motion. The trigger mechanism of chaos and SMR is established by identifying the chaos trigger lines to analyze the response regime qualitatively. In the aim to evaluate the weight of the negative stiffness compared to the cubic nonlinearity parameter, four different categories of bistable NES are presented: weak, modest, strong and abnormal bistable NES. Their classification is mainly related to the overlapping of SIM unstable region and chaos region in SIM structure. Weak bistable NES still behaviors like a cubic NES. Modest bistable NES can more easily trigger the SMR. Few chaos motions in strong bistable NES are observed, and SMR almost disappears in abnormal bistable NES. A frequency sweep test shows the broadest range of SMR for a modest bistable NES case. The characteristic response regimes of weak, modest and strong bistable NES are observed in the experiment as the numerical predictions.

In the fourth chapter, a method to estimate the energy pumping time, which defines a process of phase trajectory descent along with the right branch of SIM, has been studied. The expression is abstracted through the multiple scales method. The Hamiltonian system is a foundation for calculating the equivalent point for a damping system under a transient impulsive excitation. In the harmonic excitation case, a particular integration is proposed to describe the descent process for SMR. A procedure for estimating the energy time is introduced. Robustness of calculation is well verified under different parameter perturbations and for both transient and harmonic excitations. It has been found that a more significant NES damping, a more considerable value of negative stiffness or a smaller value of cubic nonlinearity parameter K accelerate the descent process in SMR. The experimental results also show the feasibility of this estimation method in a low energy input case.

In the fifth chapter, a cubic NES with a collision is studied to approach a realistic

environment better. The dynamic modeling has been re-written to adapt to the non-smooth condition. The length of clearance mainly determines the behaviors of this novel configuration. If the clearance is narrow, the requirements for SMR emergence are disrupted. So no SMR is observed in this case. The asymptotic analysis gives the harmonic excitation amplitude threshold to predict the collision occurrence. Better vibration mitigation is found compared with cubic NES in this case. VIC NES performs the same as cubic NES for a modest clearance case when the collision does not appear. However, the collision seems not to affect the excitation threshold of SMR occurrence, which appears simultaneously with impact. A larger clearance does not affect the SMR disappearance significantly. Generally, the collision reduces the distribution area of SMR and leads to the SMR disappearing in a lower amplitude excitation, compared with pure cubic NES. The conventional asymptotic analysis of Vibro-Impact (VI) NES and cubic NES can describe the different regimes of VIC NES with enough accuracy. By designing the length of clearance, VIC NES can adapt various amplitude excitations, which offers the possibility of reforming cubic NES without changing the cubic nonlinearity parameter. The experimental results prove that the collision corrupts the robustness of SMR. The narrower the clearance length, the more limited the frequency range for SMR appearrance.

Following this work, several points of research can be considered:

- Theoretical research
  - SMR is a high efficient energy dissipation method, whose threshold of emergence and disappearance can be well predicted by the existing analytical method. However, NES performs over a wide frequency range, where the trigger mechanism of SMR still requires a more careful study for the wider excitation frequency $\sigma \neq 0$ cases.
  - SMR in modest bistable NES involves the chaos motion. This stage lacks an accurate description. So the prediction of SMR emergence is still a challenge, far less prediction in other frequency conditions.
  - The current main system is replaced by a simplified mass block. In the actual damping design, the main system may have a variety of vibration modes, and the damping effect of NES in other modes is worth discussing.
  - A design criteria under the random excitation of seismic activity can be further studied. The possibility of using deep learning techniques to predict and design system parameters is also worth investigating.
  - As bistable NES can lower the threshold of SMR excitation, tri-stable or multi-stable structures should also achieve this effect, and the specific activation process and the corresponding response regimes deserve in-depth study.
- Experimental research
  - Since control of the pre-compression length of linear spring can adapt different amplitude excitations (or different energy levels), an active control method by applying a linear actuator to control pre-compression length can be further studied.

  - The excited experimental device requires four springs to construct a nonlinear spring. The possibility of substituting certain linear spings with magnetic components can be considered.

- Application

  - With the existence of cubic nonlinearity, a better vibration mitigation performance can be achieved by coupling with other nonlinearity requires further study.
  - Considering the practical application of NES, the vibration mitigation effect of NES is worth considering when the direction of excitation deviates from the direction of design tolerance or under the influence of NES installation location error.

APPENDIX A

Frequency-energy analysis

The Hamilton system reveals the main feature of a nonlinear system. The backbone branches indicate the periodic solutions of the conservative system in the Frequency-Energy Plot (FEP). At first, the backbone of in-phase (S11+) and out-phase (S11-) 1:1 resonance are sought. The influences of cubic nonlinearity parameter and negative stiffness on the deformation of the backbone are presented for bistable Nonlinear Energy Sink (NES). Then, the critical energy level of Strongly Modulated Response (SMR) occurrence and its simplified estimation is presented for the cubic NES case.

A.1 Dynamic modeling

The target system is described schematically in Fig. A.1. The Linear Oscillator (LO) m_1 is excited harmonically through the linear stiffness k_1 and connected with NES mass m_2 by a cubic nonlinearity value k_2 and linear stiffness k_3. The c_1 and c_2 are the damping of LO and NES respectively. x and y are the absolute displacement of m_1 and m_2. The motion equation is:

$$\begin{aligned} &m_1\ddot{x} + k_1 x + c_1\dot{x} + c_2(\dot{x}-\dot{y}) + k_2(x-y)^3 + k_3(x-y) = k_1 x_e + c_1\dot{x}_e \\ &m_2\ddot{y} + c_2(\dot{y}-\dot{x}) + k_2(y-x)^3 + k_3(y-x) = 0 \end{aligned} \tag{A.1}$$

The harmonic excitation is expressed as $x_e = Gcos(\omega t)$. If the linear stiffness value k_3 is shifted to be zero or negative, equation. (A.1) can describe the pure cubic and bistable

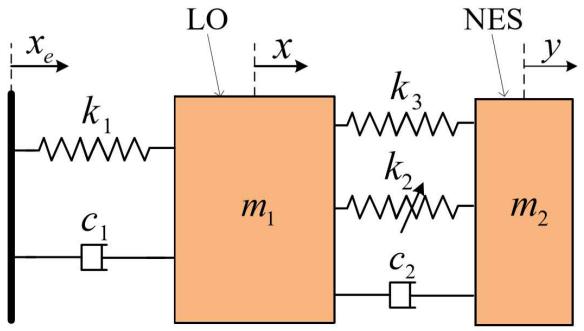

Figure A.1: Schematic of linear oscillator and NES system

NES. By introducing the variables:

$$\begin{aligned}\epsilon = \frac{m_2}{m_1}, \omega_0^2 = \frac{k_1}{m_1}, K = \frac{k_2}{m_2\omega_0^2}, \delta = \frac{k_3}{m_2\omega_0^2} \\ \lambda_1 = \frac{c_1}{m_2\omega_0}, \lambda_2 = \frac{c_2}{m_2\omega_0}, F = \frac{G}{\epsilon}, \Omega = \frac{\omega}{\omega_0}, \tau = \omega_0 t\end{aligned} \tag{A.2}$$

the equations of motion can be rewritten as:

$$\begin{aligned}&\ddot{x} + x + \epsilon\lambda_1\dot{x} + \epsilon\lambda_2(\dot{x} - \dot{y}) + \epsilon K(x - y)^3 + \epsilon\delta(x - y) = \epsilon F\cos\Omega\tau - \epsilon^2 F\lambda_1\Omega\sin\Omega\tau \\ &\epsilon\ddot{y} + \epsilon\lambda_2(\dot{y} - \dot{x}) + \epsilon K(y - x)^3 + \epsilon\delta(y - x) = 0\end{aligned} \tag{A.3}$$

Since ϵ is a small parameter, the term containing ϵ^2 in Eq. A.3 can be ignored in the following deduction.

To study the features of in-phase (S11+) and out-of-phase (S11-) 1:1 resonance, the frequency-energy plot depicts the main backbone branch of these synchronous period orbits. Initially, by assuming $\lambda_1 = \lambda_2 = 0$, $F = 0$, Eq. (A.3) is converted into the Hamiltonian version. Then the complex variables $\psi_1 e^{i\Omega\tau} = \dot{x} + i\Omega x$ and $\psi_2 e^{i\Omega\tau} = \dot{y} + i\Omega y$ where $i^2 = -1$ are introduced into Eq. (A.3). This complexification approach is also applied [Lee *et al.*, 2005a]. The $\psi_j, j = 1, 2$ represents the 'slow' complex part variation of amplitude, $\bar{\psi}_j, j = 1, 2$ is the corresponding conjugate complex and the Ω is the 'fast' oscillation of frequency. By averaging over the fast frequency, it gives:

$$\begin{aligned}&\dot{\psi}_1 - \frac{i\delta\varepsilon\left(\psi_1 - \psi_2\right)}{2\Omega} - \frac{i\psi_1}{\Omega} + \frac{i\Omega\psi_1}{2} + \frac{3iK\varepsilon}{8\Omega^3}\left(\psi_2^2\bar{\psi}_2 - \psi_1^2\bar{\psi}_1\right. \\ &\left.+\psi_1^2\bar{\psi}_2 - \psi_2^2\bar{\psi}_1 - 2\psi_1\psi_2\bar{\psi}_2 + 2\psi_1\bar{\psi}_1\psi_2\right) = 0 \\ &\dot{\psi}_2 + \frac{i\delta\varepsilon\left(\psi_1 - \psi_2\right)}{2\Omega} + \frac{i\Omega\psi_2\varepsilon}{2} + \frac{3iK\varepsilon}{8\Omega^3}\left(-\psi_2^2\bar{\psi}_2 + \psi_1^2\bar{\psi}_1\right. \\ &\left.-\psi_1^2\bar{\psi}_2 + \psi_2^2\bar{\psi}_1 + 2\psi_1\psi_2\bar{\psi}_2 - 2\psi_1\bar{\psi}_1\psi_2\right) = 0\end{aligned} \tag{A.4}$$

To study the evolution of amplitude, the polar forms $\psi_1 = A_1 e^{i\Theta_1}$ and $\psi_2 = A_2 e^{i\Theta_2}$ are substituted. The A_1, A_2, Θ_1 and Θ_2 represent the slow evolution of amplitudes and phases of 1:1 resonance of LO and NES. Obviously, on the periodic solution branch $S11\pm$, the condition $\Theta_1 = \Theta_2$ is trivially satisfied according to [Romeo *et al.*, 2015b]. Then Eq. (A.5) is obtained in the following forms:

$$\begin{aligned}&\frac{\Omega A_1}{2} - \frac{\epsilon\delta\left(A_1 - A_2\right) + A_1}{2\Omega} - \frac{3}{8}\frac{K\varepsilon\left(A_1 - A_2\right)^3}{\Omega^3} = 0 \\ &\frac{\Omega A_2\epsilon}{2} + \frac{\epsilon\delta\left(A_1 - A_2\right)}{2\Omega} + \frac{3}{8}\frac{K\epsilon\left(A_1 - A_2\right)^3}{\Omega^3} = 0\end{aligned} \tag{A.5}$$

The approximate responses $x(\tau) = (A_1/\Omega)cos(\Omega\tau)$ and $y(\tau) = (A_2/\Omega)cos(\Omega\tau)$ can be obtained by solving the above amplitude equation (Eq. (A.5)). The amplitude of $x(\tau)$ and $y(\tau)$ are given by: $Y(\Omega) = A_1/\Omega$ and $V(\Omega) = A_2/\Omega$ respectively where:

$$\begin{aligned}A_1 &= \frac{2}{3}\frac{\Omega^3\sqrt{K\left(\Omega^2\varepsilon + \Omega^2 - 1\right)\left(\Omega^4 - \Omega^2\delta\varepsilon - \Omega^2\delta - \Omega^2 + \delta\right)}\sqrt{3}\varepsilon}{K\left(\Omega^2\varepsilon + \Omega^2 - 1\right)^2} \\ A_2 &= -\frac{2}{3}\frac{\sqrt{3}\sqrt{K\left(\Omega^2\varepsilon + \Omega^2 - 1\right)\left(\Omega^4 - \Omega^2\delta\varepsilon - \Omega^2\delta - \Omega^2 + \delta\right)}\Omega\left(\Omega^2 - 1\right)}{K\left(\Omega^2\varepsilon + \Omega^2 - 1\right)^2}\end{aligned} \tag{A.6}$$

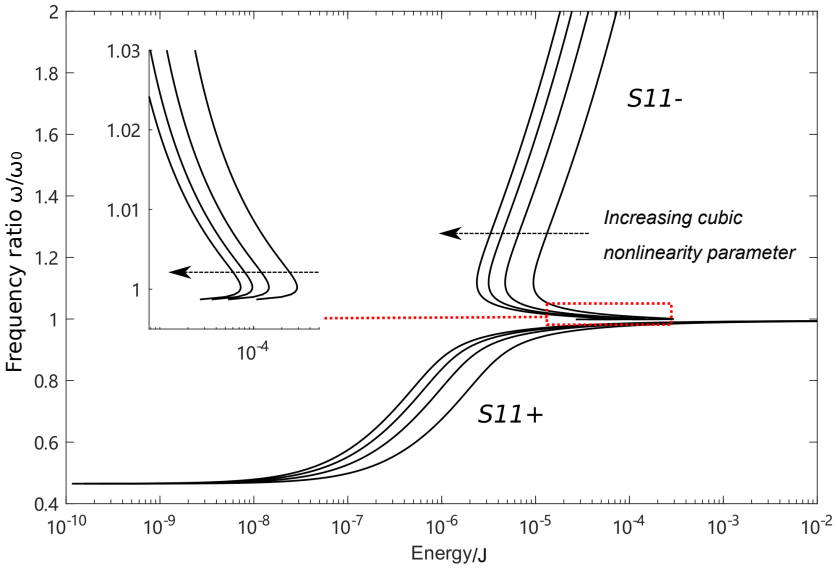

Figure A.2: Frequency-energy plot for the different cubic nonlinearity parameters K, $\epsilon = 0.01$, $\delta = -0.44$, (K values are selected as 1000, 2000, 3000 and 4000 respectively, following the direction of the arrow). Zoomed insert represents detailed curve trends in the region in the red frame, near the frequency 1

.

The conservative energy of the system follows:

$$E(\Omega) = \frac{1}{2}\varepsilon\delta(V-Y)^2 + \frac{1}{4}\varepsilon K(V-Y)^4 + \frac{1}{2}Y^2 \tag{A.7}$$

Combining the expression of Y and V, Eq. (A.7) leads to Fig. A.2 and A.3 under the influence of K and δ. The curve is divided into two branches by the forbidden zone [Lee *et al.*, 2008], where the ratio of two real positive amplitudes becomes negative. The $S11-$ exists only the upper branch ($\Omega > 1$) and the $S11+$ exists for $\Omega < \sqrt{1/(1+\varepsilon)}$. The saddle points on the $S11-$ can be calculated by deriving the conservative system energy with respect to Ω, $\dot{E(\Omega)} = 0$. The two real roots correspond to the frequency of Ω_1 and Ω_2 of saddle point 1 and point 2, and their energy levels $E_1 = E(\Omega_1), E_2 = E(\Omega_2)$ (see Fig. A.4). The energy interval $[E_1, E_2]$ plays an essential role in Targeted Energy Transfer (TET) mechanism on the $S11-$ branch. And the optimal TET energy region corresponds to the interval $[E_1, E_2]$ in the detailed frequency-energy plot in Fig.A.4.

Fig. A.2 shows the influence of increasing K values on the energy level of saddle point 2. A lower K can adapt to the higher energy level for efficient TET. An interesting phenomenon is that the ratio of energy interval E_1/E_2 is almost constant in Fig. A.2, which shows the parallel translation of the upper $S11-$ branch on the logarithmic axis with the variation of K.

Increasing negative stiffness results in extending the distance between the saddle points $[E_1, E_2]$ in Fig. A.3. It improves the performance of energy transfer for relatively high energy input. Hence, K and δ can be tailored to absorb certain input energies.

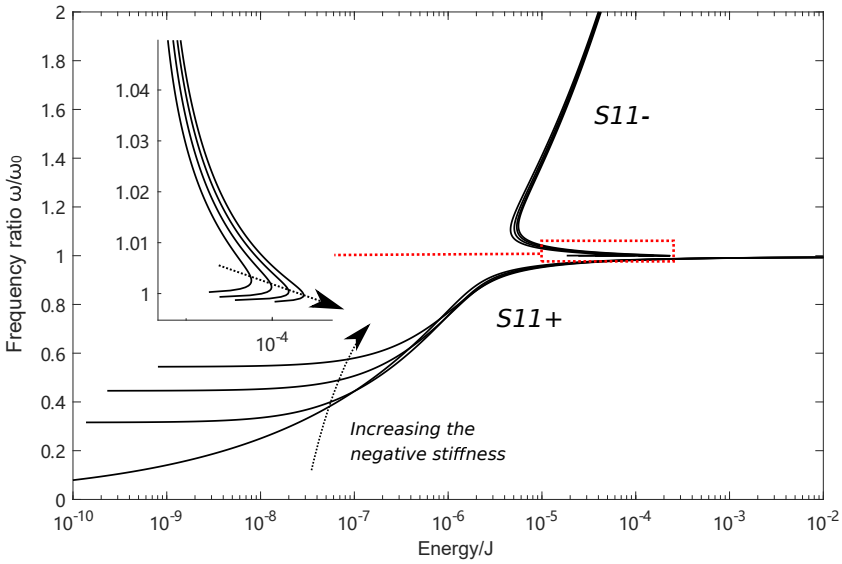

Figure A.3: Frequency-energy plot for the different linear negative stiffnesses δ ($\epsilon = 0.01$, $K = 1742$, δ value is selected as 0, -0.2, -0.4 and -0.6 respectively, following the direction of the arrow). Zoomed plot represents detailed curve trends in the region marked in red frame, near the frequency 1

A.2 Influence of damping and cubic nonlinearity on conservative energy

The saddle points on the $S11-$ can be calculated by deriving the conservative system energy with respect to Ω, $\dot{E}(\Omega) = 0$. The two real roots correspond to the frequency of Ω_1 and Ω_2 of saddle point 1 and point 2, and their energy levels $E_1 = E(\Omega_1), E_2 = E(\Omega_2)$ (see Fig. A.4). The energy interval $[E_1, E_2]$ plays an essential role in TET mechanism on the $S11-$ branch. And the optimal TET energy region corresponds to the interval $[E_1, E_2]$ in the detailed of frequency-energy plot in Fig.A.4.

To describe the conservative energy $E(\Omega)$ in a cubic non-conservative system, the critical energy level ($G = 0.22$mm and $G = 0.38$mm) before the SMR occurs and after it disappears are presented with zero initial condition in Fig. A.4. The system parameters for the simulation are selected as $\epsilon = 0.01, K = 1742, \lambda_1 = 1.67, \lambda_2 = 0.167$. Those parameters are also fixed for the simulation in following section.

The energy level when SMR appears (blue line) almost coincides with the saddle point (ω_1, E_1), and the energy level when SMR disappears (red line) is close to the endpoints of the upper branch energy level E_1. The conservative energy level when SMR disappears (red line in Fig. A.4) is much lower than that when SMR occurs. This shows that energy has been dissipated through the SMR mechanism even if the input energy continues to increase from blue line state to red line state.

The influence of the damping parameter on the conservative energy in the systems is analyzed in Fig. A.5. The red curve is the SMR interval, which is an unstable region. Its stability is confirmed by Floquet theory. Under the various damping parameters, the level of conservative energy necessary to trigger the SMR is almost constant, about $5.7 \times 10^{-5} J$. For the energy level for SMR to disappear, the λ_2 have a more significant impact on the

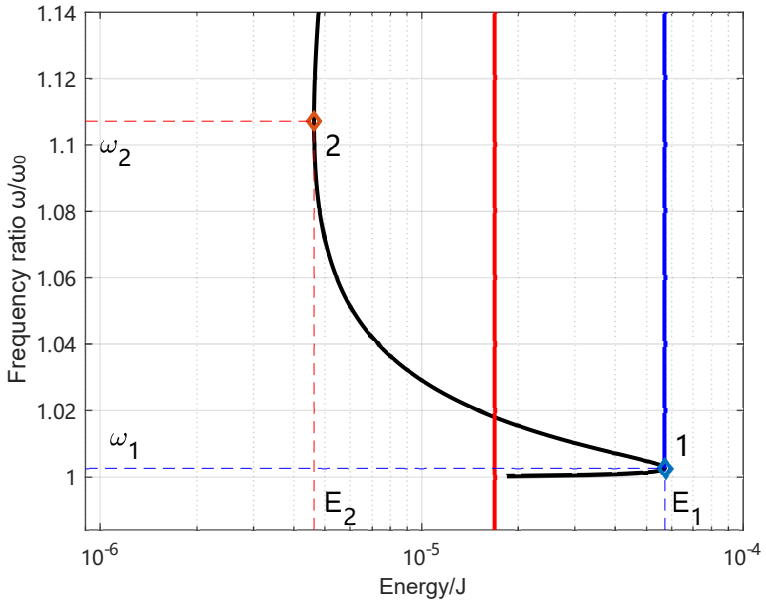

Figure A.4: Energy range of intensive energy exchange in cubic NES case. The black curve is the backbone of the frequency-energy relation, the blue line is the threshold energy for SMR appearance (G = 0.22mm), and the red line is the threshold energy (G = 0.38mm) for SMR disappearance. Both critical energy levels are simulated in a zero initial condition.

determination of the critical value, the curve groups with the same λ_2 result in similar local minima.

To explain why the trigger conservative energy level is the same under different damping conditions, a 'weak damping' assumption is proposed, where λ_2 tends to be zeros. On the SIM, the ratio of the amplitude of LO and NES at the singularity point $[Z_{2,1}, Z_{1,1}]$ is 1.5. The exsitence of the small parameter ϵ results in the conservative energy is mainly governed the amplitude of LO, so it becomes $E \approx \frac{1}{2}Y^2 = \frac{8}{81K}$. The trigger energy level is determined mainly by the cubic nonlinearity parameter K.

In order to verify the correctness of this approximation, the critical energy levels calculated using the different methods are compared in Tab. A.1. The first column is the energy level at the saddle point (E_1, ω_1). The stable amplitude of LO and NES before the SMR appears is calculated using the numerical method that forms the second column. The third column is the predicted trigger energy level. In the same cubic nonlinearity condition, the three critical trigger energy levels are practically the same, which confirms that this approximation $\frac{8}{81K}$ is correct and is determined mainly by K.

It can be clearly observed that the conservative energy when SMR starts to occur is the same as the energy level of a saddle point in Fig. A.6, which shows the frequency-energy relationship for different cubic nonlinearity parameters. This means that the conservative energy threshold at the saddle point (E_1, ω_1) can be considered as an indication that SMR occurs. It is difficult to obtain an analytical expression for the energy level at the saddle point based on the previous discussion. However, the simulations of different damping parameters and different cubic nonlinearity parameters in Fig. A.5 and A.6 reveal that the SMR always happens when the system's conservative energy achieves its critical value.

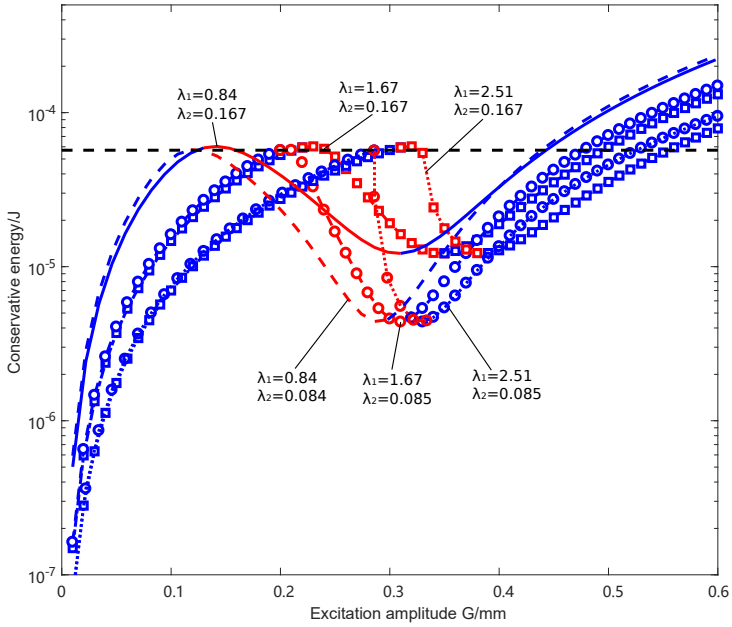

Figure A.5: Variety of the conservative energy in the different damping systems ($\epsilon = 0.01, K = 1742$). The blue curve is calculated by stable solution, the red curve is calculated by unstable amplitude, the black dashed line represents the energy level $5.7 \times 10^{-5} J$

Table A.1: The comparison of SMR occurs energy level in different cubic nonlinearity parameters K cases

K	Energy level in saddle point/J	Calculated trigger energy level/J	$\frac{8}{81K}$
2613	3.82e-5	3.81e-5	3.83e-5
1742	5.73e-5	5.71e-5	5.67e-5
871	1.15e-4	1.15e-4	1.15e-4

This critical energy level is determined mainly by the cubic nonlinearity parameter K without considering the damping condition. This can help us predict the occurrences of SMR without having precise knowledge of the damping parameters in cubic NES case.

The conservative system shows the inherent properties of the non-conservative system. An increase in cubic nonlinearity parameter leads the frequency-energy backbone of the conservative system to move to a lower energy level. This movement implies that the corresponding NES system can sustain a lower optimal energy input in a non-conservative system. The negative stiffness acts as the opposite of cubic nonlinearity parameter. Before the SMR occurs, the conservative energy level of the cubic NES system is always located at the saddle point of the $S11-$ branch. The cubic nonlinearity parameter mainly determines this critical energy level. So this saddle point can be considered as an indication that SMR occurs.

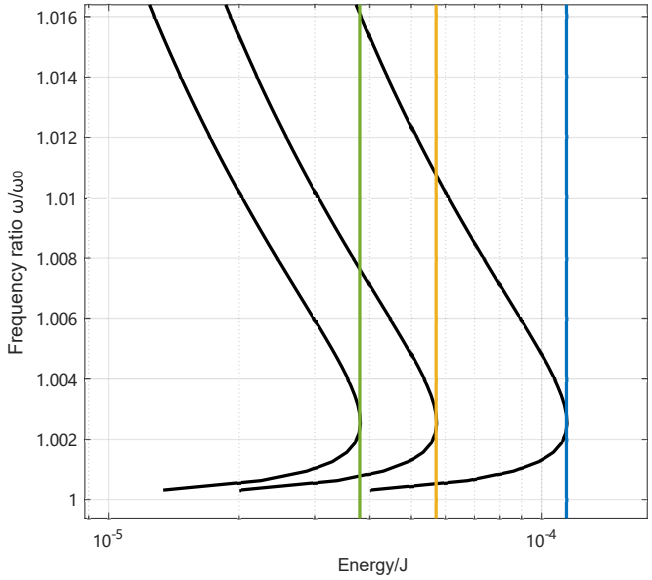

Figure A.6: Critical energy level triggering SMR for different cubic nonlinearity parameters K on the frequency-energy plot (blue: $K = 2613$; yellow: $K = 1742$; green: $K = 871$). The K of black backbones from right to left are same with condition corresponding to tangent colourful lines

Glossary of principle abbreviation

AA:	Action-Angle
CX-A:	Complexification-averaging
DOF:	Degree Of Freedom
ER:	Electrorheological
FEP:	Frequency Energy Plot
FFT:	Fast Fourier Transform
HBM:	Harmonic Balance Method
HCVI NES:	Hybrid Cubic Vibro-Impact Nonlinear Energy Sink
IHBM:	Incremental Harmonic Balance Method
LCO:	Limit Cycle Oscillation
LE:	Lyapunov exponent
LNM	Linear Normal Mode
LO:	Linear Oscillator
LPT:	Limiting Phase Trajectory
MR:	Magnetorheological
MS NES:	Magnetic-Strung Nonlinear Energy Sink
MSM:	Multiple Scales Method
NES:	Nonlinear Energy Sink
NNM:	Nonlinear Normal Mode
ODE:	Ordinary Differential Equation
SIM:	Slow Invariant Manifold
SMR:	Strongly Modulated Response
TET:	Targeted Energy Transfer
TMD:	Tuned Mass Damper
VI NES:	Vibro-Impact Nonlinear Energy Sink
VIC NES:	Vibro-Impact Cubic Nonlinear Energy Sink
WT:	Wavelet Transforms

Bibliography

[Ahmadabadi et Khadem, 2014] Ahmadabadi, Z. N. et Khadem, S. (2014). Nonlinear vibration control and energy harvesting of a beam using a nonlinear energy sink and a piezoelectric device. *Journal of Sound and Vibration*, 333(19):4444–4457. *Cited page 29*

[Al-Shudeifat *et al.*, 2013] Al-Shudeifat, M. A., Wierschem, N., Quinn, D. D., Vakakis, A. F., Bergman, L. A. et Spencer Jr, B. F. (2013). Numerical and experimental investigation of a highly effective single-sided vibro-impact non-linear energy sink for shock mitigation. *International journal of non-linear mechanics*, 52:96–109. *Cited page 65*

[Aldemir *et al.*, 2001] Aldemir, U., Bakioglu, M. et Akhiev, S. (2001). Optimal control of linear buildings under seismic excitations. *Earthquake engineering & structural dynamics*, 30(6):835–851. *Cited page 9*

[Avramov et Mikhlin, 2010] Avramov, K. et Mikhlin, Y. (2010). Nonlinear normal modes for vibrating mechanical systems. review of theoretical developments. *Applied Mechanics Reviews*. *Cited page 19*

[Babitsky, 2013] Babitsky, V. I. (2013). *Theory of vibro-impact systems and applications*. Springer Science & Business Media. *Cited page 15*

[Bakre et Jangid, 2007] Bakre, S. et Jangid, R. (2007). Optimum parameters of tuned mass damper for damped main system. *Structural Control and Health Monitoring: The Official Journal of the International Association for Structural Control and Monitoring and of the European Association for the Control of Structures*, 14(3):448–470. *Cited page 7*

[Bapat, 1995] Bapat, C. (1995). The general motion of an inclined impact damper with friction. *Journal of Sound and Vibration*, 184(3):417–427. *Cited page 15*

[Bapat *et al.*, 1983] Bapat, C., Popplewell, N. et McLachlan, K. (1983). Stable periodic motions of an impact-pair. *Journal of Sound and Vibration*, 87(1):19–40. *Cited page 15*

[Bapat et Sankar, 1985] Bapat, C. et Sankar, S. (1985). Single unit impact damper in free and forced vibration. *Journal of Sound and Vibration*, 99(1):85–94. *Cited page 15*

[Bellet *et al.*, 2012] Bellet, R., Cochelin, B., Côte, R. et Mattei, P.-O. (2012). Enhancing the dynamic range of targeted energy transfer in acoustics using several nonlinear membrane absorbers. *Journal of Sound and Vibration*, 331(26):5657–5668. *4 citations pages ix, 13, 14, et 24*

[Bellet *et al.*, 2010] Bellet, R., Cochelin, B., Herzog, P. et Mattei, P.-O. (2010). Experimental study of targeted energy transfer from an acoustic system to a nonlinear membrane absorber. *Journal of Sound and Vibration*, 329(14):2768–2791. *4 citations pages x, 13, 24, et 26*

[Bergeot *et al.*, 2016] Bergeot, B., Bellizzi, S. et Cochelin, B. (2016). Analysis of steady-state response regimes of a helicopter ground resonance model including a non-linear energy sink attachment. *International Journal of Non-Linear Mechanics*, 78:72–89. *Cited page 28*

[Bergeot *et al.*, 2017] Bergeot, B., Bellizzi, S. et Cochelin, B. (2017). Passive suppression of helicopter ground resonance using nonlinear energy sinks attached on the helicopter blades. *Journal of Sound and Vibration*, 392:41–55. *Cited page 28*

[Bitar *et al.*, 2020] Bitar, D., Savadkoohi, A. T., Lamarque, C.-H., Gourdon, E. et Collet, M. (2020). Extended complexification method to study nonlinear passive control. *Nonlinear Dynamics*, 99(2):1433–1450. *Cited page 21*

[Bitaraf *et al.*, 2010] Bitaraf, M., Ozbulut, O. E., Hurlebaus, S. et Barroso, L. (2010). Application of semi-active control strategies for seismic protection of buildings with mr dampers. *Engineering Structures*, 32(10):3040–3047. *Cited page 9*

[Boroson *et al.*, 2017] Boroson, E., Missoum, S., Mattei, P.-O. et Vergez, C. (2017). Optimization under uncertainty of parallel nonlinear energy sinks. *Journal of Sound and Vibration*, 394:451–464. *Cited page 31*

[Braydi *et al.*, 2020] Braydi, O., Gogu, C. et Paredes, M. (2020). Robustness and reliability investigations on a nonlinear energy sink device concept. *Mechanics and Industry*, 21(6):603. *Cited page 57*

[Cai *et al.*, 2007] Cai, C., Wu, W. et Araujo, M. (2007). Cable vibration control with a tmd-mr damper system: Experimental exploration. *Journal of structural engineering*, 133(5):629–637. *Cited page 8*

[Cao *et al.*, 2020] Cao, Y., Yao, H., Li, Q., Yang, P. et Wen, B. (2020). Vibration mitigation and dynamics of a rotor-blade system with an attached nonlinear energy sink. *International Journal of Non-Linear Mechanics*, 127:103614. *Cited page 28*

[Chavarette *et al.*, 2010] Chavarette, F. R., Balthazar, J. M., Felix, J. L. *et al.* (2010). Remarks on an optimal linear control design applied to a nonideal and an ideal structure coupled to an essentially nonlinear oscillator. *Journal of computational and nonlinear dynamics*, 5(2):1–8. *Cited page 31*

[Cheung *et al.*, 1990] Cheung, Y., Chen, S. et Lau, S. (1990). Application of the incremental harmonic balance method to cubic non-linearity systems. *Journal of Sound and Vibration*, 140(2):273–286. *Cited page 20*

[Cho *et al.*, 2020] Cho, S. G., Chang, S. et Sung, D. (2020). Application of tuned mass damper to mitigation of the seismic responses of electrical equipment in nuclear power plants. *Energies*, 13(2):427. *Cited page 8*

[De Souza et Caldas, 2004] De Souza, S. L. et Caldas, I. L. (2004). Calculation of lyapunov exponents in systems with impacts. *Chaos, Solitons & Fractals*, 19(3):569–579. *Cited page 23*

[Dekemele *et al.*, 2019] Dekemele, K., Van Torre, P. et Loccufier, M. (2019). Performance and tuning of a chaotic bi-stable nes to mitigate transient vibrations. *Nonlinear Dynamics*, 98(3):1831–1851. *4 citations pages 23, 57, 65, et 103*

[Dekemele *et al.*, 2020] Dekemele, K., Van Torre, P. et Loccufier, M. (2020). Design, construction and experimental performance of a nonlinear energy sink in mitigating multi-modal vibrations. *Journal of Sound and Vibration*, 473:115243. *3 citations pages x, 25, et 26*

[Duan *et al.*, 2021a] Duan, N., Lin, S., Wu, Y., Sun, X.-M. et Zhong, C. (2021a). Stability analysis of a pipe conveying fluid with a nonlinear energy sink. *Science China Information Sciences*, 64(5):1–15. *Cited page 27*

[Duan *et al.*, 2021b] Duan, N., Wu, Y., Sun, X.-M. et Zhong, C. (2021b). Vibration control of conveying fluid pipe based on inerter enhanced nonlinear energy sink. *IEEE Transactions on Circuits and Systems I: Regular Papers*, 68(4):1610–1623. *Cited page 27*

[Erturk et Inman, 2011] Erturk, A. et Inman, D. J. (2011). Broadband piezoelectric power generation on high-energy orbits of the bistable duffing oscillator with electromechanical coupling. *Journal of Sound and Vibration*, 330(10):2339–2353. *Cited page 14*

[Fang *et al.*, 2021] Fang, S., Chen, K., Xing, J., Zhou, S. et Liao, W.-H. (2021). Tuned bistable nonlinear energy sink for simultaneously improved vibration suppression and energy harvesting. *International Journal of Mechanical Sciences*, 212:106838. *Cited page 12*

[Fang *et al.*, 2017] Fang, X., Wen, J., Yin, J. et Yu, D. (2017). Highly efficient continuous bistable nonlinear energy sink composed of a cantilever beam with partial constrained layer damping. *Nonlinear Dynamics*, 87(4):2677–2695. *3 citations pages ix, 12, et 14*

[Farid, 2021] Farid, M. (2021). Dynamics of a hybrid cubic vibro-impact oscillator and nonlinear energy sink. *arXiv preprint arXiv:2106.02123*. *Cited page 118*

[Farshidianfar et Saghafi, 2014a] Farshidianfar, A. et Saghafi, A. (2014a). Global bifurcation and chaos analysis in nonlinear vibration of spur gear systems. *Nonlinear Dynamics*, 75(4):783–806. *2 citations pages 22 et 65*

[Farshidianfar et Saghafi, 2014b] Farshidianfar, A. et Saghafi, A. (2014b). Identification and control of chaos in nonlinear gear dynamic systems using melnikov analysis. *Physics Letters A*, 378(46):3457–3463. *Cited page 22*

[Frahm, 1911] Frahm, H. (1911). Device for damping vibrations of bodies. US Patent 989,958. *Cited page 7*

[Fuller *et al.*, 1996] Fuller, C. C., Elliott, S. et Nelson, P. A. (1996). *Active control of vibration*. Academic Press. *Cited page 9*

[Gendelman, 2011] Gendelman, O. (2011). Targeted energy transfer in systems with external and self-excitation. *Proceedings of the Institution of Mechanical Engineers, Part C: Journal of Mechanical Engineering Science*, 225(9):2007–2043. *Cited page 24*

[Gendelman, 2012] Gendelman, O. (2012). Analytic treatment of a system with a vibro-impact nonlinear energy sink. *Journal of Sound and Vibration*, 331(21):4599–4608. *Cited page 15*

[Gendelman, 2008] Gendelman, O. V. (2008). Targeted energy transfer in systems with non-polynomial nonlinearity. *Journal of Sound and Vibration*, 315(3):732–745. *2 citations pages 20 et 34*

[Gendelman et Lamarque, 2005] Gendelman, O. V. et Lamarque, C.-H. (2005). Dynamics of linear oscillator coupled to strongly nonlinear attachment with multiple states of equilibrium. *Chaos, Solitons & Fractals*, 24(2):501–509. *Cited page 11*

[Gendelman et Starosvetsky, 2006] Gendelman, O. V. et Starosvetsky, Y. (2006). Quasi-Periodic Response Regimes of Linear Oscillator Coupled to Nonlinear Energy Sink Under Periodic Forcing. *Journal of Applied Mechanics*, 74(2):325–331. *Cited page 15*

[Gourc, 2013] Gourc, E. (2013). *Etude du contrôle passif par pompage énergétique sous sollicitation harmonique: Analyses théoriques et expérimentales*. Thèse de doctorat, Toulouse, INSA. *4 citations pages ix, 12, 34, et 125*

[Gourc *et al.*, 2012] Gourc, E., Michon, G., Seguy, S. et Berlioz, A. (2012). Design optimisation of a nonlinear energy sink embedded on a harmonically forced linear oscillator: theoretical and experimental developments. *In International Design Engineering Technical Conferences and Computers and Information in Engineering Conference*, volume 45004, pages 589–598. American Society of Mechanical Engineers. *2 citations pages 10 et 22*

[Gourc *et al.*, 2014] Gourc, E., Michon, G., Seguy, S. et Berlioz, A. (2014). Experimental investigation and design optimization of targeted energy transfer under periodic forcing. *Journal of Vibration and Acoustics*, 136(2). *2 citations pages 30 et 133*

[Gourc *et al.*, 2015a] Gourc, E., Michon, G., Seguy, S. et Berlioz, A. (2015a). Targeted energy transfer under harmonic forcing with a vibro-impact nonlinear energy sink: analytical and experimental developments. *Journal of Vibration and Acoustics*, 137(3). *4 citations pages x, 10, 25, et 26*

[Gourc *et al.*, 2015b] Gourc, E., Seguy, S., Michon, G., Berlioz, A. et Mann, B. (2015b). Quenching chatter instability in turning process with a vibro-impact nonlinear energy sink. *Journal of Sound and Vibration*, 355:392–406. *Cited page 27*

[Gourdon *et al.*, 2007] Gourdon, E., Alexander, N. A., Taylor, C. A., Lamarque, C.-H. et Pernot, S. (2007). Nonlinear energy pumping under transient forcing with

strongly nonlinear coupling: Theoretical and experimental results. *Journal of sound and vibration*, 300(3-5):522–551. *2 citations pages ix et 10*

[Grinberg *et al.*, 2012] Grinberg, I., Lanton, V. et Gendelman, O. (2012). Response regimes in linear oscillator with 2dof nonlinear energy sink under periodic forcing. *Nonlinear Dynamics*, 69(4):1889–1902. *3 citations pages ix, 16, et 17*

[Guckenheimer et Holmes, 2013] Guckenheimer, J. et Holmes, P. (2013). *Nonlinear oscillations, dynamical systems, and bifurcations of vector fields*, volume 42. Springer Science & Business Media. *2 citations pages 22 et 74*

[Guo *et al.*, 2017] Guo, H., Liu, B., Yu, Y., Cao, S. et Chen, Y. (2017). Galloping suppression of a suspended cable with wind loading by a nonlinear energy sink. *Archive of Applied Mechanics*, 87(6):1007–1018. *Cited page 28*

[Habib et Romeo, 2017] Habib, G. et Romeo, F. (2017). The tuned bistable nonlinear energy sink. *Nonlinear Dynamics*, 89(1):179–196. *Cited page 16*

[Harne et Wang, 2013] Harne, R. L. et Wang, K. (2013). A review of the recent research on vibration energy harvesting via bistable systems. *Smart materials and structures*, 22(2):023001. *Cited page 28*

[Hoang *et al.*, 2008] Hoang, N., Fujino, Y. et Warnitchai, P. (2008). Optimal tuned mass damper for seismic applications and practical design formulas. *Engineering structures*, 30(3):707–715. *Cited page 7*

[Huang *et al.*, 2019] Huang, D., Li, R. et Yang, G. (2019). On the dynamic response regimes of a viscoelastic isolation system integrated with a nonlinear energy sink. *Communications in Nonlinear Science and Numerical Simulation*, 79:104916. *Cited page 31*

[Hui *et al.*, 2008] Hui, L., Hongbin, G. et Dawei, C. (2008). Application of high-speed solenoid valve to the semi-active control of landing gear. *Chinese Journal of Aeronautics*, 21(3):232–240. *Cited page 9*

[Jazar *et al.*, 2007] Jazar, G., Mahinfalah, M. et Deshpande, S. (2007). Design of a piecewise linear vibration isolator for jump avoidance. *Proceedings of the Institution of Mechanical Engineers, Part K: Journal of Multi-body Dynamics*, 221(3):441–449. *Cited page 29*

[Jian *et al.*, 2021] Jian, Z., Minglong, X., Zhichun, Y. et Yingsong, G. (2021). Suppressing nonlinear aeroelastic response of laminated composite panels in supersonic airflows using a nonlinear energy sink. *Chinese Journal of Aeronautics*, 34(2):376–385. *Cited page 27*

[Jiang *et al.*, 2005] Jiang, D., Pierre, C. et Shaw, S. (2005). Nonlinear normal modes for vibratory systems under harmonic excitation. *Journal of sound and vibration*, 288(4-5):791–812. *Cited page 19*

[Jiang *et al.*, 2003] Jiang, X., McFarland, D. M., Bergman, L. A. et Vakakis, A. F. (2003). Steady state passive nonlinear energy pumping in coupled oscillators: theoretical and experimental results. *Nonlinear Dynamics*, 33(1):87–102. *3 citations pages 10, 15, et 24*

[Johnson *et al.*, 2013] Johnson, D. R., Thota, M., Semperlotti, F. et Wang, K. (2013). On achieving high and adaptable damping via a bistable oscillator. *Smart Materials and Structures*, 22(11):115027. *Cited page 14*

[Jutte et Kota, 2008] Jutte, C. V. et Kota, S. (2008). Design of Nonlinear Springs for Prescribed Load-Displacement Functions. *Journal of Mechanical Design*, 130(8). 081403. *Cited page 29*

[Karnopp *et al.*, 1974] Karnopp, D., Crosby, M. J. et Harwood, R. A. (1974). Vibration Control Using Semi-Active Force Generators. *Journal of Engineering for Industry*, 96(2):619–626. *Cited page 8*

[Kerschen *et al.*, 2008] Kerschen, G., Gendelman, O., Vakakis, A. F., Bergman, L. A. et McFarland, D. M. (2008). Impulsive periodic and quasi-periodic orbits of coupled oscillators with essential stiffness nonlinearity. *Communications in Nonlinear Science and Numerical Simulation*, 13(5):959–978. *Cited page 19*

[Kerschen *et al.*, 2007] Kerschen, G., Kowtko, J. J., McFarland, D. M., Bergman, L. A. et Vakakis, A. F. (2007). Theoretical and experimental study of multimodal targeted energy transfer in a system of coupled oscillators. *Nonlinear Dynamics*, 47(1): 285–309. *2 citations pages ix et 18*

[Kerschen *et al.*, 2005] Kerschen, G., Lee, Y. S., Vakakis, A. F., McFarland, D. M. et Bergman, L. A. (2005). Irreversible passive energy transfer in coupled oscillators with essential nonlinearity. *SIAM Journal on Applied Mathematics*, 66(2):648–679. *2 citations pages 19 et 24*

[Kremer et Liu, 2014] Kremer, D. et Liu, K. (2014). A nonlinear energy sink with an energy harvester: transient responses. *Journal of sound and vibration*, 333(20):4859–4880. *Cited page 29*

[Krenk, 2005] Krenk, S. (2005). Frequency Analysis of the Tuned Mass Damper. *Journal of Applied Mechanics*, 72(6):936–942. *3 citations pages ix, 7, et 9*

[Lamarque *et al.*, 2011] Lamarque, C.-H., Gendelman, O. V., Savadkoohi, A. T. et Etcheverria, E. (2011). Targeted energy transfer in mechanical systems by means of non-smooth nonlinear energy sink. *Acta mechanica*, 221(1):175–200. *5 citations pages ix, 16, 20, 21, et 22*

[Lee *et al.*, 2008] Lee, Y., Vakakis, A. F., Bergman, L., McFarland, D., Kerschen, G., Nucera, F., Tsakirtzis, S. et Panagopoulos, P. (2008). Passive non-linear targeted energy transfer and its applications to vibration absorption: a review. *Proceedings of the Institution of Mechanical Engineers Part K Journal of Multi-body Dynamics*, 222(2):77–134. *2 citations pages 16 et 151*

[Lee *et al.*, 2007a] Lee, Y. S., Kerschen, G., McFarland, D. M., Hill, W. J., Nichkawde, C., Strganac, T. W., Bergman, L. A. et Vakakis, A. F. (2007a). Suppressing aeroelastic instability using broadband passive targeted energy transfers, part 2: experiments. *AIAA journal*, 45(10):2391–2400. *Cited page 27*

[Lee *et al.*, 2005a] Lee, Y. S., Kerschen, G., Vakakis, A. F., Panagopoulos, P., Bergman, L. et McFarland, D. M. (2005a). Complicated dynamics of a linear oscillator with a light, essentially nonlinear attachment. *Physica D: Nonlinear Phenomena*, 204(1-2):41–69. *5 citations pages 10, 18, 19, 24, et 150*

[Lee *et al.*, 2009] Lee, Y. S., Nucera, F., Vakakis, A. F., McFarland, D. M. et Bergman, L. A. (2009). Periodic orbits, damped transitions and targeted energy transfers in oscillators with vibro-impact attachments. *Physica D: Nonlinear Phenomena*, 238(18):1868–1896. *Cited page 15*

[Lee *et al.*, 2007b] Lee, Y. S., Vakakis, A. F., Bergman, L. A., McFarland, D. M. et Kerschen, G. (2007b). Suppression aeroelastic instability using broadband passive targeted energy transfers, part 1: Theory. *AIAA journal*, 45(3):693–711. *Cited page 27*

[Lee *et al.*, 2005b] Lee, Y. S., Vakakis, A. F., Bergman, L. A., McFarland, D. M. et Kerschen, G. t. (2005b). Triggering mechanisms of limit cycle oscillations in a two degree-of-freedom wing flutter model. *In International Design Engineering Technical Conferences and Computers and Information in Engineering Conference*, volume 47381, pages 1863–1872. *Cited page 27*

[Li *et al.*, 2017a] Li, T., Gourc, E., Seguy, S. et Berlioz, A. (2017a). Dynamics of two vibro-impact nonlinear energy sinks in parallel under periodic and transient excitations. *International Journal of Non-Linear Mechanics*, 90:100–110. *2 citations pages 15 et 16*

[Li *et al.*, 2018] Li, T., Lamarque, C.-H., Seguy, S. et Berlioz, A. (2018). Chaotic characteristic of a linear oscillator coupled with vibro-impact nonlinear energy sink. *Nonlinear Dynamics*, 91(4):2319–2330. *Cited page 23*

[Li *et al.*, 2017b] Li, T., Qiu, D., Seguy, S. et Berlioz, A. (2017b). Activation characteristic of a vibro-impact energy sink and its application to chatter control in turning. *Journal of Sound and Vibration*, 405:1–18. *Cited page 119*

[Li *et al.*, 2016] Li, T., Seguy, S. et Berlioz, A. (2016). Dynamics of cubic and vibro-impact nonlinear energy sink: analytical, numerical, and experimental analysis. *Journal of Vibration and Acoustics*, 138(3). *2 citations pages 21 et 25*

[Li *et al.*, 2017c] Li, T., Seguy, S. et Berlioz, A. (2017c). On the dynamics around targeted energy transfer for vibro-impact nonlinear energy sink. *Nonlinear Dynamics*, 87(3):1453–1466. *4 citations pages ix, 15, 16, et 22*

[Li *et al.*, 2017d] Li, X., Zhang, Y., Ding, H. et Chen, L. (2017d). Integration of a nonlinear energy sink and a piezoelectric energy harvester. *Applied Mathematics and Mechanics*, 38(7):1019–1030. *2 citations pages 24 et 28*

[Lian *et al.*, 2018] Lian, J., Zhao, Y., Lian, C., Wang, H., Dong, X., Jiang, Q., Zhou, H. et Jiang, J. (2018). Application of an eddy current-tuned mass damper to vibration mitigation of offshore wind turbines. *Energies*, 11(12):3319. *Cited page 8*

[Lin *et al.*, 2015] Lin, G.-L., Lin, C.-C., Chen, B.-C. et Soong, T.-T. (2015). Vibration control performance of tuned mass dampers with resettable variable stiffness. *Engineering Structures*, 83:187–197. *Cited page 8*

[Liu *et al.*, 2008] Liu, Y., Matsuhisa, H. et Utsuno, H. (2008). Semi-active vibration isolation system with variable stiffness and damping control. *Journal of sound and vibration*, 313(1-2):16–28. *Cited page 8*

[Lu *et al.*, 2017] Lu, X., Liu, Z. et Lu, Z. (2017). Optimization design and experimental verification of track nonlinear energy sink for vibration control under seismic excitation. *Structural Control and Health Monitoring*, 24(12):e2033. *Cited page 28*

[Lu *et al.*, 2014] Lu, Z., Lu, X., Jiang, H. et Masri, S. F. (2014). Discrete element method simulation and experimental validation of particle damper system. *Engineering Computations*. *Cited page 15*

[Malatkar et Nayfeh, 2007] Malatkar, P. et Nayfeh, A. H. (2007). Steady-state dynamics of a linear structure weakly coupled to an essentially nonlinear oscillator. *Nonlinear Dynamics*, 47(1):167–179. *2 citations pages 10 et 20*

[Manevitch, 2001] Manevitch, L. (2001). The description of localized normal modes in a chain of nonlinear coupled oscillators using complex variables. *Nonlinear Dynamics*, 25(1):95–109. *2 citations pages 20 et 35*

[Manevitch *et al.*, 2014] Manevitch, L., Sigalov, G., Romeo, F., Bergman, L. et Vakakis, A. (2014). Dynamics of a linear oscillator coupled to a bistable light attachment: analytical study. *Journal of Applied Mechanics*, 81(4). *Cited page 14*

[Manevitch, 1999] Manevitch, L. I. (1999). Complex representation of dynamics of coupled nonlinear oscillators. *In Mathematical models of non-linear excitations, transfer, dynamics, and control in condensed systems and other media*, pages 269–300. Springer. *Cited page 18*

[Mann et Sims, 2009] Mann, B. et Sims, N. (2009). Energy harvesting from the nonlinear oscillations of magnetic levitation. *Journal of sound and vibration*, 319(1-2):515–530. *3 citations pages ix, 13, et 14*

[Marian et Giaralis, 2014] Marian, L. et Giaralis, A. (2014). Optimal design of a novel tuned mass-damper–inerter (tmdi) passive vibration control configuration for stochastically support-excited structural systems. *Probabilistic Engineering Mechanics*, 38:156–164. *Cited page 7*

[Mattei *et al.*, 2016] Mattei, P.-O., Ponçot, R., Pachebat, M. et Côte, R. (2016). Nonlinear targeted energy transfer of two coupled cantilever beams coupled to a bistable light attachment. *Journal of Sound and Vibration*, 373:29–51. *Cited page 14*

[McFarland *et al.*, 2005a] McFarland, D. M., Bergman, L. A. et Vakakis, A. F. (2005a). Experimental study of non-linear energy pumping occurring at a single fast frequency. *International Journal of Non-Linear Mechanics*, 40(6):891–899. *5 citations pages ix, x, 13, 14, et 26*

[McFarland *et al.*, 2005b] McFarland, D. M., Kerschen, G., Kowtko, J. J., Lee, Y. S., Bergman, L. A. et Vakakis, A. F. (2005b). Experimental investigation of targeted energy transfers in strongly and nonlinearly coupled oscillators. *The Journal of the Acoustical Society of America*, 118(2):791–799. *Cited page 24*

[Mikhlin et Perepelkin, 2011] Mikhlin, Y. et Perepelkin, N. (2011). Non-linear normal modes and their applications in mechanical systems. *Proceedings of the Institution of Mechanical Engineers, Part C: Journal of Mechanical Engineering Science*, 225(10): 2369–2384. *Cited page 19*

[Morlet *et al.*, 1982a] Morlet, J., Arens, G., Fourgeau, E. et Giard, D. (1982a). Wave propagation and sampling theory—part ii: Sampling theory and complex waves. *Geophysics*, 47(2):222–236. *Cited page 24*

[Morlet *et al.*, 1982b] Morlet, J., Arens, G., Fourgeau, E. et Glard, D. (1982b). Wave propagation and sampling theory—part i: Complex signal and scattering in multilayered media. *Geophysics*, 47(2):203–221. *Cited page 24*

[Müller, 1995] Müller, P. C. (1995). Calculation of lyapunov exponents for dynamic systems with discontinuities. *Chaos, Solitons & Fractals*, 5(9):1671–1681. *Cited page 23*

[Musienko *et al.*, 2006] Musienko, A., Lamarque, C.-H. et Manevitch, L. I. (2006). Design of mechanical energy pumping devices. *Journal of vibration and control*, 12(4): 355–371. *Cited page 10*

[Nagarajaiah et Sonmez, 2007] Nagarajaiah, S. et Sonmez, E. (2007). Structures with semiactive variable stiffness single/multiple tuned mass dampers. *Journal of Structural Engineering*, 133(1):67–77. *Cited page 8*

[Nayfeh *et al.*, 1980] Nayfeh, A. H., Mook, D. T. et Holmes, P. (1980). *Nonlinear oscillations*. John Wiley & Sons, Inc., New York. *Cited page 20*

[Neyfeh et Balachandran, 1995] Neyfeh, A. et Balachandran, B. (1995). Applied nonlinear dynamics: analytical, computational and experimental methods. *Cited page 20*

[Nguyen et Pernot, 2012] Nguyen, T. A. et Pernot, S. (2012). Design criteria for optimally tuned nonlinear energy sinks—part 1: transient regime. *Nonlinear Dynamics*, 69(1):1–19. *2 citations pages 31 et 106*

[Nishihara et Asami, 2002] Nishihara, O. et Asami, T. (2002). Closed-Form Solutions to the Exact Optimizations of Dynamic Vibration Absorbers (Minimizations of the Maximum Amplitude Magnification Factors) . *Journal of Vibration and Acoustics*, 124(4):576–582. *Cited page 7*

[Nomura *et al.*, 2007] Nomura, Y., Furuta, H. et Hirokane, M. (2007). An integrated fuzzy control system for structural vibration. *Computer-Aided Civil and Infrastructure Engineering*, 22(4):306–316. *Cited page 9*

[Nucera *et al.*, 2008] Nucera, F., Iacono, F. L., McFarland, D., Bergman, L. et Vakakis, A. (2008). Application of broadband nonlinear targeted energy transfers for seismic mitigation of a shear frame: Experimental results. *Journal of sound and vibration*, 313(1-2):57–76. *Cited page 15*

[Nucera *et al.*, 2007] Nucera, F., Vakakis, A. F., McFarland, D., Bergman, L. et Kerschen, G. (2007). Targeted energy transfers in vibro-impact oscillators for seismic mitigation. *Nonlinear Dynamics*, 50(3):651–677. *Cited page 15*

[Oliva *et al.*, 2017] Oliva, M., Barone, G. et Navarra, G. (2017). Optimal design of nonlinear energy sinks for sdof structures subjected to white noise base excitations. *Engineering Structures*, 145:135–152. *Cited page 31*

[Paredes, 2000] Paredes, M. (2000). *Développement d'outils d'assistance à la conception optimale des liaisons élastiques par ressorts*. Thèse de doctorat, INSA de Toulouse. *Cited page 30*

[Paredes, 2013] Paredes, M. (2013). Analytical and experimental study of conical telescoping springs with nonconstant pitch. *Journal of Mechanical Design*, 135(9): 094502. *Cited page 29*

[Paredes et Rodriguez, 2009] Paredes, M. et Rodriguez, E. (2009). Optimal design of conical springs. *Engineering with computers*, 25(2):147. *3 citations pages x, 29, et 30*

[Parulekar et Reddy, 2009] Parulekar, Y. et Reddy, G. (2009). Passive response control systems for seismic response reduction: A state-of-the-art review. *International Journal of Structural Stability and Dynamics*, 9(01):151–177. *Cited page 7*

[Patil *et al.*, 2015] Patil, R., Reddy, P. et Laxminarayana, P. (2015). Development of buckling equation for conical spring and its experimental verification. *American Journal of Engineering and Technology Research*, 15(1):67–81. *Cited page 29*

[Patil *et al.*, 2014] Patil, R. V., Reddy, P. R. et Laxminarayana, P. (2014). Comparison of cylindrical and conical helical springs for their buckling load and deflection. *International Journal of Advanced Science and Technology*, 73:33–50. *Cited page 30*

[Pennisi *et al.*, 2018] Pennisi, G., Mann, B., Naclerio, N., Stephan, C. et Michon, G. (2018). Design and experimental study of a nonlinear energy sink coupled to an electromagnetic energy harvester. *Journal of Sound and Vibration*, 437:340–357. *3 citations pages x, 25, et 26*

[Peterka, 1996] Peterka, F. (1996). Bifurcations and transition phenomena in an impact oscillator. *Chaos, Solitons & Fractals*, 7(10):1635–1647. *Cited page 125*

[Pilipchuk, 2015] Pilipchuk, V. (2015). Closed-form solutions for oscillators with inelastic impacts. *Journal of Sound and Vibration*, 359:154–167. *2 citations pages 11 et 119*

[Preumont et Seto, 2008] Preumont, A. et Seto, K. (2008). *Active control of structures*. John Wiley & Sons. *Cited page 9*

[Qiu, 2018] Qiu, D. (2018). *Theoretical and experimental study of tuned nonlinear energy sink: application to passive vibration control*. Thèse de doctorat, INSA de Toulouse. *4 citations pages ix, 8, 13, et 75*

[Qiu *et al.*, 2018a] Qiu, D., Li, T., Seguy, S. et Paredes, M. (2018a). Efficient targeted energy transfer of bistable nonlinear energy sink: application to optimal design. *Nonlinear Dynamics*, 92(2):443–461. *5 citations pages ix, 17, 22, 31, et 71*

[Qiu *et al.*, 2019a] Qiu, D., Paredes, M. et Seguy, S. (2019a). Variable pitch spring for nonlinear energy sink: Application to passive vibration control. *Proceedings of the Institution of Mechanical Engineers, Part C: Journal of Mechanical Engineering Science*, 233(2):611–622. *5 citations pages x, 12, 30, 46, et 52*

[Qiu *et al.*, 2018b] Qiu, D., Seguy, S. et Paredes, M. (2018b). Tuned nonlinear energy sink with conical spring: design theory and sensitivity analysis. *Journal of Mechanical Design*, 140(1):011404. *7 citations pages ix, 12, 14, 47, 54, 90, et 140*

[Qiu *et al.*, 2019b] Qiu, D., Seguy, S. et Paredes, M. (2019b). Design criteria for optimally tuned vibro-impact nonlinear energy sink. *Journal of Sound and Vibration*, 442:497–513. *Cited page 31*

[Quinn *et al.*, 2011] Quinn, D. D., Triplett, A. L., Bergman, L. A. et Vakakis, A. F. (2011). Comparing linear and essentially nonlinear vibration-based energy harvesting. *Journal of vibration and acoustics*, 133(1). *Cited page 28*

[Rahman *et al.*, 2015] Rahman, M., Ong, Z. C., Chong, W. T., Julai, S. et Khoo, S. Y. (2015). Performance enhancement of wind turbine systems with vibration control: A review. *Renewable and Sustainable Energy Reviews*, 51:43–54. *Cited page 7*

[Ramlan *et al.*, 2010] Ramlan, R., Brennan, M., Mace, B. et Kovacic, I. (2010). Potential benefits of a non-linear stiffness in an energy harvesting device. *Nonlinear dynamics*, 59(4):545–558. *Cited page 28*

[Reboucas *et al.*, 2018] Reboucas, G. F. d. S., Santos, I. F. et Thomsen, J. J. (2018). Validation of vibro-impact force models by numerical simulation, perturbation methods and experiments. *Journal of Sound and Vibration*, 413:291–307. *Cited page 119*

[Roberson, 1952] Roberson, R. E. (1952). Synthesis of a nonlinear dynamic vibration absorber. *Journal of the Franklin Institute*, 254(3):205–220. *Cited page 12*

[Robertson *et al.*, 2012] Robertson, W., Cazzolato, B. et Zander, A. (2012). Theoretical analysis of a non-contact spring with inclined permanent magnets for load-independent resonance frequency. *Journal of Sound and Vibration*, 331(6):1331–1341. *Cited page 13*

[Rodriguez *et al.*, 2005] Rodriguez, E., Paredes, M. et Sartor, M. (2005). Analytical Behavior Law for a Constant Pitch Conical Compression Spring. *Journal of Mechanical Design*, 128(6):1352–1356. *Cited page 29*

[Romeo *et al.*, 2015a] Romeo, F., Manevitch, L., Bergman, L. et Vakakis, A. (2015a). Transient and chaotic low-energy transfers in a system with bistable nonlinearity. *Chaos: An Interdisciplinary Journal of Nonlinear Science*, 25(5):053109. *2 citations pages 23 et 65*

[Romeo *et al.*, 2015b] Romeo, F., Sigalov, G., Bergman, L. A. et Vakakis, A. F. (2015b). Dynamics of a linear oscillator coupled to a bistable light attachment: numerical study. *Journal of Computational and Nonlinear Dynamics*, 10(1):011007. *3 citations pages 14, 53, et 150*

[Rosenberg, 1960] Rosenberg, R. M. (1960). Normal Modes of Nonlinear Dual-Mode Systems. *Journal of Applied Mechanics*, 27(2):263–268. *Cited page 19*

[Saeed *et al.*, 2020] Saeed, A. S., AL-Shudeifat, M. A., Vakakis, A. F. et Cantwell, W. J. (2020). Rotary-impact nonlinear energy sink for shock mitigation: analytical and numerical investigations. *Archive of Applied Mechanics*, 90(3):495–521. *4 citations pages ix, 13, 21, et 22*

[Saha *et al.*, 2008] Saha, C., O'donnell, T., Wang, N. et McCloskey, P. (2008). Electromagnetic generator for harvesting energy from human motion. *Sensors and Actuators A: Physical*, 147(1):248–253. *Cited page 13*

[Sánchez et Carlevaro, 2013] Sánchez, M. et Carlevaro, C. M. (2013). Nonlinear dynamic analysis of an optimal particle damper. *Journal of Sound and Vibration*, 332(8):2070–2080. *Cited page 15*

[Savadkoohi *et al.*, 2011] Savadkoohi, A. T., Manevitch, L. I. et Lamarque, C.-H. (2011). Analysis of the transient behavior in a two dof nonlinear system. *Chaos, Solitons & Fractals*, 44(6):450–463. *Cited page 16*

[Schleiter et Altay, 2022] Schleiter, S. et Altay, O. (2022). Identification and semi-active control of structures with abrupt stiffness degradations. *Mechanical Systems and Signal Processing*, 163:108131. *Cited page 8*

[Selwanis *et al.*, 2021] Selwanis, M. M., Franzini, G. R., Béguin, C. et Gosselin, F. P. (2021). Wind tunnel demonstration of galloping mitigation with a purely nonlinear energy sink. *Journal of Fluids and Structures*, 100:103169. *Cited page 28*

[Shaw *et al.*, 2013] Shaw, A., Neild, S., Wagg, D., Weaver, P. et Carrella, A. (2013). A nonlinear spring mechanism incorporating a bistable composite plate for vibration isolation. *Journal of Sound and Vibration*, 332(24):6265–6275. *Cited page 14*

[Shaw et Pierre, 1991] Shaw, S. et Pierre, C. (1991). Non-linear normal modes and invariant manifolds. *Journal of sound and Vibration*, 150(1):170–173. *Cited page 19*

[Shaw et Pierre, 1994] Shaw, S. W. et Pierre, C. (1994). Normal modes of vibration for non-linear continuous systems. *Journal of sound and vibration*, 169(3):319–347. *Cited page 19*

[Shi *et al.*, 2018] Shi, W., Wang, L., Lu, Z. et Zhang, Q. (2018). Application of an artificial fish swarm algorithm in an optimum tuned mass damper design for a pedestrian bridge. *Applied Sciences*, 8(2):175. *Cited page 8*

[Sigalov *et al.*, 2012] Sigalov, G., Gendelman, O., Al-Shudeifat, M., Manevitch, L., Vakakis, A. et Bergman, L. (2012). Resonance captures and targeted energy transfers in an inertially-coupled rotational nonlinear energy sink. *Nonlinear dynamics*, 69(4):1693–1704. *Cited page 19*

[Soong et Costantinou, 2014] Soong, T. T. et Costantinou, M. C. (2014). *Passive and active structural vibration control in civil engineering*, volume 345. Springer. *Cited page 9*

[Stanton *et al.*, 2012] Stanton, S. C., Mann, B. P. et Owens, B. A. (2012). Melnikov theoretic methods for characterizing the dynamics of the bistable piezoelectric inertial generator in complex spectral environments. *Physica D: Nonlinear Phenomena*, 241(6): 711–720. *Cited page 23*

[Starosvetsky et Gendelman, 2008] Starosvetsky, Y. et Gendelman, O. (2008). Strongly modulated response in forced 2dof oscillatory system with essential mass and potential asymmetry. *Physica D: Nonlinear Phenomena*, 237(13):1719–1733. *3 citations pages 10, 16, et 37*

[Starosvetsky et Gendelman, 2010] Starosvetsky, Y. et Gendelman, O. (2010). Bifurcations of attractors in forced system with nonlinear energy sink: the effect of mass asymmetry. *Nonlinear Dynamics*, 59(4):711–731. *Cited page 46*

[Stefanski, 2000] Stefanski, A. (2000). Estimation of the largest lyapunov exponent in systems with impacts. *Chaos, Solitons & Fractals*, 11(15):2443–2451. *Cited page 23*

[Stefański et Kapitaniak, 2003] Stefański, A. et Kapitaniak, T. (2003). Estimation of the dominant lyapunov exponent of non-smooth systems on the basis of maps synchronization. *Chaos, Solitons & Fractals*, 15(2):233–244. *Cited page 23*

[Strogatz, 2018] Strogatz, S. H. (2018). *Nonlinear dynamics and chaos with student solutions manual: With applications to physics, biology, chemistry, and engineering*. CRC press. *Cited page 23*

[Sun *et al.*, 2020] Sun, Q., Retnanto, A. et Amani, M. (2020). Seismic vibration for improved oil recovery: A comprehensive review of literature. *International Journal of Hydrogen Energy*, 45(29):14756–14778. *Cited page 7*

[Symans et Constantinou, 1999] Symans, M. D. et Constantinou, M. C. (1999). Semi-active control systems for seismic protection of structures: a state-of-the-art review. *Engineering structures*, 21(6):469–487. *Cited page 9*

[Tian *et al.*, 2019] Tian, W., Li, Y., Li, P., Yang, Z. et Zhao, T. (2019). Passive control of nonlinear aeroelasticity in hypersonic 3-d wing with a nonlinear energy sink. *Journal of Sound and Vibration*, 462:114942. *Cited page 27*

[Touzé et Thomas, 2006] Touzé, C. et Thomas, O. (2006). Non-linear behaviour of free-edge shallow spherical shells: effect of the geometry. *International Journal of non-linear Mechanics*, 41(5):678–692. *Cited page 29*

[Trabelsi, 2014] Trabelsi, H. (2014). *Contribution à la prise en compte d'exigences dynamiques en conception préliminaire de systèmes complexes*. Thèse de doctorat, Ecole Centrale Paris; École nationale d'ingénieurs de Sfax (Tunisie). *Cited page 30*

[Tripathi *et al.*, 2017] Tripathi, A., Grover, P. et Kalmár-Nagy, T. (2017). On optimal performance of nonlinear energy sinks in multiple-degree-of-freedom systems. *Journal of Sound and Vibration*, 388:272–297. *Cited page 10*

[Vakakis, 1997] Vakakis, A. (1997). Non-linear normal modes (nnms) and their applications in vibration theory: an overview. *Mechanical systems and signal processing*, 11(1):3–22. *Cited page 19*

[Vakakis, 2001] Vakakis, A. (2001). Inducing passive nonlinear energy sinks in vibrating systems. *J. Vib. Acoust.*, 123(3):324–332. *Cited page 10*

[Vakakis *et al.*, 2008] Vakakis, A. F., Gendelman, O. V., Bergman, L. A., McFarland, D. M., Kerschen, G. et Lee, Y. S. (2008). *Nonlinear targeted energy transfer in mechanical and structural systems*, volume 156. Springer Science & Business Media. *3 citations pages 16, 31, et 71*

[Wang *et al.*, 2015] Wang, J., Wierschem, N. E., Spencer Jr, B. F. et Lu, X. (2015). Track nonlinear energy sink for rapid response reduction in building structures. *Journal of Engineering Mechanics*, 141(1):04014104. *3 citations pages 10, 12, et 28*

[Wang *et al.*, 2019] Wang, S., Hua, L., Yang, C., Han, X. et Su, Z. (2019). Applications of incremental harmonic balance method combined with equivalent piecewise linearization on vibrations of nonlinear stiffness systems. *Journal of Sound and Vibration*, 441:111–125. *Cited page 20*

[Wang, 2011] Wang, Y. (2011). Time-delayed dynamic output feedback h_∞ controller design for civil structures: A decentralized approach through homotopic transformation. *Structural Control and Health Monitoring*, 18(2):121–139. *Cited page 9*

[Wei *et al.*, 2018] Wei, Y., Dong, X., Guo, P., Peng, Z. et Zhang, W. (2018). Enhanced targeted energy transfer by vibro impact cubic nonlinear energy sink. *International Journal of Applied Mechanics*, 10(06):1850061. *Cited page 118*

[Wierschem *et al.*, 2013] Wierschem, N. E., Hubbard, S. A., Luo, J., Fahnestock, L. A., Spencer Jr, B., Quinn, D. D., McFarland, D. M., Vakakis, A. F. et Bergman, L. A. (2013). Experimental blast testing of a large 9-story structure equipped with a system of nonlinear energy sinks. *In International Design Engineering Technical Conferences and Computers and Information in Engineering Conference*, volume 55997, page V008T13A090. American Society of Mechanical Engineers. *Cited page 28*

[Wierschem *et al.*, 2012] Wierschem, N. E., Quinn, D. D., Hubbard, S. A., Al-Shudeifat, M. A., McFarland, D. M., Luo, J., Fahnestock, L. A., Spencer Jr, B. F., Vakakis, A. F. et Bergman, L. A. (2012). Passive damping enhancement of a two-degree-of-freedom system through a strongly nonlinear two-degree-of-freedom attachment. *Journal of sound and vibration*, 331(25):5393–5407. *Cited page 13*

[Wolf *et al.*, 1985] Wolf, A., Swift, J. B., Swinney, H. L. et Vastano, J. A. (1985). Determining lyapunov exponents from a time series. *Physica D: nonlinear phenomena*, 16(3):285–317. *2 citations pages 23 et 72*

[Wu *et al.*, 2021] Wu, Z., Seguy, S. et Paredes, M. (2021). Basic constraints for design optimization of cubic and bistable nes. *Journal of Vibration and Acoustics*, pages 1–51. *Cited page 139*

[Xiang et Nishitani, 2014] Xiang, P. et Nishitani, A. (2014). Optimum design for more effective tuned mass damper system and its application to base-isolated buildings. *Structural Control and Health Monitoring*, 21(1):98–114. *Cited page 8*

[Yang *et al.*, 2019] Yang, T., Liu, T., Tang, Y., Hou, S. et Lv, X. (2019). Enhanced targeted energy transfer for adaptive vibration suppression of pipes conveying fluid. *Nonlinear Dynamics*, 97(3):1937–1944. *Cited page 27*

[Yang *et al.*, 2015] Yang, Y., Dai, W. et Liu, Q. (2015). Design and implementation of two-degree-of-freedom tuned mass damper in milling vibration mitigation. *Journal of Sound and Vibration*, 335:78–88. *Cited page 8*

[Yao *et al.*, 2002] Yao, G., Yap, F., Chen, G., Li, W. et Yeo, S. (2002). Mr damper and its application for semi-active control of vehicle suspension system. *Mechatronics*, 12(7):963–973. *2 citations pages 8 et 9*

[Yao *et al.*, 2019] Yao, H., Cao, Y., Ding, Z. et Wen, B. (2019). Using grounded nonlinear energy sinks to suppress lateral vibration in rotor systems. *Mechanical systems and signal processing*, 124:237–253. *Cited page 11*

[Yao *et al.*, 2018] Yao, H., Cao, Y., Zhang, S. et Wen, B. (2018). A novel energy sink with piecewise linear stiffness. *Nonlinear Dynamics*, 94(3):2265–2275. *Cited page 12*

[Zang et Chen, 2017] Zang, J. et Chen, L.-Q. (2017). Complex dynamics of a harmonically excited structure coupled with a nonlinear energy sink. *Acta Mechanica Sinica*, 33(4):801–822. *Cited page 16*

[Zhang *et al.*, 2017] Zhang, W., Liu, Y., Cao, S., Chen, J., Zhang, Z. et Zhang, J. (2017). Targeted energy transfer between 2-d wing and nonlinear energy sinks and their dynamic behaviors. *Nonlinear Dynamics*, 90(3):1841–1850. *Cited page 27*

[Zhang *et al.*, 2009] Zhang, W., Yao, M. et Zhang, J. (2009). Using the extended melnikov method to study the multi-pulse global bifurcations and chaos of a cantilever beam. *Journal of Sound and Vibration*, 319(1-2):541–569. *2 citations pages 22 et 23*